Search for Supersymmetry in Tau Lepton Final States with the ATLAS Detector

Dissertation
zur
Erlangung des Doktorgrades (Dr. rer. nat.)
der
Mathematisch-Naturwissenschaftlichen Fakultät
der
Rheinischen Friedrich-Wilhelms-Universität Bonn

von
Steffen Schaepe
aus
Bonn

Bonn, Juni 2015

Dieser Forschungsbericht wurde als Dissertation von der Mathematisch-Naturwissenschaftlichen Fakultät der Universität Bonn angenommen und ist auf dem Hochschulschriftenserver der ULB Bonn `http://hss.ulb.uni-bonn.de/diss_online` elektronisch publiziert.

1. Gutachter:	Prof. Dr. Klaus Desch
2. Gutachter:	Prof. Dr. Norbert Wermes

Tag der Promotion:	04.11.2015
Erscheinungsjahr:	2016

Contents

1

Introduction

The Standard Model of elementary particles and forces is a showcase for a scientific theory. From its first foundations in the early 1960s, the Standard Model has been extended and refined. Since its early days, every experimental finding in particle physics could be described within the Standard Model and many predictions have been successfully tested – up to the discovery of the Higgs boson in 2012 [1].

At the same time, this theory inspired experiments of ever increasing ingenuity and an astonishing race for ever more energy and precision, culminating in the fascinating Large Hadron Collider and its associated experiments. Many technological advances have been made to enable scientists to pursue their curiosity and fill in the last white spaces in the landscape of the Standard Model.

The Standard Model describes the constituents of matter and the interactions between those on a fundamental, microscopic level. Describing the normal, everyday world is achieved with only three matter particles and two interactions. Including radioactivity in the framework requires the introduction of one additional matter particle, one additional interaction and the concept of anti-matter. But the Standard Model offers much more. In a laboratory environment, other, short lived forms of matter can be produced. In fact there are so many possible forms of matter that people referred to them as a "particle zoo" in the late 1960s. Within the Standard Model all of them could be ordered and described by introducing two additional, heavier copies of the particles that make up ordinary matter. Millions of measurements[1] from experiments performed over more than five decades can be described by only three interactions acting on thirteen different particles.

At the same time, it becomes more and more evident that this theory cannot be the "final word" in particle physics. Some evident shortcomings give very strong hints that the present theory is a (tremendously successful!) approximation which will not be able to provide all explanations up to the highest energies. One very promising and arguably the best studied candidate for an extension of the Standard Model is Supersymmetry.

---

[1] INSPIRE-HEP, the international database of particle physics publications contains 1 094 781 entries to date (19th May 2105) [2]. The 2014 edition of the "Review of particle physics" [3] alone includes 3283 new measurements compared to the 2013 edition

There are many possibilities to search for the influence of physics beyond the Standard Model. One approach are indirect searches, where the presence of undiscovered massive particles manifests in a tiny deviation of measured observables from the predictions of the Standard Model. This can be studied in precision measurements, e.g. of the electroweak symmetry breaking or in flavor physics. Another approach are direct searches. Here one uses high energies and high luminosities to directly produce the new particles and observe their decay products. Although the predicted phenomenologies of Supersymmetry vary over a wider range of possible decay signatures, a few properties are likely to occur in many variants. Due to the high mass of the produced new particles, one expects their decay products to carry a large momentum, also and especially in a direction perpendicular to the beam direction (transverse momentum, p_T). Additionally, often the existence of new, weakly interacting particles is predicted. Those particles can escape undetected, causing an imbalance of the measured energy in the transverse plane (missing transverse energy, $\not{E}_T$). For the detection, one can either focus on signatures where the predicted abundance of new particles is as large as possible, or where the expected backgrounds from the Standard Model are minimal. Both approaches come with their own specific challenges and difficulties.

In this thesis, the latter approach is followed. The search for Supersymmetry in events with large missing transverse momentum, jets and at least two tau leptons in $20\,\mathrm{fb}^{-1}$ of $\sqrt{s} = 8\,\mathrm{TeV}$ proton–proton collision data with the ATLAS detector will be described. This particular signature is highly unlikely to occur in the Standard Model but is predicted by many theories of new physics. The topic of this thesis is the last and most mature analysis of a long-term program that followed the ever increasing performance of the Large Hadron Collider and resulted in three publications [4–6] with two more ([7, 8]) being in preparation. Most figures have been produced in this thesis. Figures that are included in refereed publications carry the official "ATLAS" label. The earlier analyses are outlined in detail in the thesis of Dörthe Kennedy [9] and Anthony Rose [10], respectively. The analysis is tailored to be combined with orthogonal search channels for signatures with one single tau [11] and one single lighter lepton plus at least one tau [12]. Some details of the analysis might be easier to understand in the light of this design choice.

Unfortunately, no evidence for any physics beyond the Standard Model is found. However, the non-discovery is translated into a significant reduction of the possible settings of various Supersymmetry scenarios.

In this thesis, first, the Standard Model and Supersymmetry will be explained in Section 2. The tools for the search, the LHC accelerator and the ATLAS detector will be introduced in Section 3. To find the unexpected, it is crucial to understand the expected to a high level of detail. To that end some explanations on the simulation of the Standard Model will be given in Section 4. The main analysis is presented in four steps: A selection is established to isolate configurations that might be promising for catching some glimpses of new physics (Section 5). Then the expected level of background from known processes is estimated (Section 6) together with its uncertainty (Section 7). Finally, those expectations are compared to the experimental observations and consequences for possible supersymmetric models beyond the Standard Model are inferred (Section 8).

2
Theory

The Standard Model (SM) of particle physics describes the fundamental particles and the interaction between them on microscopic level. It is a very successful theory in the sense that nearly all experimental results obtained in laboratory experiments so far can accurately be described within the framework of the SM. The SM has a few shortcomings, however, and it is generally believed to only be a low-energy approximation of a more complex theory.

In this chapter, first the SM is introduced and a short overview of its foundations and features is given. Then a few examples of the shortcomings of the SM are discussed and finally Supersymmetry (SUSY) as one – and arguably the most attractive – possibility for a high-energy completion of the SM is introduced.

2.1 Standard Model of particle physics

In principle, the particle content of the SM can be summarized in one picture (Figure 2.1). It shows an overview of the matter particles (in purple and green) and the messenger particles (in orange). Matter particles are grouped in three families where the respective families only differ in the masses of the particles but are otherwise identical. Ordinary, stable matter is made out of the particles of the first family only. The second and third families have to be produced in experiments and are short-lived. The messenger particles convey different types of interactions between them. Not all matter particles participating in all types of interactions (indicated by the shaded areas).

In the SM, fermions are described by the components of a field Ψ_μ. The kinematics of these field components are determined by the Lagrange density $\mathscr{L}$ via the Euler-Lagrange equations. The Lagrangian has to be invariant under local gauge transformations, which leads to the introduction of additional gauge fields that couple to the fermion fields. These gauge fields can be interpreted as messengers that convey interactions between the fermions.

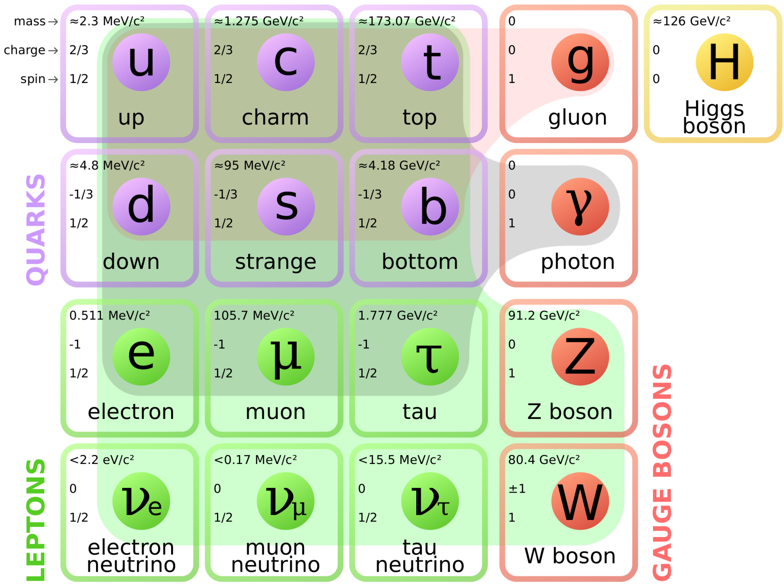

Figure 2.1: Particles of the Standard Model. The overview gives the masses, spins and electric charges of the fermions and bosons of the SM. It also depicts which particles participate in which type of interaction. (from [13])

In the following, a short introduction into the theory behind the SM will be given. The matter particles will be taken for granted[1] and emphasis will be put on the description of the interactions between the particles. The overview is loosely based on [14].

2.1.1 Electroweak interaction

Electrodynamics and the weak interaction originate from two separate ideas. Electrodynamics describes the interactions of electrically charged matter with electric and magnetic fields, while the weak interaction is responsible for e.g. radioactive decays. For electromagnetic interactions, already in the late 1940s there was a working quantum gauge theory (Quantum-Electrodynamics, QED) which described the observable phenomena on a microscopic level. The weak interaction was interpreted as a contact interaction between four fermions without protecting gauge symmetry. This approach has serious flaws, e.g. diverging cross sections for increasing energies. This is remedied by unifying electromagnetic and weak interaction in one quantum field theory with a common set of gauge groups and exchange bosons.

In the following, QED will be briefly presented as an educative example to demonstrate some basic concepts of gauge theories. Following the unification of weak and electromagnetic theory into a consistent picture of both interactions will be outlined.

Quantum-electrodynamics

In classic electrodynamics, the interaction between an electron with four-momentum p^μ and an electromagnetic field A^μ is modeled by replacing the momentum $p^\mu \rightarrow p^\mu + eA^\mu$ [15].

---

[1] The history of the discovery of the various particles and the brilliant ideas behind their detection and classification could easily fill a whole thesis.

For a quantum theory of the electron, the classical equation of motion is replaced by the Dirac-Equation

$$(i\gamma^\mu \partial_\mu - m)\Psi = 0$$

where the partial derivative acting on the electron wave function Ψ replaces the classical momentum. Introducing an electrodynamic interaction analogously to the classical case, one can replace the momentum operator to obtain

$$(i\gamma^\mu(\partial_\mu - ieA_\mu) - m)\Psi = 0.$$

This ad-hoc description can also be obtained from first principle. In general, physical observables are independent of phases of the wave function, i.e. the transformation $\Psi(x) \to e^{i\alpha}\Psi(x)$ does not alter the free Lagrangian

$$\mathscr{L} = i\overline{\Psi}\gamma^\mu \partial_\mu \Psi - m\overline{\Psi}\Psi.$$

Imposing local gauge invariance, i.e. the invariance of the equations of motion when applying a phase-transformation that is a function of space-time itself $\Psi(x) \to e^{i\alpha(x)}\Psi(x)$, this is obviously not the case for the momentum term in the Lagrangian anymore. The invariance can however be recovered by replacing the derivative with the "covariant derivative"

$$D_\mu = \partial_\mu - ieA_\mu$$

where the auxiliary vector field transforms as $A_\mu \to A_\mu + \frac{1}{e}\partial_\mu \alpha$.

The Lagrangian

$$\mathscr{L} = i\overline{\Psi}\gamma^\mu D_\mu \Psi - m\overline{\Psi}\Psi = \overline{\Psi}(i\gamma^\mu(\partial_\mu - ieA_\mu) - m)\Psi$$

is invariant under the local phase transformation and matches the equation obtained by introducing the external electrodynamic field.

The transformation applied in this case is a general element of the U(1) gauge group. Requiring the invariance of the Lagrangian under transformations from this group, an additional vector field has to be introduced with the properties of the electrodynamic field. Adding a gauge invariant term using the field strength tensor $F_{\mu\nu} = \partial_\mu A_\nu - \partial_\nu A_\mu$ to allow the propagation of the gauge field one obtains the Lagrangian of QED

$$\mathscr{L}_{\text{QED}} = \overline{\Psi}(i\gamma^\mu \partial_\mu - m)\Psi + e\overline{\Psi}\gamma^\mu A_\mu \Psi - \frac{1}{4}F_{\mu\nu}F^{\mu\nu}.$$

The new field can be identified with the photon field, propagating and coupling to charged fields, respectively.

Summarizing the above, an invariance of a freely propagating field under a given group transformation is imposed. To ensure this invariance, an additional field had to be introduced to gauge the transformation. This led to a gauge interaction and is completed by adding a propagation term for the gauge field to the Lagrangian which is invariant under the transformation. This approach is a general description of how the interactions of the fermion fields in the SM are mathematically modeled.

In the case of QED, the gauge field can be identified with the photon. In this theory it is the quantum of the electromagnetic field and conveys the interaction between any charged field by coupling to them. Historically, QED was the first gauge quantum field theory formulated. It allowed precisely calculating and explaining differences between measurements and classical quantum dynamics as e.g. the Lamb shift in the spectrum of the hydrogen atom [16].

One of the virtues of quantum field theories like QED is the possibility to compute prediction of observables in perturbation theory in orders of the coupling constant between the matter fields and the gauge bosons. In leading-order (LO), only the minimal possible number of interactions between the incoming and the outgoing particles is considered. This is represented by tree-like Feynman graphs, where the lines symbolize the propagation of particles and the contact between the lines stands for an interaction. Figure 2.2 a) shows an example for a LO scattering process in QED. The solid lines symbolize the incoming and outgoing fermions, while the dashed line stands for the photon being exchanged. At next-to-leading-order (NLO), one allows for one additional set of interaction. Multiple possibilities exist for one defined process, which all have to be considered. Figure 2.2 b) and c) show two possible NLO graphs for the same process as depicted in 2.2 a). The additional interactions lead to closed loops in the graphs, which is why NLO is frequently referred to as "one-loop order". Going beyond NLO leads to graphs with multiple loops.

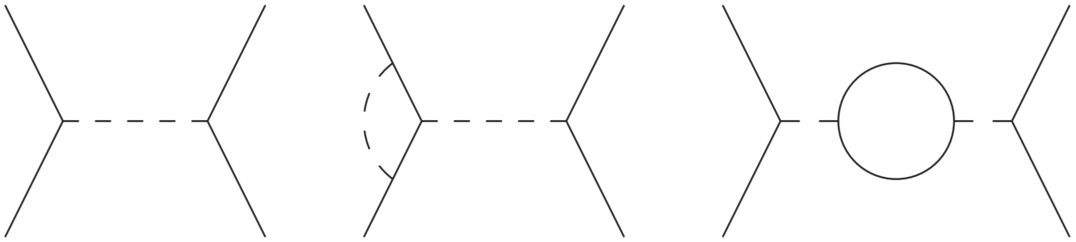

(a) Leading-order (b) Next-to-leading-order vertex (c) Next-to-leading-order propagator

Figure 2.2: Example for Feynman graphs in QED. Figure a) shows a simple scattering process in leading-order. Figures b) and c) show next-to-leading-order versions of the same graph.

Electroweak unification

From experimental results [17, 18] it was known since the 1950s that the weak interaction violates parity and acts only on left-handed particles (and right-handed antiparticles). To reflect this behavior, one can extend the fields that describe the matter content of the SM by splitting them up into a left- and a right-handed component which are treated differently. For a unified theory of weak and electromagnetic interaction, not only the left-handed fields can be considered. Since the electromagnetic coupling does not depend on any parity state, the right-handed fields have to be included as well. For this reason, two symmetry transformations are considered, the SU(2) which acts on the "Isospin" of left-handed fermions only, and the U(1) transformation which is independent on the chirality and acts on the "Hypercharge" [19–21]. Both symmetries come with their own gauge fields, analogously to the introduction of the photon field in QED. The SU(2) has three gauge fields instead of one as in the case of the U(1) symmetry group due to its more complex group structure.

For the leptons, the right-handed electron also couples to the photon, while the right-handed neutrino would not participate in any interaction and is not included in the Standard Model[2]. This finding has to be reflected in the electroweak theory as well. The left-handed particles are grouped into doublets (ν_L, ℓ_L) which are subject to both the isospin and the hypercharge interaction while the right-handed

---

[2] Note that within the SM neutrinos are massless and a right-handed neutrino would not even couple to gravity.

charged lepton ℓ_R carries only a hypercharge. The resulting Lagrangian

$$\mathscr{L}_{\text{ew}} = \left(\overline{\nu}_L, \overline{\ell}_L\right) \gamma^\mu \left(i\partial_\mu - g\frac{\vec{\tau}}{2} \cdot \vec{W}_\mu - g'\frac{Y_L}{2} B_\mu\right) \begin{pmatrix} \nu_L \\ \ell_L \end{pmatrix} +$$
$$\overline{\ell}_R \gamma^\mu \left(i\partial_\mu - g'\frac{Y_R}{2} B_\mu\right) \ell_R - \frac{1}{4}\vec{W}_{\mu\nu}\vec{W}^{\mu\nu} - \frac{1}{4}B_{\mu\nu}B^{\mu\nu}$$

with

$$B^{\mu\nu} = \partial^\mu B^\nu - \partial^\nu B^\mu \qquad \text{and} \qquad W_i^{\mu\nu} = \partial^\mu W_i^\nu - \partial^\nu W_i^\mu - g\varepsilon^{ijk} W_j^\mu W_k^\nu$$

describes the interaction of the leptons with both the messengers W of the isospin and B of the hypercharge interaction. $\vec{\tau}$, ε^{ijk} and g are the generators, structure constants and coupling of the SU(2) symmetry and $Y_{R/L}$ and g' are the charge and the coupling of the U(1) symmetry.

Obviously, this introduces four new vector fields W_1^μ, W_2^μ, W_3^μ and B^μ, which do not correspond to the observed gauge Bosons $W^\pm$, Z and γ, so these fields mix to obtain the physical fields:

$$W_\mu^\pm = \frac{1}{\sqrt{2}}\left(W_\mu^1 \mp iW_\mu^2\right)$$

$$\begin{pmatrix} A_\mu \\ Z_\mu \end{pmatrix} = \begin{pmatrix} \cos\theta_W & \sin\theta_W \\ -\sin\theta_W & \cos\theta_W \end{pmatrix} \begin{pmatrix} B_\mu \\ W_\mu^3 \end{pmatrix}$$

The weak mixing angle θ_W also relates the couplings to the electric charge

$$g\sin\theta_W = g'\cos\theta_W = e.$$

For quarks, the electroweak interaction works very similarly. Left-handed up- and down-type quarks are grouped into an SU(2) doublet, while all right-handed quarks remain singlets only coupling to the hypercharge. An additional complication arises from the fact that all quarks have masses. In general, the mass eigenstates and the eigenstates under the electroweak interaction do not have to be identical. In the lepton sector, there is no mass eigenstate for the up-type fermions, the neutrinos. Accordingly, for those particles only the weak eigenstate is well defined.

In the quark sector, the up-type quarks are chosen to have congruent mass- and electroweak eigenstates. The full SU(2) doublets are the pairs

$$\begin{pmatrix} u \\ d' \end{pmatrix}, \begin{pmatrix} c \\ s' \end{pmatrix}, \begin{pmatrix} t \\ b' \end{pmatrix}$$

where the down-type coupling eigenstates are related to the mass eigenstates by the Cabibbo-Kobayashi-Maskawa matrix [22, 23] (CKM matrix)

$$\begin{pmatrix} d' \\ s' \\ b' \end{pmatrix} = \begin{pmatrix} V_{ud} & V_{us} & V_{ub} \\ V_{cd} & V_{cs} & V_{cb} \\ V_{td} & V_{ts} & V_{tb} \end{pmatrix} \begin{pmatrix} d \\ s \\ b \end{pmatrix}.$$

2.1.2 Strong interaction

In the 1960s a wealth of new particles with similar properties was discovered in accelerator experiments ("particle zoo"). Soon it became evident that these particles could not be fundamental and there had to be an underlying structure. It was proposed that all the observed particles were actually composites of a few fundamental "quarks" [24, 25]. By introducing an ordering scheme, one could relate a zoo of observed states to only three underlying quarks that were combined in states of either three quarks or one quark and one antiquark [26]. This approach is somewhat similar to the arrangement of the chemical elements in the periodic table of elements [27] according to the configuration of their electron shell. The quark model became widely accepted when the Ω^- state that was predicted by the model, but not yet discovered, was observed with exactly the properties predicted by the quark model [28].

The force needed to bind the quarks can neither be the electromagnetic nor the weak force since both of them are too weak for that purpose. It is hence called the "strong" interaction. From observations within the quark model[3], one can conclude that the charge of quarks under the strong force has to have three values [29], called "red", "blue" and "green".

The corresponding gauge symmetry is a $SU(3)_c$ transformation. Requiring the Lagrangian of "Quantum Chromodynamics" (QCD) [30] to be invariant under this transformation one obtains the form

$$\mathscr{L}_{\text{QCD}} = \overline{q}(i\gamma^\mu\partial_\mu - m)q - g_s(\overline{q}\gamma^\mu T_a q)G^a_\mu - \frac{1}{4}G^a_{\mu\nu}G^{\mu\nu}_a$$

with $G^a_{\mu\nu} = \partial_\mu G^a_\nu - \partial_\nu G^a_\mu - g_s f_{abc} G^b_\mu G^c_\nu$. Here q is the quark field (there are actually six of them, one for each quark flavor), G_μ the massless gluon field, g_s the coupling constant and T_a and f_{abc} the generators and structure constants of the $SU(3)_c$, respectively. To preserve invariance, one has to introduce eight gluons which all carry a color charge themselves. Note that the quark fields are still subject to the electroweak interaction as well, i.e. each quark field also has a left- and right-handed component that couple to the gauge bosons of the electroweak interaction!

In a very simplified way this Lagrangian can be described as

$$\mathscr{L}_{\text{QCD}} = \text{“}\overline{q}q\text{”} + \text{“}G^2\text{”} + g_s\text{“}\overline{q}qG\text{”} + g_s\text{“}G^3\text{”} + g_s^2\text{“}G^4\text{”}$$

with the corresponding graph representations:

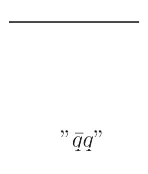

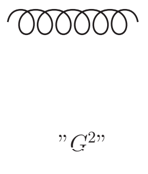

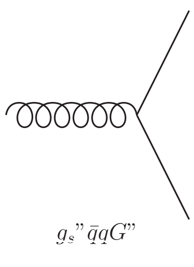

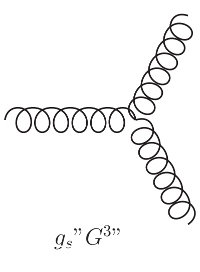

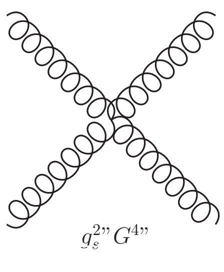

While the first three graphs represent the propagation of quarks and gluons and the coupling of a gluon to a quark, the latter two graphs represent the self-coupling of gluons, which is unique to QCD. This self-coupling of the force carriers has some implications on the nature of the strong force. Despite the gluons

---

[3] I.e. the existence of the Δ^{++} resonance of the proton is only possible if the strong interaction part of its wave function is antisymmetric which is not possible with a "normal" charge with only two values.

being massless, the range of the strong interaction is very limited. When separating two color-charged quarks, the self-coupling of the gluons leads to a very strong force between the quarks which increases with the distance. The energy of the binding eventually surpasses the threshold for the production of additional quark-antiquark pairs. Those additional colored particles bind with the separated quarks, thus preventing the observation of bare color charge ("confinement").

QCD features a strongly running of the coupling constant α_s (c.f. Figure 2.3), which is large at low energies and small at high energies. As a consequence, at very short length scales and corresponding high momenta the quark can be considered as free ("asymptotic freedom" [31, 32]). The perturbative description of QCD is hence only possible at high energies. At low energies the coupling becomes too large, forcing quarks into bound states of three quarks ("baryon") or a quark and an antiquark ("meson"). Phenomenological approaches like the "Bonn Model" [33–35] are needed to describe the masses and decays of these bound states.

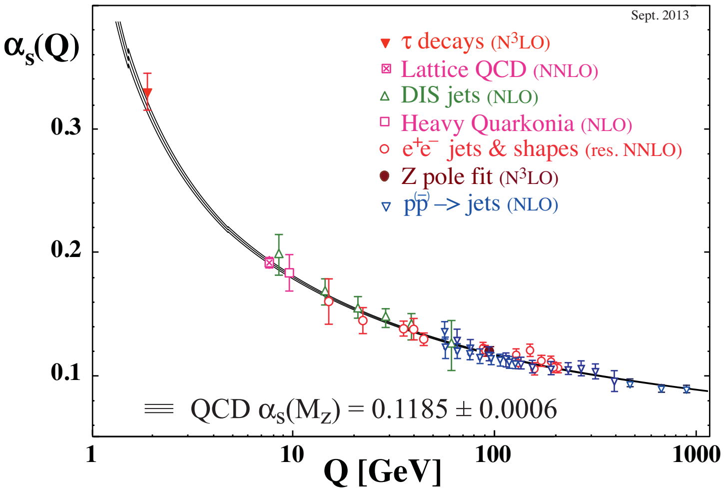

Figure 2.3: "Running" of the strong coupling constant α_s as measured by various experiments (figure from [3]).

A direct consequence of the coupling of the strong force is the structure of the proton. In a naive quark model, it consists of two up quarks and one down quark, bound together by gluons. This picture does not fit the results of scattering experiments at a broad range of energies and values of momentum transfer, which revealed that the picture is more complex. Due to increasing coupling strength at low energies, virtual quark-antiquark pairs can be created and annihilated and gluons can be radiated and absorbed. In that picture, the proton consists of a wealth of different quarks of all flavors and gluons ("partons"). If two protons collide, only two of the partons collide and the rest of the partons remain relatively unaffected by the collision ("spectators"). The cross section for producing any particle X in a proton–proton collision $\sigma_{pp\to X}$ can be factorized as

$$\sigma_{pp\to X} = \sum_{a,b} \int_0^1 \int_0^1 \mathrm{d}x_1 \mathrm{d}x_2 f_a(x_1, Q^2) f_b(x_2, Q^2) \hat{\sigma}_{ab\to X}(\hat{s}).$$

Here a, b denote the partons, x_1 and x_2 the fraction of the proton momentum that is carried by one parton and $\sqrt{\hat{s}} = \sqrt{x_1 x_2}\sqrt{s}$ the available center of mass energy for a collision of two partons from two protons with the full center of mass energy $\sqrt{s}$. The proton structure is described by means of “parton distribution functions” (PDFs) $f_a(x,Q^2)$ which parametrize the probability to find a parton a with a momentum fraction x in a scattering process with momentum transfer Q^2. The PDFs cannot be computed from theory but have to be parametrized from measurements. One examples of proton PDFs at two different Q^2 are displayed in Figure 2.4. A precise knowledge and understanding of the proton PDFs is essential for the interpretation and simulation of proton–proton collisions.

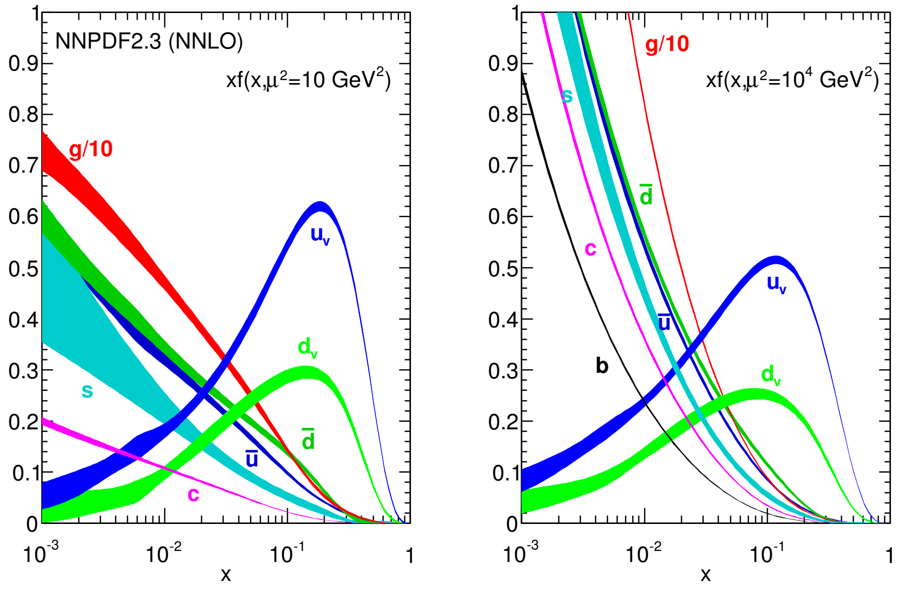

Figure 2.4: Parton density functions from a global fit to experimental data with NNPDF 2.3 [36]. Shown is the product of the momentum fraction and actual density function $x \times f(x)$ for two different values of momentum transfer μ(figure from [3]).

2.1.3 Higgs mechanism

None of the Lagrangians formulated above contains any mass terms, except for the QED. The reason for this is that any explicit mass term, for both fermions and gauge bosons is forbidden. For gauge bosons, an explicit mass term would directly break the gauge invariance. For fermions, a mass term would directly lead to a coupling of left- and right-handed fields, which again would break the gauge invariance of the electroweak theory[4]. However, from measurement and practical experience the masses of the fermions and the W and Z is well established. This flaw of the theory is remedied by introducing the Higgs-mechanism [37–40].

---

[4] For this reason an explicit mass term for the electron can be introduced in QED: here the handedness of the fields does not play a role.

In addition to the fields already introduced four new scalar fields are added to the SM, in the form of one weak isospin doublet of complex fields with hypercharge $Y = 1$

$$\phi = \begin{pmatrix} \phi^+ \\ \phi^0 \end{pmatrix}$$

with $\phi^+ = \frac{1}{\sqrt{2}}(\phi_1 + i\phi_2)$ and $\phi^0 = \frac{1}{\sqrt{2}}(\phi_3 + i\phi_4)$.

Additionally to having the normal SM operators acting on the Higgs field, a potential $V(\phi)$ is introduced containing a "mass" and a "self-interaction" term:

$$\mathscr{L}_{\text{Higgs}} = \left| \left(i\partial_\mu - g\frac{\vec{\tau}}{2} \cdot \vec{W}_\mu - g'\frac{Y_L}{2}B_\mu \right) \phi \right|^2 + V(\phi)$$

with

$$V(\phi) = \mu^2 \phi^\dagger \phi + \lambda (\phi^\dagger \phi)^2.$$

While λ has to be positive for the potential to be bound from below, μ^2 can be chosen to be negative. In that case the potential has a "Mexican Hat" shape. The minimum forms a rim which is not located at the origin but at

$$\langle \phi \rangle = \sqrt{\frac{-\mu^2}{2\lambda}} =: \frac{1}{\sqrt{2}} v.$$

While the potential preserves electroweak symmetry, the ground state does not. Due to the rotational symmetry of the potential the ground state can be chosen anywhere around the rim. It is typically fixed in the neutral part of the doublet to conserve QED symmetry

$$\phi_0 = \frac{1}{\sqrt{2}} \begin{pmatrix} 0 \\ v \end{pmatrix}.$$

This way the electrically charged component of the Higgs field does not acquire a vacuum expectation value which in turn ensures that the photon remains massless.

Fluctuations around the ground state can be parametrized introducing a scalar field h adding to the ground state

$$\phi(x) = \frac{1}{\sqrt{2}} \begin{pmatrix} 0 \\ v + h(x) \end{pmatrix}.$$

Fluctuation in the other three originally introduced fields can be absorbed into a SU(2) phase which by construction leaves the observable physics invariant. Inserting the chosen ground state for ϕ into the Lagrangian $\mathscr{L}_{\text{Higgs}}$, one obtains not only mass terms for the W and B bosons, but also a mass term for the h field and hW^+W^-, hhW^+W^-, hZZ, $hhZZ$ as well as hhh and $hhhh$ couplings. After rotation the masses of the bosons turn out to be

$$m_W = \frac{1}{2} v g, \quad m_Z = \frac{1}{2} v \sqrt{g^2 + g'^2} = \frac{m_W}{\cos\theta_W}, \quad m_\gamma = 0, \quad \text{and} \quad m_h = \sqrt{2\lambda} v.$$

By this construction the electroweak gauge bosons and the Higgs boson[5] acquire their masses. The

---

[5] Note that the mass $m_h = \sqrt{2\lambda} v$ is only valid at leading-order. At higher orders it receives large corrections from loops of all other SM particles which leads to the hierarchy problem (c.f. Section 2.1.5).

fermions are still massless after introducing the Higgs field. The same field can opportunistically also give masses to the fermions of the SM. Due to its quantum numbers the Higgs couples to one isospin doublet and one singlet at a time. The Lagrangian for this “Yukawa” coupling reads (e.g. for the electron)

$$\mathscr{L}_{\text{Yukawa}} = -G_e \left[\left(\overline{\nu}_e, \overline{e}\right)_L \begin{pmatrix} \phi^+ \\ \phi^0 \end{pmatrix} e_R + \overline{e}_R \left(\phi^-, \phi^0\right) \begin{pmatrix} \nu_e \\ e \end{pmatrix}_L \right].$$

Inserting the ground state values this simplifies to

$$\mathscr{L}_{\text{Yukawa}} = -\frac{G_e}{\sqrt{2}} v \left(\overline{e}_L e_R + \overline{e}_R e_L\right) - \frac{G_e}{\sqrt{2}} \left(\overline{e}_L e_R + \overline{e}_R e_L\right) h = -m_e \overline{e} e - \frac{m_e}{v} \overline{e} e h$$

when setting $G_e = \sqrt{2}\frac{m_e}{v}$. The coupling of the fermion fields to the Higgs field provide a mass term for the fermions and a coupling of the fermions to the Higgs boson, where the coupling is proportional to the masses of the fermions. For this reason the observation of the decay of the Higgs boson into two fermions, e.g. in two taus [41], is needed in addition to the observation of the decay into gauge boson to really establish the observed state as the Higgs boson of the SM.

For the quark masses the mechanism works similarly. The only difference is that also the up-type partners of the isospin doublet carry a mass. To give mass to those using the Yukawa couplings, one has to introduce a second Higgs doublet which can be chosen to be essentially the conjugate of ϕ. This results in mass terms and Higgs boson couplings analogously to the electron case.

2.1.4 Physics of the tau decay

The decay of the tau lepton is an interesting and very diverse topic in itself. In contrast to the muon the tau, with a mass of 1.78 GeV, is relatively heavy, so many decay modes are accessible. Due to the importance for the analysis documented in this thesis, a short overview will be given.

The tau always decays weakly into a tau neutrino and a W^* boson. The W in turn decays either to a lepton-neutrino pair or into two quarks (c.f. Figure 2.5 a)). In a hadron collider environment, with the undetermined boost of the initial state, the light lepton decays are barely distinguishable from the direct production of light leptons. Only the hadronic decays are accessible. Figure 2.5 b) gives an overview of the six most abundant decay modes. They represent only a small fraction of the possible decay modes accessible. Reference [3] e.g. lists 131 measured branching fractions and gives upper limits for 39 more. These values are determined from global fits [42] to measurements and limits, mainly obtained at electron-positron colliders designed for the production of hadrons with b-quarks.

Obviously, the main hadronic tau decay modes feature a low number of pions in the final state. Due to charge conservation, an odd number of charged pions has to be included, dominantly one or three of them. The 10% of “other” decay modes comprise also signatures with K-mesons, in total however they only amount to a few percent. The low multiplicity is accompanied by a general “narrowness” of the jets[6] initiated by the hadronic decay products of the tau, which can be used to distinguish taus from quark or gluon jets, as depicted in Figure 2.5 c). Bare quarks and gluons carry a color charge which has to be “dressed” in the observable final object. While the tau is a color neutral singlet, a quark or gluon carries a color charge itself. The color exchange that is needed to achieve a singlet final state in the tau

---

[6] The final states of multiple charged and neutral particles that emerge from the production of a strongly interacting particle or a hadron decay of a tau are referred to as “jets”. For a precise definition c.f. Section 3.3.1.

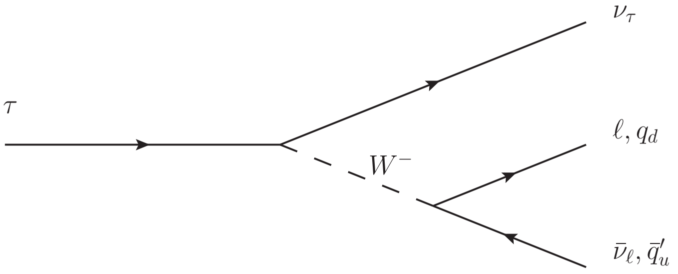

(a) Decay graph

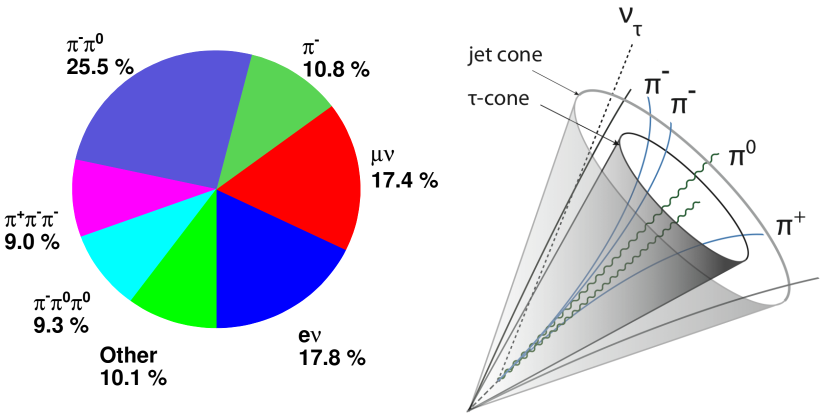

(b) Branching fractions

(c) Difference to quark/gluon jets

Figure 2.5: Physics of the tau decay. Figure a) shows the decay graph while figure b) gives the most important decay channels (numbers from [3]).

decay happens only between the two quarks produced in the weak decay of the tau itself. In the simplest case they can just bind to form a single charged pion.

For a quark- (or analogously gluon-) initiated jet this is not the case. The quark has to interact with another object, either a second quark that is produced at the same time or with the remnants of the proton collisions. This “color flow” is a higher order, low energy QCD effect that has to be modeled phenomenologically (e.g. see [43]). Its effect however is clear: in a jet initiated by a single colored particle, more particles are produced in a wider cone with more activity outside the original direction of the quark, compared to a tau initiated jet.

Naturally, there is a considerable overlap and there are still plenty of jets that look like a tau. For that reason, sophisticated identification techniques are employed to separate jets and taus (c.f. Section 3.3.4). On the other hand, this interplay between tau identification and higher order QCD effects makes the modeling and understanding of how jets can fake taus a very delicate and complicated issue which ultimately causes much of the complications that had to be overcome in this analysis.

2.1.5 Shortcomings of the Standard Model

Despite its tremendous success, the SM has a few shortcomings. One of the most severe ones is the so called “hierarchy problem” [44–47] as e.g. seen in the Higgs mass:

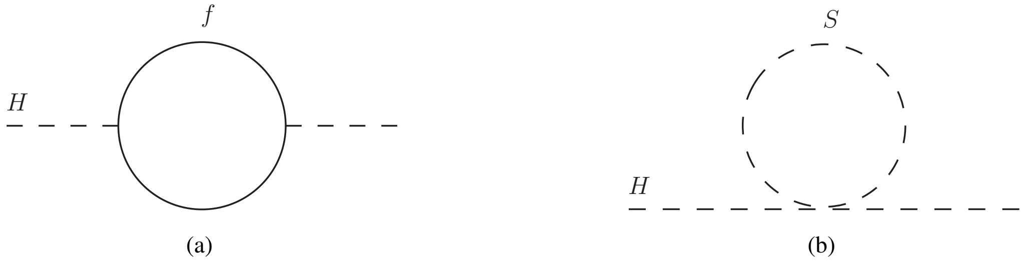

Figure 2.6: One-loop contributions of both fermions (a) and scalars (b) to the Higgs mass. The Higgs boson, being a spin 0 particle, acquires positive mass contributions by both type of graphs leading to the hierarchy problem

Due to the coupling of the Higgs, it acquires mass corrections at one-loop level from every fermion of the SM as depicted in Figure 2.6 a). These corrections are dominated by top quark loops since the t has the largest Yukawa coupling of all SM particles. Assuming the Higgs Yukawa coupling $-\lambda_f H \overline{f} f$, the loop yields a mass correction

$$\Delta m_H^2 = -\frac{|\lambda_f|^2}{8\pi^2}\Lambda_{\mathrm{UV}} + \cdots$$

where Λ_{UV}^2 can be interpreted as the mass scale at which the SM is not valid anymore. This naturally happens at the Planck scale $M_P = 2.4 \times 10^{18}\,\mathrm{GeV}$ where quantum gravity effects become strong. If this was the case, the mass corrections would be some 30 orders of magnitudes larger than the observed Higgs mass which would have to be countered by an appropriate bare mass of the Higgs – an incredible fine-tuning would be needed.

Considering the coupling of a scalar to the Higgs with $-\lambda_S|H|^2|S|^2$ one obtains a one-loop correction

$$\Delta m_H^2 = \frac{\lambda_S}{16\pi^2}\Lambda_{\mathrm{UV}} - \cdots$$

(c.f. Figure 2.6 b)). If one postulates that for each SM fermion there are two scalars with $\lambda_S = |\lambda_f|^2$ (i.e. equal mass due to the Yukawa-couplings to the Higgs field), the contributions to the Higgs mass would naturally cancel without any tuning needed. As will be shown later, this is exactly the effect of Supersymmetry [48–53].

Another shortcoming arises from cosmology: By indirect observations, e.g. of rotational velocities of galaxies, the cosmic microwave background and the expansion of the universe, one can conclude that the universe must contain not only “ordinary” matter but also a kind of weakly interacting “dark matter” and some form of “dark energy”. Latest measurements as depicted in Figure 2.7 show the baryonic content of the universe to contribute less than 5% to the total energy content. But only that part is covered in the SM.

Supersymmetry can provide candidates for the dark matter [55, 56] – although the nature of dark energy remains still mysterious and an exiting topic for future research.

Another shortcoming of the SM is the lack of providing the right structure for unifying the three

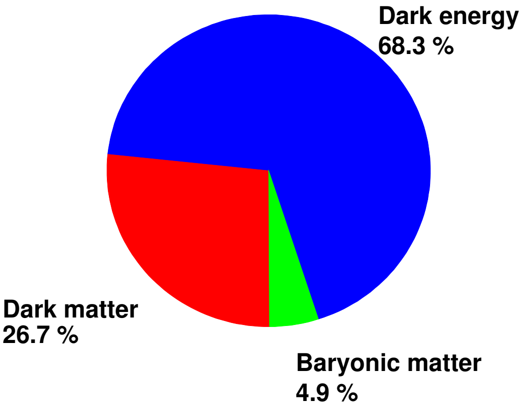

Figure 2.7: Distribution of matter and energy in the universe. Data taken from [54].

known fundamental forces. One of the virtues of the SM is the unification of the weak and the electromagnetic interaction in one common theory. Similarly, one hopes to be able to deduce the electroweak theory and QCD from one common "Grand Unified Theory" (GUT). For this to work the gauge couplings of the three forces have to meet in one point. This is not the case in the SM where there is a few orders of magnitude between the intersection of the running of the three coupling strength (c.f. Section 2.8). Assuming the electroweak precision measurements at LEP, esp. of the electroweak missing angle θ_W, a unification within the SM can be excluded by more than seven standard deviations. Assuming Supersymmetry however, the runnings are modified in a way the couplings unite in one point [52, 57–64]. Assuming a Supersymmetric unification of the coupling allows to obtain a prediction of the electroweak mixing angle at the unification scale, which matches remarkably well to the values measured at existing experiments [65].

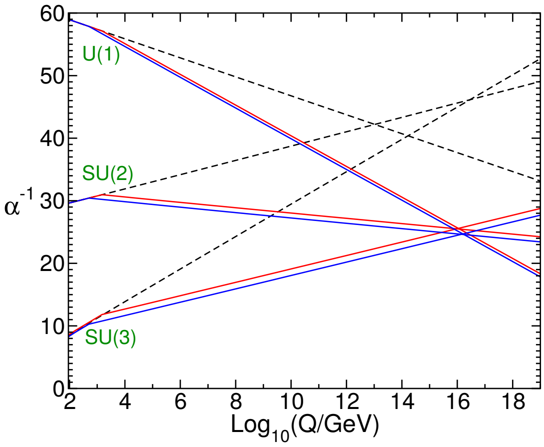

Figure 2.8: Running of the coupling constants of the three fundamental forces with and without Supersymmetry (from [66]).

2.2 Supersymmetry

The concept behind SUSY [67–75] is very simple yet intriguing: A symmetry between bosons and fermions is postulated. A new operator Q is introduced that transfers between fermions and bosons.

$$Q\,|\text{boson}\rangle = |\text{fermion}\rangle\,, \qquad Q\,|\text{fermion}\rangle = |\text{boson}\rangle\,.$$

Due to this transformation properties, Q has to be fermionic itself. SUSY is hence a fermionic extension of the Poincaré spacetime. Indeed, the Coleman-Mandula theorem [76] states that the Poincaré group already contains all possible symmetry generators in four dimensional spacetime. In the Haag-Łopuszański-Sohnius extension [77] it was later laid out that this does only hold for bosonic generators. A full maximal content is only achieved when including one additional fermionic *Supersymmetry* that follows the algebra

$$\begin{aligned}\left\{Q,Q^\dagger\right\} &= P^\mu\\ \{Q,Q\} &= \left\{Q^\dagger,Q^\dagger\right\} = 0\\ [P^\mu,Q] &= \left[P^\mu,Q^\dagger\right] = 0.\end{aligned}$$

Moreover the SUSY generator commutes also with the gauge generators, leading to equal gauge interactions for the SM and SUSY versions of one particle type and the particles are expected to have the same masses.

2.2.1 Minimal Supersymmetric Standard Model

The SM does not offer the particle content to realize the symmetry described before. The particle content is essentially to be doubled resulting in the Minimal Supersymmetric Standard Model (MSSM) [48, 78–81]. For each SM fermion, an additional scalar superpartner is introduced. Since each fermion has essentially two (spin) degrees of freedoms it has to have two superpartners. Conveniently the SM fermions are treated as Weyl spinors in SUSY, e.g. $e = (e_L\, e_R)$, having two components which are eigenstates of the weak interaction instead of spin eigenstates. For each of these components, a superpartner exists, e.g. $\widetilde{e}_L, \widetilde{e}_R$, where the index now purely denotes the charges under the electroweak interaction. Since the partners are scalars, the left and right labeling has no resemblance in helicity.

For each gauge vector boson a fermionic partner is introduced. Since the massless gauge bosons of the SM before electroweak symmetry breaking carry only two possible spin states, the degrees of freedoms even out in the gauge sector.

For the superpartners introduced this way, the following naming convention is commonly used: For fermions the superpartner is denoted with an “s” prefix, e.g. the superpartner of the tau lepton is the “stau”. Generally this convention is also employed when speaking of all fermions (“sfermions”) or all particles in general (“sparticles”). The superpartners of the SM bosons are denoted with an “ino” appendix, i.e. the superpartner of the gluon is called “gluino”. Generally this is also used when referring to a whole class of bosons (“gauginos”).

Also the Higgs sector has to be extended. It can be shown that a SM Higgs in SUSY could cause triangle gauge anomalies, i.e. the gauge invariance in the coupling of three gauge bosons is violated by a Higgs loop. Moreover, the “trick” to provide Yukawa masses to both up- and down-type quarks with one Higgs field using the conjugate does not work with the additional symmetry. Hence two Higgs fields are introduced, one for the up-type fermions H_u with hypercharge $Y = \frac{1}{2}$ and one for the down-type fermions H_d with $Y = -\frac{1}{2}$. Both have a charged and a neutral component.

The SM fields and their SUSY partners are grouped in supermultiplets that share the same charge under the gauge interactions. Table 2.1 lists the chiral supermultiplets that contain a spin-0 and a spin-$\frac{1}{2}$ part and Table 2.2 lists the gauge supermultiplets.

Names		Spin 0	Spin $\frac{1}{2}$	SU(3)$_C$, SU(2)$_L$, U(1)$_Y$
Squarks, quarks	Q	$(\widetilde{u}_L\ \widetilde{d}_L)$	$(u_L\ d_L)$	$(3,2,\frac{1}{6})$
(3 families)	$\bar{u}$	$\widetilde{u}_R^*$	$u_R^\dagger$	$(\bar{3},1,-\frac{2}{3})$
	$\bar{d}$	$\widetilde{d}_R^*$	$d_R^\dagger$	$(\bar{3},1,\frac{1}{3})$
Sleptons, leptons	L	$(\widetilde{\nu}\ \widetilde{e}_L)$	$(\nu\ e_L)$	$(1,2,-\frac{1}{2})$
(3 families)	$\bar{e}$	$\widetilde{e}_R^*$	$e_R^\dagger$	$(1,1,1)$
Higgs, Higgsinos	H_u	$(H_u^+\ H_u^0)$	$(\widetilde{H}_u^+\ \widetilde{H}_u^0)$	$(1,2,\frac{1}{2})$
	H_d	$(H_d^0\ H_d^-)$	$(\widetilde{H}_d^0\ \widetilde{H}_d^-)$	$(1,2,-\frac{1}{2})$

Table 2.1: Chiral supermultiplets in the MSSM together with their transformation properties under the SM gauge interactions and their U(1) hypercharge. Spin-0 fields are complex scalars while spin-$\frac{1}{2}$ are left-handed Weyl spinors (from [66]).

Names	Spin $\frac{1}{2}$	Spin 1	SU(3)$_C$, SU(2)$_L$, U(1)$_Y$
gluino, gluon	$\widetilde{g}$	g	$(8,1,0)$
Wino, W boson	$\widetilde{W}^{(1,2,3)}$	$W^{(1,2,3)}$	$(1,3,0)$
Bino, B boson	$\widetilde{B}^0$	B^0	$(1,1,0)$

Table 2.2: Gauge supermultiplets in the MSSM together with their quantum numbers under the SM gauge interactions (from [66]).

With these supermultiplets, a superpotential can be written as

$$W_{\mathrm{MSSM}} = \bar{u}\mathbf{y_u}QH_u - \bar{d}\mathbf{y_d}QH_d - \bar{e}\mathbf{y_e}LH_d + \mu H_u H_d,$$

in analogy to the Higgs potential and the Yukawa couplings in the SM. Here $\mathbf{y_u}$, $\mathbf{y_d}$ and $\mathbf{y_e}$ are 3×3 matrices in family space which determine the Yukawa couplings after electroweak symmetry breaking. Due to the much larger masses in the third generations it is useful to approximate them in a way that the other families are neglected, i.e.

$$\mathbf{y_u} = \begin{pmatrix} 0 & 0 & 0 \\ 0 & 0 & 0 \\ 0 & 0 & y_t \end{pmatrix}, \quad \mathbf{y_d} = \begin{pmatrix} 0 & 0 & 0 \\ 0 & 0 & 0 \\ 0 & 0 & y_b \end{pmatrix}, \quad \mathbf{y_e} = \begin{pmatrix} 0 & 0 & 0 \\ 0 & 0 & 0 \\ 0 & 0 & y_\tau \end{pmatrix}.$$

Electroweak symmetry breaking is slightly more complicated than in the SM due to the dual Higgs fields. Again, gauge symmetries can be exploited to rotate the ground states into the neutral components of the Higgs doublets. Each of the neutral fields obtains an own vacuum expectation value

$$v_u = \langle H_u^0 \rangle, \qquad v_d = \langle H_d^0 \rangle$$

where the quadratic sum is fixed by the Z mass and the gauge coupling, and the ratio is usually parametrized by an angle β:

$$v_u^2 + v_d^2 = v^2 = 2\frac{m_Z}{g^2 + g'^2} \approx (174\,\mathrm{GeV})^2, \qquad \frac{v_u}{v_d} =: \tan\beta.$$

As in the SM, three of the degrees of freedom of the Higgs field are used to generate the masses of the physical gauge bosons. In SUSY five degrees of freedom remain which yield five physical Higgs bosons, two CP-even scalars h^0 and H^0, one CP-odd scalar A^0 and two charged states H^+ and its conjugate H^-. Commonly h^0 labels the lightest of the Higgs bosons. Its mass is at tree level bound from above by the Z mass. This is, however, not the hard upper bound on the observable Higgs mass. Loops of heavy fermions and scalars, dominantly the top and stop, lead to large positive corrections that result in an upper limit of

$$m_{h^0} \lesssim 135\,\mathrm{GeV}$$

which is in accordance with the determined mass of the neutral particle recently discovered in the search for the SM Higgs boson [1].

2.2.2 External constraints

While the theory presented above is conceptual elegant and highly predictive, it is unfortunately not compatible with all fundamental observations and general theoretical considerations. In the following some constraints are presented that have to be considered when refining the theory.

Experimental considerations

The superpotential introduced in the last section is not complete in the sense that it contains not all terms that are invariant under gauge and SUSY transformations. Terms that violate either lepton number (L) or baryon number (B) conservation have been omitted. Introducing B- or L-violating terms in the theory has dramatic consequences that would render SUSY incompatible with established observations and measurements. Most strikingly an inclusion of all allowed terms would lead to a rapid decay of the proton in contrast to the observed lifetime which has been measured to be larger 2.1×10^{29} years [3]. But also individual L- or B-violating processes that might protect the proton can easily generate predictions that are incompatible with the many measured limits on such decays. In the SM in contrast, there are no allowed terms that violate B or L so their conservation is ensured naturally.

Instead of forcing the conservation of baryon and lepton number individually in the MSSM, one elegant way is to introduce a new fundamental symmetry called *R-parity* which for a particle with spin s is defined as:

$$P_R = (-1)^{3(B-L)+2s}.$$

This symmetry is in fact a kind of SUSY quantum number with all particles of the SM having $R_P = 1$ and all particles added by assuming SUSY having $R_P = -1$. This fundamental symmetry has a few important phenomenological consequences:

- The lightest SUSY particle (LSP) has to be stable. If it is electrically neutral and interacts only weakly with the baryonic matter of the SM, it can provide a viable candidate for cosmological dark matter.
- Each heavier SUSY particle (sparticle) has eventually to decay to an odd number of LSPs and an arbitrary number of particles of the SM.
- In collider experiments, sparticles can only be produced in pairs since they result from a $R_P = 1$ initial state.

Another important constraint comes from the non-observation of SUSY to date. If it was an exact symmetry, a scalar, electrically charged particle of 511 keV mass, the selectron, would have been observed yet. Since this is obviously not the case, SUSY has to be broken in the sense that the superpartners of the SM have to have a different mass. Within the MSSM, SUSY is not broken, so it has to be extended by adding additional fields at a higher mass scale. Indeed many such mechanisms have been proposed and some will be discussed later.

Theoretical considerations

The values of the gauge couplings generally depend on the energy scale they are evaluated at. This behavior is described by the Renormalization Group Equations (RGEs) that quantify the change of the gauge coupling with a change of the momentum scale. The actual running depends on the field content of the theory and hence the gauge couplings of the three fundamental forces g_1, g_2 and g_3[7] unify in SUSY at a scale of about $Q_{\text{GUT}} = 2 \times 10^{16}\,\text{GeV}$ to one common value g_u.

Naturally, one may also assume that the masses of the SUSY fermions and bosons unify to a common mass $m_{1/2}$ and m_0, respectively. The couplings and mass parameters in the soft breaking Lagrangian would thus unify as

$$\left.\begin{array}{l} g_1 = g_2 = g_3 = g_u \\ M_1 = M_2 = M_3 = m_{1/2} \\ \mathbf{m}^2_{\mathbf{Q}} = \mathbf{m}^2_{\mathbf{L}} = \mathbf{m}^2_{\bar{\mathbf{u}}} = \mathbf{m}^2_{\bar{\mathbf{d}}} = \mathbf{m}^2_{\bar{\mathbf{e}}} = m_0^2 \mathbf{1} \end{array}\right\} \text{at } Q \approx 2 \times 10^{16}\,\text{GeV}.$$

The ratios of the gaugino masses and the corresponding couplings are then fixed at any scale to

$$\frac{M_1}{g_1^2} = \frac{M_2}{g_2^2} = \frac{M_3}{g_3^2} = \frac{m_{1/2}}{g_u^2}$$

which yields at the electroweak scale a mass hierarchy of

$$M_3 : M_2 : M_1 \approx 6 : 2 : 1.$$

---

[7] Up to some normalization constants that depend on the theory assumed for the actual unification the three couplings g_1, g_2 and g_3 corresponding to the hypercharge, weak isospin and strong coupling of the SM, respectively.

This has direct phenomenological consequences since the gluino mass that depends strongly on M_3, is much larger than the mass of the other gauginos.

Similar considerations are valid for the scalars. The exact mass hierarchy depends on the breaking mechanism assumed. An example of a mSUGRA scenario is displayed in Figure 2.9. The general hierarchy

$$M_3 > m_{\widetilde{q}} > M_2 > m_{\widetilde{\ell}} > M_1$$

is however quite common for many assumed breaking mechanisms.

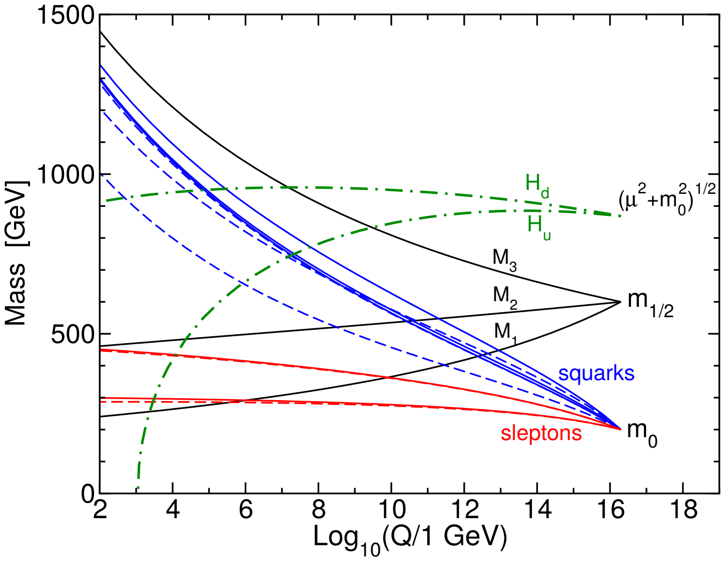

Figure 2.9: RGE running of both scalar and gaugino mass parameters assuming a mSUGRA SUSY breaking mechanism (from [66]).

2.2.3 Mass mixing

As seen in Tables 2.1 and 2.2, the SUSY partners of the Higgs and the electroweak gauge bosons carry the same quantum numbers so they can mix to mass eigenstates called neutralinos (χ^0) for $\widetilde{B}$, $\widetilde{W}^0$ and $\widetilde{H}^0_{u,d}$ and charginos ($\chi^\pm$) for $\widetilde{W}^\pm$ and $\widetilde{H}^\pm_{u,d}$, respectively. In the neutralino sector, the mass matrix is determined by

$$\mathbf{M}_{\widetilde{\chi}^0} = \begin{pmatrix} M_1 & 0 & -c_\beta s_W m_Z & s_\beta s_W m_Z \\ 0 & M_2 & c_\beta c_W m_Z & -s_\beta c_W m_Z \\ -c_\beta s_W m_Z & c_\beta c_W m_Z & 0 & -\mu \\ s_\beta s_W m_Z & -s_\beta c_W m_Z & -\mu & 0 \end{pmatrix}$$

where $s_\beta = \sin\beta$, $c_\beta = \cos\beta$ (β being the angle determining the ratio of the vacuum expectation values of the two Higgs fields), $s_W = \sin\theta_W$, $c_W = \cos\theta_W$ and μ the Higgs mass parameter from the superpotential. The mass matrix can be diagonalized resulting in the masses of the four neutralinos. In scenarios where $m_Z << |\mu \pm M_1|$, $|\mu \pm M_2|$, the mixing results in a dominantly bino-like $\widetilde{\chi}^0{}_1$, a wino-like $\widetilde{\chi}^0{}_2$ and Higgsino like $\widetilde{\chi}^0{}_3$ and $\widetilde{\chi}^0{}_4$. The lightest neutralino is often the lightest SUSY particle and stable in R-parity conserving scenarios. Due to its weak coupling it is a good candidate for dark matter [55, 56].

In the chargino sector, the charge conjugate states have equal masses. The resulting 2×2 mixing matrix can be written in explicit mass terms for the two charginos

$$m^2_{\widetilde{\chi}_1^\pm, \widetilde{\chi}_2^\pm} = \frac{1}{2}\left[|M_2|^2 + |\mu|^2 + 2m_W^2 \mp \sqrt{(|M_2|^2 + |\mu|^2 + 2m_W^2)^2 - 4|\mu M_2 - m_W^2 \sin 2\beta|^2}\right].$$

In the same limit of $m_Z << |\mu \pm M_1|$, $|\mu \pm M_2|$ this yields a wino like $\widetilde{\chi}^\pm{}_1$ and a Higgsino like $\widetilde{\chi}^\pm{}_2$.

Mixing also happens in the fermionic sector of SUSY. Both the Yukawa terms in the superpotential and the trilinear couplings in the soft breaking Lagrangian (c.f. Section 2.2.5) couple left- to right-handed superfields, giving rise to a mixture of the respective sparticles. Due to the large difference between the third family and the lighter families, Yukawa couplings and the strong experimental constraints of flavor changing processes, the mixing is expected to play a role only in the third generation.

Of particular interest for the analysis described here is the mixing of the stau. It is described by the mixing matrix

$$\mathbf{M}^2_{\widetilde{\tau}} = \begin{pmatrix} m^2_{\widetilde{\tau}_L} + m^2_\tau + \Delta_L & m_\tau(A_0 - \mu \tan\beta) \\ m_\tau(A_0 - \mu \tan\beta) & m^2_{\widetilde{\tau}_R} + m^2_\tau + \Delta_R \end{pmatrix}$$

$$\text{with} \qquad \Delta_L = \left(-\frac{1}{2} + \sin^2\theta_W\right) m_Z^2 \cos 2\beta \qquad \text{and} \qquad \Delta_R = \frac{1}{3}\sin^2\theta_W m_Z^2 \cos 2\beta.$$

The off-diagonal elements cause a mixing of the left- and right-chiral states to two mass eigenstates $\widetilde{\tau}_1$ and $\widetilde{\tau}_2$. Depending on the values of the other theory parameters in the mixing matrix, the lighter of these states can be significantly lighter than the chirality eigenstates which automatically renders the $\widetilde{\tau}_1$ the lightest slepton. Since the off-diagonal elements scale with the mass of the SM particle, mixing in the first and second generation can be neglected and the mass eigenstates equal the chiral eigenstates.

Besides the tau, mixing is of particular importance in the top-stop system. For SUSY to provide a viable solution to the hierarchy problem, the superpartners must not acquire too large masses. In practice, the mass corrections to the Higgs boson by top loops matter the most due to the very large Yukawa coupling of the top. Consequently the mass of the lighter stop mass eigenstate is the most relevant mass term in the cancellation by the SUSY partners. At the same time, the large Yukawa coupling of the top results in a large mixing of $\widetilde{t}_L$ and $\widetilde{t}_R$, generally making the $\widetilde{t}_1$ the lightest squark.

2.2.4 The gravitino

SUSY can generally be extended to describe gravity as well by promoting the global symmetry to a local symmetry. This local Supersymmetry is then called *Supergravity* [82–89]. While theoretically of great interest, the general concepts are not very relevant for collider physics, except for the gauge field of the local SUSY transformation. This is the graviton with spin $s_{\text{graviton}} = 2$ and its superpartner, the gravitino, with $s_{\text{gravitino}} = 3/2$.

In unbroken SUSY, the graviton and its superpartner are both massless. However after spontaneous breaking, the gravitino absorbs the degrees of freedoms associated with the breaking ("goldstino"), in the very same way the W and Z absorb degrees of freedom in the electroweak symmetry breaking.

This way it acquires a mass that depends strongly on the scale of the SUSY breaking

$$m_{3/2} \sim \frac{\langle F \rangle}{M_P}$$

where $\langle F \rangle$ is an energy scale associated with the breaking mechanism and M_P is the Planck mass.

While the graviton couples only with gravitational interaction strength, the gravitino can also couple to any particle-sparticle pair via its goldstino component. The exact coupling strength depends on the masses of the involved particles, the gravitino itself and the breaking scale. Generally it is smaller than the MSSM couplings but can be large enough to lead to prompt decays.

2.2.5 SUSY breaking

As already mentioned and shown in detail in [66], the breaking of SUSY cannot be attributed to any possible mechanism inside the MSSM. For general considerations, it is useful to simply parametrize our current ignorance by introducing all possible SUSY breaking terms in the Lagrangian $\mathscr{L}_{\text{soft}}^{\text{MSSM}}$ that are *soft* in the sense that they yield masses of the sparticles that are in the TeV range and still useful for keeping SUSY as a possible solution to the shortcomings of the SM.

$$\begin{aligned}
\mathscr{L}_{\text{soft}}^{\text{MSSM}} = & -\frac{1}{2}\left(M_3\widetilde{g}\widetilde{g} + M_2\widetilde{W}\widetilde{W} + M_1\widetilde{B}\widetilde{B} + \text{h.c.}\right) \\
& -\left(\widetilde{\overline{u}}\mathbf{a_u}\widetilde{Q}H_u - \widetilde{\overline{d}}\mathbf{a_d}\widetilde{Q}H_d - \widetilde{\overline{e}}\mathbf{a_e}\widetilde{L}H_d + \text{h.c.}\right) \\
& -\widetilde{Q}^\dagger\mathbf{m_Q^2}\widetilde{Q} - \widetilde{L}^\dagger\mathbf{m_L^2}\widetilde{L} - \widetilde{\overline{u}}\mathbf{m_{\overline{u}}^2}\widetilde{\overline{u}}^\dagger - \widetilde{\overline{d}}\mathbf{m_{\overline{d}}^2}\widetilde{\overline{d}}^\dagger - \widetilde{\overline{e}}\mathbf{m_{\overline{e}}^2}\widetilde{\overline{e}}^\dagger \\
& -m_{H_u}^2 H_u^* H_u - m_{H_d}^2 H_d^* H_d - \left(bH_uH_d + \text{h.c.}\right).
\end{aligned}$$

$M_{1,2,3}$ denote gaugino mass parameters, $\mathbf{a_{u,d,e}}$ are 3×3 matrices in family space that parametrize trilinear couplings, $\mathbf{m^2_{Q,L,\overline{u},\overline{d},\overline{e}}}$ are again family-space matrices yielding sparticle mass terms and $m^2_{H_u,H_d}$ and b are additional Higgs mass contributions.

The origin of the breaking is transfered into some high-energy “hidden” regime in this approach. The soft SUSY breaking introduces more than 100 additional parameters [90], which make the theory far from predictive. However, there are serious constraints from observation that somehow limit the arbitrariness of the parameter choice. Off-diagonal terms in the mass matrices would directly result in flavor mixing in the SUSY sector. By one-loop effects, this would also propagate into the SM realm which is highly constrained by measurements. Another possible source of flavor mixing are the trilinear couplings. This can be avoided, assuming they are of the same structure as the Yukawa couplings in the superpotential and only differ from them by a common constant factor A_0

$$\mathbf{a_u} = A_0\mathbf{y_u}, \quad \mathbf{a_d} = A_0\mathbf{y_d}, \quad \mathbf{a_e} = A_0\mathbf{y_e}.$$

Besides these considerations, some theoretically well motivated speculations over the origin of the breaking exist and are exploited to generate benchmark simulations searches can be tuned to. These ideas and the resulting signal models are introduced in this section. The theory behind the breaking is only sketched, for a detailed explanation the reader is referred to [66] and the references therein.

Gauge mediated breaking

In Gauge Mediated SUSY Breaking (GMSB) [91–96], the breaking happens in a hidden regime. Here, additional so called "messenger" supermultiplets exist. These multiplets acquire their (very high) mass by coupling to a gauge singlet S. SUSY is broken in this mass generation process by having S acquiring a two-fold vacuum expectation value $\langle S\rangle$ and $\langle F_S\rangle$ that breaks the mass degeneracy for the messenger supermultiplets. For those, the following mass relations hold:

$$m^2_{\text{fermions}} = |y_S \langle S\rangle|^2, \quad m^2_{\text{scalars}} = |y_S \langle S\rangle|^2 \pm |y_S \langle F_S\rangle|.$$

Obviously, the symmetry is broken if $\langle F_S\rangle \neq 0$.

The symmetry is then communicated to the MSSM by loop diagrams, where the MSSM particles couple to messenger loops by means of the normal gauge couplings (hence the name "gauge" mediated). An example is depicted in Figure 2.10. The gaugino mass are generated in one-loop order, whereas the scalar masses need two-loop diagrams.

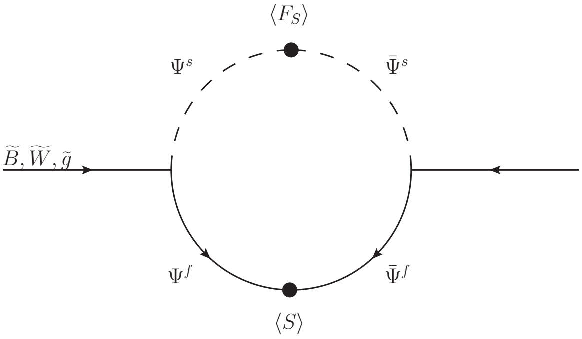

Figure 2.10: Contributions to the gaugino masses by one-loop diagrams in GMSB. Ψ^f and Ψ^s denote the fermionic and scalar content of the messenger multiplets, respectively.

One of the very attractive features of GMSB is that the breaking happens based on the SM quantum numbers so it is intrinsically flavor blind. Many of the simplifying assumptions introduced in Section 2.2.2, especially the suppression of flavor changing terms in the superpotential and the soft breaking Lagrangian, come naturally.

Phenomenology The one distinctive feature of GMSB is the LSP, which is always the gravitino. Since breaking is connected to the GUT scale, well below the Planck scale, the mass of the gravitino is in the keV range. Due to the low coupling of the gravitino, it is only relevant in the last decay in every decay chain which is dominantly the decay LSP → $\widetilde{G}$ where the next-to-lightest SUSY particle (NLSP) decays into the gravitino and a matching SM particle.

GMSB can be described by six parameters only:

$\langle S \rangle$ gives the mass scale of the messenger fields.

Λ denotes the ratio of the two vacuum expectation values associated to the mass-generating supermultiplet S:

$$\Lambda = \frac{\langle F_S \rangle}{\langle S \rangle}.$$

N_5 is the number of messenger fields[8].

$C_{\widetilde{G}}$ is a mass scale parameter for the gravitino.

$\tan\beta$ quantifies the ratio of the vacuum expectation values of the two Higgs fields.

$\mathrm{sgn}(\mu)$ is the sign of the Higgs mass parameter.

The masses of the gauginos and the scalars of the MSSM depend on these parameters. In a simplified approach

$$M_{\text{gauginos}} \propto \Lambda N_5, \qquad M_{\text{scalars}} \propto \Lambda\sqrt{N_5}.$$

Λ and N_5 have the greatest influence on the mass spectrum of a GMSB SUSY model. Λ scales the masses of all sparticles. N_5 determines the hierarchy between gauginos and scalars. The differing dependence is based on the differing loop order in which the messenger fields give mass to the SUSY particles. For $N_5 = 1$ the LSP is a neutralino. In a case of a larger N_5 the gaugino masses increase more than the scalar masses so the lightest scalar, typically the lightest slepton becomes the NLSP. Consequently, the last decay step and by this the phenomenology of the model depend strongly on N_5:

$$\begin{aligned} N_5 = 1: &\qquad \chi_1^0 \to \gamma\widetilde{G} \\ N_5 = 3: &\qquad \widetilde{\ell} \to \ell\widetilde{G} \end{aligned}$$

Also $\tan\beta$ has significant influence on the phenomenology as it determines the mixing. For low values, there is no significant mixing in the stau and the masses of the sleptons are more or less degenerate. For higher values, the mixing increases and the $\widetilde{\tau}_1$ becomes the NLSP.

$\langle S \rangle$ has to be large enough to ensure the messengers do not play a direct role. $\mathrm{sgn}(\mu)$ has relatively little influence on observables at the electroweak scale. $C_{\widetilde{G}}$ determines the lifetime of the NLSP. If it is large, the NLSP is (meta-) stable, resulting in possibly charged, long-lived particles.

For the analysis of this thesis, a GMSB model is chosen with

$$N_5 = 3, \qquad \langle S \rangle = 250\,\text{TeV}, \qquad C_{\widetilde{G}} = 1, \qquad \mu > 1.$$

Λ is varied between 40 TeV and 110 TeV while the $\tan\beta$ range is scanned between 2 and 62. Figure 2.11 gives an overview of the resulting grid.

Within the grid, areas of different NLSPs are marked. For very low Λ, there is still a neutralino NLSP. This area is not considered in this analysis since there are no taus present in the final state. For the rest of the grid, the nature of the NLSP depends on $\tan\beta$. For low values there is a co-NLSP zone

---

[8] The index '5' is linked to the assumed unification of the SM couplings in a SU(5) GUT at the breaking scale.

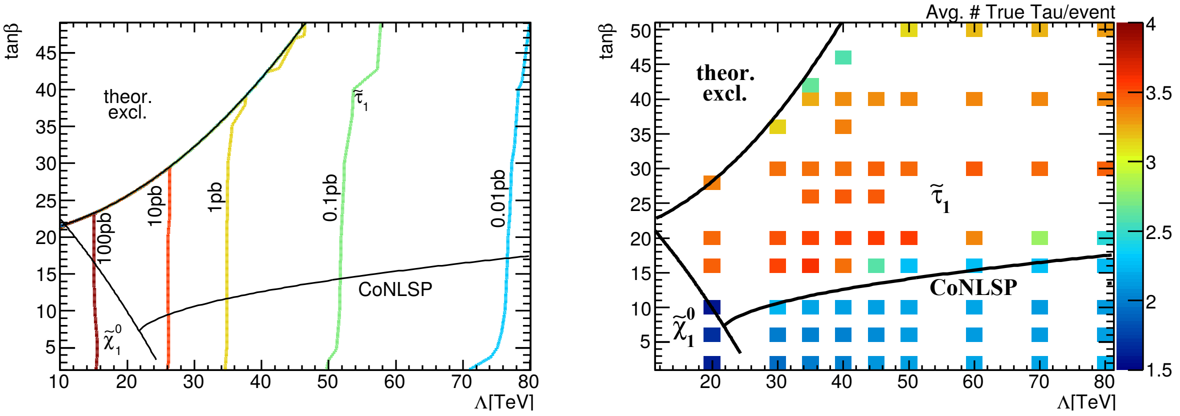

(a) NLO cross section

(b) Average number of taus

Figure 2.11: NLO cross section (a) and average number of true taus with $p_T > 20\,\mathrm{GeV}$ per event for the GMSB grid. The study is based on a gird for an earlier analysis but has the same parameter values fixed [97]. The lines in the grid denote regions with varying LSP.

where all sleptons are of essentially equal mass and have hence similar probabilities to decay into the gravitino. For larger $\tan\beta$, the mixing dominates and decreases the mass of the $\tilde{\tau}_1$ so it becomes the dominant NLSP. The three-body-decay of the first and second generation sleptons to a stau, a tau and a light lepton becomes accessible as soon as the mass difference between the slepton generations exceeds 1.8 GeV. Accordingly, the number of taus increases with $\tan\beta$ over the whole grid (c.f. Figure 2.11 b)), reaching a maximum of four (two taus in every decay chain). At the upper border of the grid there is a zone which is excluded theoretically, meaning the parameters yield unphysical mass spectra, e.g. tachyonic states. The cross section in contrast is largely independent on $\tan\beta$ (c.f. Figure 2.11 a)). It depends dominantly on the masses of the squarks and the gluino, which depend only on Λ in the chosen parametrization.

Figure 2.12 displays the mass spectra for two different points in the GMSB grid.

With all it's attractive features, GMSB has one big drawback: Within GMSB it is practically impossible to push the lightest Higgs up to values that it has been found at. For the outlined grid, this tension is simply ignored. There are several ways to achieve physical Higgs masses in GMSB without changing the phenomenology, e.g. by introducing additional vector-like quarks [98]. Thus the general signatures predicted by the GMSB model are still very interesting to search for.

Another way is to modify GMSB in a way it allows for physical Higgs masses. A first step is to relax constraints on the physics in the hidden sector, effectively decoupling the breaking mechanism from its effect at the electroweak scale while still preserving the typical characteristics of a gauge mediated breaking. This class of models is referred to as “General Gauge Mediation” (GGM) [99]. Also this class of models generally fails to accommodate a physical Higgs mass [100]. Consequently they are extended to preserve the characteristics of gauge mediation but treat the masses of the involved particles in a “natural” [101, 102] way keeping only the masses of the particles that are needed to ensure a physical Higgs mass at a low values and decouple the other particles. The resulting class of models is referred to as “Natural Gauge Mediation” (nGM) [103] models.

In nGM, only the stop, the gluino and the Higgsinos have to be light (the gravitino remains the light

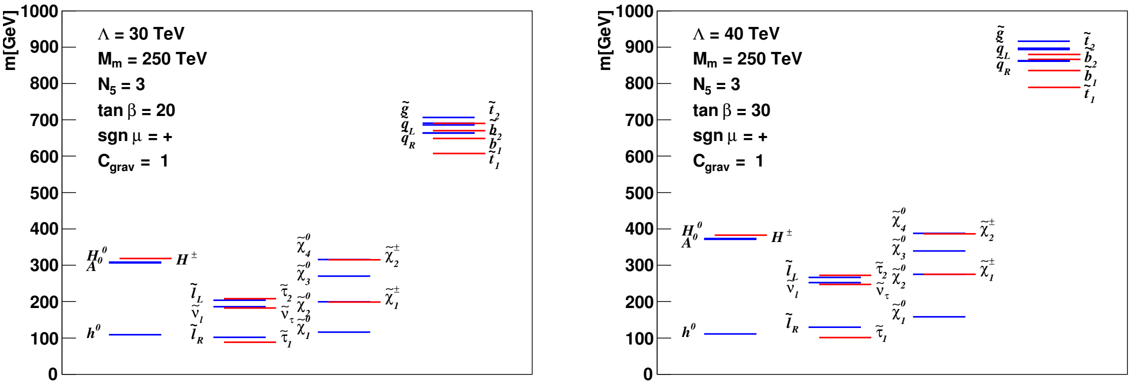

(a) $\Lambda = 30\,\mathrm{TeV}, \quad \tan\beta = 20$

(b) $\Lambda = 40\,\mathrm{TeV}, \quad \tan\beta = 30$

Figure 2.12: Mass spectra for two different points from the GMSB grid.

LSP anyway). All other particles can be decoupled. Additional light particles can be introduced to achieve a certain signature without breaking the naturalness that ensures physical Higgs masses. Here, this is the stau which serves as the NLSP. To ensure conservative limits on the sparticle masses, the nGM scenario is split in two grids, one where only the gluino is light and another where only the stop is light. Only the former case is considered in this analysis, for the latter case another search exploiting the special characteristics of the stop is in preparation. This leaves $m_{\tilde{g}}$ and $m_{\tilde{\tau}}$ as free parameters for the grid. The other parameters are fixed to

$$m_0 = 2.5\,\mathrm{TeV}, \qquad M_1 = M_2 = 2.5\,\mathrm{TeV}, \qquad A_0 = 0, \qquad \mu = 400\,\mathrm{GeV}.$$

As a result, the possible decay modes are

1. $\tilde{g} \to g\tilde{\chi}^0 \to g\tau\tilde{\tau} \to g\tau\tau\tilde{G}$,
2. $\tilde{g} \to qq'\tilde{\chi}^0 \to qq'\tau\tilde{\tau} \to qq'\tau\tau\tilde{G}$,
3. $\tilde{g} \to qq'\tilde{\chi}^\pm \to qq'\nu_\tau\tilde{\tau} \to qq'\nu_\tau\tau\tilde{G}$.

The second and third modes employ an off-shell squark in the first decay. The relative fraction between these three modes depends on the ratio of the gluino and the squark mass parameters. For light gluinos, the first process dominates. As the gluino mass rises that shifts more towards the second and third chain. For $m_{\tilde{g}} > 1\,\mathrm{TeV}$, the latter processes dominate entirely with a roughly equal sharing between them. Quarks in these decays are almost entirely from the third family. Since the gauginos are more or less pure Higgsinos, the decay coupling is of Yukawa type and hence highly enhanced for top and bottom quarks. Due to the large squark masses, certain production modes are suppressed as mentioned in Section 2.2.6.

The choice of μ influences the mass of the chargino and the neutralino. Since those are produced in the first decay step, the choice is somewhat arbitrary as long as they are sufficiently separated from both the gluino and the stau. This has been checked and is the case for $\mu = 400\,\mathrm{GeV}$.

Gravity mediated breaking

Gravity is another possibility to communicate SUSY breaking from a hidden sector to the electroweak scale. In this scenario, the breaking itself usually happens at the Planck scale. The effect is then communicated to the MSSM scale by gravitational interactions, including Supergravity. The general framework is not intrinsically flavor blind, so further assumptions are needed. Often so called "minimal" constraints are imposed leading to minimal Supergravity SUSY breaking (mSUGRA) [104–109].

MSUGRA is highly predictive by reducing the number of free parameters to only five. While in principle the RGEs could start from the breaking scale and parameters could be imposed there, it is common to start from the unification scale instead. In that case, the five parameters are the familiar common scalar mass m_0, the common gaugino mass $m_{1/2}$, the common trilinear couplings A_0 and the two Higgs sector parameters $\tan\beta$ and $\mathrm{sgn}(\mu)$. Figure 2.9 shows an examples of the RGE mass evolution in an mSUGRA scenario with $m_0 = 200\,\mathrm{GeV}$, $m_{1/2} = -A_0 = 600\,\mathrm{GeV}$, $\tan\beta = 10$ and $\mu > 0$.

Due to the high breaking scale, the gravitino does not play a role in mSUGRA. Instead, parameters have to be chosen to ensure the $\widetilde{\chi}^0{}_1$ becomes the LSP to evade cosmological constraints. The mSUGRA scenario has the big advantage that many different phenomenologies can be described within the framework. In contrast to GMSB it is also possible to generate a light Higgs that has a mass of about 126 GeV as measured at the LHC. One choice of parameters that ensures physical Higgs masses over a wide range of m_0 and $m_{1/2}$ values is $\tan\beta = 30$, $A_0 = -2m_0$ and $\mu > 0$. The resulting grid is commonly used in ATLAS for various searches.

Unfortunately, in this scenario the number of taus in the final state is very limited. Although there is a significant tau content for some regions, in general the multiplicity is small so a search for multi-tau final states is not promising.

R-parity violating mSUGRA The picture changes if one allows for R-parity violating (RPV) terms. Originally, R-parity was introduced to protect the proton from decaying and evade bounds from non-observation of lepton or baryon number breaking processes. The same effect can also be achieved by allowing only single terms that violate L or B conservation. One examples of such a theory is bilinear R-parity violation (bRPV) [110, 111] where the superpotential and the soft breaking Lagrangian are extended by one term each

$$W_{\mathrm{bRPV}} = W_{\mathrm{MSSM}} + \varepsilon L H_u, \quad \mathscr{L}_{\mathrm{bRPV}} = \mathscr{L}_{\mathrm{soft}} - B\varepsilon \widetilde{L} H_u.$$

This addition has two effects: first, the neutralinos can mix with the neutrinos. The mixing is effectively extended to have not only the neutral Wino, Bino and the two neutral Higgsinos but also three neutrinos. This offers a very elegant method to generate neutrino masses and predict neutrino mixing parameters. Existing mass and mixing measurements constrain the choice of ε. Second, the term allows a decay of the neutralino LSP in a lepton and a gauge boson. If the gauge boson is not accessible kinematically, a three-body decay via an off-shell W or Z happens. The rest of the mSUGRA determined decay chains are not altered.

The phenomenological consequence is a boost in the numbers of leptons compared to R-parity conserving (RPC) mSUGRA. This comes at the cost of less missing transverse momentum since the neutralino LSP decays and does not leave the detector undetected. However, most of the LSP decays feature one or more neutrinos, so there is still a good chance to get a significant amount of $\not{E}_T$.

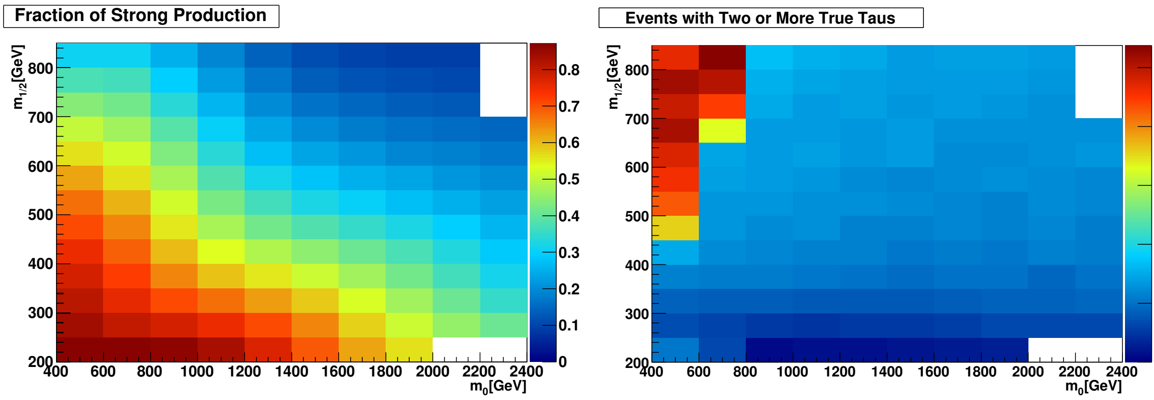

(a) Fraction of strong production

(b) Fraction of events with ≥ 2 taus

Figure 2.13: Characteristics of the bRPV mSUGRA grid. Figure a) shows the fraction of events that are produced via strong interaction and figure b) shows the fraction of events that have at least two true tau leptons in the final state.

Figure 2.13 shows some characteristics about the resulting bRPV mSUGRA grid. For this analysis to be sensitive, production of the SUSY state has to happen via strong interaction to ensure a sufficiently large number of high p_T jets. At the same time, multiple tau leptons are needed to fulfill the search signature. Obviously, there is an exclusion potential in the low m_0 region of the grid.

2.2.6 Supersymmetry at the LHC

The LHC with its unprecedented energy range is an excellent tool to search for evidence for any heavy particle as predicted by SUSY. The general purpose experiments ATLAS and CMS are flexible enough to detect and reconstruct virtually every possible decay topology within SUSY. In the following, production and decay channels as to be expected at the LHC are presented.

Production

With the general properties of SUSY outlined above, the possible signatures in a hadron collider are quite evident.

First, assuming R-parity conservation, sparticles will always be produced in pairs. The production of the partner particles happens via gauge interactions. Since in a hadron collider the initial state carries a color charge, production processes via the strong force will largely dominate. Figures 2.14 and 2.15 show Feynman graphs for the strong production of sparticles from initial states with only gluons or gluons and quarks or only quarks, respectively. Note that in all cases squarks and/or gluinos are produced. The t- and u-channel productions feature a virtual sparticle. For this reason they can be suppressed should the respective sparticle happen to be heavy. This is e.g. the case for the second and third production mode from two quarks in the nGM model.

Apart from the strong interaction, also the electroweak interaction can be responsible for producing sparticles from a hadronic initial state. Due to the lower relative interaction strength, this is generally only relevant when the masses of the sparticles carrying color charge are too large to be accessible at

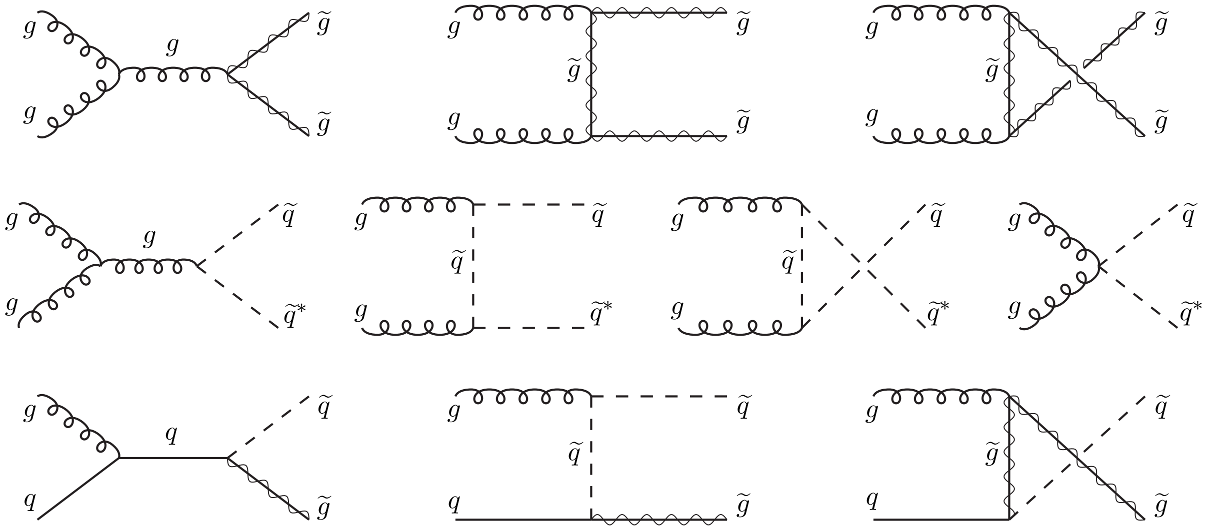

Figure 2.14: Production graphs for SUSY particles that are produced via the strong interaction from initial states with gluons or quarks and gluons (from [66]).

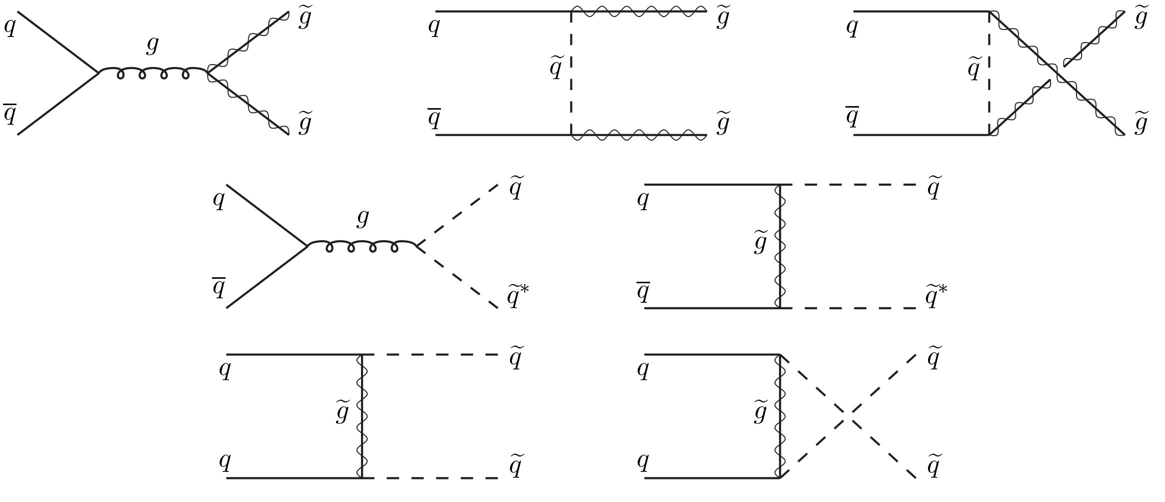

Figure 2.15: Production graphs for SUSY particles that are produced via the strong interaction from initial states with quarks (from [66]).

the available energy. This is e.g. the case for high Λ values in the GMSB scenario. Figures 2.16 depicts the possible weak production modes for sparticles at the LHC. Note that the couplings to charginos and neutralinos can be either a gauge or a Yukawa coupling, depending on the process and the mixing considered.

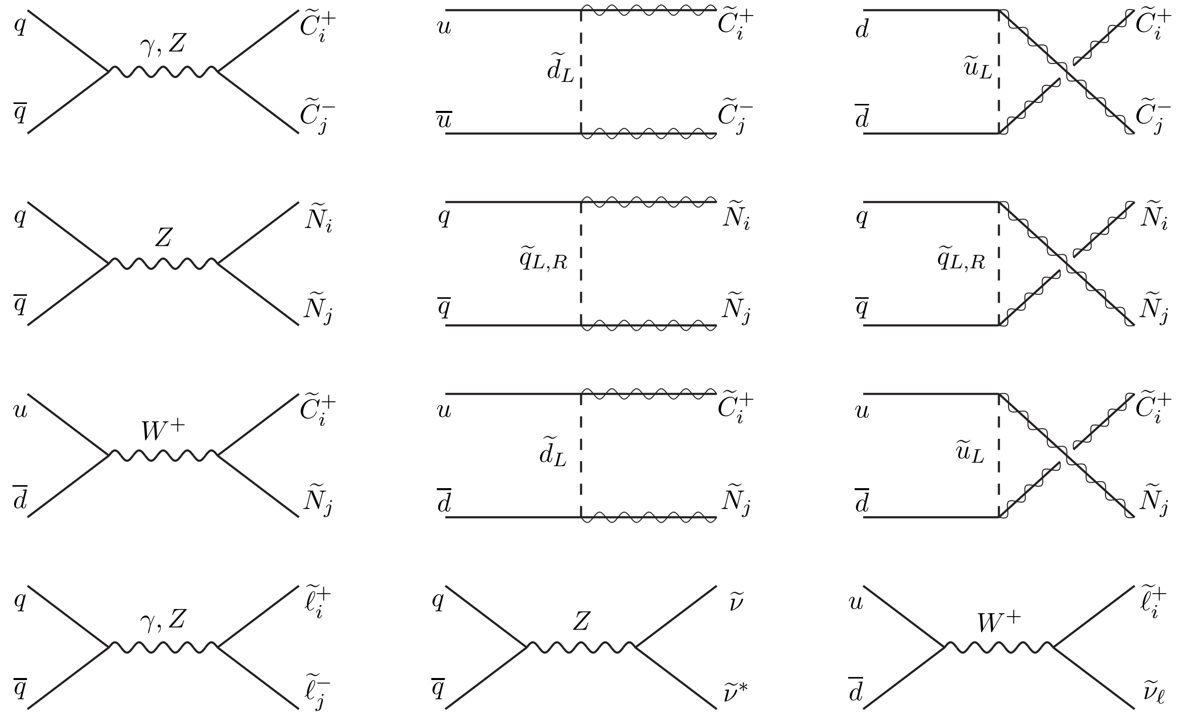

Figure 2.16: Production graphs for SUSY particles that are produced via the electroweak interaction from initial states with quarks. Here, "C" denotes charginos and "N" neutralinos in contrast to the notation used otherwise (from [66]).

Generally, also the associate production of a neutralino or chargino together with a squark or gluino is possible, featuring an even lower cross section than pure electroweak production processes.

Decay

The decay of the sparticles determines the signature observable in the detector.

Assuming the generally plausible mass hierarchy, decay chains start from colored particles. The gluino can only decay in a squark and a quark

$$\widetilde{g} \to \widetilde{q}q.$$

The squark in turn decays electroweakly to either a neutralino or a chargino

$$\widetilde{q} \to \widetilde{\chi}^0 q, \qquad \widetilde{q} \to \widetilde{\chi}^\pm q'.$$

The actual neutralino or chargino generation the squark decays into depends both on the chirality of the squark and the mixing of the gauginos. A right-handed squark will decay preferably in a bino dominated gaugino while a left-handed squark will prefer the stronger isospin coupling and pick a wino dominated state, even if it is more heavily. The Higgsino dominated states play a role only for the third generation squarks since here the Yukawa coupling is of significant strength.

In case of an inverted mass hierarchy in the colored sector, the squark can directly decay into a gluino

$$\tilde{q} \to \tilde{g} q.$$

The gluino in turn can only decay via an off-shell squark in a three body decay

$$\tilde{g} \to \tilde{\chi}^0 q q', \qquad \tilde{g} \to \tilde{\chi}^{\pm} q q'.$$

The neutralinos and charginos decay via their gauge or Higgs content. The most likely two-body decays are

$$\tilde{\chi}^0{}_i \to Z \tilde{\chi}^0{}_j, \quad W \tilde{\chi}^{\pm}{}_j, \quad h^0 \tilde{\chi}^0{}_j, \quad \ell \tilde{\ell}, \quad \nu \tilde{\nu},$$

$$\tilde{\chi}^{\pm}{}_i \to W \tilde{\chi}^0{}_j, \quad Z \tilde{\chi}^{\pm}{}_j, \quad h^0 \tilde{\chi}^{\pm}{}_j, \quad \ell \tilde{\nu}, \quad \nu \tilde{\ell}.$$

The couplings would allow also for the decays into a heavier Higgs boson or a quark and a squark. Due to the common mass hierarchy these decay modes are often highly suppressed or not allowed.

In case there is no open two body decay, e.g. in case of a small splitting between $\tilde{\chi}^0{}_2$ and $\tilde{\chi}^0{}_1$, the heavier sparticle can decay to the lighter one in a three body decay including an off-shell gauge boson or Higgs.

The sleptons decay via electroweak interactions in cases where either a neutralino or chargino is lighter

$$\tilde{\ell} \to \ell \tilde{\chi}^0{}_i, \quad \tilde{\ell} \to \nu \tilde{\chi}^{\pm}{}_i, \quad \tilde{\nu} \to \nu \tilde{\chi}^0{}_i, \quad \tilde{\nu} \to \ell \tilde{\chi}^{\pm}{}_i.$$

Again the generation the slepton decays into depends on the chirality of the slepton and the mixing of the gauginos. Decays via Yukawa couplings to the Higgsino content is highly unlikely due to the relatively small couplings and the usually higher mass of the Higgsino dominated gauginos.

Finally, in cases where the gravitino is light, every sparticle can decay into its SM partner and a gravitino. Since the coupling for this decay is usually very small, it is only significant for the next-to-lightest SUSY particle (NLSP) which has no other decay channel open.

Figure 2.17 shows a typical decay tree for a production of two squarks via gluon fusion in a gauge mediated breaking scenario (explained below) relevant for the analysis described in this thesis. In this case, the gravitino is the LSP and the stau the NLSP. The colored sparticles are heavier than the other particles in the MSSM. This decay would lead to a signature of multiple jets, multiple taus and missing transverse momentum.

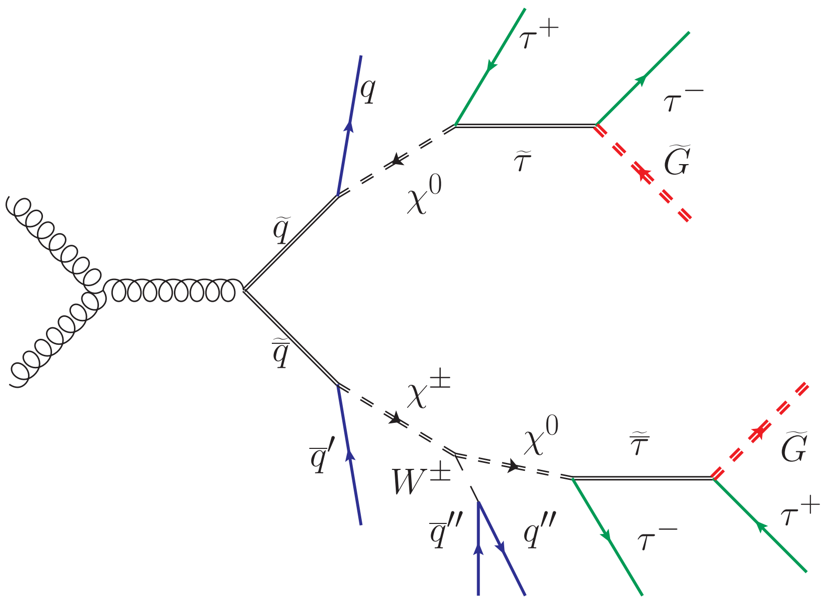

Figure 2.17: Typical decay graph in a GMSB scenario. The blue objects are detectable as jets, the green ones as taus and the red objects cause a signature of missing transverse momentum.

2.2.7 Current status of SUSY

Despite all its theoretical virtues, no sign of SUSY has been observed yet, but many past and present measurements can be used to infer properties of SUSY if it should be existing. These measurements are not limited to the most recent results of direct SUSY searches. On the contrary, low energy measurements, observations from flavor physics, astrophysical constraints and especially the measurement of the SM-like Higgs boson do limit the possible implementations of SUSY severely.

To quantify the impact of all these constraints simultaneously, global parameter fits are performed that use a global likelihood function including a large set of seemingly unconnected measurements. Using these likelihoods, large parameter spaces of various SUSY models are sampled. Involved Monte Carlo techniques are employed to derived preferred corners of the parameter space where the SUSY predictions are at least as compatible with all measurements as the SM and hopefully even allow to incorporate small deviations from the SM predictions. The p-value of individual points to agree with all measurements is assessed using toy Monte Carlo.

Indeed, these studies find that many “high scale” models that make explicit assumptions about the SUSY breaking and predict mass spectra and couplings based on these assumptions – as e.g. mSUGRA – are under severe stress by the current existing set of measurements [113][9]. In Figure 2.18, a parameter scan in the $m_0 - m_{1/2}$ and in the $A_0 - \tan\beta$ planes is displayed. These plots represents two dimensional projections of the total five dimensional scan. For the best fit point, also a distribution for evaluating the p-value for this point is displayed. With $4.9 \pm 0.7\%$ even the best fit point is at the edge of being excluded at 95% C.L.

These type of models cover only a tiny fraction of the possible solutions to the full MSSM. Giving

---

[9] More precisely the constraint MSSM (CMSSM) has been studied in this reference. For all practical purpose the CMSSM is identical to mSUGRA, however.

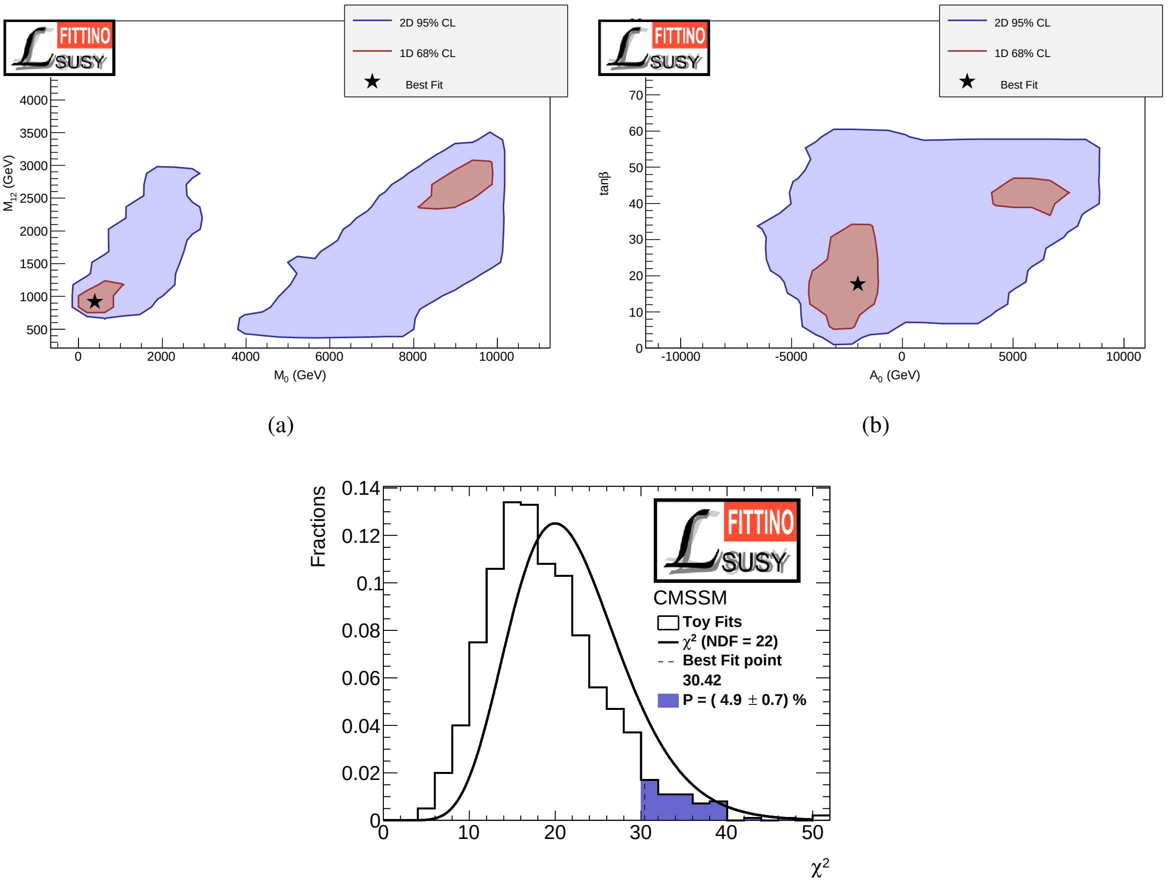

(a)

(b)

(c)

Figure 2.18: Results of the parameter scan for the CMSSM/mSUGRA in the $m_0 - m_{1/2}$ (a) and the $A_0 - \tan\beta$ (b) planes. For the best fit point the distribution used to derive the p-value is also shown. (plots from [112], updated version of the ones included in [113])

up on the high predictive power and only considering the most stringent theoretical constraints (like the suppression of flavor changing processes at low energies), one can construct models like the phenomenological MSSM (pMSSM) [114, 115]. Having in the order of 20 free parameters, this class of models is still not arbitrary, but allows for much more possible mass spectra and coupling structures within the MSSM. Indeed, parameter scans show that within the pMSSM current measurements leave a lot of room for possible realizations of SUSY [116]. Interestingly, even mass spectra that seem to be ruled out by studying other "high scale" models are still perfectly compatible within these more involved scenarios. In case of the MSSM, gluino masses down to 1 000 GeV and stau masses down to 100 GeV are perfectly valid, which is well below the range that is excluded in typical high scale model searches.

2.3 Background processes

Estimating background contributions and their uncertainties is a major part of every search for new physics. With the sufficient knowledge about the physics of the SM, one can identify the contributions that are likely to dominate one respective search. In this analysis, the signature is defined by the presence of two tau leptons, large missing transverse momentum and at least one high p_T and one additional jet.

Figure 2.19 gives an overview of various SM processes and their production cross section as measured by the ATLAS experiment. For comparison, typical a typical cross section for SUSY production has been added to the figure.

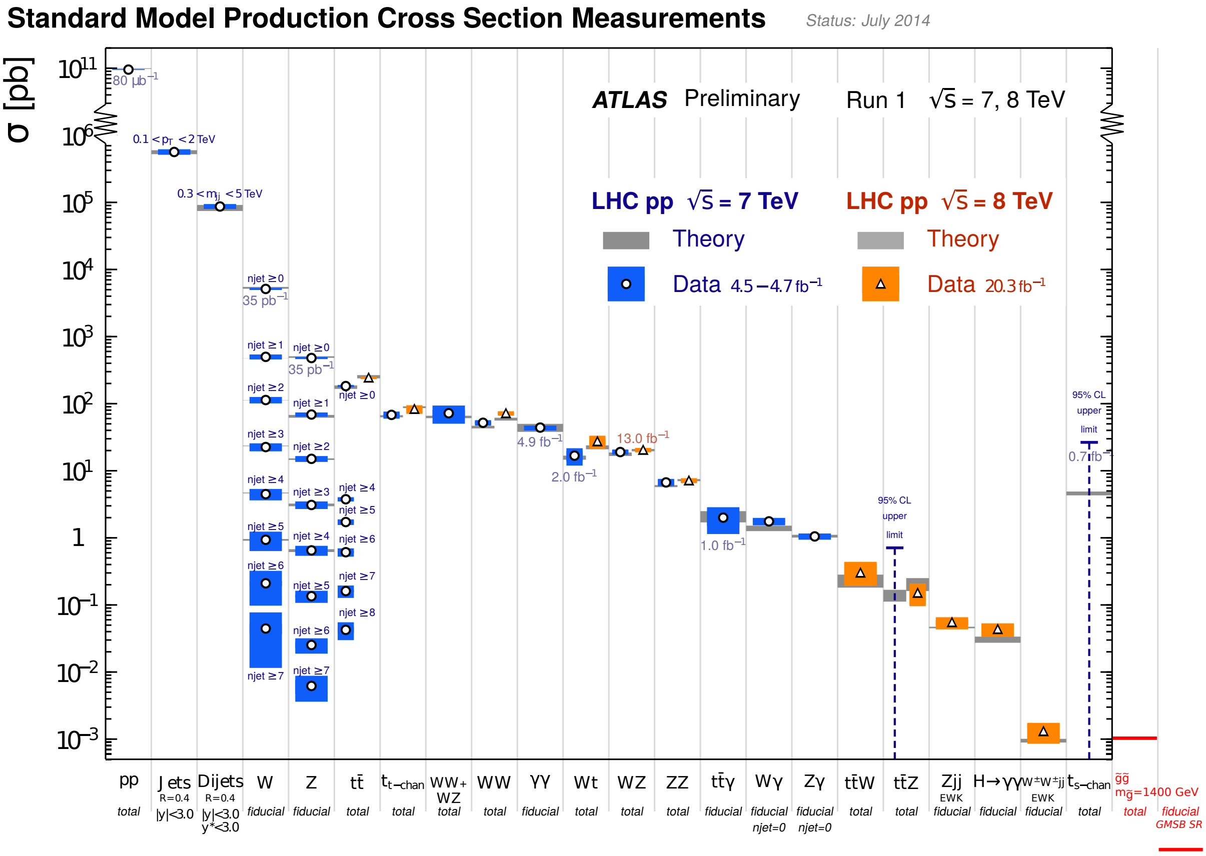

Figure 2.19: Summary of several Standard Model total and fiducial production cross section measurements, corrected for leptonic branching fractions, compared to the corresponding theoretical expectations. All theoretical expectations were calculated at NLO or higher. The W and Z vector-boson inclusive cross sections were measured with 35 pb^{-1} of integrated luminosity from the 2010 dataset. All other measurements were performed using the 2011 dataset or the 2012 dataset. The luminosity used for each measurement is indicated close to the data point. Uncertainties for the theoretical predictions are quoted from the original ATLAS papers. They were not always evaluated using the same prescriptions for PDFs and scales. For the di-jets measurement, $y^* = |y_1 - y_2|/2$ [117]. To the right a typical SUSY production and fiducial cross section (production of a gluino pair with $m_{\tilde{g}} = 1400\,\text{GeV}$, assuming an acceptance of 2% , c.f. Section 8.2) has been added to the overview, showing the relative magnitudes of the searched-for signal.

The largest cross section by far is attributed to the production of multiple jets. Luckily, the acceptance for multijets production is highly suppressed in the studied final state since it contains neither taus nor any possible source of missing transverse momentum. Hence both tau leptons and $\not{E}_T$ have to result from mis-measurements and/or mis-identification. Despite this suppression, this background cannot be neglected no matter how small the mis-identification probabilities for the underlying objects are due to the huge cross section for multijets production.

The next process in the cross section ranking is the production of a W boson. Due to the analysis requirements, additional jets are needed to produce a sufficiently high number of hadronic objects (jets or taus with hadronic decays). Figure 2.20 displays three example Feynman graphs for the various decay modes of the W with the minimal number of jets from initial state and final state radiation needed to yield enough objects.

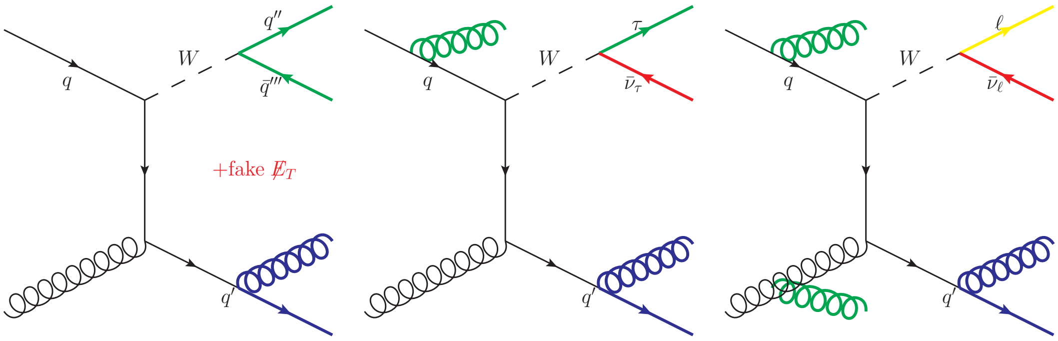

(a) (b) (c)

Figure 2.20: Example production graphs for W+jets production with four hadronic objects in the final state. The blue objects are detectable as jets, the green ones as taus and the red objects cause a signature of missing transverse momentum. Yellow objects must not be reconstructed. a) shows the case where the W decays into two quarks. Two taus have to be mis-identified and $\not{E}_T$ has to arise from a mis-measurement of the jets. b) shows the case where the W decays into a τ and a neutrino. One additional jet from ISR/FSR is needed, but only one tau has to arise from mis-identification and the neutrino causes real $\not{E}_T$. c) shows the case where the W decays into a light lepton. Here again two taus have to be faked, an additional jet is needed and the light lepton must escape detection.

In the case of a W decay into quarks, one additional jet is needed resulting in the highest cross section. The final state contains neither taus nor any source of $\not{E}_T$ and is indistinguishable from pure multijets production (without any specialized selection), which has a far higher cross section still. In the case where the W decays into a tau and a neutrino, two additional jets are needed reducing the cross section significantly. This final state has one true tau and a neutrino as source of $\not{E}_T$, so only one tau has to be faked by a quark or gluino. In practice, the latter is the only relevant decay mode for this search.

The signature where the W decays into a light lepton and a neutrino can be neglected for all practical purpose. Not only is even one more additional jet needed reducing the cross section even further, but again two taus have to be faked and the light lepton must not be detected – which is highly unlikely due to the large efficiency of the corresponding reconstruction algorithms. For this reason, signatures with light leptons will be neglected in the description of the following processes.

Following in the cross section ranking is the production of Z bosons. Figure 2.21 displays possible minimal Feynman graphs of different decay modes.

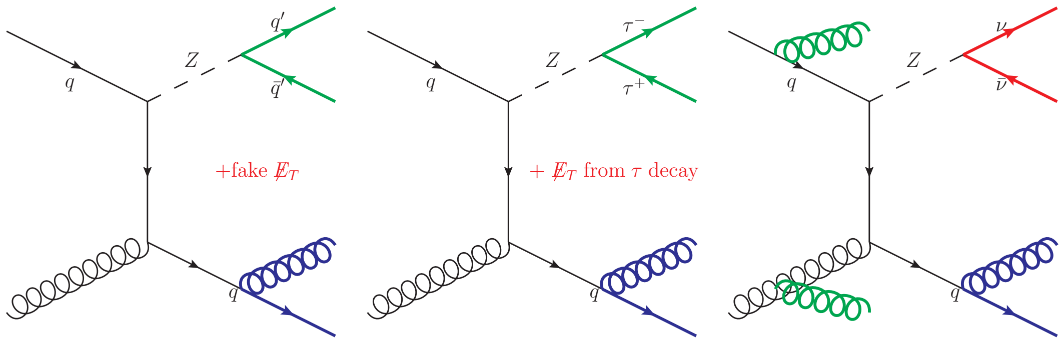

(a) (b) (c)

Figure 2.21: Example production graphs for Z+jets production with four hadronic objects in the final state. The blue objects are detectable as jets, the green ones as taus and the red objects cause a signature of missing transverse momentum. a) shows the case where the Z decays into two quarks. Two taus have to be mis-identified and $\not\!\!E_T$ has to arise from a mis-measurement of the jets. b) shows the case where the Z decays into two τ. Here two real tau leptons are present and the neutrinos from the tau decays causes real $\not\!\!E_T$. c) shows the case where the Z decays into two neutrinos. Here again two taus have to be faked and two more jets are needed but the neutrinos cause real $\not\!\!E_T$. Decay modes into light leptons are omitted due to the small probability to miss a light lepton in the reconstruction.

Again, the decay modes into two quarks results in the same signature as for W+jets with a quark decay of the W or pure multijets production. More relevant are signatures where the Z decays into two taus. Here, all requested final state objects are really present without the need for any fakes. Since the neutrinos from the τ decays are the only source of missing energy, these events can rather efficiently be rejected with a suitable selection (c.f. Section 5). Topologies with invisible Z decays into neutrinos are in contrast much more likely to produce sufficiently high and well isolated $\not\!\!E_T$. Here again, two tau candidates have to be faked by other hadronic objects and two additional jets are needed.

Next in the list of cross sections is the production of $t\bar{t}$. Figure 2.22 again shows some minimal examples. Since in this case two vector bosons are involved, there are many possible combinations.

The remaining contributions are a multijets-like signature and signatures involving real tau leptons. The case where both top decay into a tau and a neutrino is a priory irreducible and has to be reduced by a suitable selection. The configuration where one top decays hadronically needs in contrast a fake tau to pass the selection. Due to the higher branching ratio of the quark decay and the relatively weak rejection power of the tau identification employed in this search, this process is still relevant and has to be considered. In general, $t\bar{t}$ production is distinguishable from other SM backgrounds by the presence of two b-jets. Unfortunately, this is also the case for many SUSY scenarios that favor third generation sparticles. For this reason b-jets will not be used as a selection characteristics in this analysis, but to separate W+jets from $t\bar{t}$ events in control and validation measurements.

From the long list of other SM processes also Dibosons production can yield irreducible backgrounds. Since the production cross section is rather low, especially since at least two additional jets have to be present, this process constitutes only a minor background source, compared to $t\bar{t}$.

Other backgrounds like the decay of a Standard Model Higgs into two tau leptons, low-mass Drell-Yan production and associate production of $t\bar{t}$ with a vector boson have been checked and found to be negligible.

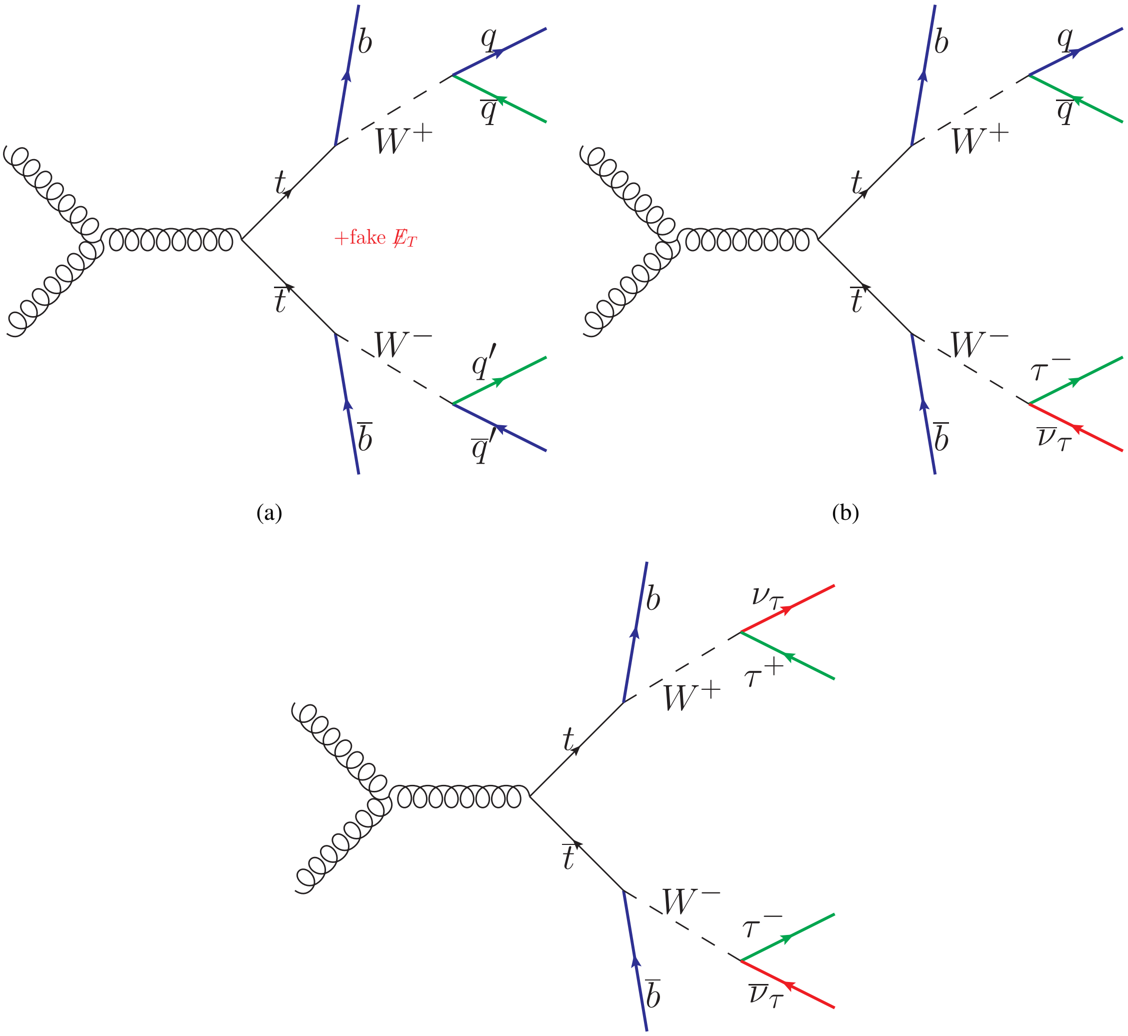

(a) (b)

(c)

Figure 2.22: Example production graphs for $t\bar{t}$ production with four hadronic objects in the final state. The blue objects are detectable as jets, the green ones as taus and the red objects cause a signature of missing transverse momentum. a) shows the case where both top quark decay into two quarks (plus a b-jet). Two taus have to be mis-identified and $\not\!\!E_T$ has to arise from a mis-measurement of the jets. b) shows the case where one top decays into a τ and a neutrino (plus a b-jet) and the other decays into a b-jet and two quarks. One tau has to arise from mis-identification and the neutrino causes real $\not\!\!E_T$. c) shows the case where both top quarks decay into a τ and a neutrino (plus a b-jet). All final state objects are present without the need for any fakes. Combinations with decay modes into light leptons are omitted due to the small probability to miss a light lepton in the reconstruction.

3
Experimental setup

The presence of SUSY will most likely manifest itself in the presence of distinct decay patterns of previously not observed heavy particles. To be able to find SUSY in this way one has to be able to produce these particles, to measure the signatures of the decay products, and to reconstruct their properties. These three experimental requirements are excellently fulfilled in the Large Hadron Collider accelerator and the ATLAS detector, which are presented in the following, together with the techniques used to reconstruct and identify individual objects from the measured signatures.

3.1 The LHC accelerator

The Large Hadron Collider (LHC) [118] is an accelerator and collider which is located in an underground tunnel of 27 km circumference at the Swiss-French border near Geneva. The LHC consists of two rings where protons with energies of up to 7 TeV are stored and collided. The protons are grouped in 2808 “bunches” which are separated by 25 ns[1].

The protons are accelerated to 450 GeV in the injector complex comprising the Proton Synchrotron Booster (PSB) [119], the Proton Synchrotron (PS) [120] and the Super Proton Synchrotron (SPS) [121] (c.f. Figure 3.1). At the same time, the bunch structure for the LHC is created by staggering subsequent fills of one accelerator in the next, larger accelerator. The beam is then guided to the LHC, where it is then accelerated to the desired energy. The beam circulates clockwise in one of the rings and counterclockwise in the other.

For the acceleration of charged particles with charge q, the energy gain on passing an electric field $\vec{E}$ over a distance s

$$\Delta E_{\text{kin}} = \int_{\vec{s}} \left(\vec{F} \cdot \mathrm{d}\vec{s} \right) = q \int_{\vec{s}} \left(\vec{E} \cdot \mathrm{d}\vec{s} \right)$$

---

[1] For the 2012 running data which this thesis is based on the beam energy was 4 TeV with a 50 ns bunch spacing

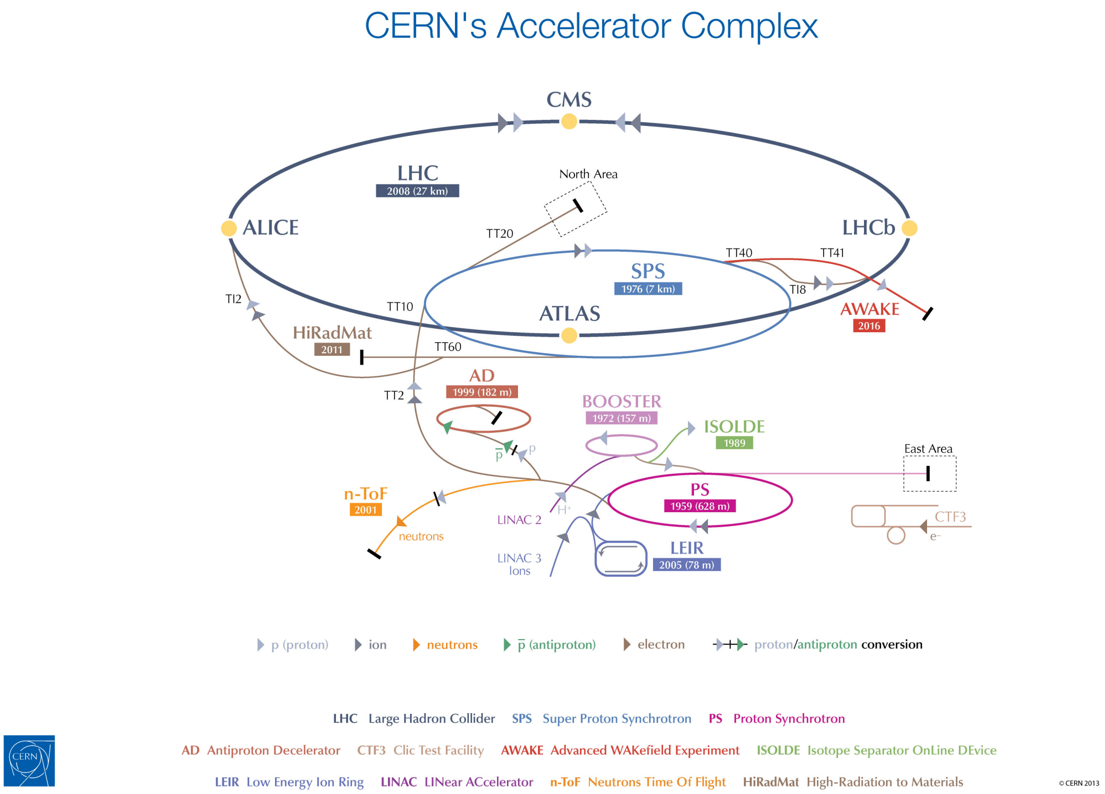

Figure 3.1: CERN's accelerator complex including the LHC and its injectors [122].

is exploited. Technically this is realized by feeding high frequency radio waves to a cylindrical cavity. With an appropriate design, a standing wave forms inside the cavity with a longitudinal component on the axis where the particles pass. For an accelerating effect, the protons have to be in phase with the field in the cavities. The LHC uses eight superconducting cavities per ring which are fed by a 400.8 MHz microwave source and which create a gradient of 5.5 MV/m. By guiding the protons in a ring, the same cavities are passed many times and accelerate the beam at each revolution until the desired beam energy is reached. Alternatively, one can also build a linear accelerator with a large straight line equipped with many cavities[2], which is however less cost-effective for the acceleration of protons.

A charged particle moving with velocity $\vec{v}$ experiences a force in a magnetic field $\vec{B}$ perpendicular to its direction of movement and the direction of the magnetic field line.

$$F_{\text{Lorentz}} = q\left(\vec{v} \times \vec{B}\right)$$

This Lorentz force is exploited to guide charge particles in an arc in the field of magnetic dipoles ultimately forming a full circle. The LHC uses 1232 dipole magnets of 15 m length each. The coils are made of superconducting Niobium-Titanium cable which is cooled down to 1.9 K, making the LHC the

---

[2] For the next large electron–positron collider, a linear accelerator is indeed the favored option. Currently there are two proposed projects, CLIC [123] and the ILC [124].

largest cryogenic installation world wide [125]. The dipoles are able to generate a field of up to 8.36 T and feature a special "two in one" design which allows both beams with particles of the same charge circulating in opposite direction to be deflected in only one magnet.

Magnets are not only used to deflect but also to focus the protons. With a combination of magnetic quadrupole structures, a net focusing effect in all directions can be achieved. Aberrations that occur in the focusing and other disturbances of the beam quality are remedied by introducing higher order multipole magnets. The LHC has 858 quadrupoles and uses multipoles up to dodecapoles.

When deflecting charged particles they lose energy which they radiate off as synchrotron radiation. The energy loss for relativistic particles ($v \approx c$) with mass m in a circular accelerator with radius R scales like

$$\Delta E_{\text{sync}} \propto \frac{q^2 E^4}{R m^4}.$$

The synchrotron radiation increases with the fourth power of the energy but scales also with the fourth power of the inverse mass. It is much stronger for light particles like electrons than for the relatively heavy protons. For an electron at the Large Electron Positron collider (LEP) that was located at the LHC tunnel before, the loss due to synchrotron radiation was roughly 3 GeV per turn at 100 GeV beam energy, compared to 6 keV at nominal energy at the LHC. That energy loss has to be compensated by the accelerating cavities and effectively limits the maximum energy for circular electron accelerators.

After acceleration the protons are stored for up to 12 hours and brought to collision at four interaction points where the four large experiments ATLAS, CMS, ALICE and LHCb are located. The ATLAS (A Toroidal LHC ApparatuS) detector is used for the analysis presented in this thesis and is described in detail below. CMS (Compact Muon Solenoid) is located at the opposite side of the LHC ring. It features a design and physics program similar to the ATLAS detector. LHCb (LHC beauty) is only sensitive in the very forward regions where ATLAS and CMS are lacking acceptance. The physics program is focused on flavor physics in the b quark sector. ALICE (A Large Ion Collider Experiment) is designed to study collision of lead ions, which can also be accelerated and collided at the LHC[3].

3.2 The ATLAS detector

The ATLAS detector is a multi-layer, multi-purpose detector designed to detect the decay products of heavy particles produced in proton–proton collisions at the LHC. Figure 3.2 shows a LEGO® model[4] of the ATLAS detector.

The detector has a typical onion-like structure with several layers of detectors being stacked from the inside where the collisions happen to the outside. It has a cylindrical shape where particles emerging from the collisions transverse to the beam directions are detected in the barrel part while particles being emitted close to the beam are measured in so called end-caps. ATLAS uses a right-handed coordinate system with its origin at the nominal interaction point (IP) in the center of the detector and the z-axis along the beam pipe. The x-axis points from the IP to the center of the LHC ring and the y-axis points

---

[3] Since the heavy ion program of the LHC is not relevant for this work it will not be discussed further.

[4] This model was assembled as outreach project as part of this thesis. It was originally designed by Sasha Mehlhase and has been build after his instructions. It consists of 9500 individual LEGO® bricks and has a length of roughly 1 m and a diameter of 0.5 m. The model has been used in several outreach workshops and has been displayed at an exhibition at the Deutsche Museum Bonn [126] and at several university events.

upward. Cylindrical coordinates (r,ϕ) are used in the transverse plane, ϕ being the azimuthal angle around the beam pipe. The pseudorapidity η is used as third coordinate and is defined in terms of the polar angle θ as $\eta = -\ln\tan(\theta/2)$. This quantity is used instead of the polar angle since it is invariant under logitudinal Lorentz boosts[5]. This has the advantage that – in contrast to the polar angle – differences in the pseudorapidity between two particles $\Delta\eta$ are invariant of the boost parallel to the beam axis which is not known in a hadron collider. Using these coordinates a boost invariant distance measure

$$\Delta R = \sqrt{(\Delta\eta)^2 + (\Delta\phi)^2}$$

is defined which is universally employed to quantify the distance between physical objects in the detector.

In this section, a brief overview of the different functional components of the detector and the comprising sub-detectors will be given. A bit more in-depth explanation of the working principle and the operation of a modern detector will be given for the Transition Radiation Tracker. A detailed discussion of the full detector setup can be found in [127].

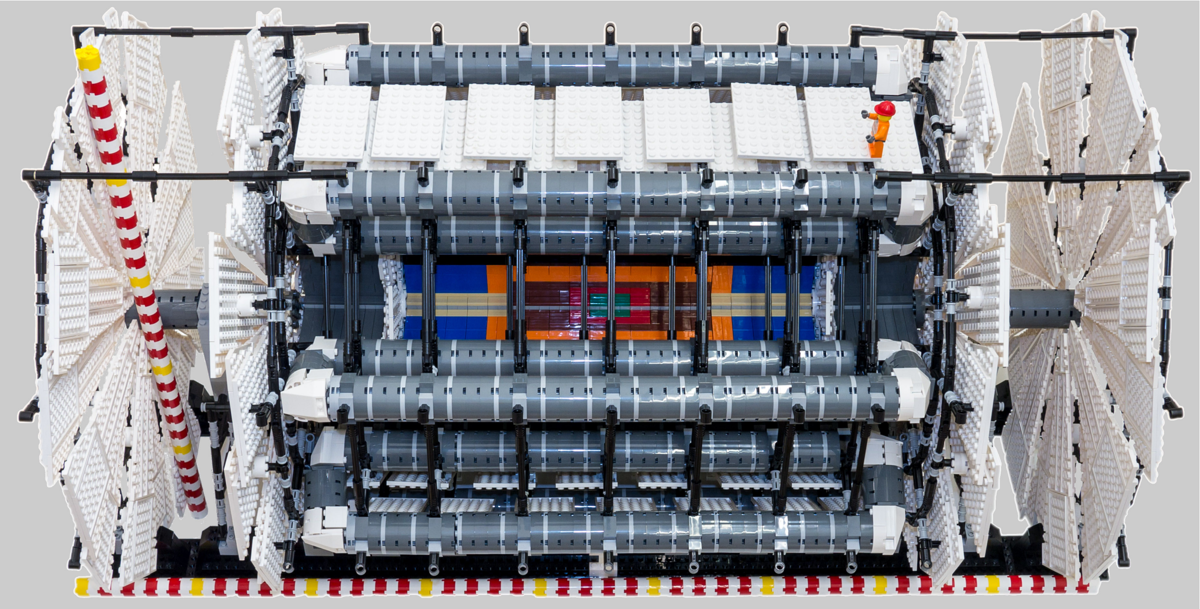

Figure 3.2: LEGO® model [128] of the ATLAS detector. The model is roughly to scale with the LEGO® man. All sub-detectors are included: The Pixel detector is modeled in green, the SCT is red and the TRT brown. The calorimeters are displayed in orange (electromagnetic calorimeter), black (tile calorimeter) and blue (forward calorimeter), respectively. The muon system consists of the white tiles, while magnets are modeled in gray.

---

[5] This is only exactly true for massless particles where the pseudorapidity η equals the relativistic rapidity $y = \frac{1}{2}\ln\frac{E+p_L}{E-p_L}$ with the longitudinal momentum p_L parallel to the beam direction. For all practical purpose in this work, the mass of the measured particles is much smaller than their momentum so this difference is small.

3.2.1 Inner detector

The inner detector (ID) is designed to record the tracks of charged particles transversing the detector volume. At the same time it is used to reconstruct the momentum of these particle. For that purpose the whole detector is immersed in a magnetic field of 2 T which is generated by a superconducting solenoid coil enclosing the volume of the ID. In this magnetic field the trajectories of charged particles are bend by the Lorentz force much like the protons in the magnetic field of the LHC. From the radius of the curvature one can compute the momentum of the particles assuming they carry one unit of elementary charge. Figure 3.3 shows a drawing of the ID. It comprises three sub-detectors employing different techniques for particle detection.

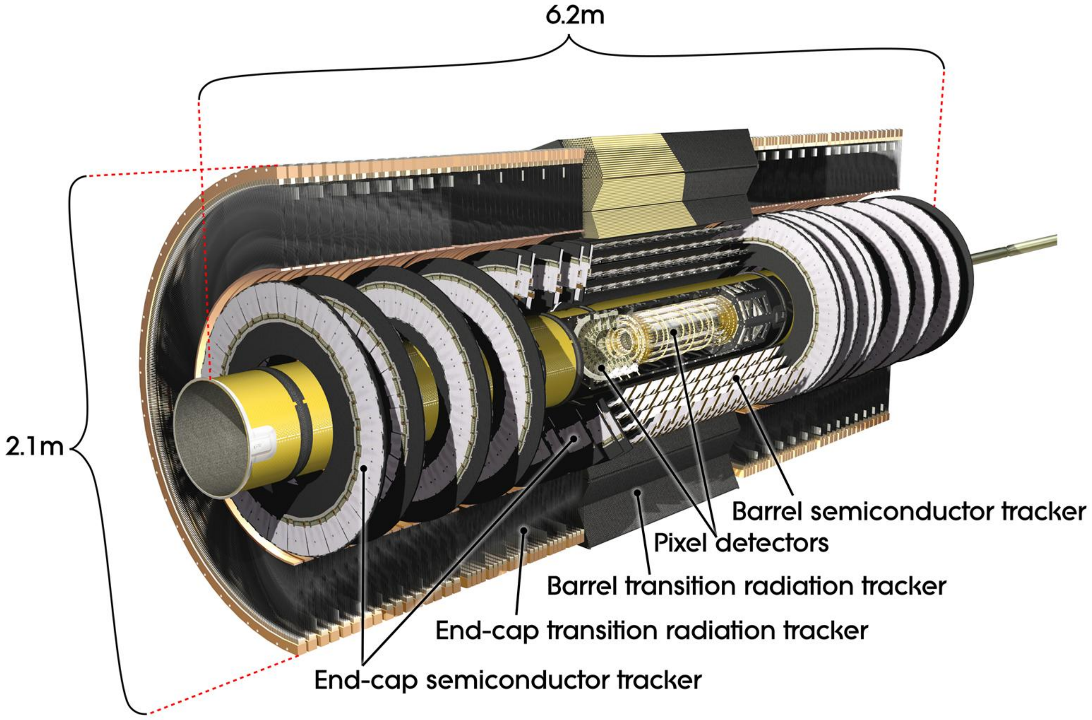

Figure 3.3: Drawing of the ATLAS inner detector with all sub-detectors [129].

Pixel detector

The innermost part of the ID consists of the Pixel detector. It comprises three disks in the end-cap regions and three layers in the barrel regions, covering a rapidity region $|\eta| < 2.5$. The innermost layer is located at a radial distance of 50.5 mm from the IP, just outside the beam pipe. The outermost layer resides at a radius of 122.5 mm. The sensitive elements of this sub-detector are over 80 million silicon pixels with a size of $400\,\mu\text{m} \times 50\,\mu\text{m}$ which are grouped in chips and modules. The division into small individual sensor elements has been chosen to compensate for the very high occupations at the center of the detector just next to the interactions. The Pixel detector is designed to allow a precise reconstruction of the interaction vertex and a precise first tracking step.

Silicon Tracker

The Silicon Tracker (SCT) encloses the Pixel detector. The barrel part consists of four layers at radii between 299 mm and 514 mm. Each end-cap comprises nine disks in a configuration that ensures tracking up to $|\eta| = 2.5$. Each detector module holds two layers of 768 active silicon strips with a pitch of 80 µm in back-to-back configurations. The two layers are rotated with respect to each other by 20 mrad thus allowing for a position measurement along the direction of the strips. The length of the strips depends on the position in the detector and varies between 5 cm and 12 cm. The design of the detector allows for at least four precision measurements with an $r\phi$ resolution of 17 µm and a z-resolution of 580 µm for each charged particle traversing the detector volume.

Transition Radiation Tracker

The Transition Radiation Tracker (TRT) is the outermost tracking detector in the ATLAS inner detector volume and extends to a radius of 1 082 mm from the interaction region. Its design was driven by the need to get continuous tracking with a long lever arm and electron identification in the pseudorapidity range $|\eta| < 2$, providing a point resolution of 130 µm.

The TRT is explained in some more detail as an example of an ATLAS sub-detector. The description follows the content of [130].

Design In contrast to the other inner tracking detectors, the TRT is not a semiconductor detector but a gaseous detector. It consists of 4 mm diameter straw tubes made from a multilayer film reinforced with carbon fibers and containing a 30 µm gold plated tungsten wire in the center [131]. The straw wall is set to a voltage of -1.5 kV while the wire is kept at ground potential. Thus the charge clusters created through primary ionization undergo avalanche multiplication close to the wire.

Basically each straw operates as a single drift chamber. The basic working principles of gaseous detectors in general and drift chambers in particular can be found in many text books, e.g. in [132].

The straws are filled with a gas mixture of 70% Xenon, 27% CO_2 and 3% Oxygen. Gas composition and high voltage are chosen to ensure that the maximum drift time for hits close to the wall is below 50 ns with a gas amplification factor of 2.5×10^4. The gas gain is continuously monitored by the Gas Gain Stabilization System and the high voltage is adjusted to keep the gain value stable. The system achieves a stabilization of the gain factor on a 2% level compensating changes in temperature, pressure and gas composition.

For electron identification the TRT exploits transition radiation (TR), soft X-ray photons emitted by charged particles traversing a boundary between material layers of varying refractive index. The emitted photons are detected in the straw tubes through absorption by Xenon atoms and subsequent ionization. In this way TR deposits a much higher energy in a single straw than an ionizing particle usually does. In ATLAS, usually only electrons reach a velocity which exceeds the threshold for generating transition radiation, thus the detection of a TR photon indicates the passage of an electron. The emission of TR happens in dedicated radiators which are interleaved with the straws. By introducing multiple layers of radiator material and choosing the spacing between those in the right way, the emission of TR can be stimulated coherently, amplifying the yield of emitted transition radiation.

The barrel region covers the range $|\eta| < 1$ and comprises 52544 straws parallel to the beam axis arranged in 73 layers [133]. Each straw has a length of 144 cm and the outermost 64 straw layers are electrically split in the middle so both sides can be read out independently. The innermost nine layers are split in three parts with only the outer 31.2 cm being read out while the middle parts remain inactive. This design was chosen to ensure that the hit rate of a single readout channel is kept below 20 MHz at LHC design luminosity. As radiator, a matrix of oriented polymer fibers was chosen filling the TRT volume and embedding the straws. Mechanically, the barrel consists of three layers of 32 modules which provide stabilization and cooling for the straws they contain. The modules are arranged in a non-projective geometry to avoid insensitive gaps.

The end-cap region covers the range $1 < |\eta| < 2$. Each end-cap contains 122880 37 cm long straws in 160 layers [134]. The straws are oriented radially and are mechanically and electrically arranged in 20 wheels of eight layers. Thin polymer foils are interleaved with the wheels and serve as radiator.

In total each track traversing the detector volume crosses approximately 35 straws (except in the gap region between end-cap and barrel) over a distance of roughly half a meter. With these measurements, the TRT significantly improves the momentum resolution for charged tracks.

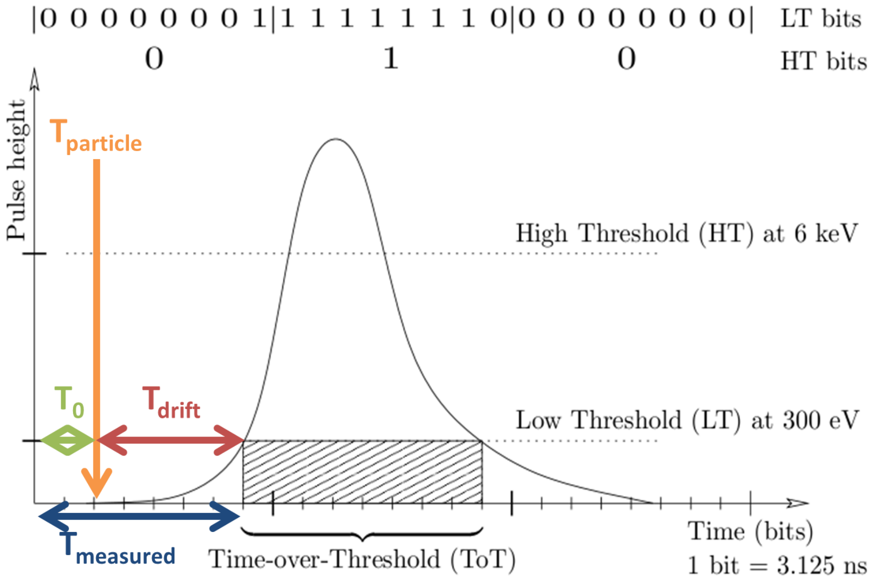

Figure 3.4: Digitization and timing of a TRT pulse. The colored arrows are depicting different timings important for the reconstruction of a physical hit (figure from [130]).

Signal Formation and Digitization A charged particle crossing a straw causes primary ionization in the drift gas thus creating charge clusters. In the electric field of the straw, the electrons drift towards the wire where they are multiplied in an electromagnetic avalanche. A transition radiation photon, created in one of the radiator layers, is absorbed in the Xenon gas and creates primary ionization as well. The individual straws are directly coupled to the ASDBLR[6] front-end chip, where the analogue pulses are amplified, shaped and the slow ion drift tail of the signal is suppressed [135]. This way, the net signal is the superposition of several smaller signals each generated when a primary cluster reaches the wire. An illustration is shown in Figure 3.4. The ASDBLR moreover contains two independent

---

[6] Amplifier-Shaper-Discriminator with Baseline Restoration

discriminators set to different thresholds. The lower one is set to approximately 300 eV which is well below the median energy deposition of a minimum ionizing particle. The upper one is set to 6 keV and thus primarily sensitive to energy deposition by a TR photon. Those thresholds are tuned with reference to the electronic noise and a test pulser on the ASDBLR chip once a week during special calibration runs. In practice, the low threshold is set in a way to give a uniform noise detector occupancy of 2% while the high threshold is tuned to give a uniform probability for high threshold hits over the detector.

The ASDBLRs are coupled to DTMROC[7] digitization chips. For each triggered event, 75 ns (i.e. three bunch crossings) of the signal are digitized with different timing characteristics.

The low threshold signal (LT) is digitized in bins of 3.125 ns width. Its leading edge (i.e. the first bin in a readout window which is high) corresponds to the arrival of the first cluster at the wire determining the drift time and hence the distance of closest approach of the track to the wire. The trailing edge contains the same information about the last ionization cluster and can be used for e.g. pileup suppression. The time over threshold (ToT, i.e. the time between leading and trailing edge) contains information about the distance the particle traveled through the straw, its deposited energy etc. and can be used for particle identification. By design, the maximal pulse length of a real signal is about 50 ns so the readout timing has to be adjusted with respect to the collision timing in a way that 50 ns are contained within the readout window. This is done using cosmic and single beam events with an achieved precision below 1 ns. The high threshold signal (HT) is only sampled three times per readout window. The mere presence of a HT hit indicates a possible electron so no further timing is required. The tracking is done with the LT hits.

Figure 3.4 shows also some timings relevant for the readout. The readout window is adjusted relative to the LHC clock in a way that the pulse is completely contained in the readout window. This adjustment is made in hardware during special calibration runs once per week. The “physical” time of arrival of a particle T_{particle} is not coincident with the start of the readout window but has an offset T_0 due to time of flight and signal propagation time along the straw. This offset is calibrated offline for every run and chip (see Sec. 3.2.5) [136]. The measured time T_{measured} contains the drift time T_{drift} and this offset.

Particle Identification The TRT offers two different ways of identifying particles. For separating pions from electrons, the fraction of high threshold hits on a track can be used. As described above, the probability for generating a transition radiation photon and a subsequent high threshold hit is much higher for electrons than for pions. An example plot for the onset of transition radiation can be seen in Figure 3.5. At high values of γ (above $\gamma = 1000$), a nearly pure sample of electrons is obtained from photon conversions. For low values of γ, all selected tracks in the event are used and assumed to have the mass of the charged pion. As expected from the production of TR, the probability of a HT hit increases for particles with a γ-factor above 1000, which enables the TRT to separate electrons from pions over a momentum range between 1 GeV and 150 GeV.

The second possibility of identifying particles in the TRT is by utilizing the specific energy deposit $\mathrm{d}E/\mathrm{d}x$ in the gas volume. As an estimator for this quantity, the measured time over threshold is taken as a starting point. After applying various corrections to accommodate for physical variation (e.g. the actual length of the track passing through the straw varies with the distance to the wire and the incident angle of the passing particle) a good estimator for the specific energy loss can be achieved as demonstrated in Figure 3.5. Proton and kaon bands are clearly visible and distinguishable.

---

[7] Digital Time Measurement Read-Out Chip

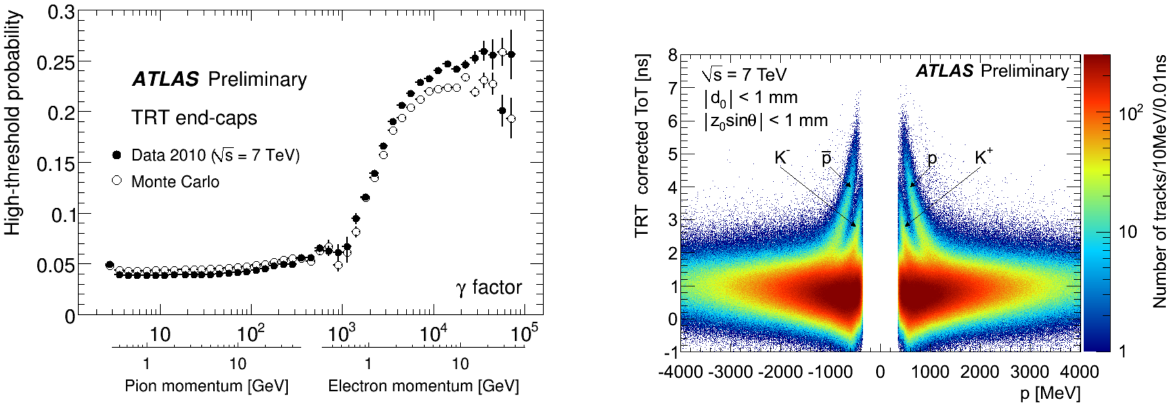

(a) HT probability

(b) ToT estimator

Figure 3.5: Particle identification with the TRT. Figure a) displays the probability of a TRT high threshold hit as a function of the Lorentz factor, $\gamma = \frac{E}{m}$, for the TRT end-cap region, as measured in 7 TeV collision events. Figure b) shows an estimator for specific charged particle energy loss based on the time over threshold measured by the TRT. The estimator demonstrates the capability to use ToT as an observable for particle identification for heavily ionizing particles. The tracks are required to have at least one pixel, at least six SCT and at least 15 TRT hits (figures from [130]).

3.2.2 Calorimeters

The calorimeter system is intended to stop both charged and neutral particles and measure their respective energies. Due to the very different interactions of different particle species with matter there are several types of calorimeters which enclose each other. Figure 3.6 displays a drawing where the different calorimeters are nicely visible.

Electrons and photons undergo a cascade production reaction that involves only electrons, positrons and photons. Those electromagnetic showers[8] are comparably narrow and loose their energy on a short length scale. The inner calorimeter layer is the “electromagnetic calorimeter” (ECAL) which is designed for the purpose of measuring these particles.

In contrast to that any hadrons escaping (protons, neutrons, charged pions and kaons) initiate hadronic showers that show a much larger extension, both lateral and longitudinal and have a much larger fluctuation[9]. To contain and measure those particles as well, the ECAL is enclosed by a larger and coarser “hadronic calorimeter” (HCAL).

The forward regions of the detector show again a different situation. Here, the flux of particles is particularly high due to the boost of the colliding protons. The calorimeters have to be adapted to the more demanding conditions to prevent radiation damage after a short time of operation.

---

[8] Electromagnetic showers are characterized by the radiation length X_0 as the distance after which the average energy of an incoming electron decreased to $1/e$ of its initial energy due to bremsstrahlung.

[9] Hadronic showers are characterized by the interaction length λ analogously to X_0 for electromagnetic showers.

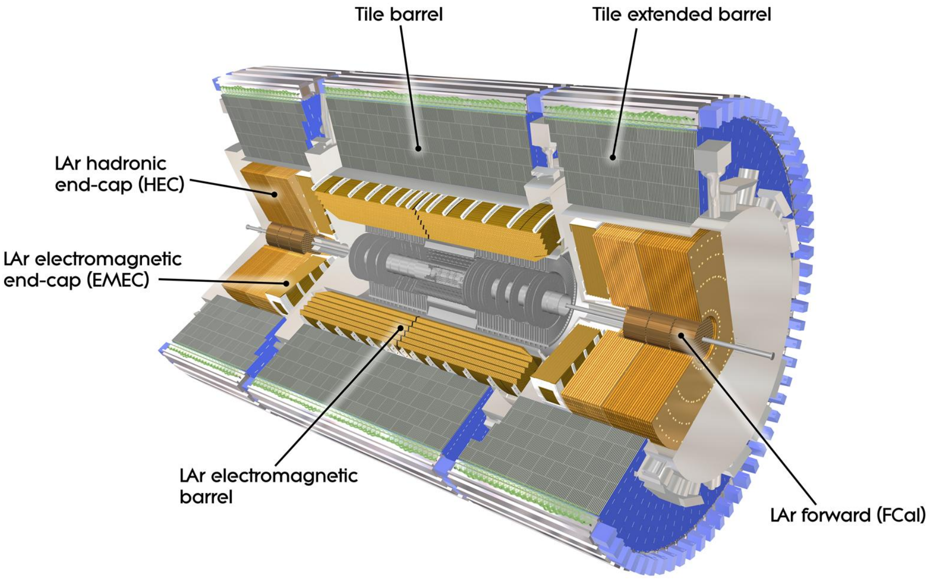

Figure 3.6: Drawing of the ATLAS calorimeter system with all sub-detectors [137].

Electromagnetic calorimeter

Similar to the inner detectors, the ECAL consists of a barrel part covering the region $|\eta| < 1.475$ and an end-cap part extending up to $|\eta| = 3.2$. In the central region $|\eta| < 2.5$, the calorimeter has three layers with the innermost having a very fine segmentation down to $\Delta\eta \approx 0.003$ to allow the precision measurement of photons. The largest, second layer has a typical granularity of $\Delta\eta \times \Delta\phi = 0.025 \times 0.025$. The depth of the ECAL varies between 22 and 38 X_0 depending on η.

The ECAL uses an accordion structure where steel clad lead plates are folded in a zig-zag fashion – much like an accordion. Those absorber plates are stacked interleaved with electrodes. A gap of 2.1 mm between the absorber and the electrode is maintained by a honeycomb spacer structure. The gaps are filled with liquid Argon, which acts as an ionization and detection medium.

Since the boiling point of Argon is 87 K, the electromagnetic calorimeters have to be kept at cryogenic temperatures. They are thus housed in three cryostats, one for each end-cap and one for the barrel.

Hadronic calorimeter

For the energy measurement of hadronic particles two very different techniques are employed. In the barrel region $|\eta| < 1.7$ a sandwich structure made from steel and plastic scintillator tiles is used (Tile Calorimeter, Tilecal). The Tilecal has a depth of 7.4λ and is located outside the electromagnetic calorimeter (c.f. Figure 3.6). It consists of 64 wedge-like modules that form a hermetic barrel. The scintillating tiles are connected to photomultipliers using wavelength shifting fibers. Fibers from multiple tiles are grouped together to form three layers of cells, 1.5, 4.1 and 1.8 λ thick, respectively. The first and second layer cells have a lateral size of $\Delta\eta \times \Delta\phi = 0.1 \times 0.1$ in the first and second and 0.2×0.1 in the third layer.

The hadronic end-cap calorimeter (HEC) uses again a liquid Argon technique. Here, the absorbers consist of copper plates that are stacked parallel to the beam direction. The HEC covers the range $1.5 < |\eta| < 3.2$ and is housed in the same cryostat as the end-cap ECAL. The HEC comprises two submodules with 24 copper plates of 25 mm and 16 plates of 50 mm thickness, respectively. Between each pair of absorber layers, there is a gap of 8.5 mm that is filled with liquid Argon. In the center of each gap, a segmented readout electrode is located providing a readout granularity of 0.1×0.1 for $|\eta| < 2.5$ and 0.2×0.2 for larger values of η.

Forward calorimeter

In the very forward direction, the calorimeter system is completed by the forward calorimeter (FCAL) covering pseudorapidities up to $|\eta| = 4.9$. In this region, the detector has to deal with very high occupancy and radiation doses. It was hence chosen to utilize the liquid Argon technique as well. To cope with the high particle fluxes, the Argon gaps have to be much smaller than in the other sub-detectors. This is achieved by manufacturing the FCAL from a metal matrix in which ten-thousands of holes parallel to the beam axis are drilled. In these holes, small rods are inserted as electrodes with a sub-millimeter gap remaining between rod and matrix which is then filled with Argon.

Each side of the FCAL consists of three modules, the innermost machined from copper while the outermost consist of tungsten. The copper module is optimized for the measurement of electromagnetic showers and has a depth of $28X_0$ while the tungsten modules are optimized for hadronic showers and have a depth of 3.6λ each.

3.2.3 Muon system

The outer part of the ATLAS detector is made up by the muon systems. Muons, undergoing neither hadronic interactions nor emitting significant amounts of bremsstrahlung, are the only (detectable) particles escaping the detector. For detecting and measuring the muons, an independent tracking system is installed outside the calorimeters. Figure 3.7 shows a drawing of the ATLAS detector where the muon chambers are visible as light blue components outside the central part.

The muon system covers the pseudorapidity range $|\eta| < 2.7$. It is designed to achieve a momentum resolution of 10% for a 1 TeV muon track. To achieve this resolution, an additional magnet system is installed outside the central detector. It consists of eight air-core coils arranged parallel to the beam axis that generate a toroidal magnetic field of approximately 0.5 T around the detector. In the end-cap regions, it is complemented by the end-cap toroids, which generate a field of approximately 1 T. While in the barrel region each coil is housed in its own cryostat, the eight coils of each end-cap toroid system share one common cryostat.

The muon system consists of different detector types fulfilling different purposes. The precision measurement of the muon tracks is performed by Monitored Drift Tube (MDT) chambers. They are installed in three layers around the barrel toroid coils forming three cylinders of 5 m, 7.5 m and 10 m, respectively. They are also installed in the forward region, where they form wheels at a distance of 7.4 m, 10.8 m, 14 m and 21.5 m from the interaction point, respectively. Only in the forward regions ($2 < |\eta| < 2.7$) of the innermost wheels, Cathode Strip Chambers (CSCs) are used instead to cope with the high particle rates and provide a better timing resolution.

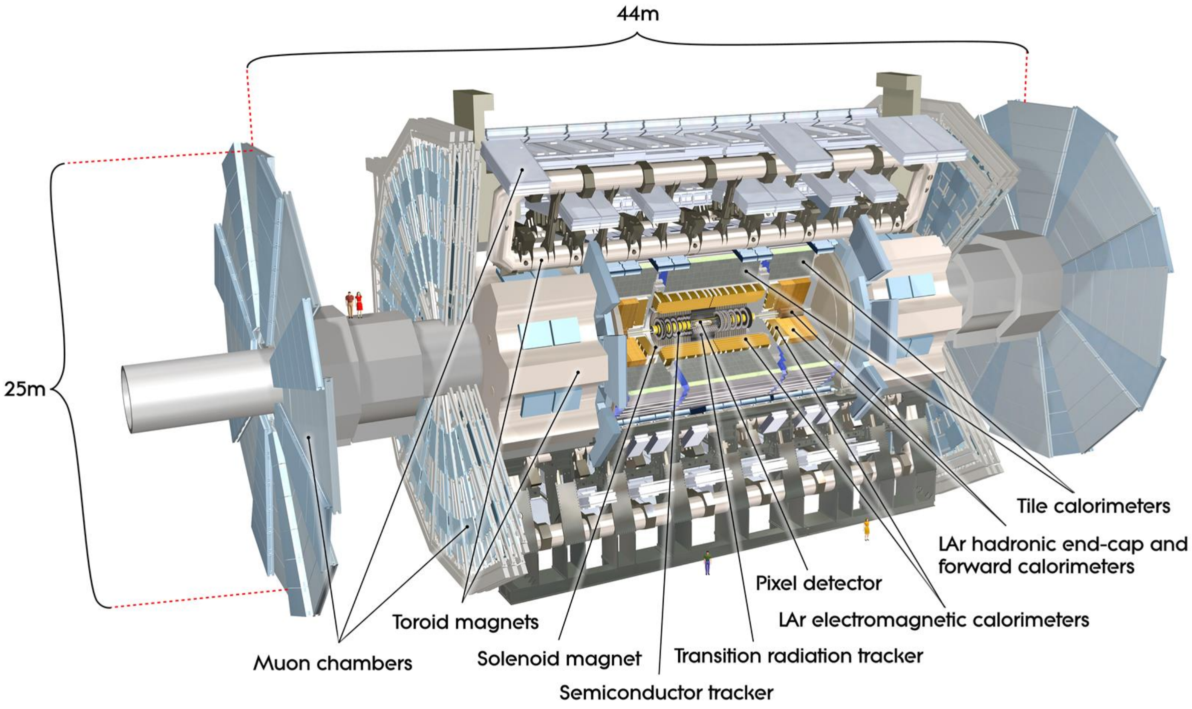

Figure 3.7: Drawing of the ATLAS detector with all sub-detectors [138].

The MDTs use a technique very similar to the TRT. Each chamber comprises up to 432 individual drift tubes of approximately 3 cm diameter. The tubes are filled with a mixture of Argon and CO_2 at a pressure of 3 bar. The tubes achieve a tracking resolution of 80 µm which results in an average resolution of ~ 35 µm per chamber. To achieve this resolution, the position of each tube and deformations of the chambers have to be monitored with high precision. For that purpose the MDT chambers are equipped with a special optical monitoring system that allows an alignment precision in the 100 µm regime. The required precision is achieved in combination with a track based alignment.

The CSCs are gaseous detectors as well, but with a planar geometry and readout. Essentially they are regular multi-wire proportional chambers (MWPC) with segmented cathode planes. The segmentation is perpendicular in the two cathodes, so a two dimensional measurement is obtained by reading out both cathode signals. The wire signal is not read out. The segmentation of the cathode in the bending plane of the tracks is of the order of 5 mm resulting in a resolution of 60 µm per plane. In the other direction, the segmentation is coarser leading to a resolution of 5 mm. The CSCs are functional for rates up to 1 000 Hz /cm^2, compared to a limiting rate of 150 Hz /cm^2 for the MDTs.

The muon system is used not only for measuring muons, but also for providing a fast muon trigger. For that purpose, special trigger chambers are employed that are mounted interleaved with the tracking chambers. The trigger chambers have to provide a fast reaction time and a high time resolution. Some coarse spatial resolution is also required to obtain a rough estimate of the track momentum. This segmentation is also used to provide a second space coordinate in the regions where MDTs, which by construction can only provide a measurement perpendicular to the straw direction, are used for tracking.

Two different techniques are chosen due to the different requirements in the barrel and the end-caps. In the barrel, Resistive Plate Chambers (RPCs) are used which are basically parallel plate gaseous detectors. The plates are segmented perpendicular to each other with strip widths of 25 mm to 35 mm. The PRCs achieve a timing jitter of less than 10 ns, good enough to assign individual muons to single LHC bunch crossings.

In the end-cap, Thin Gap Chambers (TGCs) are used. Those are again essentially MWPC detectors where the distance between wires and cathode is smaller than between the wires. Combined with a highly quenching gas mixture, this leads to a high rate stability and fast timing characteristics. The cathode plates are segmented perpendicular to the wire directions so a two dimensional coordinate information can be reconstructed. In this setup, the wires are measuring the bending coordinate, while the cathode strips measure the azimuthal direction. Wires are grouped to reduce the numbers of readout channels, with the grouping depending on the location in the chambers to ensure the desired η resolution. The timing resolution is good enough to assign more than 99% of the measured hits to the correct bunch crossing.

3.2.4 Trigger

At design luminosity, every 25 ns a collision happens in the center of the ATLAS detector. At this rate it is impossible to record every event. Therefore, a fast decision system, the trigger, is employed to select which events are to be recorded and which are to be discarded.

The ATLAS trigger comprises three levels. The Level 1 trigger (L1) runs on custom hardware and is implemented close to the detector. The Level 2 trigger (L2) and the event filter (EF) are running mainly on commercially available computing hardware and are commonly referred to as the high level trigger (HLT).

The Level 1 trigger uses detector information with a reduced granularity. It can process information from the muon trigger chambers and from the calorimeters. The L1 is mainly intended to preselect events of possible interest. It has a maximum acceptance rate of 75 kHz and a latency of 2.5 µs. This maximum decision time is limited by the buffers in the detector electronics which can store the information of one bunch crossing only for that time. For accepted events, the data is transferred from the detector to the data acquisition system (DAQ).

Accepted events are further processed in the L2. This trigger uses the full details of the detector information, albeit only in a region of interest (RoI) around the possible trigger object. The L2 has a maximum acceptance rate of 3.5 kHz and an average running time of 40 ms. If an event is accepted by the L2, the full data is transferred to the EF computing farm where a full event reconstruction is performed. Based on this information, the more complex EF trigger algorithms are run and a final trigger decision is obtained. The EF triggering step can take up to several seconds and produces an output rate of at most 200 Hz, which is then moved to permanent storage. Although the EF algorithms can make use of the full detector information, the objects and physical quantities are still slightly different between EF and the offline reconstruction. The main reason for that is the lack of calibration and correction information, which is only derived a posteriori, based on the data taken. Also due to computing and time restrictions, it is not possible to run e.g. very complex multivariate identification algorithms on EF level.

For the analysis documented in this thesis a trigger combining information on jets and $\not{E}_T$ is employed. On L1, both trigger types rely on calorimeter "trigger towers" of a fixed size of $\Delta\eta \times \Delta\phi =$

0.2×0.2, which contain the full depth of both the electromagnetic and the hadronic calorimeters. Jets are found by a sliding window algorithm. One window of the size of 2×2 trigger towers is used to find local maxima. The energy of the candidate jets is summed over up to 4×4 trigger towers depending on the threshold of the actual trigger. The $\not{E}_T$ L1 trigger is constructed using a map of all trigger towers over the whole detector.

On L2, the jet definition is refined by using a simple clustering algorithm on smaller towers ($\Delta\eta \times \Delta\phi = 0.1 \times 0.1$) in a RoI around the L1 trigger jet. At L2, calibrations and thresholds can be applied per cell, significantly improving the measurement of the energy of the jet. Due to the RoI concept, no significant improvements of the $\not{E}_T$ trigger can be achieved on L2.

On EF level finally, full jet algorithms are applied to calibrated cells. Also $\not{E}_T$ is refined using the full calorimeter granularity. Studies about trigger thresholds and the correspondence between energy measurements on trigger level and on offline level are documented in Section 5.3.

3.2.5 Operating the detector

Taking data with the ATLAS detector is not a self-running task. With its large number of sub-detectors and the high complexity of each one of them, it is not easy to monitor whether the detector is working as intended or not.

To ensure the best possible performance of the data and the fastest possible delivery after the end of the run, a “36-hour calibration loop” procedure has been installed. Right after the data taking, a small portion (typically 10%) of the whole data stream is reconstructed. This “express stream” data is examined by shifters and experts for data quality (DQ) to spot possible problems that went unnoticed during data taking. This data is also used to verify or update calibrations of the various detectors, to reconstruct the actual position of the beam spot and to identify and flag periods of non-optimal conditions, e.g. due to a higher noise level in some sub-detector.

Only after all sub-system experts sign off a given run, which is to happen within 36 hours after the end of the run, the full dataset is processed with the updated conditions and all events are reconstructed. This full processing is then again examined by the DQ shifters and experts. Based on their findings, a so called “Good Runs List” (GRL) is created, which lists all data taking periods where the whole detector was in optimal running condition on the granularity of a “Lumi Block” (LB), which corresponds to one minute of data taking.

Again, some insight into operating the ATLAS detector will be given on example of the TRT, however very similar tasks are performed in every sub-detector. First, the task of calibrating the detector based on data and on specific calibration information will be discussed (this part is again taken from [130]), then some details on the monitoring of the quality of the recorded data will be given.

Event data model

Events that pass at least one of the triggers are recorded on disk. They are sorted in different data streams according to the triggers they were selected by. Events that were triggered by an electron or photon trigger are recorded in the “EGamma” stream. Events that caused a muon trigger are sorted into the “Muon” stream and all other events end up in the “JetTauEtmiss” stream. Only the latter one is considered in this work.

After being recorded, the processing and reconstruction of the data is performed in multiple steps following the ATLAS Event Data Model (EDM) [139]. First, the RAW byte-stream data from the detector is grouped into Raw Data Objects (RDO), which is essentially a computational modeling of the detector objects. On these objects all low-level reconstruction like tracking and clustering of calorimeter cells is run and results in the Event Summary Data (ESD). This intermediate data format contains still the relevant basic data, like a selection of individual detector hits but also some basic reconstructed physics objects. It can be used e.g. for performing re-fits of tracks or advanced identification algorithms that need access to individual calorimeter cells. In the next step, the underlying information is removed and the reconstruction and identification of the physics objects is refined, resulting in the Analysis Object Data (AOD). At this processing step, the data size is drastically reduced and the files contain only high level physics objects. In a last step, Derived Physics Data (D3PD[10]) is produced.

D3PDs do not hold an object representation anymore but are “flat n-tuples”, i.e. they contain a list of individual float and integer variables per event collected in a ROOT [140] TTree structure. In the D3PD production step, updated recommendations of the individual performance groups like e.g. updated calibrations can be implemented. All production steps are versioned ensuring identical reconstruction algorithms for all reconstructions. The relevant D3PD production release for this analysis is p1512 for simulations and p1542 for data.

Data Quality Monitoring

The first key component to ensure a stable operation and high quality data are the shifters in the control room during operation. Indeed, the whole detector has to be supervised at all times. This does not only cover the obvious parts like monitoring voltages, pressures, gas flows etc., but also the monitoring of the quality of the data that is recorded. To assess the DQ, a set of histograms is defined. These histograms show primary and derived physical quantities that allow a take on the performance of both the detector and the reconstruction algorithms. For the TRT, those histograms comprise occupancy plots, both on hit and on track level, resolution plots, tracking quality plots and many more. Although the human eye is the ultimate tool in judging the quality, the sheer number of distributions to check for each run makes it impracticable to rely on shifters alone. Automatic evaluation algorithms are needed to draw the shifters attention to possibly problematic distributions instead.

Figure 3.8 gives an examples of a monitoring plot and an automatic check. Displayed in the plot is the distribution of the time residuals, i.e. the difference between the measured drift time and the drift time expected from the track fit. The large tails to both high and low values are due to outliers, spurious hits that are falsely assigned to a given track and hits where the drift time could not be measured due to noise. Those tails do not give any insight into the working of the detector. The gaussian core on the other hand does, since the width is highly sensitive to the calibration applied. A very small deviation from the ideal calibration already leads to a significant widening of that core. To monitor this, an algorithm has been developed that iteratively narrows the fitting range of a gaussian fit until a stable solution is reached. Thresholds can be set on both the center and the width of the fit. Exceeding these thresholds will trigger a notification to the shifter who in turn can verify the automatic result and ask for an update of the calibration if needed.

---

[10] DPDs can be produced from any intermediate step in the EDM chain. They are labeled according to the base format they are derived from, e.g. D3PD for DPDs derived from AODs, the third step in the EDM.

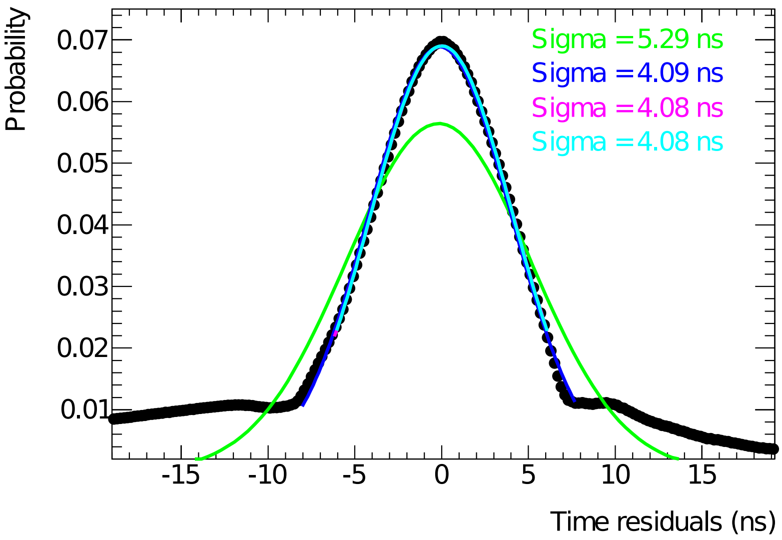

Figure 3.8: Example for the “iterative gauss fit” DQ algorithm that finds a gaussian core of an arbitrarily shaped distribution and measures its width. The fit range is iteratively narrowed based on the result of the last fit until the width of the resulting distribution converges.

Figure 3.9 shows another example. Here the number of reconstructed tracks versus the ϕ coordinate in the detector is displayed. From first principle, this distribution is expected to be flat. However inefficiencies lead to small deficits in certain ranges, e.g. where a part of any of the tracking detectors is permanently broken. Such inefficiencies have to be taken into account in the tracking when running the final reconstruction. Monitoring data for these effects proves difficult for both automatic checks and human shifter, since known inefficiencies have to be separated from new inefficiencies. To facilitate this, an algorithm has been developed that looks for outliers, i.e. entries that are further away from the mean of a distribution than expected from the uncertainties of the individual entries and for the flatness of a histogram. The flatness is evaluated by fitting a sine function to the distribution and setting thresholds on the amplitude. To enable an efficient checking even in the presence of known defects, all checks can be done not only on absolute values but also in comparison to a given reference.

Figure 3.9 depicts the individual steps in this check. Subfigure a) shows the data alone. Four inefficiencies are clearly visible. Subfigure b) shows the same distribution overlayed with a reference. Obviously, one of these inefficiencies is new (in this case it was caused by a failure in the high voltage supply). Looking at the ratio of both distributions in subfigure c) this new inefficiency translates into a deep dip which can easily be identified. Subfigure d) finally shows the ratio with the peak of the dip removed and the sine fitted to the distribution. The two remaining data points at the edge of the dip introduce a clear skew in the distribution. Both the outlier and the skew would have raised the alarm in that case. Note that even without the two points the distribution is not completely flat but shows a small skew with slightly lower occupancies for low angles and higher values for large angles. This is caused by a small displacement of the beam spot with respect to the reference histogram. While this would be detectable with the algorithm, the configuration is chosen such that a deviation in that size is below the warning threshold.

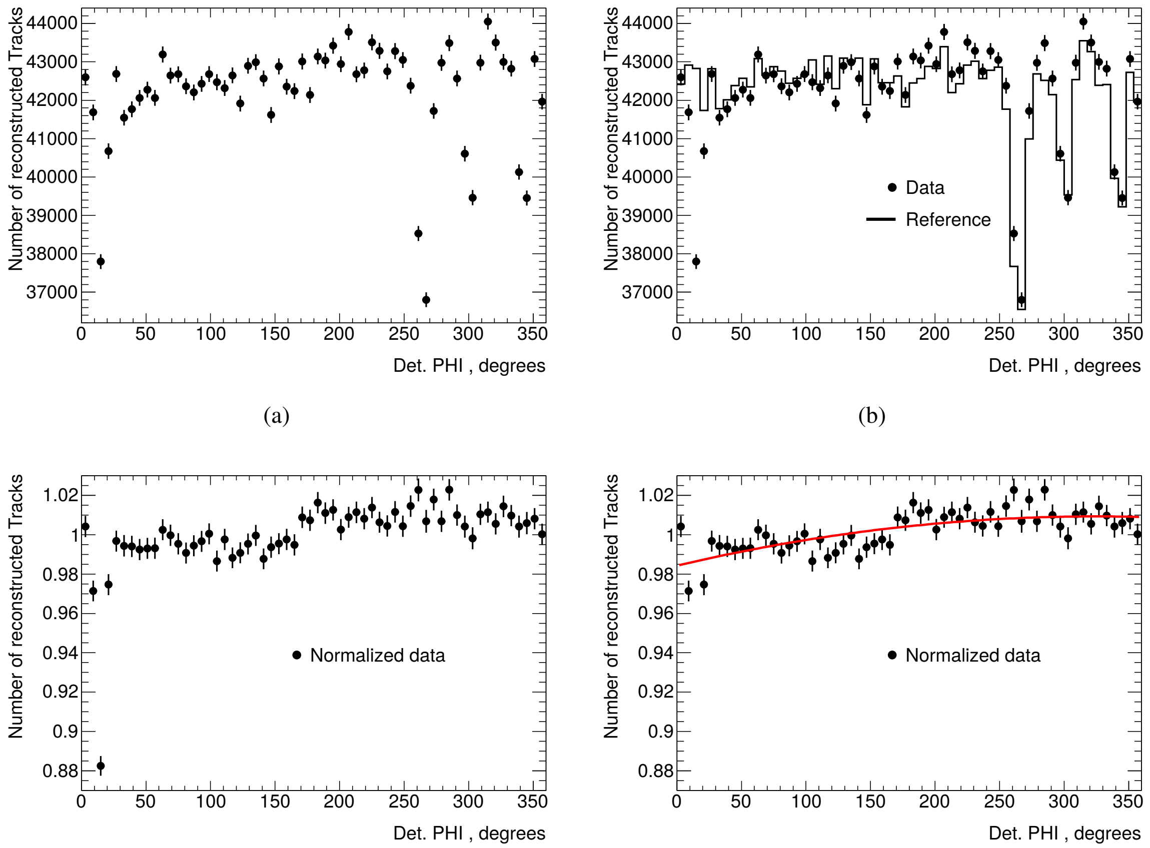

(a)

(b)

(c)

(d)

Figure 3.9: Example for the “outlier and flatness test” DQ algorithm. Figure a) shows the track occupancy versus the ϕ coordinate. Figure b) shows the same, only overlaid with a reference distribution. A newly developed region of inefficiency is clearly visible to the eye. Figure c) displays the ratio of the test and the reference distribution. Figure d) shows the results of the automatic control algorithm. The data point deviating most from a flat distribution is identified as outlier while the two neighboring points distort the subsequent fit to deviate from a straight line. Both issues would independently result in the plot to be marked to be checked by a shifter

Calibration

Calibrating the TRT is essential for ensuring its high precision and reliability. By design, each drift-type detector measures a time which has to be converted into one or more spatial coordinates. This conversion requires a mapping which is often highly sensitive to external effects and has to be calibrated regularly.

There are two different quantities requiring a regular offline calibration with collisions data. T_0, the time between the beginning of the readout window and the physical arrival of a particle originating from the bunch crossing associated with that window. And the relation between the measured (and corrected) drift time and the distance of closest approach of the track to the wire ($r-t$ relation).

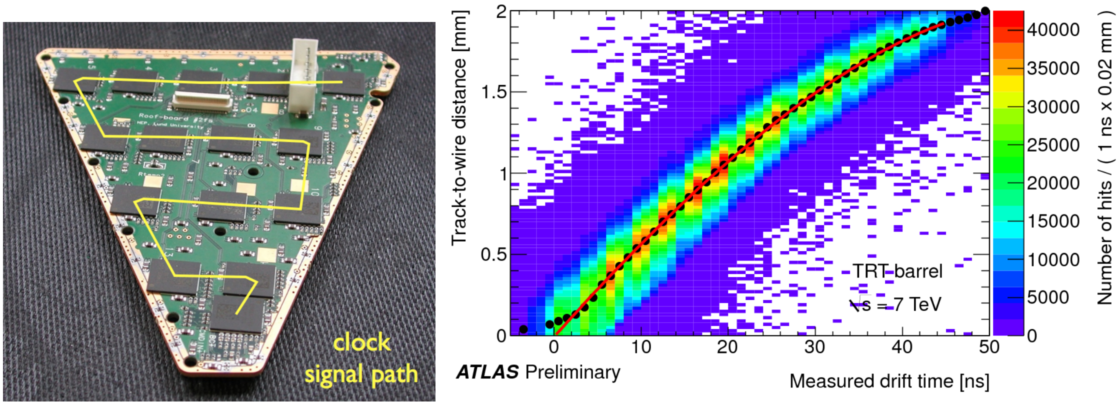

(a) Signal path on the frontend board

(b) $r-t$ calibration curve

Figure 3.10: Calibration of the TRT. Figure a) shows the signal path of the timing signal along one frontend board. Readout chips are fed serially so the timing offset has to be calibrated (T_0 calibration). Figure b) shows an examples of a $r-t$ calibration curve. The track-to-wire distance computed from the track fit is plotted versus the measured drift time. Dots show time-slice-wise fit means of the distributions while the red curve represents the calibration used(figures from [130]).

In hardware, the timing of the readout window can only be tuned for single readout boards in fixed steps of 0.5 ns. Within a given board, there is still a timing spread of up to 3 ns. For the desired resolution, a precision in the order of 100 ps has to be achieved. One of the main effects requiring offline calibration is illustrated in Figure 3.10. The timing signal is distributed to the different DTMROCs on a readout board serially resulting in a small offset between neighboring chips. The offset is measured for every straw in each run and a calibration is run on the level of single chips. Straws connected to one chip were found to show no major variations in timing. Experience shows that calibration constants have to be updated every few weeks. The main reasons for such frequent updates are linked to the slow drifts of the time reference provided by the LHC and replacements of single hardware components in the readout or triggering chain.

The $r-t$ relation is measured by comparing the measured drift time with the distance of closest approach computed from the overall track fit. An example can be seen in Figure 3.10. This relation is affected by changes in the high voltage or the gas composition and by the presence or absence of the magnetic field. Since both quantities are calibrated iteratively and in parallel and are related to each other, one point has to be fixed in the $r-t$ relation to ensure fit convergence. This is taken to be the drift radius of 1 mm at a drift time of 18 ns.

Datataking performance

The data this thesis is build upon has been recorded between March and November 2012 with a center of mass energy of 8 TeV. In that period, 22.8 fb^{-1} of integrated luminosity[11] have been delivered by the LHC (c.f. Figure 3.11) in 308 individual runs. The luminosity is determined using the same procedure as described in [141] and has an uncertainty of 2.8%. 21.3 fb^{-1} of the delivered luminosity have been recorded by ATLAS which corresponds to 93.5% datataking efficiency. This inefficiency is driven by the time needed to bring the detector to full working conditions after "stable beams" have been declared by the operators of the accelerator. After requiring all sub-detectors being in optimal conditions based on the results of the DQ assessment, 20.3 fb^{-1} remain to be analyzed, which corresponds to an efficiency of 95.5%. That implies that the detector was working so stable that more data was lost in the time needed to actually turn on the detector than by malfunctions of individual subsystems. The recording efficiency of every subsystem alone exceeded 99% in 2012 (c.f. [142]). The instantaneous luminosity in that period peaked at $7.73 \times 10^{33}\,\text{cm}^{-2}\,\text{s}^{-1}$ which corresponds to more than 40 interactions per bunch crossing. On average, at each bunch crossing about 21 individual collisions happened. While one of them might lead to an interesting signature, the others are so called "Pileup" events of limited physics interest which have to be taken care of in reconstruction, calibration and simulation.

In total, 3.15 billion individual events have been recorded. 748 million of these ended up in the JetTauEtmiss data stream and are hence considered for this analysis. After requiring the one single jet + $\not{E}_T$ trigger used for this work to be activated and all sub-detectors being in optimal conditions, 200 million data events remain to be analyzed.

---

[11] The luminosity L relates the rate of events of a given physics process n with cross section σ and the accelerator parameters as $n = \sigma \times L$.

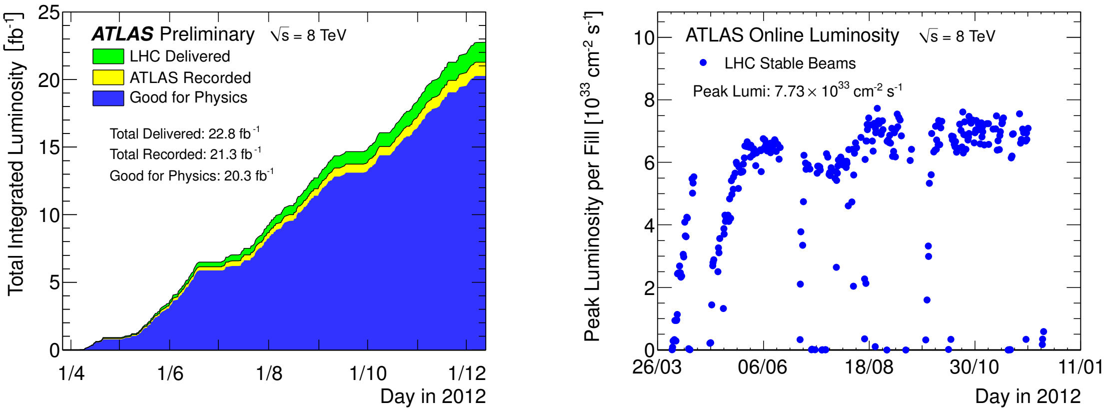

(a) Integrated Luminosity (b) Peak Luminosity

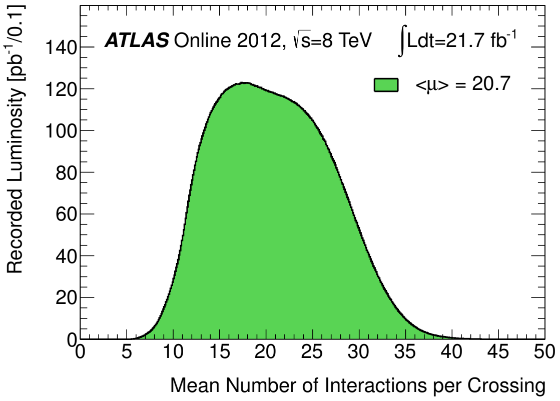

(c) Pileup

Figure 3.11: Luminosity in the 2012 data taking of the ATLAS detector. Displayed are the integrated luminosity (a), the peak luminosity per LHC Fill (b) and the distribution of numbers of interactions per bunch crossing (c).

3.3 Object reconstruction

Thanks to the multitude of specialized sub-detectors, ATLAS can reconstruct and identify virtually every (meta-)stable particle being produced in collision events. Figure 3.12 depicts how different particles leave traces in different parts of the detector.

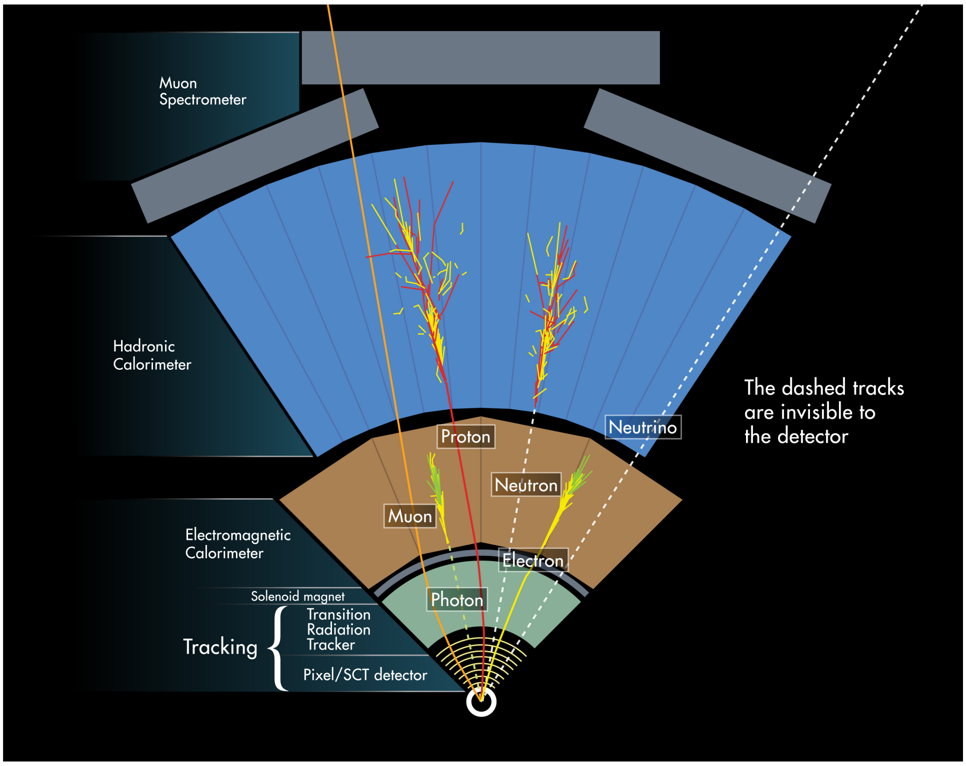

Figure 3.12: Signatures of various objects in the ATLAS detector. Different particles interact differently with matter leaving signatures in varying sets of sub-detectors. [143]

The other way round, observed signatures can be used to infer the nature of the particle causing them, e.g. finding signatures in all sub-detectors well aligned with respect to each other is a "smoking gun" for a muon.

In the following, the reconstruction and identification of the physics objects used in this analysis is presented.

3.3.1 Jets

Jets are final state objects that are the result of strongly interacting particles (quarks and gluons). Due to confinement, these objects hadronize immediately after production. This results in a spray of particles which are more or less collimated. Since the originally produced partons are not accessible at measurement levels, one has to find a way to classify a bundle of final state particles unambiguously as one object.

The same question arises on the theory level as well. Due to the coupling structure of QCD, additional emissions of low energy partons or a collinear splitting are highly likely and not fundamentally distinguishable from a single parton at higher order calculations. For that reason, a jet definition has to be a) “collinear safe” and b) “infrared safe” meaning the observable must not change if one a) splits a hard object into two softer, collinear objects or b) adds an additional, low energy particle.

Finally, a jet algorithm has to perform on detector level, e.g. on calorimeter cells, in the same way as on theory (partons) or on simulated events (simulated final state particles). Only this way one can compare between theory, simulation and experiment.

One class of algorithms that fulfill these conditions are jet clustering algorithms. They are generally defined by an iterative approach, where the possible constituents are pairwise clustered until a defined stop condition is met. For the exploited jet algorithms, there are two distance measures:

$$\begin{aligned} d_{ij} &= \min\left(\left(k_T^{2p}\right)_i, \left(k_T^{2p}\right)_j\right) \frac{\left(\Delta R_{ij}\right)^2}{R} \\ d_{iB} &= \left(k_T^{2p}\right)_i \end{aligned}$$

where k_T^{2p} is the magnitude of the transverse momentum of an object, ΔR_{ij} is the distance in ϕ–η space and R and p are free parameters.

In each iteration, d_{ij} is computed for each pair of object and d_{iB} is computed for each individual object. These are then collected in a list sorted by magnitude. If a d_{ij} is the smallest entry, the underlying objects are grouped together and the list is remade. If a d_{iB} is the smallest object, it is considered as a jet and removed from the list.

The parameter R governs the size of a jet. The larger R, the larger the resulting jets get. The parameter p steers the priorities of the clustering process. Common choices are $p = 1$ (k_T algorithm [144]), $p = 0$ (Cambridge/Aachen algorithm [145, 146]) and $p = -1$ (anti-k_T algorithm [147]).

For $p = 1$, soft constituents are merged first. In some way this mimics the soft radiation process of QCD. The advantage of the k_T variant is that the substructure of the jet is preserved by the ordering of the merging. The disadvantage is the large number of soft jets that remain not merged and is “lost”. In the Cambridge/Aachen variant, objects are merged only according to their geometrical vicinity and regardless of their momentum. While this preserves the substructure of a jet (the last merge is the one over the largest distance), it leads to a highly irregular structure.

The anti-k_T algorithm starts with hard objects and iteratively merges soft objects to them. This leads to a regular structure of the hardest jets with the softer objects being interleaved between them. While this eradicates any information of the structure, the regularity of the jet area is a highly beneficial feature for calibration and correction for pileup events.

For ATLAS, these and some other jet implementations have been tested. The anti-k_T algorithm with a distance parameter of $R = 0.4$ has been shown to exhibit the best performance in a “standard” physics analysis. Other approaches are used where the jet structure is crucial, e.g. when trying to identify highly boosted top quarks decaying in one large jet.

On detector level, jets are formed on so called topo-clusters of calorimeter cells [148]. That means that each individual calorimeter cell that has an energy entry above a defined noise threshold is considered in the clustering. Clusters start with calorimeter cells having a signal to noise ratio of $\frac{S}{N} > 4$. In the next step all neighbors and neighbors of neighbors are added that have $\frac{S}{N} > 2$. Finally all neighboring cells of that cluster are added regardless of their content. In cases where the resulting cluster has two distinct maxima, it is split and cells lying in between the tow sub-clusters are shared.

The resulting clusters are then calibrated using a local hadronic calibration. This implies that the “hadron-nes” of a cluster is derived from the cluster properties and a calibration is applied based on the estimated fraction of hadronic energy in the cluster. The calibration includes corrections for invisible and escaped energy as well as for dead material and detector effects. It also (partially) cancels the non-compensating[12] properties of the ATLAS calorimeters.

The resulting jets are then further calibrated to the Jet Energy Scale (JES) [149]. The JES contains corrections for pileup following [150] and the direction of the jet with respect to the reconstructed vertex. It is derived from Monte Carlo simulations by comparing the reconstructed energy of a jet with its true energy. In a last step, residual corrections derived from auxiliary measurements are applied to measured jets in data.

For the analysis, “baseline” jets are required to have at least $p_T > 20\,\mathrm{GeV}$ and must have been reconstructed in the region $|\eta| < 2.8$. A jet cleaning is applied to distinguish real jets from spurious calorimeter measurements associated to beam particles, cosmic muons or noise. The cleaning is explained in [149] and the “Looser” working point is employed for this analysis. Jets failing the cleaning but satisfy the other minimal selection criteria are flagged as “bad” jets.

A further, tighter jet selection is introduced to help distinguishing jets from hard interactions from those originating from pileup events. It is realized by raising the transverse momentum requirement to $p_T > 30\,\mathrm{GeV}$ and requiring the jets to be reconstructed within the coverage of the tracking detectors ($|\eta| < 2.5$). Additionally, the jet-vertex-fraction (JVF) [151] is calculated for each jet. This number encodes the estimated fraction of the energy of a jet that originates from the primary interaction vertex and is evaluated by matching tracks to a given jet. For central, low energy jets ($|\eta| < 2.4$, $p_T < 50\,\mathrm{GeV}$) the JVF is required to be larger than 0.5. Jets fulfilling these criteria are flagged as “signal” jets.

3.3.2 B-jets

Jets emerging from b-quarks have a slightly different topology than “light flavor” jets. In the first hadronization step, the b binds with a light quark to a hadron. Typically, b-hadrons have a much longer lifetime than light flavor hadrons, resulting in a measurable flight distance before they decay. This results in a slight displacement of the jet with respect to other jets from the same interaction vertex. Additionally, b-hadrons have often very distinctive decay modes, e.g. including light leptons that can be identified even inside the residual jet activity from the hadronization process. Multiple algorithms have been developed to identify (“tag”) b-jets based on these characteristics [152]: The IP3D tagger uses the “impact parameter”, i.e. the displacement of the jet axis with respect to the reconstructed primary vertex, the SV1 tagger tries to reconstruct a secondary vertex based on the tracks within the jets and the JetFitter algorithm tries to identify decays of b- hadrons and links them to a secondary decay vertex. The discrimination power of these three approaches is enhanced by combining them within an artificial neural network resulting in the MV1 tagger [153]. The MV1 algorithm calculates a flavor weight between zero and one for each jet, where the jet is more likely to originate from a b-quark the higher the flavor weight.

By choosing a fixed cut value on the flavor weight, a defined combination of efficiency for b detection and light flavor jet rejection can be achieved. The efficiencies for various cut values are calibrated in

---

[12] A calorimeter is called compensating if the response depends only on the energy of a stopped particle and not on the type of the particle.

dedicated analyses [154] using the b-quarks that are produced in the decay of top quarks as a benchmark. The rate for light flavor jets to be erroneously tagged as b-jets is calibrated differently on an inclusive sample [153]. For this analysis, a cut is chosen that corresponds to a detection efficiency of 60% with a rejection factor for light flavor jets of about 600. The information about the flavor of the jet is in general only used to separate W+jets and top quark background contributions, hence the actual choice of the working point is not of paramount importance. It was decided to employ a cut value in the middle of the range of working points provided. As to be seen later (c.f. Section 6.2.2) this choice results in a sufficiently clean sample of top quark events.

3.3.3 Light leptons

Light leptons do not play a large role in the analysis presented in this thesis. Their only use is to ensure that there is no overlap to parallel searches for events with taus and light leptons as e.g. in detail described in [12]. Details to the reconstruction and identification of electrons and muons can be found there and e.g. in [155, 156] for electrons and [157–159] for muons, respectively.

For this analysis only the loosest possible identification strength (“baseline”) is employed – leading to the strongest possible veto condition. Electrons are required to have $p_T > 20\,\text{GeV}$ and $|\eta| < 2.47$ while muons must have $p_T > 10\,\text{GeV}$ and $|\eta| < 2.4$. No isolation requirement is imposed to the light leptons.

3.3.4 Tau leptons

Tau leptons are the key signature particles in this work and many analysis steps are driven by the special properties of the tau leptons. In general in ATLAS, “tau leptons” refers to the hadronic decay products of the original tau leptons. Due to the unknown initial state and the various possible sources of unmeasured energy, a reconstruction of the leptonic decay modes is de-facto impossible. Due to the neutrino in the tau decay, the hadronic decay products do not carry the full energy of the original tau but only a fraction. In a hadron collider environment however, this “visible” part is generally the only achievable way of “seeing” taus. The following summary is largely compiled from [160]. A comprehensive overview of the reconstruction of hadronic taus and the performance thereof can be found there.

The tau reconstruction is seeded by jets with a p_T of at least 10 GeV reconstructed using the same algorithms as described above (although without the JES calibration). For each jet, a tau vertex association (TV) is performed. The TV matches good quality tracks in a cone with size $\Delta R = 0.2$ around the jet direction to reconstructed primary vertices in the event. The vertex which “contributes” the highest fraction to the tau p_T is chosen as reference for the tau reconstruction. For events with relatively low total energy like $Z \to \tau\tau$, the tau vertex coincides in more than 90% with the vertex with the highest total transverse momentum. For harder topologies, this number rises to more than 99%.

The visible momentum of the tau $p_{T,\text{vis}}$ is calculated from the topo cluster of the seed jet. First the barycenter of the jet cluster is calculated assuming no mass for each cell. Then the four vectors of all cells in a cone of $\Delta R = 0.2$ around the barycenter are recalculated using the tau vertex. The sum of those constitutes the visible four momentum of the tau assuming again zero mass. Tracks in the “core region” of $\Delta R < 0.2$ around the visible tau direction are associated to the tau if they have $p_T > 1\,\text{GeV}$ and at least seven hits in the silicon trackers (Pixel and SCT) with at least two of them in the Pixel detector. Additionally, the impact parameters to the tau vertex have to fulfill $|d_0| < 1\,\text{mm}$ in the transverse plane and $|z_0 \sin\theta| < 1.5\,\mathrm{mm}$ in longitudinal direction. Tracks fulfilling the same quality criteria in the "isolation region" $0.2 < \Delta R < 0.4$ are needed for the calculation of identification variables.

Special care is taken to identify possible π^0 from the tau decays. Both cluster shapes and track information in the core region are used to identify possible π^0 and assign a likelihood to them. The information about the π^0 is used in the tau identification described in the following.

The tau objects reconstructed this way do not offer a good discrimination against jets. As outlined in Section 2.1.4, there are some subtle differences that can be exploited to distinguish hadronic tau decays from QCD jets. A first suppression can be gained by requiring tau candidates to have either one or three associated tracks, since this covers 99.9% of all hadronic tau decays [3]. But even then, some – especially high p_T, quark initiated – jets can be tightly collimated as well and end up having only very few reconstructed tracks. To increase the rejection power, a multivariate Boosted Decision Tree (BDT) [161] discriminate implemented in the TMVA package [162] is constructed from the following variables:

Centrality fraction $f_{\mathbf{cent}}$ Ratio of the transverse energy in a cone of $\Delta R < 0.1$ around the tau direction over the transverse energy in a $\Delta R < 0.2$ cone. A possible bias due to pileup is remedied by applying a correction based on the number of reconstructed primary vertices in the event.

Leading track momentum fraction $f_{\mathbf{track}}$ Ratio of the transverse momentum of the highest p_T track in the core region over the transverse energy in a $\Delta R < 0.2$ cone. Again a pileup correction is applied the same way as for f_{cent}.

Track radius $R_{\mathbf{track}}$ Distance of the tracks to the direction of the tau. All tracks in the core and isolation region are used p_T-weighted.

Leading track IP significance $S_{\mathbf{lead\ track}}$ Significance of the impact parameter of the track with the highest p_T in the core region.

Number of tracks in isolation region $N^{\mathbf{iso}}_{\mathbf{track}}$

Maximum track separation $\Delta R_{\mathbf{max}}$ Maximum distance between any track in the core region and the tau direction.

Transverse flight path significance $S^{\mathbf{flight}}_{\mathbf{T}}$ Significance of the decay length of the secondary vertex reconstructed from the core region tracks. Only defined for multi-track candidates

Track mass $m_{\mathbf{track}}$ Invariant mass of the four momenta of all tracks in the core and isolation regions.

Track-plus-π^0-system mass $m_{\pi^0\,\mathbf{+track}}$ Invariant mass of the four momenta of all tracks in the core regions and all reconstructed π^0.

Number of π^0 N_{π^0} in the core region.

Track-plus-π^0-system fraction $p_T^{\pi^0\,\mathbf{+track}}/p_T$ Ratio of the combined p_T of all tracks and π^0 in the core region to the p_T measured from the calorimeter measurement.

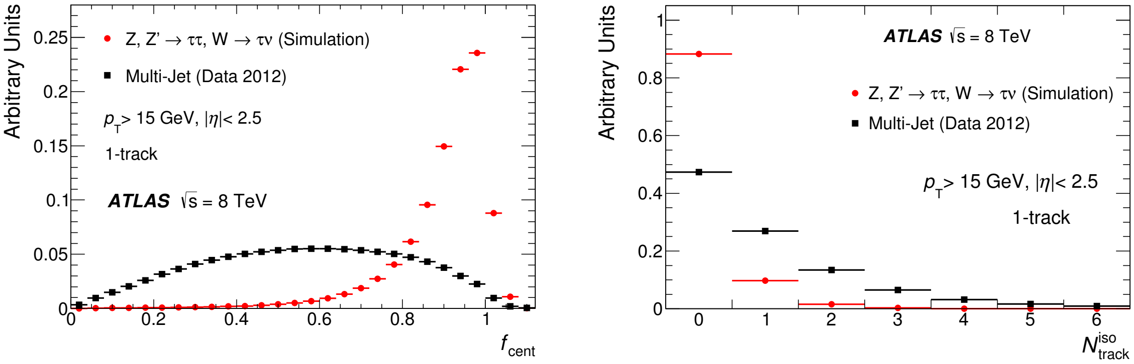

(a) f_{cent}, one-track candidates

(b) R_{track}, one-track candidates

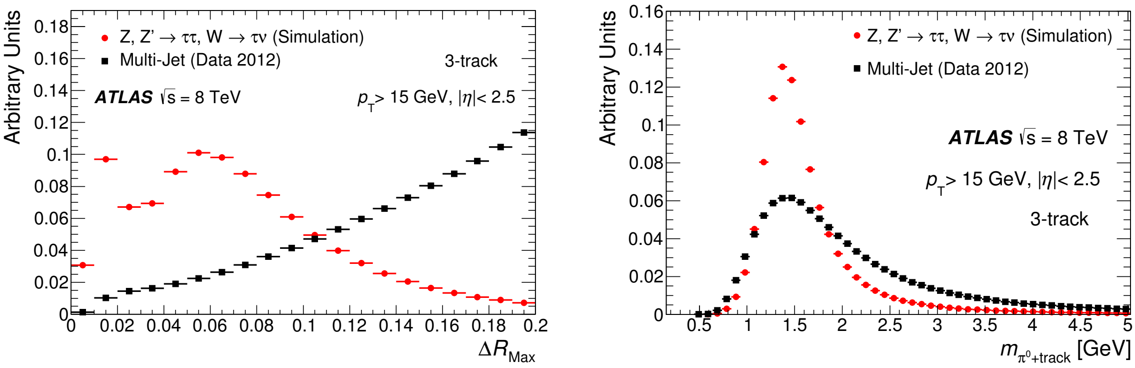

(c) $\Delta R_{\max}$, three-track candidates

(d) $m_{\pi^0\,\text{+track}}$, three-track candidates

Figure 3.13: Example distributions for discriminating variables to distinguish taus from jets. For each variable a signal distribution from a $Z \to \tau\tau$ simulation and a background distribution from data applying a di-jet selection are displayed. Figures a) and b) show candidates with one track, figures c) and d) with three tracks (all figures from [160]).

Figure 3.13 shows example distributions for some of the variables.

A BDT is trained for one-track and three-track candidates separately on a set of true taus from simulation and jets from data, obtained by applying a di-jet selection. The signal efficiency is defined as the fraction of true hadronic taus with n associated tracks being reconstructed as having n tracks and passing the tau identification criteria. The background efficiency is defined as the fraction of jets being reconstructed as taus with n tracks in a background dominated sample. Figure 3.14 displays the inverse background efficiency versus the signal efficiency in two p_T ranges. Three working points “loose”, “medium” and “tight” are defined that correspond to a fixed signal efficiency, independent of the p_T of the tau candidate. Due to the selection of the input variables, the efficiency is independent of the pileup. For this analysis, the loose working point is selected. Since two tau leptons are required, a higher efficiency and a lower rejection are preferred to maximize the acceptance of the search.

Taus cannot only be confused with jets but also with electrons. Both one-track hadronic tau decays and electrons have isolated tracks and collimated clusters in the calorimeters. A second BDT is trained to distinguish taus from electrons. It uses various shower shape variables and the fraction of high

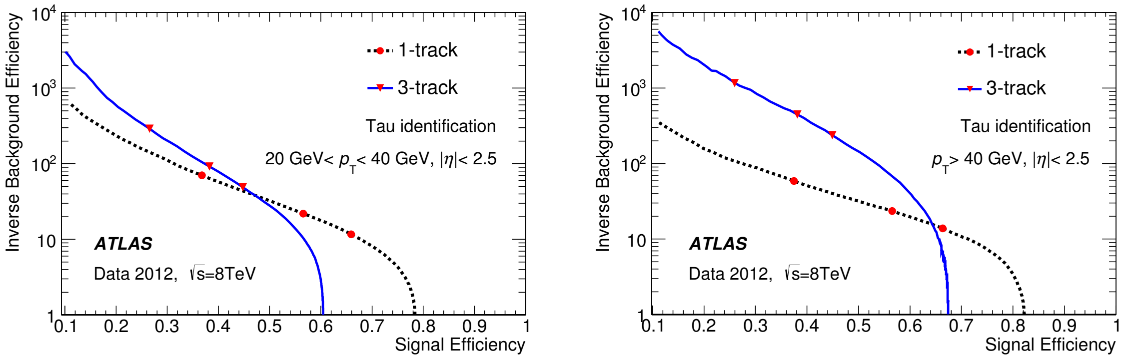

(a) $20\,\text{GeV} < p_T < 40\,\text{GeV}$

(b) $p_T > 40\,\text{GeV}$

Figure 3.14: Inverse background efficiency vs. signal efficiency for one-track and three-track tau candidates in two different p_T ranges. The red dots on the curves correspond to the three working points mentioned in the text (all figures from [160]).

threshold hits in the TRT as input variables. The electron BDT is trained separately in different η regions to account for the different detector capabilities. Again, three working points are defined with the “loose” one, corresponding to 95% signal efficiency, being employed in this analysis.

The energy of the taus is reconstructed from calorimeter cells that have been calibrated for the typical composition in jets (local calibration). Since taus have a somewhat different constitution and the energy is reconstructed from a tighter cone, additional corrections are needed to ensure a reliable measurement of the tau energies. These corrections are derived from simulation. Figures 3.15 a) and b) show these calibration functions. On top of this, additional small corrections are applied to compensate a small bias in the η reconstruction in poorly instrumented regions of the calorimeter and to energy shifts from pileup interactions. The achieved resolution is displayed in Figures 3.15 c) and d) separately for single-track and multi-track tau candidates in different η-regions. With about 20% it is largest for low tau energies and goes down to about 5% for high-p_T taus. In general, the resolution is better in the central part of the detector.

Summarizing, tau hadrons have to be reconstructed with one or three tracks, must have $p_T > 20\,\text{GeV}$, $|\eta| < 2.5$ and have to pass the “loose” identification criteria for both jet and electron rejection.

Performance of the tau reconstruction

Due to the complexity of the tau decays, the reconstruction performance has to be validated and cross checked between data and simulation. At the same time, these measurements serve to derive additional correction factors and to determine uncertainties that come with the tau reconstruction.

For the identification algorithm this is done using tag-and-probe techniques in events with $Z \to \tau\tau$ where one tau decays hadronically and the other one into a light lepton. The light lepton is taken as “tag”, while the presence of a hadronic tau candidate is required as “probe”. After a suitable event selection, the distribution of tracks in a cone of size $\Delta R < 0.6$ around the tau candidate direction is fitted (c.f. Figure 3.16). Templates for jets and light leptons are derived from auxiliary measurements taking contributions from various background sources into account. Templates for 1-track and 3-track

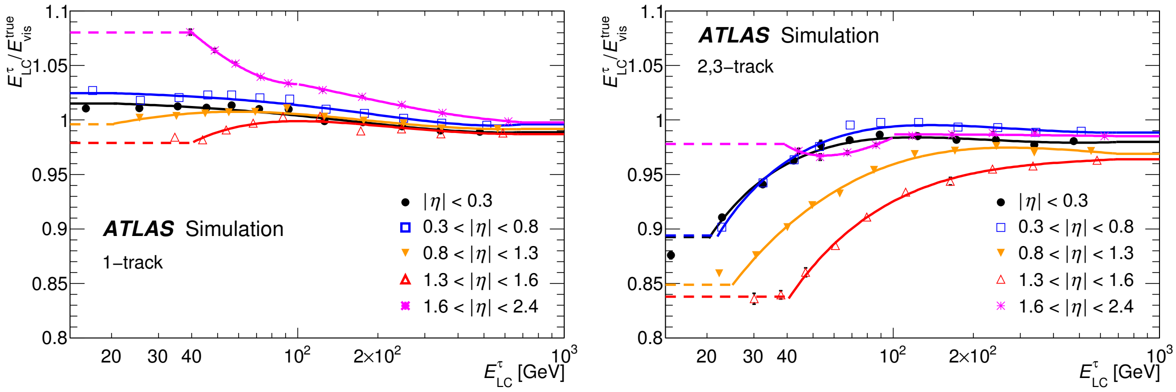

(a) Single-track   (b) Multi-track

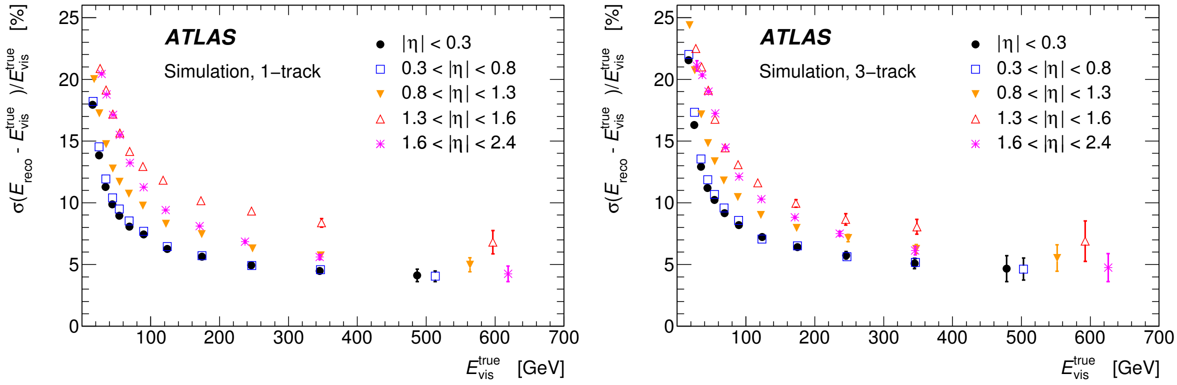

(c) Single-track   (d) Multi-track

Figure 3.15: Calibration functions (top row) as function of the local calibration energy and energy resolution (bottom row) for hadronic taus. Calibration and resolution measurement are separated for single- and multi-track tau candidates and for different η regions (all figures from [160]).

taus are derived from candidates having exactly one or three tracks in the inner core region, respectively. The relative contributions are fitted before and after applying the tau identification, thus measuring the effective efficiency and rejection.

By comparing the results between data and simulation, correction factors are derived. No significant dependence on the p_T of the tau is observed, hence the scale factors between data and simulation are measured separately for single- and multi-track candidates and for barrel and end-cap regions, respectively. The obtained factors are displayed in Figure 3.16. For the loose working point, they are generally slightly larger than one. Uncertainties from the method – dominated by uncertainties on the shape and normalization on the background templates – are propagated to the correction factors resulting in uncertainties in the order of 3%-4%. In the analysis described in this thesis, these scale factors are applied as a correction to the simulation and the uncertainty is considered as a systematic uncertainty on the final results. Similar measurements are performed for the discrimination of taus and electrons and the resulting correction factors and their respective uncertainties are applied as well.

Also the reconstruction of the tau energy is validated in data. An in-situ method is employed using

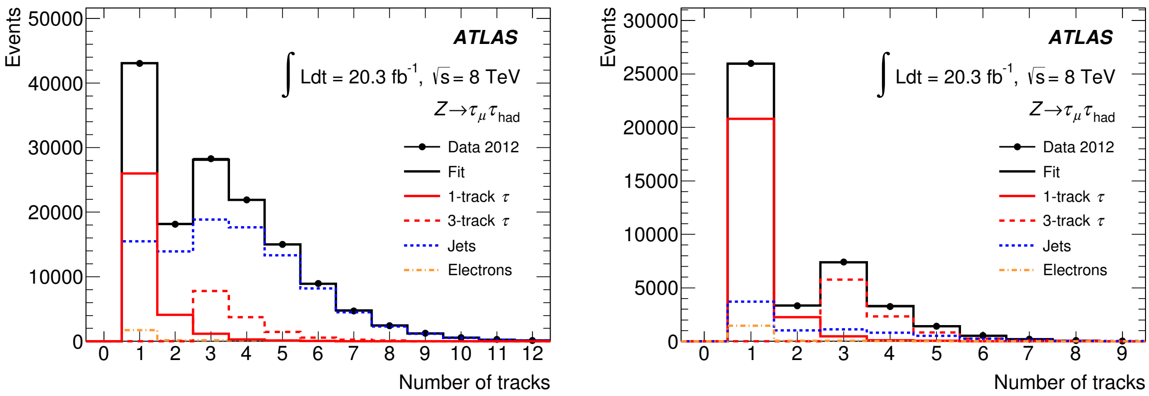

(a) Track multiplicity before tau ID (b) Track multiplicity after tau ID

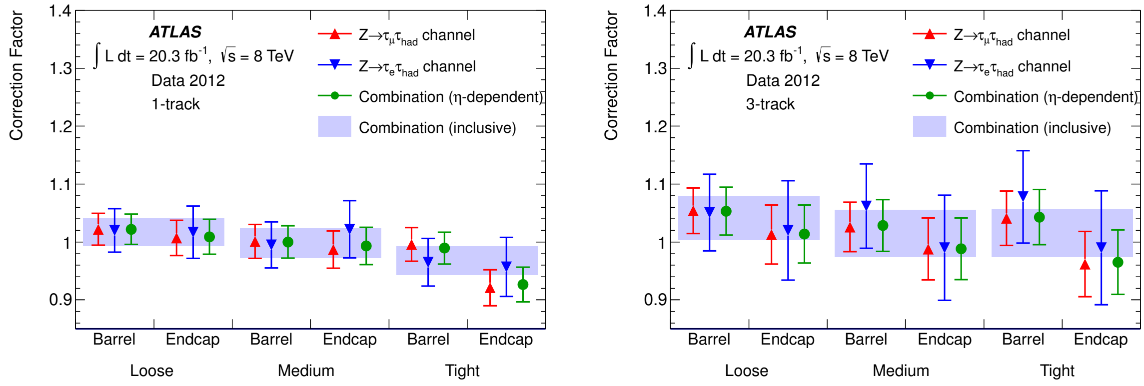

(c) Single-track correction factors (d) Multi-track correction factors

Figure 3.16: Sub-figures a) and b) show the distribution of the track multiplicity in a cone of size 0.6 around the tau candidate direction before and after applying the tau identification, respectively. Theses distributions are fitted with templates for taus and background objects to obtain the efficiency and rejection. Scale factors compensating the difference of the tau identification between data and simulation and their associated uncertainties are derived from these measurement, displayed in sub-figures c) and d) (all figures from [160]).

events with one muon and one hadronic tau. The selection is similar as for the identification measurement, dominantly events with $Z \to \tau\tau$ decays are enriched. The invisible mass of the muon and the tau is fitted allowing the tau energy to vary between data and simulation. The effective shift is determined, for which distributions in data and simulation agree best. Figure 3.17 shows the resulting distributions. A difference in the order of 1% of the nominal calibration is observed. Uncertainties on this shift in the tau energy scale are evaluated from the method and amount to below 1%. For the analysis documented in this thesis, the correction factor is applied to simulated tau candidates and the uncertainty is evaluated as uncertainty on the tau energy scale.

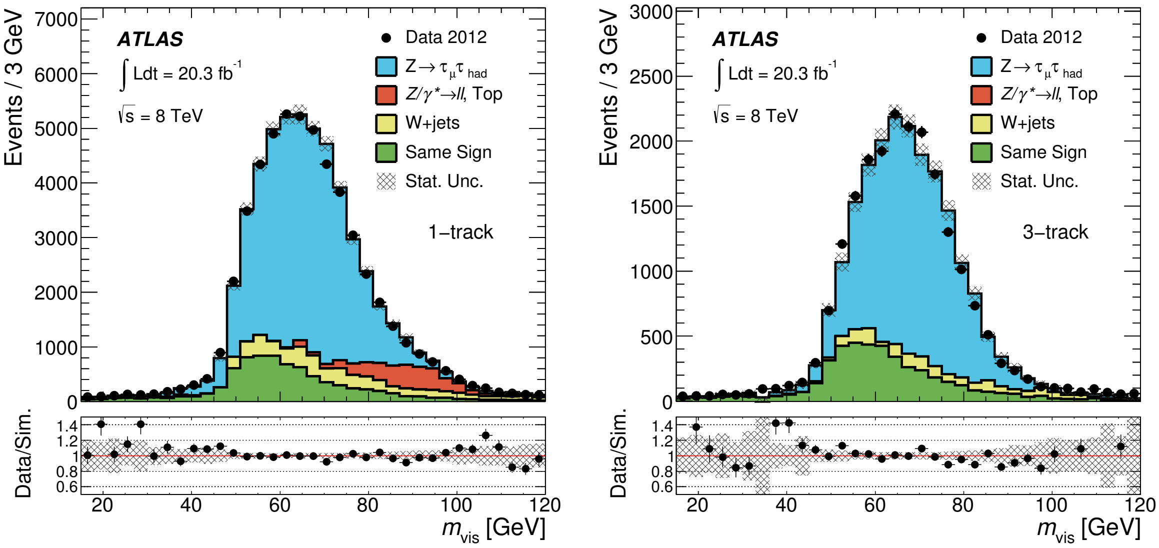

(a) Visible mass of the muon and an 1-track tau candidate

(b) Visible mass of the muon and an 1-track tau candidate

Figure 3.17: Distribution of the invariant mass of one muon and one reconstructed tau candidate for 1-track and 3-track candidates separately. The distributions are fitted allowing the tau energy calibration to float around its nominal value to determine possible corrections on the tau energy calibration (all figures from [160]).

3.3.5 Missing transverse momentum

Another important quantity, both for this analysis and for SUSY searches in general, is the missing transverse momentum $\not{p}_T$ and its magnitude $\not{E}_T$ (missing transverse energy). Momentum conservation generally ensures that all transverse momenta in one collision event should be balanced. However, if there are particles produced that carry away some of the energy and are not detectable in the experiment, this balance is disturbed. In the SM, neutrinos are the obvious candidates for causing $\not{E}_T$. In other models like SUSY there are additional neutral and only weakly interacting particles, which makes large $\not{E}_T$ one of the key signatures for physics beyond the SM. Since it is obviously not directly measurable, it is reconstructed from all reconstructed objects and additionally from unassociated energy depositions in the calorimeter [163, 164]:

$$\not{E}_{x(y)} = \not{E}^{e}_{x(y)} + \not{E}^{\gamma}_{x(y)} + \not{E}^{\tau}_{x(y)} + \not{E}^{\text{jets}}_{x(y)} + \not{E}^{\text{SoftTerm}}_{x(y)} + \not{E}^{\mu}_{x(y)}.$$

Each term is the x and y projection, respectively, of the negative sum of the four momenta of the underlying objects. In each term the objects are reconstructed and calibrated according to their "normal" reconstruction. Terms are ranked in the order as they are summed up, e.g. if one energy deposit enters as an electron it will not enter again as another object. $\not{E}_{x(y)}^{\mathrm{SoftTerm}}$ contains all jets below the reconstruction threshold of $p_T > 20\,\mathrm{GeV}$ and all tracks and clusters which are not assigned to any physics object. For those, tracks and clusters are matched to avoid double counting and exploit the higher resolution of the tracking system for low energy objects. $\not{E}_{x(y)}^{\mu}$ is build from all combined muons that have matched measurements in the inner detector and in the muon system and from all segment tagged muon, i.e. muon candidates where an inner detector track is matched to a signal in the muon system but the energy of the object was not sufficient to yield an independent measurement in the outer trackers. For combined muons the estimated energy loss in the calorimeters is subtracted from the calorimeter contributions.

Similarly, from the same objects the total transverse energy in the calorimeters $\sum E_T$ is computed as:

$$\sum E_T = \sum E_T^e + \sum E_T^\gamma + \sum E_T^\tau + \sum E_T^{\mathrm{jets}} + \sum E_T^{\mathrm{SoftTerm}}$$

One specialty of SUSY searches is that the hadronic decay products of taus are not used as independent objects but are treated as jets for the computation of $\not{E}_T$. This is common for all ATLAS SUSY analyses. As long as the signature of the search does not comprise tau leptons, it's only a matter of definition. Since this search relies heavily on tau leptons, it is not so clear however.

To assess the impact of the definition of individual objects as taus or as jets, dedicated studies have been performed which are documented in Appendix C. No indication for any bias from treating taus as jets for the $\not{E}_T$ calculation are found. For this analysis the standard "SUSY style" $\not{E}_T$ is hence used.

3.3.6 Overlap removal

In general, one physical particle traversing the detector can be reconstructed as different objects. For example, each tau will with a high probability also be reconstructed as a jet. The resulting reconstructed objects will point in the same direction. To ensure that each measured signal in the detector is only accounted for in one reconstructed object, an overlap removal procedure is applied after all individual object reconstruction algorithms. The ranking is determined by the efficiency and rejection power of the individual reconstruction algorithms. In general, light leptons can be reconstructed with the highest precission, followed by taus. Jets are very inclusive in the sense that taus, electrons and real jets in the detector are reconstructed as jets, independently of their true nature. The following scheme ensures that each signature in the detector is attributed to the most likely source:

- A (hadronic) tau candidate is rejected if it overlaps with either an electron or a muon within $\Delta R < 0.2$.
- A jet is rejected if it overlaps with a tau or an electron within $\Delta R < 0.2$.
- A muon is rejected if it overlaps with a jet within $\Delta R < 0.2$.
- Finally, an electron or a muon is rejected if it overlaps with a jet within $0.2 < \Delta R < 0.4$.

The last two steps aim at discarding light leptons that are generated by leptonic decays of secondary hadrons within a jet. The overlap removal is performed on "baseline" objects, i.e. before any further "signal" level requirements are applied.

4
Simulation

For most particle physics analyses, a reliable simulation is an nonnegotiable requirement. Simulation is used to optimize selections, predict yields and evaluate the influence of systematic uncertainties. Since generally the cross section for the production SUSY events is relatively low, one establishes selections where no or at least a very small number of events is expected by our current understanding. To do this, and to assess whether the actual observed number of events is a hint for any new processes, one needs a precise simulation of all signatures expected by the SM. Moreover one also needs simulations of signal events to quantify the sensitivity of the established selections.

In the following some general considerations about simulation in particle physics are presented, followed by details about the simulation of both background and signal events used for this analysis.

4.1 Simulating particle physics

Naturally, new phenomena are expected to first appear in the tails of kinematic distributions as predicted by the Standard Model. Those tails are difficult to simulate. Theory descriptions for extreme kinematic configurations often are lacking precision and are intrinsically difficult to calculate, e.g. the p_T of the vector boson in W+jets production. Additionally, these configurations have a very low cross section so one needs to simulate a process with very high statistics to obtain a sufficient number of events in the tail regions. Despite various attempts to remedy those limitations where possible by e.g. constructing binned Monte Carlo simulations, data-driven estimates are still needed to constrain and correct those simulations.

For the simulation of events at a hadron collider the concept of “factorization” is crucial. This term describes the separation between the hard scattering, which happens at short distances and can be computed using perturbation theory, and the long distance processes, like hadronization and the modeling of the underlying event, which can be addressed only phenomenologically. Figure 4.1 depicts this approach. The red part represents a hard scattering which can be computed up to higher orders of perturbation theory. The blue lines represent initial and final state radiations that occur from the hard incoming and outgoing particles. The purple part is the underlying event which describes the interactions of the parts of the incoming protons that do not participate in the hard scattering. These are typically processes with low momentum transfer and inaccessible for a perturbative treatment. Finally the green part symbolizes the hadronization of partons and the subsequent showering to jets which happens at a purely phenomenological level. Additionally, also the structure of the protons has to be taken into account, i.e. the probability to find a given parton carrying a given fraction of the proton momentum, which is described by the parton density function (c.f. Section 2.1.2).

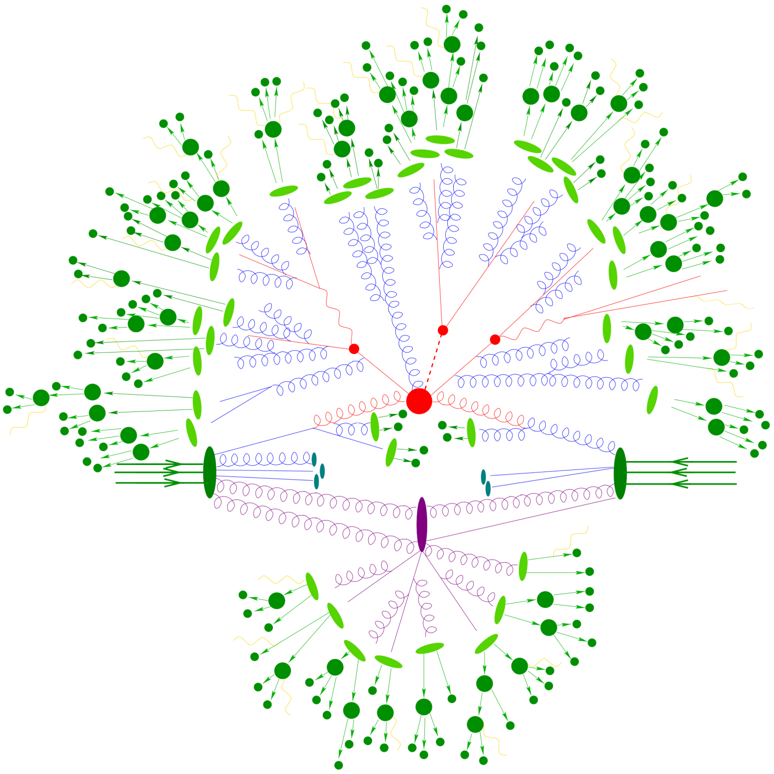

Figure 4.1: Schematic view on the simulation of a proton–proton collision at the LHC [165]. Red parts denote the hard interaction which is calculated at matrix level. Blue lines are radiation processes that are modeled in phenomenological fragmentation models. The purple part denotes the underlying event from the proton remnants while the green part symbolizes the hadronization to detectable final state particles.

Factorization can be exploited by sub-dividing the task of simulating events into smaller subtasks. At the beginning one has to determine the relevant input quantities, i.e. the masses and couplings of the considered particles. For Standard Model backgrounds this is relatively straightforward since all relevant parameters have been measured with good accuracy. For signal samples however, the particle spectrum has to be computed before any event generation is possible.

Simulation is done using a multitude of software packages. There are integrated frameworks, most notably PYTHIA [166, 167], HERWIG [168, 169] and SHERPA [170–173], that simulate the full reaction. Starting from tree-level hard interaction matrix elements, a phase-space integration is performed, parton level events are generated and the final state particles are decayed, hadronized and showered. Multi-particle final states are realized in the showering. The integrated frameworks take care of initial and final state radiation, gluon emissions etc. They also include a simulation of the underlying event.

To improve the predictions of the simulated events, more involved approaches for the matrix element calculation are employed. ALPGEN [174] was developed to improve the description of events with multiple final state partons. Matrix elements are computed at tree level in slices of final state partons. This way one can e.g. simulate the production of a W boson with up to six additional final state partons at matrix element level, which typically yields a better description than taking only the matrix element for the boson production and obtaining the additional partons from showering. ALPGEN has to be interfaced to one of the other codes for showering, hadronization and the underlying event.

Another approach is followed by MC@NLO [175–177] and POWHEG [178–180]. They offer a full NLO computation of the matrix element. At NLO, there is a strong overlap between the matrix element and the showering which has to be accounted for. Different approaches are taken to overcome this problem. In MC@NLO the characteristics of the showering are encoded in the simulation framework for the NLO matrix element. Counter-events with negative event weights are generated to subtract the effect of the showering while keeping the NLO accuracy for inclusive observables. Hence it is necessary to know the details of the showering, i.e. which simulation framework the calculated matrix elements will be interfaced to, prior to the computation. In POWHEG, a different approach is taken. Here the showering is required to be p_T-ordered. Matrix elements are then generated up to the first emission at NLO level. The subsequent showering (PYTHIA or HERWIG) is vetoed to stay below the momentum scale of the first emission.

The radiation of photons from charged particles and the decay of tau leptons can be handled externally. For SHERPA, HERWIG++ 2.5.2 and PYTHIA 8.165, the decays of tau leptons are simulated directly in the generators, while in all other cases TAUOLA 2.4 [181, 182] is used. Final state photon radiation is realized using PHOTOS [183].

All samples are processed either through the GEANT4-based simulation of the ATLAS detector [184, 185] or a fast simulation framework (AFII) where showers in the calorimeters are simulated with a parametrized description [186] and the rest of the detector is simulated with GEANT4. The fast simulation framework is used only for top quark pair production with POWHEG and the low-p_T W/Z+jets samples simulated with SHERPA. The fast simulation is validated against full GEANT4 simulation on the $t\bar{t}$ sample, where a fraction of the events were simulated in both frameworks.

The following sections give an overview of the simulated processes considered in this thesis and the tools used to generate these.

4.2 Background simulation

The most relevant backgrounds for this analysis are *W/Z*+jets and events with top quarks. For these processes, special care has been taken for choosing a simulation. Moreover, these samples are corrected and validated by comparing the resulting prediction to data in dedicated control regions (c.f. Section 6.2). Dibosons production, i.e. events where two vector bosons are produced, could in principle also produce the desired final state. However, the cross sections are much smaller. Dibosons production has hence been estimated from simulation only. Since it is not feasible to simulate QCD events in sufficient amount, multijets production is estimated from data (c.f. Section 6.1).

For the initial comparison with data, all SM background cross sections are normalized to the results of higher-order calculations when available.

***W/Z*+jets** Samples of *W*+jets and *Z*+jets events with up to four jets from matrix elements (ME) are simulated by SHERPA. To improve the agreement between data and simulation, events are re-weighted based on the p_T of the vector boson (c.f. Section 4.4.3).

W/Z+jets samples are simulated separately for events containing only light quarks at ME level (which are assumed to be massless), events containing *c*- but no *b*-quarks, and events with *b*-quarks. The simulation is binned in p_T of the produced vector boson. This separations ensures higher statistics in the tails of the various kinematic distributions. While the higher p_T slices are non-overlapping by construction, the lowest momentum regime is only covered in an inclusive sample. The overlap of the latter with the p_T-binned ones is removed by rejecting all events with a boson p_T larger 40 GeV (70 GeV in case of the *Z* decaying to neutrinos). For *Z* samples an implicit invariant mass requirement of $m_{ll} > 40\,\text{GeV}$ is applied to all events.

For the purpose of evaluating generator uncertainties, additional *W/Z*+jets samples are produced with the ALPGEN generator, which simulates *W* and Z/γ^* production with up to five accompanying partons. For each parton number all leading-order graphs are taken into account. While in the bulk samples all quarks are treated as massless and heavy quarks appear only in the showering, heavy flavor samples are produced with heavy quarks at realistic masses in the matrix elements. The overlap between these samples is removed using the ATLAS Heavy Flavor Overlap Removal [187] (HFOR) tool. In the ALPGEN samples JIMMY [188] is used for the underlying event simulation.

The theoretical cross sections for *W* and *Z* production are calculated with DYNNLO [189] with the MSTW 2008 NNLO [190] PDF set. The same ratio of the next-to-next-to-leading-order (NNLO) to leading-order cross sections is applied to the production of W/Z in association with heavy-flavor quark jets.

Top quarks Top quark pair production is simulated with POWHEG. This generator was chosen from four available ones after comparing key quantities among those (c.f. Appendix D.1). The simulation is corrected for most recent results obtained in the differential cross section measurements in $t\bar{t}$ events (c.f. Section 4.4.4).

The detector response in the POWHEG $t\bar{t}$ sample is simulated with the AFII fast simulation tool. Taus are known to be less reliably described in AFII than in the full simulation. Extensive studies showed, however, that the performance of the AFII $t\bar{t}$ sample is comparable to that of the full simulation for the phase space relevant for this analysis. These studies are documented in Appendix D.2.

Alternative samples to evaluate systematic uncertainties are generated with a very similar setting as the one used for W/Z+jets, using ALPGEN with up to four additional partons in the ME.

The inclusive $t\bar{t}$ cross section is calculated at NNLO, including resummation of next-to-next-to-leading-logarithmic (NNLL) soft gluon terms, with TOP++ 2.0 [191, 192] using MSTW 2008 NNLO PDFs.

The production of single-top-quark events in the s- and Wt-channels is simulated using MC@NLO, while for the t-channel ACER MC [193] is used. In all samples a top quark mass of 172.5 GeV is used consistently.

Approximate NLO+NNLL (next-to-next-to-leading-logarithm) calculations are used for single top quark production cross sections [194–196].

Dibosons The SHERPA MC generator is also used for simulating the production of Dibosons events (WW, WZ and ZZ). Alternative samples for the evaluation of systematic uncertainties are generated by POWHEG. The cross section is calculated at NLO with MCFM [197], using MSTW 2008 PDFs.

Table 4.1 gives an overview of the generators used for all backgrounds together with the versions, the tools used for showering and the tunes of the underlying events. A detailed list of all individual datasets is compiled in Appendix A.

	Channel	Generator	PDF set	Showering	Underlying event tune
Nominal samples	W+jets	SHERPA 1.4.1	CT10 [198]	–	SHERPA default
	Z+jets	SHERPA 1.4.1	CT10	–	SHERPA default
	$t\bar{t}$	POWHEG r2129	CT10	PYTHIA 6.426	Perugia2011C [199]
	Dibosons	SHERPA 1.4.1	CT10	–	SHERPA default
	Single t				
	s-channel and Wt	MC@NLO 4.06	CT10	HERWIG 6.520	AUET2B [200]
	t-channel	ACER MC 3.8	CTEQ6L1 [201]	PYTHIA 6.426	Perugia2011C
Systematic samples	W+jets	ALPGEN 2.14	CTEQ6L1	HERWIG 6.520	AUET2B
	$Z \to \nu\nu +$ jets	ALPGEN 2.14	CTEQ6L1	HERWIG 6.520	AUET2B
	$Z \to \ell\ell +$ jets	ALPGEN 2.14	CTEQ6L1	PYTHIA 6.427	Perugia2011C
	$t\bar{t}$	ALPGEN 2.14	CTEQ6L1	HERWIG 6.520	AUET2B
	Dibosons	POWHEG r2129	CT10	PYTHIA 8.165	AU2 [202]
Signal samples	GMSB	HERWIG++ 2.5.2	CTEQ6L1	–	UEEE [203]
	nGM	HERWIG++ 2.5.2	CTEQ6L1	–	UEEE
	bRPV mSUGRA	PYTHIA 6.426	CTEQ6L1	–	Perugia2011C

Table 4.1: Overview of the simulated samples used in this thesis for both background and signal together with the generators, the parton distribution function, the showering and the underlying event modeling used.

4.3 Signal simulation

Similarly to the expected background, events for various hypothetical SUSY models as presented in Section 2.2.5 are simulated. These samples are arranged in "grids", where two theory parameters are varied while all others are kept constant.

For GMSB, the varied parameters are Λ between 40 TeV and 110 TeV and $\tan\beta$ ranging from 2 to 62. The other parameters are fixed at $\langle S\rangle = 250\,\mathrm{TeV}$, $N_5 = 3$, $\mu > 0$ and $C_{\tilde{G}} = 1$. 79 samples are simulated using HERWIG++. For the nGM model, $m_{\tilde{g}}$ and $m_{\tilde{\tau}}$ are the only two free parameters. 70 samples are produced with HERWIG++ in a $m_{\tilde{\tau}}$ range of 117 GeV–337 GeV with $m_{\tilde{g}}$ varying between 400 GeV and 1 260 GeV for each of the stau masses. For bRPV, 125 samples are available simulated with PYTHIA. Common parameters are $A_0 = -2m_0$, $\tan\beta = 30$ and $\mu > 0$. m_0 is varied from 400 GeV to 2 200 GeV while $m_{1/2}$ is changed in the range of 200 GeV to 800 GeV.

Table 4.1 lists all used generator versions and tunes while all individual samples are compiled in Appendix B. For all signal models, the signal cross sections are calculated to next-to-leading-order in the strong coupling constant using PROSPINO2 [204] adding the re-summation of soft gluon emission at next-to-leading-logarithmic accuracy (NLO+NLL) [204–208] for strong SUSY pair production.

In the computation, uncertainties due to the choices of parameters in the generation process, the PDF uncertainties and the uncertainties on the strong coupling constant are evaluated by re-computing the cross section under different parameters. The resulting cross section values form an envelope where the median is taken as nominal value and the upper and lower extremes are symmetrized to yield one uncertainty as described in [209].

4.4 Corrections of the simulation

When comparing simulation to data, one will most likely not find perfect agreement. Many differences can be accounted for correcting individual objects or even reconstruct them differently in data and in simulation to yield the same performance. One example for this kind of corrections are tau leptons (c.f. Section 3.3.4), where scale factors on the event weight are applied for each reconstructed tau in simulation to match the reconstruction performance observed in data. Other differences depend on the properties of the full event or arise due to lack of information or precision in theoretical calculations a priori to performing the actual measurements. Corrections of the latter type, which are used in this work, are presented in the following.

4.4.1 Pileup re-weighting

The simulation of physics processes a priori to the data taking faces the challenge that the exact conditions under which the data will be recorded are not known. This is especially critical concerning the pileup, the soft proton–proton interactions that happen in the interaction point at the same time as the hard interaction of interest. Ideally, one would directly simulate the distribution observed in data. On the other hand, one needs simulated datasets prior to the actual data taking to develop and test the analysis strategies.

To remedy this contradiction, a hypothetical distribution of the number of pileup events per interaction is assumed. This distribution is compared to the real, observed pileup distribution and a re-weighting is performed to ensure an agreement between the conditions in simulation and data. Unfortunately, the number of soft interactions cannot be measured directly. Often the average number of interactions per bunch crossing $\langle \mu \rangle$ is chosen as a measure. Figure 4.2 shows the simulated (red) and measured (blue) distribution of $\langle \mu \rangle$ for the 2012 data taking and simulation campaign, respectively. Clearly the agreement is not sufficient to exclude a pileup bias on any prediction computed from the simulation.

In the same figure, the re-weighted distribution of $\langle \mu \rangle$ in the simulation is shown in green. The shape matches well the data after the re-weighting, however there is a systematic shift towards lower values. This has multiple reasons: The real quantity of interest for the effect of pileup is not the number of interactions but the activity in the detector, i.e. the number of particles from underlying interactions per area and time, which is however only accessible in dedicated analyses. For the 2012 Monte Carlo production, the pileup is modeled using PYTHIA 8. This modeling is known to not exactly describe the correspondence of the number of interactions and detector activity as seen in data. To remedy this, the number of interactions is shifted by a factor 1.09 in Monte Carlo, which was found to give the best description of the actual background due to pileup in the detector.

Additionally, the size of the beam spot is not correctly modeled in the simulation. This results in a different resolution power for nearby vertices in data and simulation. For this reason, the number of primary vertices reconstructed from the tracks in an event differ between data and simulation, even if the pileup is correctly modeled. The needed corrections to correctly describe the activity in an event result in a situation where neither the average interactions per bunch crossing nor the number of reconstructed primary vertices can match between data and simulation [210].

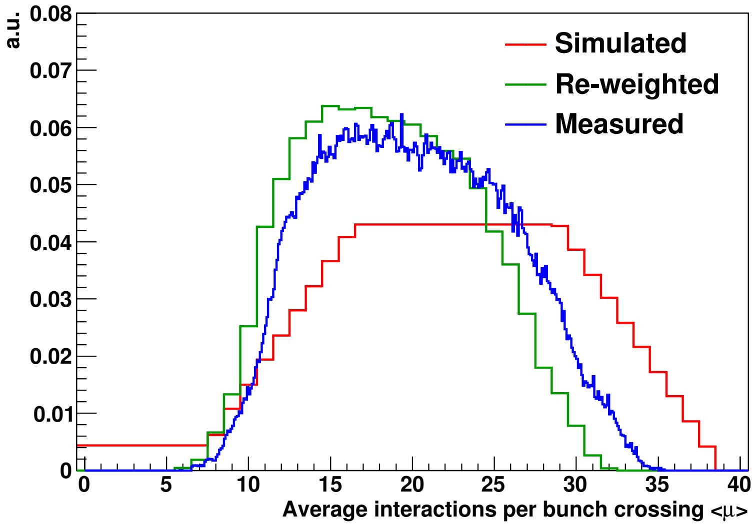

Figure 4.2: Distribution of the mean numbers of interactions per bunch crossing as simulated (red) and as measured in data (blue). A re-weighting procedure is used to bring the shape of both distributions in agreement (green). The remaining shift is due to a difference of the size of the beams at the interaction point between data and simulation.

4.4.2 B-tag re-weighting

Top quark decays pose an important background to the search presented in this thesis. To constrain the simulation, a sample of events enriched with top quark decays, especially from $t\bar{t}$ production, is selected. In this sample data is compared to simulation (c.f. Section 6.2). The enrichment is achieved by requiring jets identified as originating from a b-quark decay, which in turn is likely to be produced in the decay of a top quark (given the other selection applied). The identification of b-jets is sketched in Section 3.3.2. As explained there, the efficiency of the selection algorithms is calibrated in dedicated studies. In the context of constraining top quark simulation with data in an event sample that is defined using the detection of b-jets, one has hence to ensure that the identification yields the same results in data and in simulation.

Unfortunately this is not a-priori the case. For this reason scale factors are provided that recover the measured performance in the simulation. The corrections for b-jets depend on the kinematics of the full event, the number of real b- and c-jets and the response of the tagging algorithm and has thus to be computed on an event basis rather than on an object basis. The re-weighting is only applied to those events fulfilling all kinematic requirements on the control sample to avoid any bias in selections that do not utilize the information about b-quarks.

4.4.3 Correction of the p_T of the vector boson

The calculation of the p_T distribution of the vector boson in W/Z+jets production is one of the most difficult tasks in the theoretical calculation of collisions of strongly interacting particles. Consequently, for the simulation samples used in this analysis, previous studies have shown that the p_T of the boson is not correctly modeled in kinematic regions with high $\not{E}_T$ and hard jet p_T where little experimental data was available prior to the start of the LHC. This is exactly the configuration enforced by the trigger employed in this analysis.

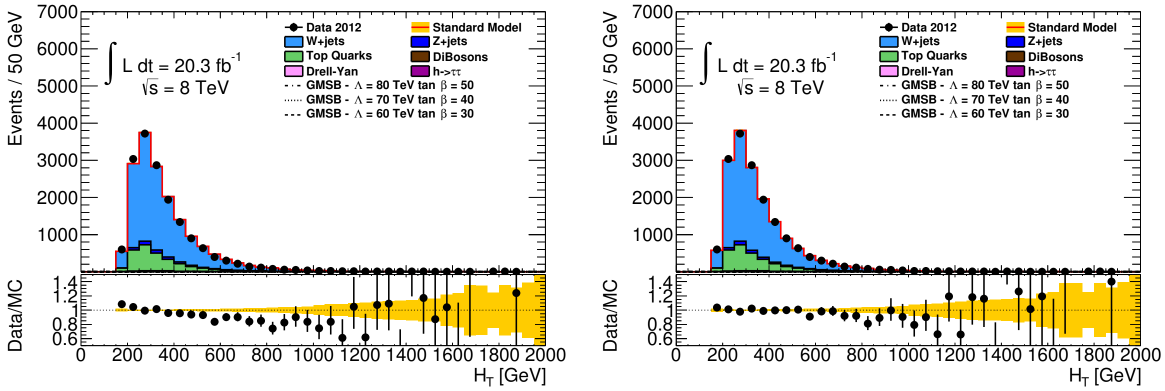

(a) H_T without boson p_T re-weighting

(b) H_T with boson p_T re-weighting

Figure 4.3: Comparison of H_T in the W kinematic control region with and without the boson p_T re-weighting procedure for the Sherpa W+jets and Z+jets samples. An improvement is clearly visible.

A correction factor in several bins of the simulated p_T of the boson has been derived in an analysis searching for decays of the stop quark into scharm quarks [211]. These correction factors have been derived in control regions that exhibit kinematic properties very similar to this search. Indeed, studies in the kinematic control regions (c.f. Section 6.3) show a slope in the data/MC ratio for distributions sensitive to boson p_T mis-modeling. This bias is removed by applying the re-weighting factors (c.f. Figure 4.3). Further studies on a potential bias introduced by varying jet multiplicities is documented in Appendix D.4.

4.4.4 Correction of the differential cross section in $t\bar{t}$ production

The LHC allows to measure detailed properties of processes that were hardly accessibly at all before. Often these measurements find results that differ from the a priori expectations, especially in complex processes that are hard to calculate to high precision. One example is the differential cross section in $t\bar{t}$ production, where the theoretical prediction is known to disagree with the most recent measurements of the differential cross section as a function of the p_T of the $t\bar{t}$ system [212, 213]. To remedy this shortcoming, events from the $t\bar{t}$ simulation are re-weighted according to the simulated-p_T of the $t\bar{t}$ system. Weights vary in four steps from 0.997 for very low $t\bar{t}$ p_T ($p_T < 40\,\text{GeV}$) to 0.570 for the highest $t\bar{t}$ p_T slice ($p_T > 340\,\text{GeV}$). Figure 4.4 shows an example distribution in a dedicated validation region before and after applying the correction. The improvement is clearly visible. Details on these validation studies are compiled in Appendix D.3.

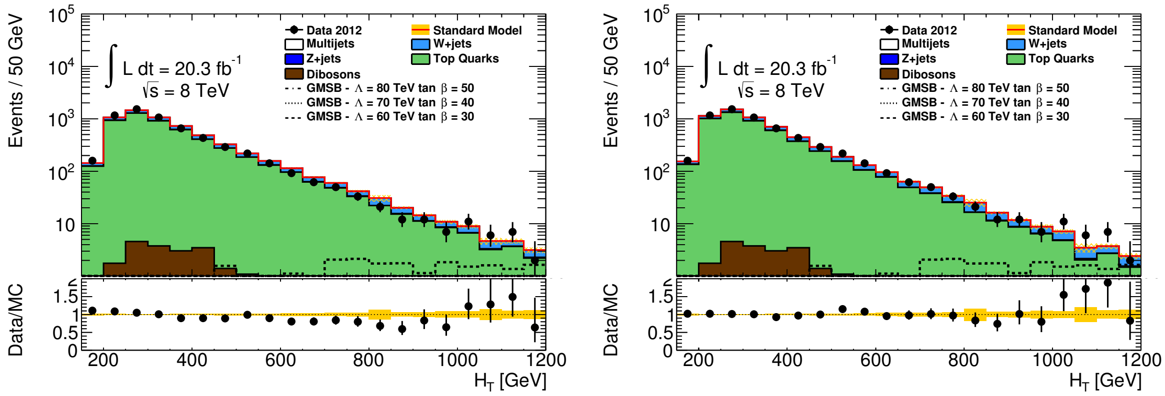

(a) H_T nominal (b) H_T re-weighted

Figure 4.4: H_T shape comparison with and without cross section re-weighting for the $t\bar{t}$ background in a specific validation region that is designed to highlight the effect of the mis-modeling.

5

Event selection & optimization

The goal of every search analysis is to isolate "signal regions" (SR) where a number of events is predicted from a new theory that is significantly higher than the expected number of background events from the Standard Model. The selection used in this analysis and how cuts on individual kinematic quantities are defined is presented in this chapter. First, the general analysis concept is motivated in Section 5.1. Then important kinematic variables that are used in the definition of the SRs are introduced in Section 5.2. The common selection that is the baseline for all signal regions is outlined in Section 5.3 and individual optimizations for the various SRs are explained in Section 5.4. The final selections are summarized in Section 5.5

5.1 Analysis concept

The target of this analysis are final states of SUSY particles being produced via the strong interaction and decaying into tau leptons. More specific, gluinos and squarks are targeted at the production side, independent of their flavor. No attempts are made to select any special initially produced particles like i.e. third generation squarks (parallel efforts that target electroweak gaugino production with tau final states and the decay of stop quarks via staus are followed by other ATLAS groups [214]).

On the decay side, final states with at least two hadronically decaying tau leptons are selected. This analysis is part of a common search for SUSY in tau final states. The other target signatures are one single hadronic tau and one hadronic tau and one light lepton. All analyses are designed to be mutually exclusive to be combined in one common exclusion in case no excess is observed (c.f. Section 8.3.4). To ensure this orthogonality, events containing a light lepton are vetoed in this analysis.

The focus on a production via squarks and gluinos implies that a high jet activity is expected in the detector. Moreover, only scenarios with neutral, long-lived LSPs or neutrino-rich final states are considered, so a large $\not{E}_T$ is also expected. Figure 5.1 shows the distribution of $p_T^{\mathrm{jet}_1}$ and $\not{E}_T$ before applying any analysis cut. The relative normalization of the background compared to the signal is biased in these distribution since some selections are applied a priori to reduce the amount of data that

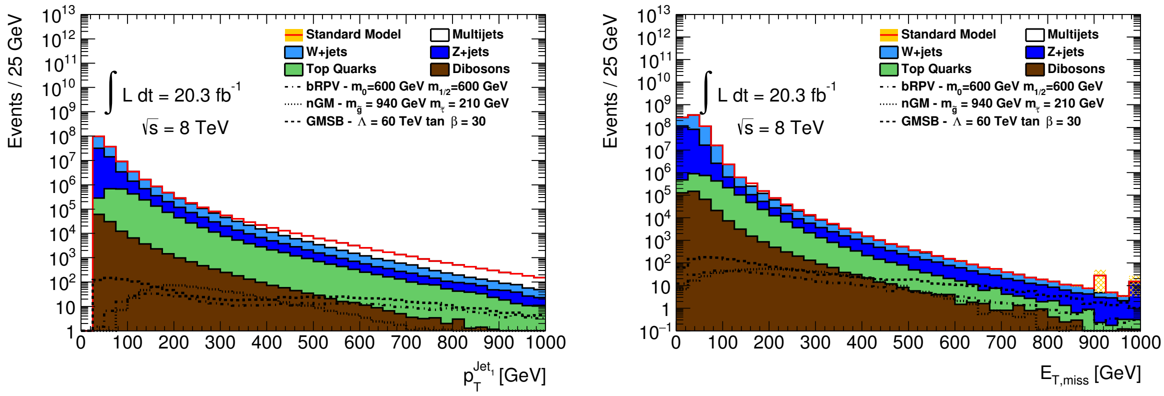

Figure 5.1: $p_T^{\mathrm{jet}_1}$ and $\not{E}_T$ before applying any analysis cuts except for the event cleaning. Note that a preselection for data reduction is applied to all samples, hence a certain bias is expected. For comparison three benchmark points from the three considered grids are shown. The much more pronounced tails in the signal simulation compared to the background simulation are however clearly visible.

has to be handled. However, it is still obvious that all considered models exhibit significantly harder tails than the expected SM backgrounds, which fall off rapidly. This is exploited for triggering and to reduce electroweak backgrounds.

Based on these characteristics, a common selection is established. Since multiple promising scenarios are studied, an individual optimization for each is performed to achieve the best possible exclusion performance in case no sign of SUSY is found.

5.2 Important kinematic variables

Several kinematic variables are used throughout the analysis to distinguish SUSY from SM backgrounds. The most important of these are defined below:

- m_T, the transverse mass formed by $\not{p}_T$ and the p_T of the tau lepton
  $m_\mathrm{T} = \sqrt{2 p_T^\tau \not{E}_T (1 - \cos(\Delta\phi(\tau, \not{p}_T)))}$.
  The sum of the transverse masses of the two leading taus $m_\mathrm{T}^{\tau_1} + m_\mathrm{T}^{\tau_2}$ is then used as a discriminating variable.

- H_T, the scalar sum of the transverse momenta of the tau candidates and the two jets with the largest transverse momenta in the event:
  $H_T = \sum_{\mathrm{all}\ \tau} p_T^\tau + \sum_{i=1,2} p_T^{\mathrm{jet}_i}$.

- the magnitude of the missing transverse momentum $\not{E}_T$;

- the number of reconstructed signal jets N_jet.

Often H_T is defined to include the sum of the p_T of all jets. However, with this definition it has been found to be correlated with N_jet since every additional jet adds at least its minimal p_T to the sum. To enable the independent optimization of a cut on N_jet, only the two leading jets which are required explicitly are considered in the computation of H_T.

5.3 Common selection

A basic event cleaning and preselection is applied that ensures that only well reconstructed events recorded with a fully functional detector enter the analysis. These preselection cuts require:

- The event originates from a data taking period included in the the GRL. This rejects *pp* collision data with unacceptable detector conditions, in the way described in Section 3.2.5. It ensures that only well reconstructed physics objects enter the analysis.
- The event has a primary vertex with at least five tracks.
- The event was not flagged as containing noise from one of the calorimeters.
- The event is not likely to contain large instrumental $\not{E}_T$ due to dis-functional cells in the Tile Calorimeter.
- The event does not contain a cosmic muon candidate (muon with large impact parameter).
- The event does not contain a badly-reconstructed muon.
- The events does not contain any "bad jets" that prevail after overlap removal.

To ensure only events matching roughly the desired kinematic properties expected from SUSY and to reduce the amount of data an initial reduction is applied. On data a trigger requiring at least 100 GeV of $\not{E}_T$ and $p_T^{\text{jet}_1} > 80\,\text{GeV}$[1] is imposed. With the initial trigger requirement applying only to data, additional kinematic cuts are imposed to the reconstructed objects in data and simulation in order to exclude trigger turn-on (c.f. Figure 5.2) effects. These trigger plateau cuts require the presence of at least two jets, one with $p_T > 130\,\text{GeV}$ and the second with $p_T > 30\,\text{GeV}$, as well as $\not{E}_T > 150\,\text{GeV}$. The same trigger is employed by the search for SUSY in events with no leptons and multiple jets [215]. In this context the efficiency is studied in detail and appropriate cuts are derived to ensure the trigger has a nearly 100% efficiency. Figure 5.2 shows the efficiency curves for both the jet and the $\not{E}_T$ terms of this combined trigger. Clearly, for a cut of $p_T^{\text{jet}_1} > 130\,\text{GeV}$ the trigger has reached a plateau. For the $\not{E}_T$ term the efficiency turn-on depends on the imposed momentum cut on the leading jet. For high momenta the trigger reaches a plateau around the value of 150 GeV chosen for this analysis.

The structure of the trigger chosen would in principle allow for a softer $p_T^{\text{jet}_1}$ cut at the cost of a harder $\not{E}_T$ cut. Also a pure $\not{E}_T$ trigger with a similar nominal threshold would be available. Studies have shown that the cut of $p_T^{\text{jet}_1} > 130\,\text{GeV}$ does not limit the signal efficiency in the interesting kinematic regions. A higher $\not{E}_T$ cut, in contrast, would cut into the acceptance for some models. For this reason the combined trigger with a relative high jet cut and a $\not{E}_T$ cut as low as possible is used.

The search channel for this analysis is defined by the presence of two taus fulfilling "loose" identification criteria and a p_T of at least 20 GeV. Due to the requirement of two taus, the rejection power of the tau identification is "squared". Hence it is desirable to use the loosest available identification level to maximize sensitivity. Additionally, a veto for events containing baseline muons or baseline electrons is applied. This veto is not designed to improve this analysis but ensures that there is no overlap between this search and other searches focusing on final states with light leptons.

---

[1] The name of the trigger item is "EF_J80_A4TCHAD_XE100_TCLCW_VERYLOOSE"

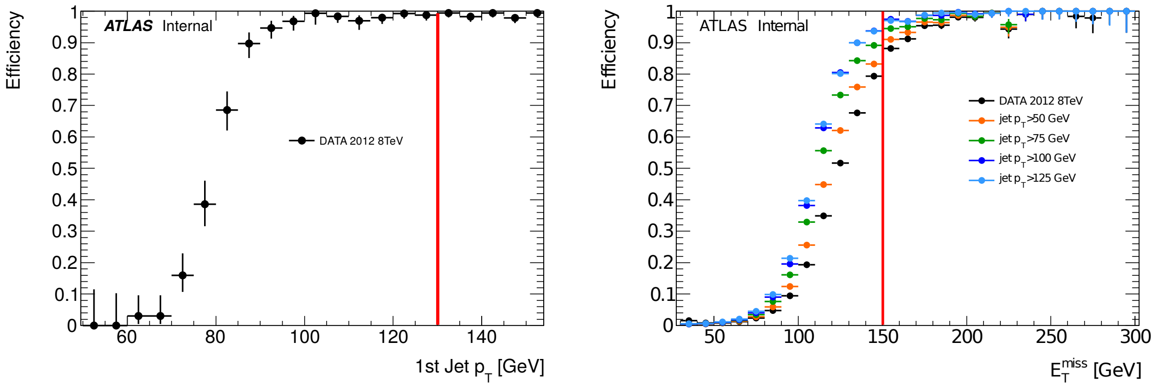

(a) $p_T^{\text{jet}_1}$ efficiency curve

(b) $\not{E}_T$ efficiency curve

Figure 5.2: Efficiency curves of the $p_T^{\text{jet}_1}$ (a) and $\not{E}_T$ (b) components of the combined trigger used in this analysis (EF_J80_A4TCHAD_XE100_TCLCW_VERYLOOSE). The turn-on curves are determined by computing the efficiency of the used trigger in a data sample that was triggered by the looser missing energy trigger EF_XE50_A4TCHAD. The $\not{E}_T$ turn-on is derived after varying cuts on $p_T^{\text{jet}_1}$. The jet turn-on is derived without any explicit $\not{E}_T$ cut (except for the intrinsic cut imposed by the trigger of the underlying data sample). Red lines indicate the threshold cuts employed in this analysis to ensure a full efficiency of the chosen trigger. Figures are taken from [216].

After requiring the trigger plateau cuts and the presence of two taus, the background from multijets production is rejected almost completely. In the remaining events the $\not{E}_T$ results from a mismeasurement of one jet while the taus are faked by collimated jets. This contribution is further reduced by requiring the leading and sub-leading jet to be separated from $\not{p}_T$ by at least a distance of 0.3 in ϕ: $\Delta\Phi(\text{jet}_{1/2}, \not{p}_T) > 0.3$.

The dominant contributions to the remaining background are W+jets, Z+jets and top quark production. Rejection cuts for these backgrounds are optimized relative to the targeted signal as outlined in the following section.

5.4 Optimization for individual signal models

Targeting multiple models implies that one has to consider more than one signal region to obtain optimal performance. Figure 5.3 shows the distributions of both H_T and N_{jet} after applying the common selection. Displayed are the expected background as well as three benchmark points from the three considered grids. In the H_T distribution one can clearly see that all signal models exhibit shapes that are shifted to higher values compared to the expected background. However, only in the case of GMSB it is significant enough to serve as a dominant separator between signal and background. On the other hand, the N_{jet} distribution is shifted to high values for nGM while for the other models no large excess over the SM expectation is visible in the higher jet bins. For this reason, cuts are optimized for each model (and in case of bRPV even for two distinct regions of the grid) individually.

The analysis cuts defining the signal region for each model are chosen by statistical optimization. The optimization is based on benchmark points for each SUSY model under investigation. They are chosen such that their kinematic properties are representative of a wide range of the parameter space, offering

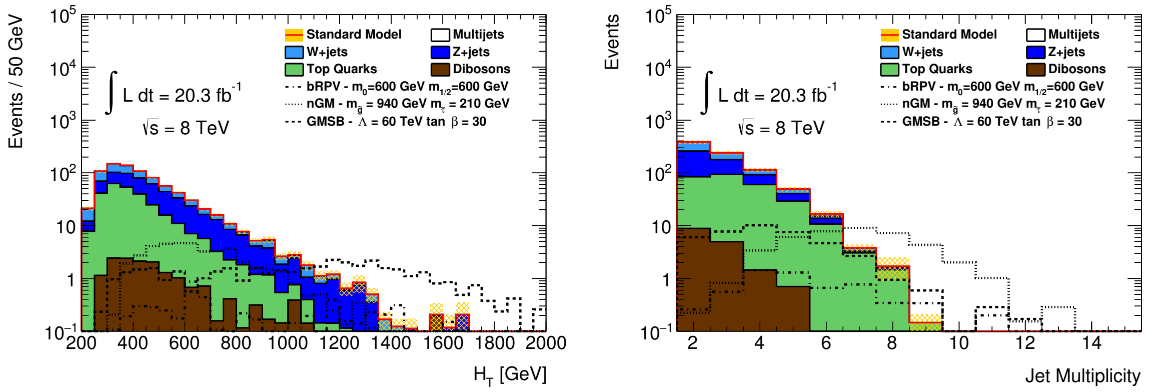

(a) H_T

(b) N_{jet}

Figure 5.3: Comparison of H_T (a) and N_{jet} (b) for three benchmark signals. All distributions are shown after applying the common selection. For comparison three benchmark points from the three considered grids are shown. The different behaviour of the different signal samples is clearly visible.

large inclusive τ production cross sections while not yet being excluded by former experiments.

The optimization procedure maximizes the Asimov approximation of the discovery significance [217]

$$z_A \equiv \sqrt{2\left[(N_{\text{Sig}}+N_{\text{BG}})\ln\left(1+\frac{N_{\text{Sig}}}{N_{\text{BG}}}\right)-N_{\text{Sig}}\right]}\,,$$

where the signal yield N_{Sig} corresponds to one of the benchmark points used for optimization and the background yield N_{BG} is the sum of all SM backgrounds, expected for 20.3 fb^{-1} of data. The quantity z_A reduces to the familiar formula $N_{\text{Sig}}/\sqrt{N_{\text{BG}}}$ in the large-statistics limit, but provides a better description of the Poisson fluctuations for low event yields.

In the case that uncertainties on the number of background events are taken into account, the formula above will overestimate the expected significance and the estimate must be modified to [218]:

$$z_A \equiv \sqrt{2\left\{(N_{\text{Sig}}+N_{\text{BG}})ln\left[\frac{(N_{\text{Sig}}+N_{\text{BG}})(N_{\text{BG}}+\sigma^2_{N_{\text{BG}}})}{N^2_{\text{BG}}+(N_{\text{Sig}}+N_{\text{BG}})\sigma^2_{N_{\text{BG}}}}\right]-\frac{N^2_{\text{BG}}}{\sigma^2_{N_{\text{BG}}}}ln\left[1+\frac{N_{\text{Sig}}\sigma^2_{N_{\text{BG}}}}{N_{\text{BG}}(N_{\text{BG}}+\sigma^2_{N_{\text{BG}}})}\right]\right\}}$$

Uncertainties due to limited Monte Carlo statistics are evaluated bin by bin. Additionally, a constant uncertainty of 30% is assumed and added in quadrature to account for the various systematic uncertainties. For all plots and scans the different background contributions are scaled with the respective correction factors obtained in the background estimation (c.f. Section 6). Corresponding uncertainties are also considered.

For background estimation and validation it is useful to have one common cut on one variable that separates signal and background for all possible hypotheses. For this analysis H_T is chosen since it is a relatively unbiased quantity that scales mainly with the masses of the particles involved in the decay chains of the events. The region $H_T < 550\,\text{GeV}$ is identified as background dominated region. Hence a minimum cut on $H_T > 600\,\text{GeV}$ is required for all signal regions.

Inclusive signal region For general considerations and for having a signal region which is maximally unbiased and minimally dependent on any assumption on the signal hypothesis, an Inclusive SR is designed. This region will not be used in the actual limit setting but will serve as a basis for comparisons and detailed studies.

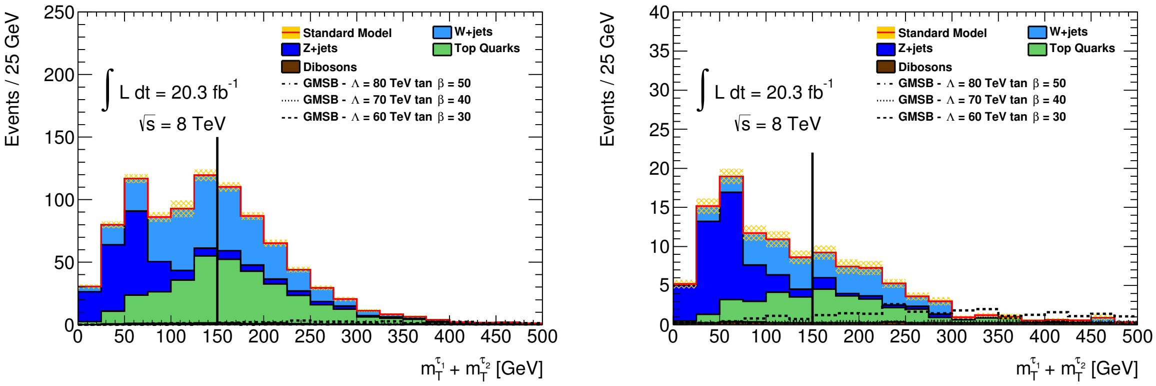

(a) After $\Delta\Phi(\mathrm{jet}_{1/2}, \not{p}_T) > 0.3$ (b) After requiring $H_T > 600\,\mathrm{GeV}$

Figure 5.4: The sum of the m_T of the two leading τ after (a) requiring separation between the leading jets and $\not{E}_T$ and (b) requiring a minimal H_T of 600 GeV. The vertical line indicates the intended cut value. The intended cut clearly suppresses most of the remaining Z+jets backgrounds.

Of all expected backgrounds, the Z+jets background contribution can be addressed most easily. Following the definition in Section 5.2, it is expected that for $Z \to \tau\tau$ background the transverse mass is small since the missing transverse momentum is mainly caused by the neutrinos of the tau decays. For the top and W+jets background a higher m_T can arise from additional neutrinos involved in the decay of a W. Similarly, in SUSY signals the missing transverse momentum is caused by the LSPs causing the transverse mass to adopt high values exceeding those from SM background.

Figure 5.4(a) shows the sum $m_{\mathrm{T}}^{\tau_1} + m_{\mathrm{T}}^{\tau_2}$. Before any cut is applied, there is a clear accumulation of Z+jets events for low regions of the $m_{\mathrm{T}}^{\tau_1} + m_{\mathrm{T}}^{\tau_2}$ distribution. To cross check correlations between this distribution and the minimal signal cut on H_T, the same distribution is shown after a H_T cut of 600 GeV in Figure 5.4(b). Still the Z contribution is peaked for low values. A cut of $m_{\mathrm{T}}^{\tau_1} + m_{\mathrm{T}}^{\tau_2} > 150\,\mathrm{GeV}$ is chosen yielding a good Z+jets suppression while avoiding a high rejection of signal events.

A cut on the transverse mass alone is unfortunately not enough to isolate possible signal signatures. To suppress SM backgrounds further, a tighter cut on H_T is also applied. It is employed as the main selection variable for the Inclusive SR due to its property of being largely unspecific to any SUSY model.

Figure 5.5 shows the obtained H_T distribution after the cut on the transverse masses of the leading taus as well as a significance scan against three GMSB benchmark points as one example. Note that the SR is not intended to target GMSB specifically. However being a general SUSY model with a quite common mass hierarchy, the GMSB points are chosen to stand for generic possible new physics scenarios here. The significance scan (including uncertainties) suggests a cut around 1.2 TeV. For comparison a $S/\sqrt{S+B+\Delta B^2}$ scan is also shown. This scan suggests a slightly softer cut demonstrating the dependence of any optimization procedure on the measure employed for quantification of the significance. Since this region is supposed to be as inclusive as possible, a conservative approach is taken. Selecting

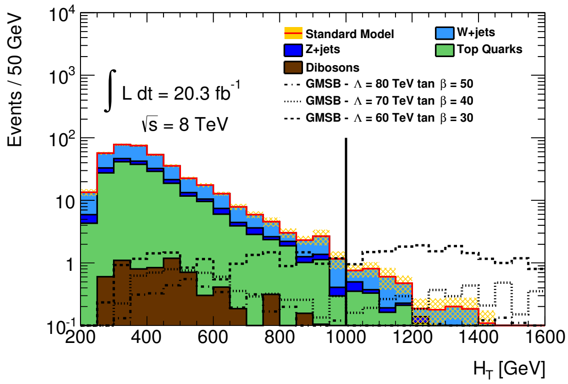

(a) H_T distribution

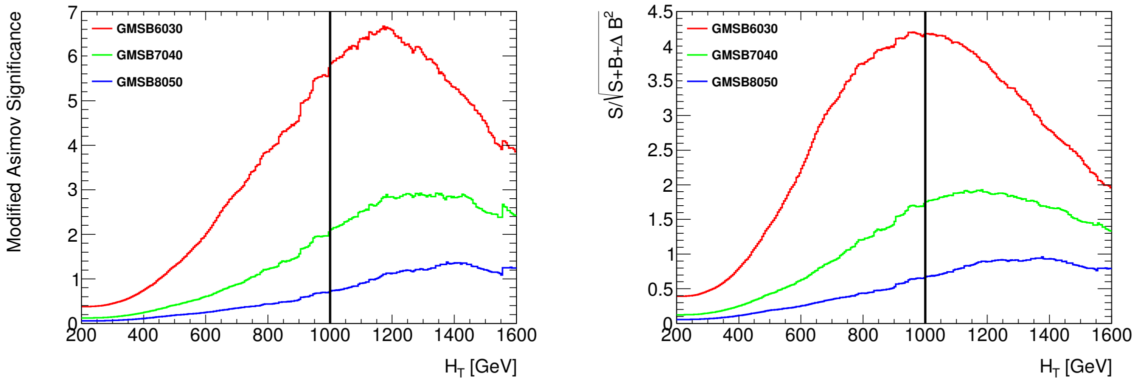

(b) "z_A" Asimov significance scan

(c) "S/B" significance scan

Figure 5.5: H_T after requiring the transverse mass cut (a). Background contributions accumulate at low values while signal predictions extend to higher values. (b) and (c) show scans of the discovery significance for the GMSB benchmark points. For comparison two different significance measures are employed with the Asimov significance being the one generally used for optimization in this analysis. The vertical lines indicate the intended cut value. All backgrounds are scaled with their respective scale factors.

events above 1 TeV yields a good background suppression while retaining sensitivity for many physics scenarios.

The background rejection and signal selection cuts are:

- $m_{\mathrm{T}}^{\tau_1} + m_{\mathrm{T}}^{\tau_2} \geq 150\,\mathrm{GeV}$
- $H_T \geq 1\,000\,\mathrm{GeV}$

Starting from this minimal selection, further optimization towards the different signal scenarios are attempted.

GMSB signal region A set of GMSB points is used as typical benchmark points in the optimization procedure. The parameters defining those points are (a) $\tan\beta = 30$, $\Lambda = 60\,\mathrm{TeV}$, (b) $\tan\beta = 40$, $\Lambda = 70\,\mathrm{TeV}$ and (c) $\tan\beta = 50$, $\Lambda = 80\,\mathrm{TeV}$.

Starting from the Inclusive signal region, it first was verified that indeed the cut of 1 000 GeV in H_T yields also an optimal exclusion performance for GMSB. For this purpose the full exclusion, including all systematic uncertainties, are computed for various H_T cuts. Note that for these and for all following exclusion plots in this section the “pseudo-observed” exclusion line gives the exclusion one would achieve assuming the number of observed events to be the integer closest to the number of expected events. It is shown to assess the influence of small changes in the expected event numbers and of the signal uncertainties. Corresponding exclusion plots are shown in Figure E.2 in Appendix E.1. Indeed relaxing the cut reduces the exclusion power while tightening the cut further increases the uncertainties with no significant exclusion gain.

Starting from the inclusive region, significance scans on various variables were performed. The two most promising ones are displayed in Figure 5.6, the rest can again be found in Appendix E.1.

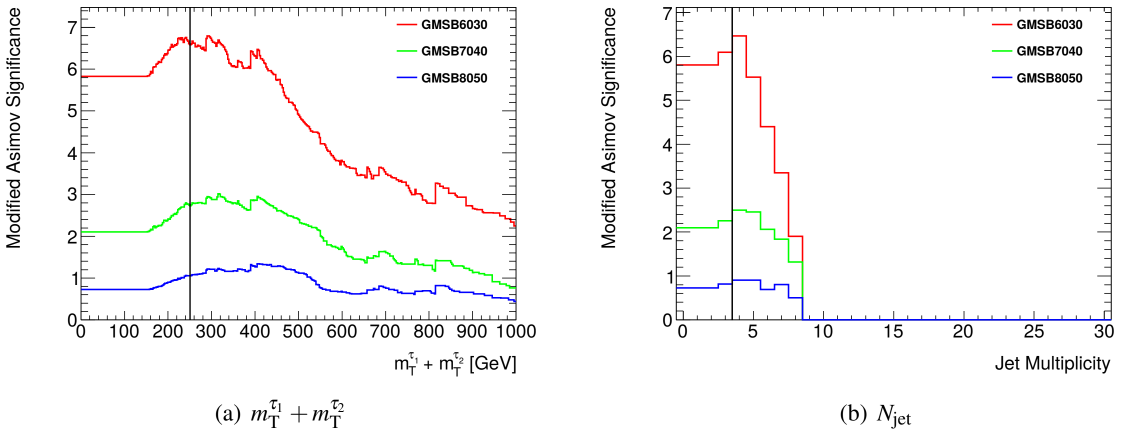

(a) $m_T^{\tau_1} + m_T^{\tau_2}$

(b) N_{jet}

Figure 5.6: Significance scans for the GMSB signal model starting from the Inclusive SR. Displayed are the two variables identified as yielding the largest separation power. The vertical lines indicate the intended cut value. All backgrounds are scaled with their respective scale factors.

To optimize the reach of the analysis for GMSB, an additional cut on N_{jet} and a tightening of the $m_T^{\tau_1} + m_T^{\tau_2}$ cut are studied, both independent on each other and in combination. A significant gain over the Inclusive signal region can only be achieved by raising the $m_T^{\tau_1} + m_T^{\tau_2}$ cut up to 250 GeV while at the same time requiring at least four jets. This set of cuts is referred to as “GMSB signal region”. A comparison of the exclusion reach of the Inclusive and the GMSB SR is displayed in Figure 5.7. A clearly wider reach of the GMSB SR is obvious - albeit at the cost of a larger uncertainty.

The position of the exclusion line is not a very elaborate measure in itself. At the end of the day, the line is a contour line at a value of around 1.6 on a plane of significance values. Differing SR cuts might however influence the overall level of the significance plane without a large effect on the position of the actual exclusion line. Figure 5.8 shows both the significance map of the Inclusive SR and the difference between GMSB SR and Inclusive SR across the grid. Note that the significance increases over a wide range of parameters by a notable margin. This is especially important for the statistical combination with other channels, where a boost of the significance in not excluded regions can contribute significantly to a possible exclusion in the combination. It is also important that although there is a slight degradation observed for lower values of Λ these are not very severe and by far compensated by the gain at higher

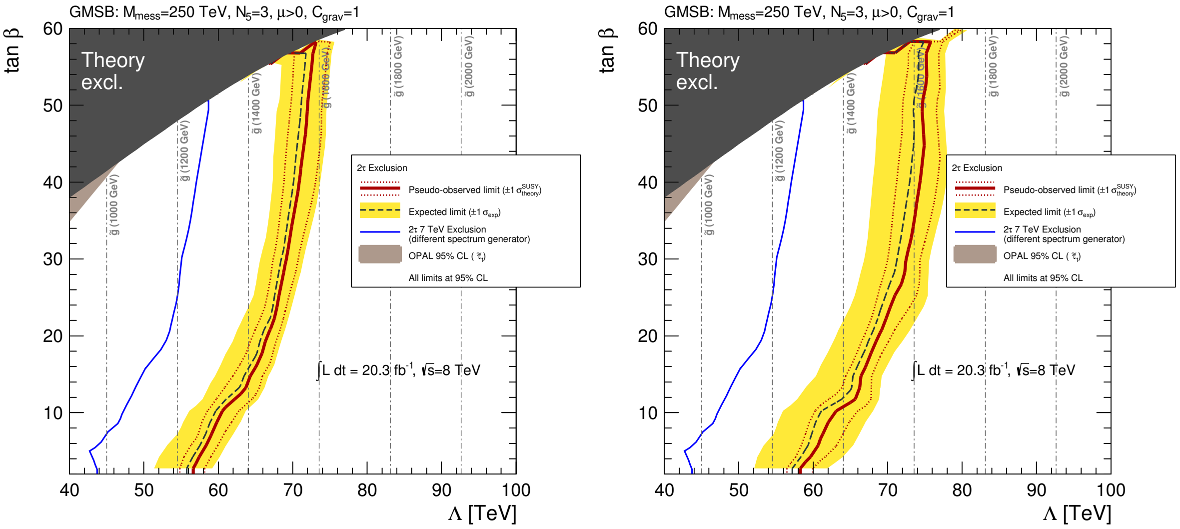

(a) Inclusive SR

(b) GMSB SR

Figure 5.7: Comparison of the exclusion reach of the inclusive and the GMSB SR on the GMSB grid. The "pseudo-observed" line gives the exclusion achieved by assuming the closest integer to the expected number of events as "observed" number of events. The GMSB SR performs better at the cost of a slightly higher uncertainty.

Λ. Significance comparisons for other possible cut combinations can be found in Appendix E.1.

The full list of background rejection and signal selection cuts for the GMSB SR is thus:

- $H_T \geq 1\,000\,\text{GeV}$
- $m_\text{T}^{\tau_1} + m_\text{T}^{\tau_2} \geq 250\,\text{GeV}$
- $N_\text{jet} \geq 4$

Natural gauge mediation signal region To optimize the cuts for the SR targeting the nGM physics model, a slice with a fixed stau mass of 210 GeV and gluino masses varying between 860 GeV and 1 180 GeV was chosen as benchmark. Earlier studies have shown that the significance of a given cut is nearly independent of the stau mass of a given signal point. Hence fixing the stau mass in the optimization will not result in any bias of the resulting cuts.

The H_T distribution is sensitive to the mass difference between the gluino and the other sparticles and is shifted to higher values than the SM background for points with large gluino mass, as displayed in Figure 5.9(a). A significance scan over different H_T (c.f. Figure 5.9(b)) cuts shows that already the minimal cut of 600 GeV is yielding a good significance for the points.

Due to the dominant $\tilde{g} \to \tilde{\chi}_{1,2}^{0,\pm} q\bar{q}$ decay in the first step of the decay chain, one expects four jets from the decay of the produced SUSY particles in the nGM signal grid. This is exploited establishing an additional cut on the jet multiplicity as done for the GMSB SR. The jet multiplicity distribution after the previous cuts is shown in Figure 5.9(c).

A cut on $N_\text{Jet} \geq 4$ increases the significance for high gluino mass points visibly while not affecting the acceptance for low mass points too much (not shown in this scan, c.f. [219]). A tighter cut on the

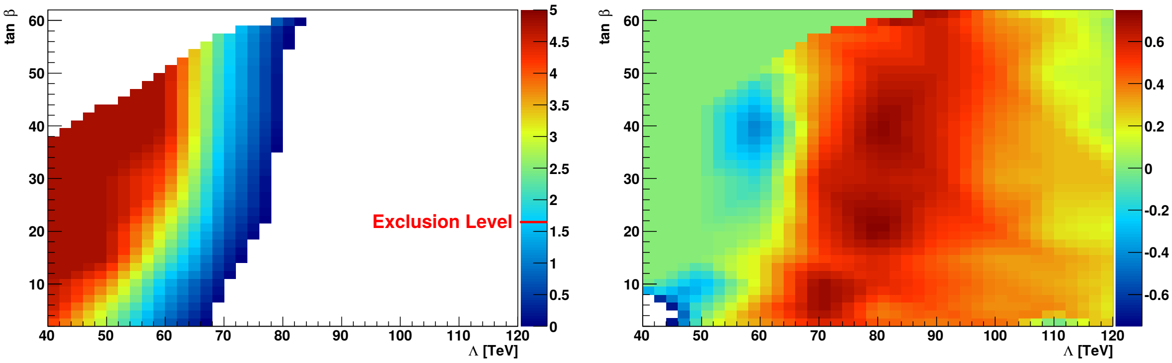

(a) Significance map Inclusive SR

(b) Difference in significance for GMSB SR

Figure 5.8: Significance map for the Inclusive SR (a). The level of the 95% CL exclusion line is indicated on the color axis. (b) shows the difference in significance between the GMSB SR and the Inclusive SR. A higher significance is achieved in the GMSB SR especially for high values of Λ.

jet multiplicity would decrease the significance for all low gluino mass points and would result in a search where the multiplicity of hadronic objects dominates the significance and not the presence of taus. Moreover, different approaches for the background estimation would have to be devised. With the current concept, requiring a large jet multiplicity in the control regions reduces the available statistics too much. While the current extrapolation from two to four jets is well described and justified, an extrapolation over a larger distance is hard to validate. Detailed studies are documented in Section 6.2.2.

$m_{\mathrm{T}}^{\tau_1} + m_{\mathrm{T}}^{\tau_2}$ scales with the stau-gravitino mass difference which exceeds the W-neutrino mass difference for all models considered here. Consequently, the distribution is shifted to higher values for the signal relative to the dominant EW backgrounds(Figure 5.9(e)). A cut value of 250 GeV at the low edge of the optimal region is chosen to keep the maximum possible sensitivity (c.f Figure 5.9(f)).

Ways of increasing the significance by tightening cuts or cutting on other variables are tested and no obvious further potential is identified (c.f. Appendix E.2).

Following this optimization one obtains the following cuts for the nGM signal region:

- $m_{\mathrm{T}}^{\tau_1} + m_{\mathrm{T}}^{\tau_2} \geq 250\,\mathrm{GeV}$
- $H_T \geq 600\,\mathrm{GeV}$
- $N_{\mathrm{Jet}} \geq 4$

Bilinear R-parity violating signal region The bRPV model shows very distinctive phenomenology depending on the region of the grid which makes it difficult to use a significance scanning approach. Instead, exclusion contours are computed on the full grid for various cut combinations. These plots are compiled in Appendix E.3.

First, a cut on H_T is studied (c.f. Figure E.5). With raising the H_T cut, the exclusion is pushed out to larger values of $m_{1/2}$. Selection cuts above 1 000 GeV yield only very little improvement towards higher values of $m_{1/2}$ while limiting the total excluded area.

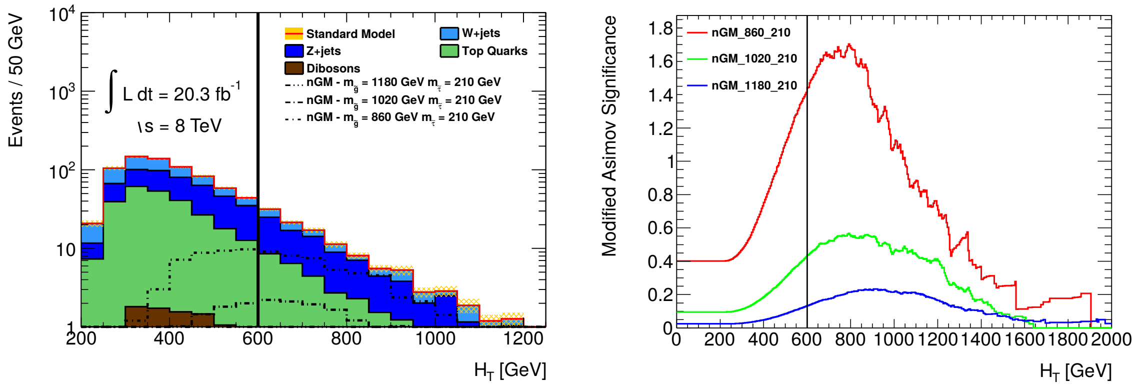

(a) H_T distribution

(b) Significance scan

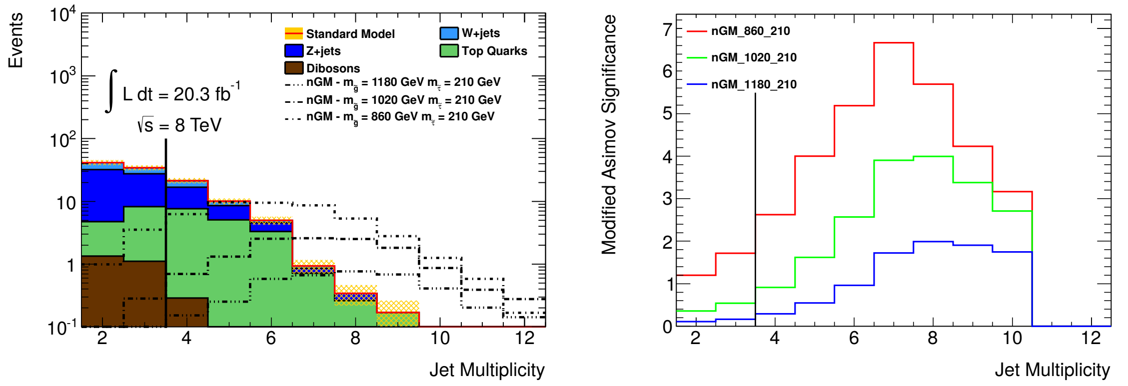

(c) N_{Jet} distribution

(d) Significance scan

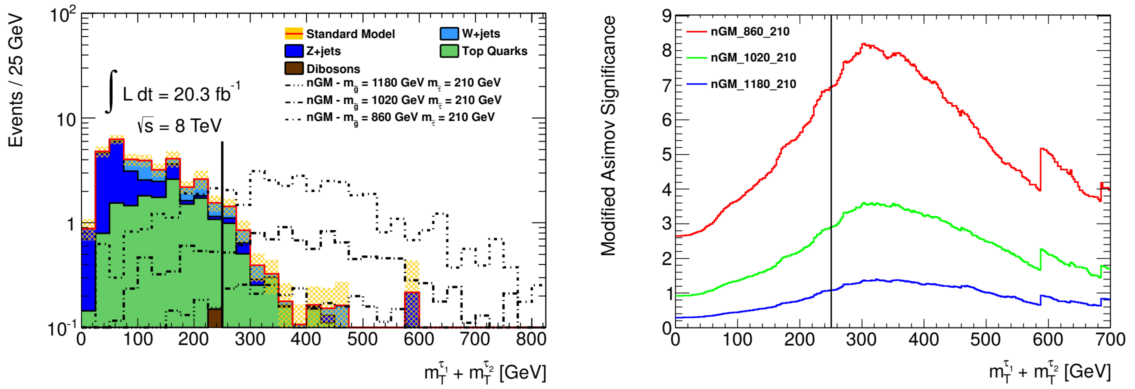

(e) $m_{\mathrm{T}}^{\tau_1} + m_{\mathrm{T}}^{\tau_2}$ distribution

(f) Significance scan

Figure 5.9: Kinematic dsitributions and significance scans for the nGM SR after consecutively applying all cuts. (a) and (b) show the H_T distribution and significance scan of the discovery significance for the various nGM signal points after the common selection. (c) and (d) show the same for N_{jet} after the $H_T > 600\,\text{GeV}$ cut and (e) and (f) for $m_{\mathrm{T}}^{\tau_1} + m_{\mathrm{T}}^{\tau_2}$ after requiring $N_{\text{jet}} \geq 4$. The vertical lines indicate the intended cut value. All backgrounds are scaled with their respective scale factors.

Subsequently, various cuts on $m_\mathrm{T}^{\tau_1} + m_\mathrm{T}^{\tau_2}$ are tested for $H_T > 1\,000\,\mathrm{GeV}$ both with (Figure E.8) and without (Figure E.6) a cut on $N_\mathrm{jet} \geq 4$ and for $H_T > 600\,\mathrm{GeV}$ with additionally requiring $N_\mathrm{jet} \geq 4$ (Figure E.7).

Two cut sets are identified yielding optimal performance for different regions of the bRPV grid, hence two tentative signal regions are established:

- bRPV $m_{1/2}$
  - $m_\mathrm{T}^{\tau_1} + m_\mathrm{T}^{\tau_2} \geq 150\,\mathrm{GeV}$
  - $H_T \geq 1\,000\,\mathrm{GeV}$
  - $N_\mathrm{Jet} \geq 4$
- bRPV m_0
  - $m_\mathrm{T}^{\tau_1} + m_\mathrm{T}^{\tau_2} \geq 200\,\mathrm{GeV}$
  - $H_T \geq 600\,\mathrm{GeV}$
  - $N_\mathrm{Jet} \geq 4$

The two exclusions are displayed in Figure 5.10. The individual strengths of the two regions can clearly be seen.

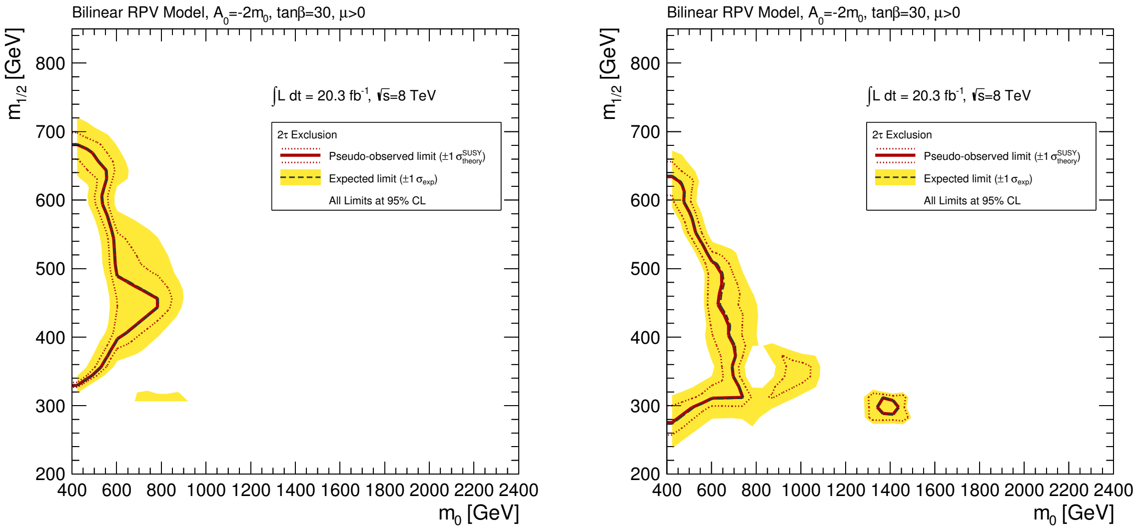

(a) bRPV $m_{1/2}$ Exclusion

(b) bRPV m_0 Exclusion

Figure 5.10: bRPV exclusion plots for the two bRPV signal regions. Systematic uncertainties are re-computed for the chosen cut value for each plot. The “pseudo-observed” line gives the exclusion achieved by assuming the closest integer to the expected number of events as “observed” number of events. While the $m_{1/2}$ signal region performs better along the $m_{1/2}$ axis for low m_0, the m_0 SR has generally the wider reach along the m_0 axis.

The two signal regions can be combined using for each grid point the SR with the best expected significance. For the final statistical combination with the other final states only the bRPV $m_{1/2}$ signal region is considered since the m_0 signal region is largely covered by the exclusions derived from the search for a light lepton and a tau in the final state.

5.5 Summary

After optimizing for different models, five similar but distinct signal regions have been defined. All signal regions feature the same selection steps up to and including the multijets rejection cut. One region is designed to be inclusive in a sense that its cuts do not rely on details of the assumed model. Depending on the targeted signal model, the other regions comprise varying cuts on $m_{\mathrm{T}}^{\tau_1} + m_{\mathrm{T}}^{\tau_2}$ and H_T. All signal specific SRs contain a cut on N_{jet} which in intentionally omitted for the Inclusive SR. All cuts are summarized in Table 5.1. For each of the SRs, an individual background estimate is performed and systematic uncertainties are calculated, as presented in the following chapters.

	Inclusive SR	bRPV $m_{1/2}$ SR	GMSB SR	nGM SR	bRPV m_0 SR
Trigger	$p_T^{\text{jet}_1} > 130\,\text{GeV}$, $p_T^{\text{jet}_2} > 30\,\text{GeV}$ $\not{E}_T > 150\,\text{GeV}$				
Tau leptons	$N_\tau^{\text{loose}} \geq 2$ $p_T > 20\,\text{GeV}$				
Light leptons	$N_\ell^{\text{baseline}} = 0$				
Multijets rejection	$\Delta\Phi(\text{jet}_{1/2}, \not{p}_T) \geq 0.3$				
Signal selection	$H_T > 1\,000\,\text{GeV}$			$H_T > 600\,\text{GeV}$	
	$m_{\mathrm{T}}^{\tau_1} + m_{\mathrm{T}}^{\tau_2} > 150\,\text{GeV}$		$m_{\mathrm{T}}^{\tau_1} + m_{\mathrm{T}}^{\tau_2} > 250\,\text{GeV}$		$m_{\mathrm{T}}^{\tau_1} + m_{\mathrm{T}}^{\tau_2} > 200\,\text{GeV}$
	–	$N_{\text{jet}} \geq 4$			

Table 5.1: Overview of the cuts defining the different signal regions used in the analysis.

6

Background estimates

As already stressed several times, a precise knowledge of the expected backgrounds is crucial for any attempt to discover new physics. Despite the best effort of both theorists and experimentalists to come up with reliable predictions by simulation, the complex signatures employed in SUSY searches require background estimates that are derived from or constrained by actual measurements.

For this search, the number of real taus offers a natural choice for a classification of background. Events that have no true tau lepton are dominated by multijets production. This process is a relevant background for all searches at the LHC, simply due to its large production cross section. For this analysis, not only both of the taus but also the missing transverse momentum have to result from a mis-measurement. This class of background is particularly challenging due to the difficult simulation of fake taus. Moreover, as a consequence of the large production cross section, Monte Carlo production with sufficiently high statistics in the kinematic tails is virtually impossible. It is hence estimated purely from data, the procedure is described in Section 6.1.

In the case where at least one tau lepton is real, the decay of an electroweak gauge boson into a tau has to be involved. Those can either result from direct *W*+jets or *Z*+jets production, or come from a decay of a top quark. These "electroweak" (EW) backgrounds are estimated from simulation, but their normalization is constrained by measurements in dedicated control regions. This procedure is described in detail in Section 6.2[1].

The background estimates are validated in dedicated validation regions (VR). For the multijets estimate, the description is included in Section 6.1, the validation of the electroweak background estimates is described in Section 6.3.

The various regimes for multijets dominated, electroweak control and electroweak validation kinematics are separated by cuts on the same variables used to define the signal regions. Figure 6.1 displays an overview of all cuts used for this purpose.

---

[1] Of course, production of electroweak gauge bosons can also result in all-hadronic final states. For the purpose of this analysis, this background class is indistinguishable from pure QCD multijets production, since it does also not contain any real missing transverse momentum.

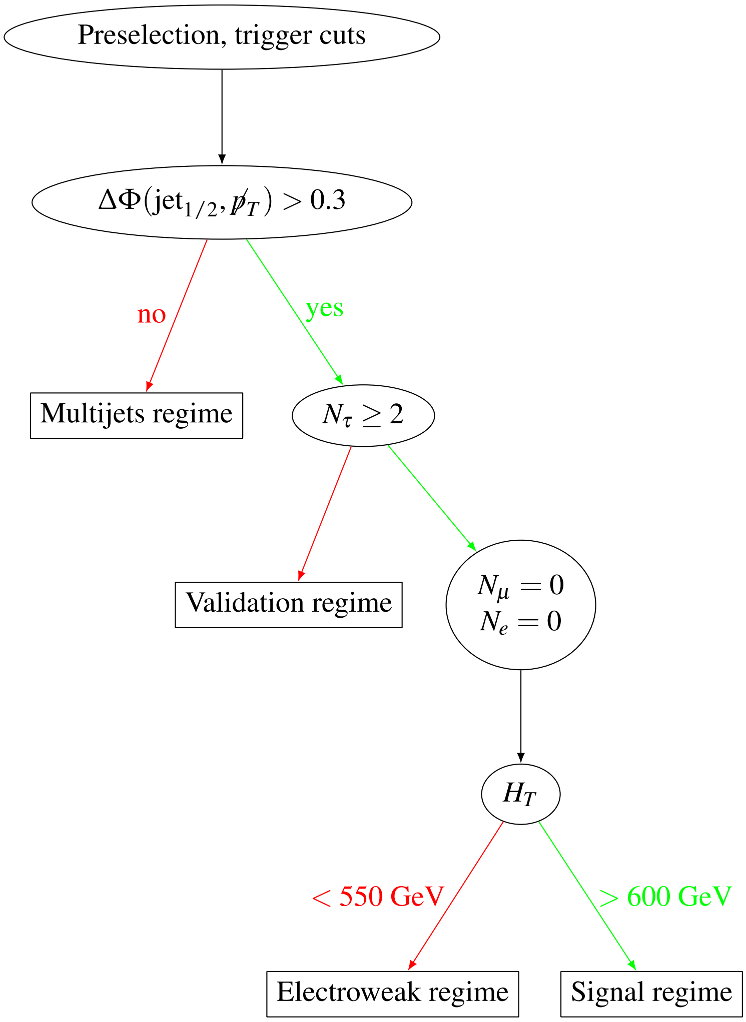

Figure 6.1: Cut flow tree showing the definition of the various background regimes (and the signal regime as detailedly outlined in Section 5). The multijets regime is used to estimate and validate background contributions with two fake taus as described in Section 6.1. The contributions from decays of electroweak gauge bosons is estimated in the electroweak regime (c.f. Section 6.2) and validated in the validation regime (c.f. Section 6.3).

6.1 Backgrounds with mis-identified tau leptons

While the problem of the fake taus is unique to this analysis, fake $\not{E}_T$ in multijets events is common to many SUSY searches. The so called “Jet Smearing” [220] technique has been developed in the context of the search for SUSY in events with $\not{E}_T$, multiple jets and no light leptons [215].

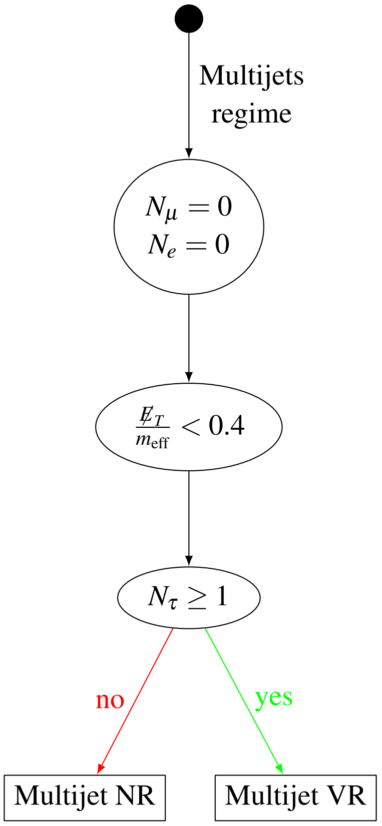

Figure 6.2: Cut flow tree showing the definitions of the multijets validation and normalization regions. The normalization is described in Section 6.1.3 while the validation is outlined in Section 6.1.4. For the definition of the “multijets regime” c.f. Figure 6.1.

This method is based on the idea that the dominant source of $\not{E}_T$ in multijets events is a mis-measurement of one or multiple jets. Following this reasoning, one can artificially produce events with fake $\not{E}_T$ by starting from well measured multijets events (c.f. Section 6.1.1) and smearing the measured jets within their physical response uncertainty (c.f. Section 6.1.2).

Applying this technique results in a large set of multijets pseudo-data. The events of this set have artificially increased $\not{E}_T$ to ensure they are above the trigger threshold. Due to the technical details of the smearing, it is not possible to preserve a correct normalization for this pseudo-data template. It has hence to be normalized in a dedicated normalization region (NR) (c.f. Section 6.1.3). On the other hand, these events have the “true” fake tau content as seen in data, assuming that the presence of a fake tau lepton in a given event is uncorrelated with the probability to get large fake $\not{E}_T$. This implies that one can expect fake efficiencies and all the subtleties that influence the fake description to be “right” by construction. A correction of a mis-modeling of fake probabilities or kinematic properties that might influence this, should not be necessary anymore. This aspect is validated in a dedicated validation region (c.f. Section 6.1.4). Figure 6.2 gives an overview of the selection of those two regions.

The resulting normalized and validated pseudo-data can then be used to obtain a prediction for the multijets background in the different signal regions (c.f. Section 6.1.5).

6.1.1 Seed selection

As a starting point for the Jet Smearing, multijets events are selected from the single-jet triggers with nominal thresholds between 55 GeV and 460 GeV[2]. Most of these triggers have been heavily prescaled throughout the 2012 data taking, meaning that only a fixed fraction of all triggered events is recorded to disk. Prescaling allows to use triggers that otherwise would result in a prohibitively large event rate. Usually, lower thresholds imply a larger prescaling factor. This is accounted for by applying an event weight according to the highest trigger one specific event has fired, and the prescaling in use for the respective run. The normal event cleaning procedure and a light-lepton veto are applied to those events.

For the smearing to work, those “seed” events are required to be well measured, i.e. not having a significant amount of missing transverse energy. Studies have shown [220] that imposing a cut directly on $\not{E}_T$ results in a bias in the jet p_T. Instead a cut on the $\not{E}_T$ significance

$$S = \frac{\not{E}_T}{\sqrt{\sum E_T}} < 0.6\,\mathrm{GeV}^{\frac{1}{2}}$$

is applied. While it has been studied in detail that this cut ensures a clear multijets domination when vetoing light leptons at the same time, this is not a priori clear for tau enriched events. To verify this, a validation is established by requiring all steps of the seed selection plus additionally one or two tau leptons. In simulation, no trigger requirement is imposed. All events having at least one jet of $p_T > 90\,\mathrm{GeV}$, the plateau threshold of the lowest single jet trigger employed in the jet selection, were considered instead.

Figure 6.3 shows both the pure $\not{E}_T$ and the $\not{E}_T$ significance S in the one tau and two tau seed selection. The large spread of the data is owed to the fact that triggers with very high prescales are employed, resulting in high weights of single data events[3].

For the high $\not{E}_T$ tails of the one tau selection, the normalization of the electroweak MC is correct within the large statistical spread of the data. One can also clearly see the strong dominance of multijets over electroweak contributions for small $\not{E}_T$ and $\not{E}_T$ significance values.

The same holds in the two tau selection, where for small $\not{E}_T$ significance values the multijets contribution is two orders of magnitude larger than the EW backgrounds. A clear statement about the normalization in the tails is not possible anymore due to the large fluctuations of data events. Since the second tau in the EW contributions is a fake tau, and those are shown to be overestimated in MC (c.f. Section 6.2), any possible normalization error would reduce the number of non-QCD events in the low $\not{E}_T$ significance region.

Concluding one can safely say that the selected seed events are clearly multijets-dominated with approximately 3% admixture of electroweak events when requiring two taus. Given the large uncertainties and the low impact on the signal region estimates of multijets production in general, this possible admixture will be neglected.

---

[2] The names of the trigger items used for the selection of the smearing seeds are EF_J460_A4TCHAD, EF_J360_A4TCHAD, EF_J280_A4TCHAD, EF_J220_A4TCHAD, EF_J180_A4TCHAD, EF_J110_A4TCHAD, EF_J80_A4TCHAD and EF_J55_A4TCHAD.

[3] The large event weights of the data in the seed selection is not accounted for in the error bars of the data points due to technical reasons. Errors on data are computed as 68% Poisson confidence intervals on the actual value, not taking into account weights, since for the main analysis all data events are unweighted.

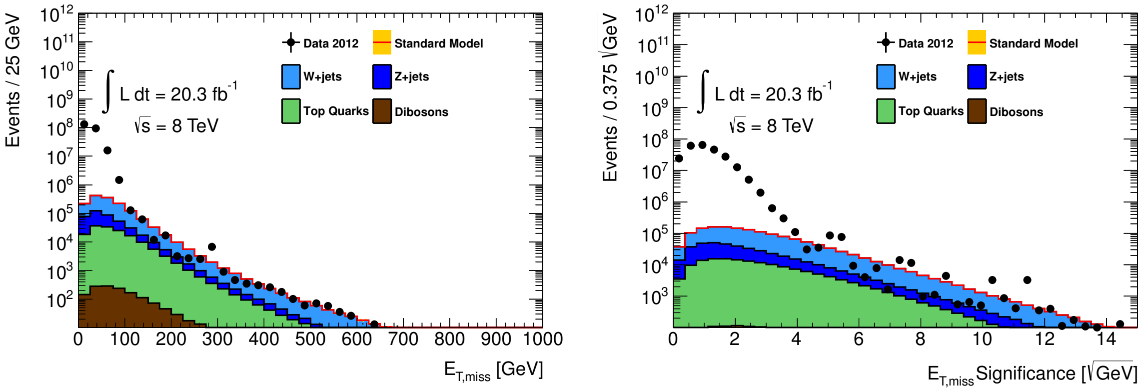

(a) 1τ $\not{E}_T$

(b) 1τ $\not{E}_T$ significance

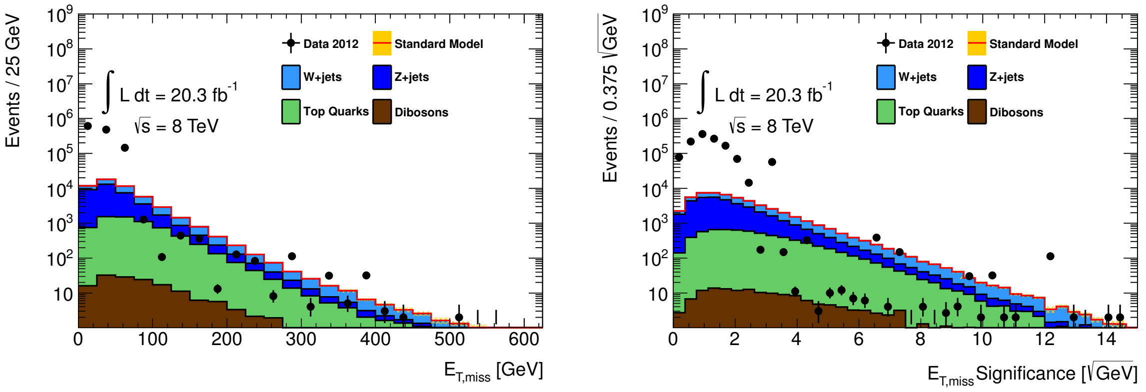

(c) 2τ $\not{E}_T$

(d) 2τ $\not{E}_T$ significance

Figure 6.3: $\not{E}_T$ and $\not{E}_T$ significance for the seed event selection for the Jet Smearing. The top row shows distributions requiring one tau lepton, the bottom row requiring two tau leptons. All plots are before the $\not{E}_T$ significance cut. A dominance of multijets events (i.e. difference between data and MC) is visible for low $\not{E}_T$ and $\not{E}_T$ significance, respectively. Data points include partially high prescaling factors that are for technical reasons **not** included in the uncertainties. The normalization of MC is taken from the nominal control regions which does not necessarily have to be identical to the normalization in the seed selection.

6.1.2 Smearing

The selected seed events are smeared according to the observed jet energy resolution. To do this, the response function of the energy measurement of jets has to be measured and parametrized. This is initially done in Monte Carlo simulation by comparing the generated and the reconstructed energy of a jet. The response functions derived this way are validated and constrained in dedicated jet response measurements in data. Details to the techniques, the measurements and the parametrization can be found in [220]. Figure 6.4 shows some examples of measured jet response shapes derived for this technique. The response can be divided into a gaussian core and a tail towards low energies.

These response shapes are used to randomly vary the energy of the jets in the selected seeds. Additionally to the techniques explained in [220], also a smearing of the jet's ϕ direction is performed, which results in an improved description of the separation between the leading jets and the (fake) $\not{E}_T$ direction.

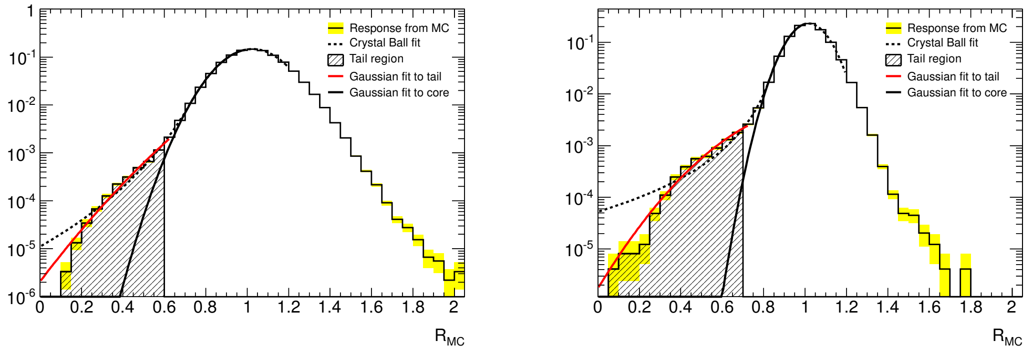

(a) 40 GeV < p_{T}(true) < 60 GeV (b) 140 GeV < p_{T}(true) < 160 GeV

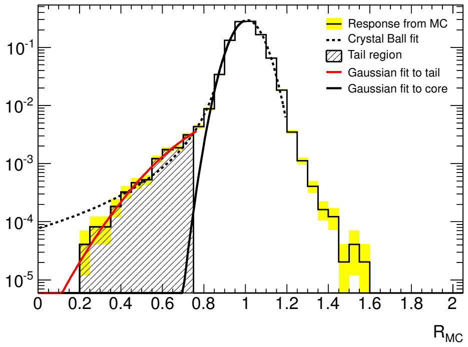

(c) 540 GeV < p_{T}(true) < 560 GeV

Figure 6.4: Example response shapes for different jet-p_T evaluated from multijets simulation. R_{MC} denotes the ratio of the reconstructed over the generated transverse momentum $R_{\mathrm{MC}} = \frac{p_T^{\mathrm{reco}}}{p_T^{\mathrm{true}}}$. The response shapes are used as an input for the Jet Smearing by randomly varying the energy of jets in the well measured seed events to create artificial $\not{E}_T$. (from [220])

Each seed event is smeared 1000 times to obtain a probability for the kinematic configuration of each event to fake a large $\not{E}_T$ signature. Since here the tau content, which is not modified by the smearing, is of paramount importance, it is not possible to keep all smeared pseudo-data events as is done in other analyses. Taking every iteration would result in a collection of events that each share the identical tau content but differ slightly in their jet content. As a result, bin-to-bin and event-to-event correlations would be introduced, depending on the quality of the seed event and the nature of the quantity considered. On the other hand, taking only one smear event from each seed event is not justified, either. Seed events might have a very different probability to result in smeared events exceeding the trigger thresholds of the analysis trigger, depending on their topology. This information is, of course, important and would be lost when accepting each seed event in only one smeared version.

As a compromise, for each seed event the particle content of the first smearing iteration that satisfies all trigger cuts is kept. Additionally, a survival probability is defined by counting how often in 1000 attempts to smear the event the resulting $\not{E}_T$ and $p_T^{\mathrm{jet}_1}$ are above the trigger thresholds. This survival probability is attributed to the event as an additional weight. Due to the weighting and the chance of discarding events entirely, the normalization of the resulting pseudo-data sample is completely arbitrary and has to be constrained externally.

6.1.3 Normalization

A normalization region is defined by inverting the cuts designed to suppress the multijets background, i.e. the $\Delta\phi$ cut between $\not{E}_T$ and the two leading p_T jets in the event. In order to further enrich the multijets contribution, an additional cut on the variable $\not{E}_T/m_{\text{eff}}$ is introduced. Events containing a reconstructed tau are vetoed to keep the normalization free of any tau related bias. The full list of requirements used to define this normalization region is:

- Cleaning cuts
- Trigger plateau cuts
- Veto events containing an electron or muon
- $\Delta\Phi(\text{jet}_1, \not{p}_T) < 0.3$ or $\Delta\Phi(\text{jet}_2, \not{p}_T) < 0.3$
- $\not{E}_T/m_{\text{eff}} < 0.4$
- $N_\tau = 0$

Figure 6.5 shows distributions of all background contributions before introducing the multijets normalization selection. The difference between data and the simulated backgrounds is due to the missing multijets contribution. The enrichment of the desired contributions by the listed cuts can be seen in the lower values for all distributions.

In the NR, a multijets normalization scale factor $\omega_{\text{multijets}}$ is determined as:

$$\omega_{\text{multijets}} = \frac{N^{data}_{\text{multijets}} - N^{nonQCD}_{\text{multijets}}}{N^{QCD}_{\text{multijets}}} \tag{6.1}$$

where $N^{data}_{\text{multijets}}$ denotes the number of data events and the other two terms denote the number of other background events from simulation and smeared pseudo-data events in the normalization region. All other MC contributions are used without applying any additional scaling. Alternatively applying the correction factors obtained in the kinematic validation region for electroweak backgrounds does not affect the obtained normalization for the multijets template (c.f. Table 6.1. A value of $\omega_{\text{multijets}} = (1.056 \pm 0.005) \times 10^{-3}$ is obtained. Distributions for several kinematic variables including the normalized smeared multijets events are shown in Figure 6.6.

In general, these distributions show a very nice agreement between data on the one hand and data-driven multijets estimate and electroweak MC simulation on the other hand. Some deviations in the shapes beyond the statistical uncertainties are visible, however. For the sub-leading jet p_T and H_T, the estimate exhibits some structure which is not visible in data. Also the missing transverse energy is slightly harder in data than in the smeared distribution.

The only larger difference is visible in the ϕ separation between the two leading jets and the missing transverse momentum. For small separations between jet and $\not{p}_T$, an excess of estimate over data for the leading jet and a slight deficit for the sub-leading jet is visible. This implies that the fraction of events where the $\not{E}_T$ arises dominantly from a mis-measurement of the leading jet is larger in the estimate than in data. This difference is not a problem for the estimation method itself, since these “extreme” topologies are rejected in the signal selection anyway. For intermediate separation regions, the agreement

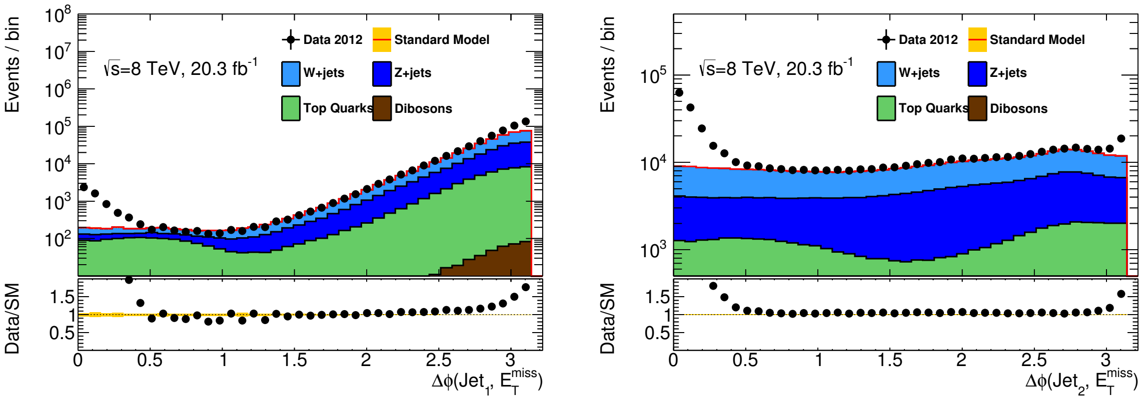

(a) $\Delta\Phi(\mathrm{jet}_1, \not{p}_T)$ (b) $\Delta\Phi(\mathrm{jet}_2, \not{p}_T)$

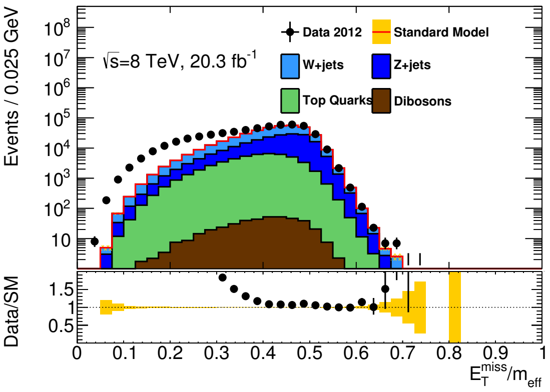

(c) $\not{E}_T / m_{\mathrm{eff}}$

Figure 6.5: Kinematic variables used to define the multijets normalization region. All displayed backgrounds are normalized to luminosity. The difference between background prediction and data can be attributed to the missing multijets background.

between estimate and data is rather good. Most importantly, this difference does not translate into any obvious problem in the kinematic variables.

To assess the significance of these deviations, the tail systematic uncertainties is applied, as described in Section 7.5. The resulting distributions are displayed in Figure 6.7. The electroweak MC prediction is also added to allow for an easy estimate where the multijets contribution to the total data is significant.

The uncertainties on the estimate are very large and cover all remaining differences between actual data and multijets pseudo-data, except for small angles in the separation between jets and $\not{E}_T$. Even here, the uncertainty nearly covers the difference between data and estimate. For intermediate separations, which are relevant for the signal selection, any difference is clearly covered.

Moreover, these plots show that the uncertainties are very conservative spanning a band which largely exceeds remaining differences in all other distributions. The size of the uncertainties does not have a large effect though, since only a very minor multijets contribution is expected in the signal regions. Only the very good description of the data in the control region and the coverage of any remaining difference within the systematic uncertainties is of importance.

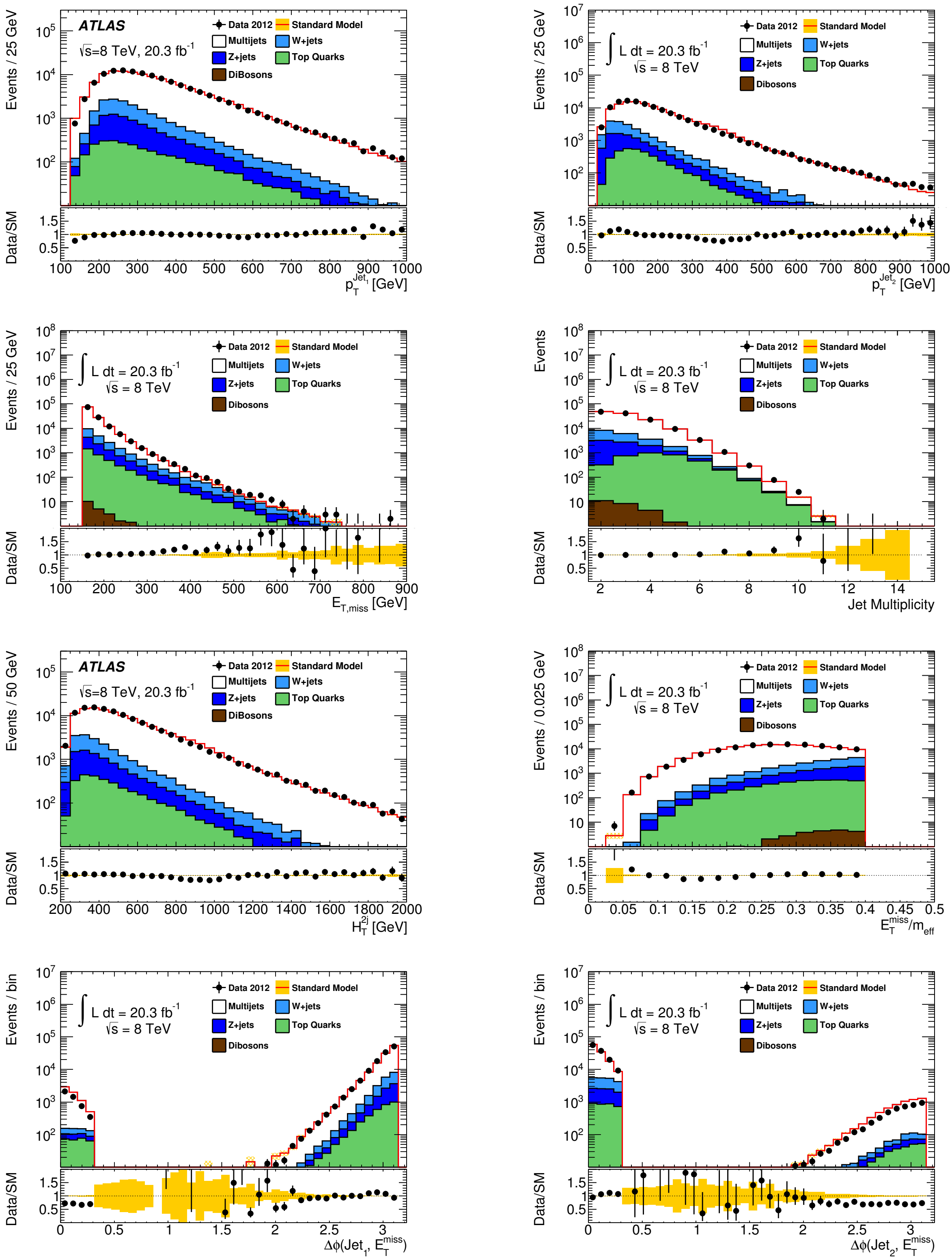

Figure 6.6: Kinematic variables in the multijets normalization region. The multijets background is taken from smeared and normalized pseudo-data. All other backgrounds are taken from simulation without any additional normalization scaling.

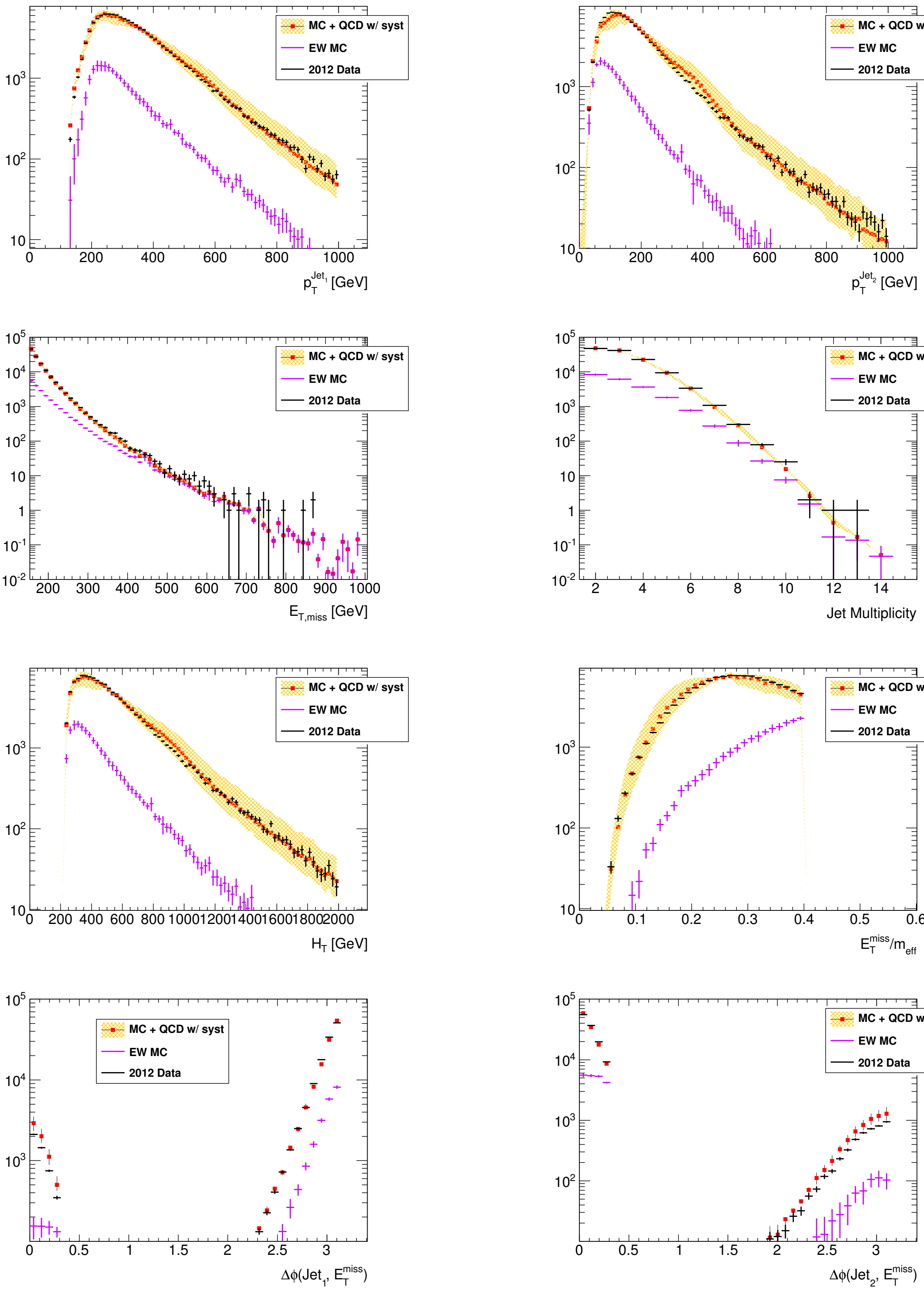

Figure 6.7: Kinematic variables in the multijets normalization region. The red markers give the multijets background taken from smeared and normalized pseudo-data plus all other backgrounds taken from simulation without any additional normalization correction applied. The shaded band gives the approximate effect of the systematic uncertainties on the Jet Smearing technique. The black markers display the data distributions. For comparison of the relative abundances, the electroweak simulation is also shown separately.

6.1.4 Validation

The observed agreement between smeared pseudo-data and actual measurement in the normalization region does not allow for a statement about the quality of the fake tau description by the obtained multijets template. To assess the performance in this critical field, a validation region is derived from the normalization region by requiring the presence of one reconstructed tau instead of vetoing any tau. For multijets, the normalization derived in the NR is applied while the EW simulation is scaled with the scale factors derived in the true-tau electroweak validation regions (c.f. Section 6.3.1). Note that the normalization of the multijets template is completely tau-blind, i.e. completely relies on the fact that the tau fakes are taken from actual data and thus should be "right" a priori.

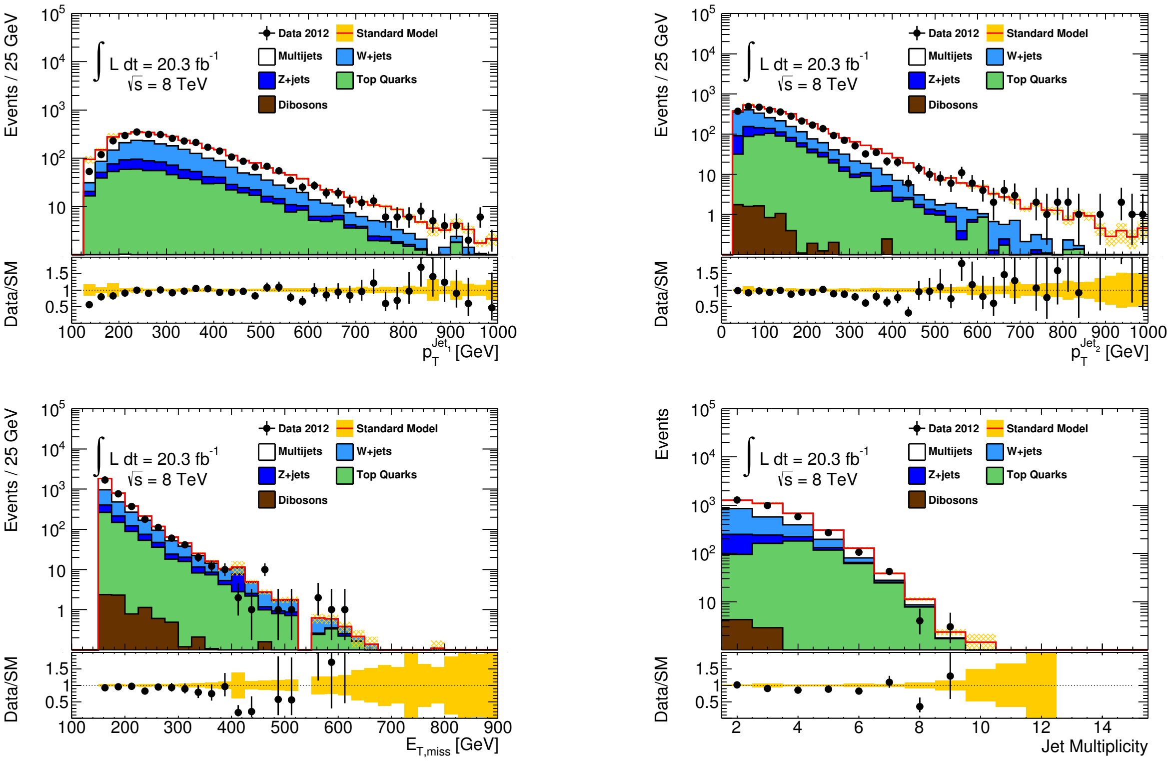

Figure 6.8: Kinematic variables in the validation region. The multijets background is taken from smeared pseudo-data normalized in the NR. All other backgrounds are taken from simulation with normalization scaling derived in the electroweak true-tau validation region.

Figures 6.8 and 6.9 show general and tau-specific kinematic distributions. The agreement is excellent with all deviations being covered by the statistical uncertainties on the background predictions alone. For very large and low p_T of the reconstructed tau, the multijets contribution to the total background estimate is significant. In both parts, data and the data-driven multijets estimate agree excellently. The distribution of the transverse mass of the tau displays an equally good agreement. This is particularly remarkable since both the fake tau and the fake $\not{E}_T$ enter this quantity. Note that even the feature in the multijets contribution around 120 GeV in $m_T^{\tau_1}$ is extremely well described.

To validate the normalization of the multijets template independently of the kinematic distributions shown above, a normalization factor has been computed analogously to the computation in the NR. Note

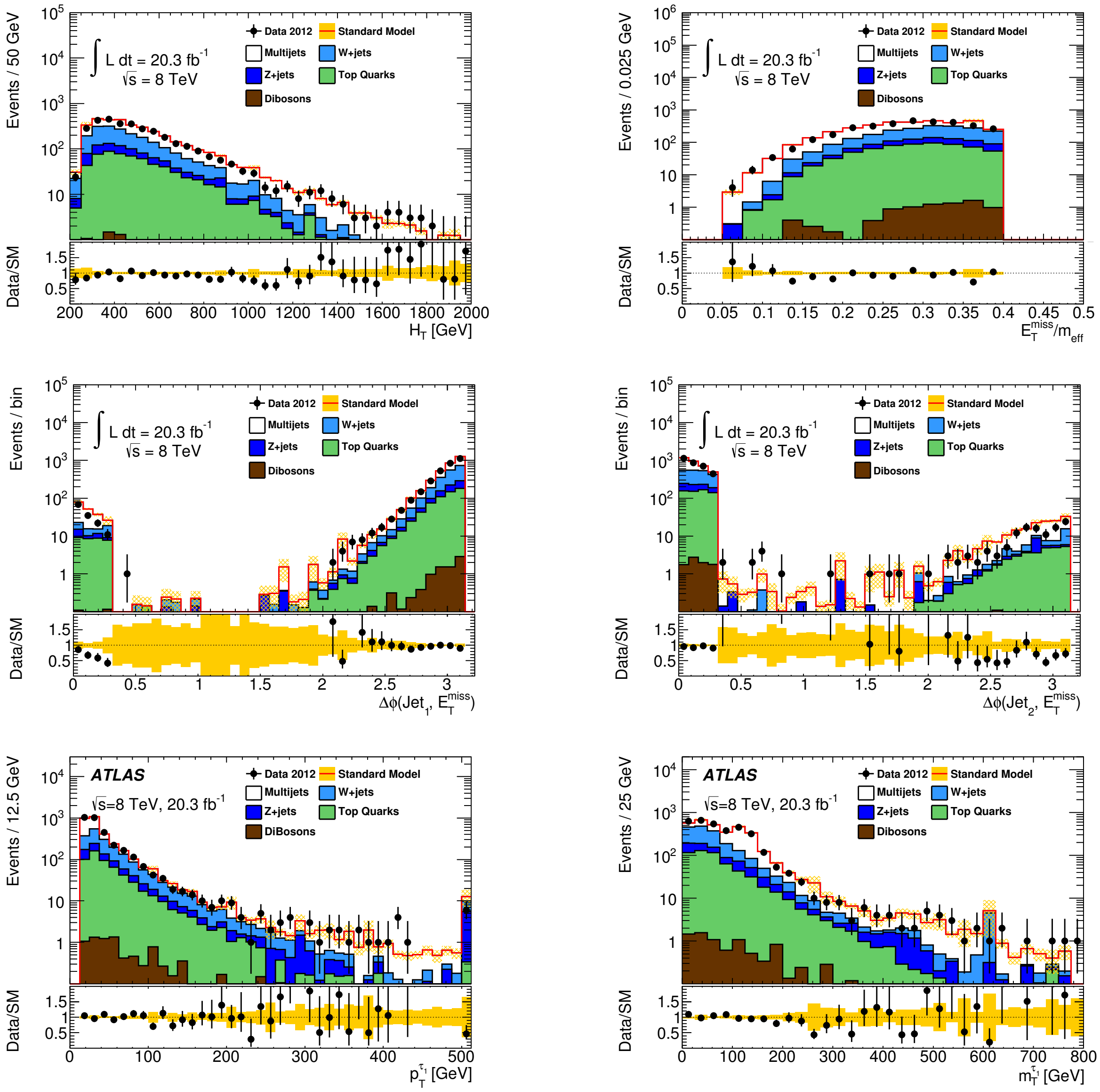

Figure 6.9: Kinematic variables in the validation region. The multijets background is taken from smeared pseudo-data normalized in the NR. All other backgrounds are taken from simulation with normalization scaling derived in the electroweak true-tau validation region.

that this factor serves only as a cross check and is not used anywhere in the analysis.

In contrast to the normalization region, the fraction of events from electroweak processes is much higher in the validation region. A significant influence of the chosen EW scaling factors on the multijets normalization cannot be excluded a priori. To asses the influence, the multijets normalization in the validation region has been computed with two different sets of scale factors for the EW backgrounds. The corrections obtained from the kinematic and the true-tau validation regions, respectively, as defined in Section 6.3 have been chosen. The different resulting normalizations for the multijets template are collected in Table 6.1.

Multijets region	EW MC scaling applied	Resulting multijets normalization
NR	Unscaled	$(1.056 \pm 0.005) \times 10^{-3}$
NR	Kinematic	$(1.065 \pm 0.006) \times 10^{-3}$
VR	Kinematic	$(0.978 \pm 0.070) \times 10^{-3}$
VR	True-tau	$(1.068 \pm 0.073) \times 10^{-3}$

Table 6.1: Multijets normalizations derived in both NR and VR and with different scalings applied to the EW MC. The normalizations of the electroweak backgrounds is derived in the electroweak validation regions. All derived multijets normalizations agree within their statistical uncertainties regardless of the treatment of the electroweak background.

All factors agree within their statistical uncertainties. Concluding, not only the assumption of the "right" fake modeling in the derived multijets background template holds to a very large extent, but also the choice of the EW MC scaling is of negligible influence for the normalization of the multijets template.

6.1.5 Results

The multijets background template, obtained by Jet Smearing, normalized in the NR and validated in VR can now be used to obtain a background estimate for the signal regions. To do this, all signal region cuts are applied to this sample. The resulting number directly gives the expected background contributions of multijets events in the respective signal regions.

Table 6.2 lists these estimates together with the electroweak estimates obtained from the procedure described in Section 6.2 for comparison. Both numbers comprise all uncertainties, both statistical and systematic. In all signal regions, the multijets contribution is less than 10% of the EW contribution. The statistical uncertainties on the data-driven estimate vary between 36% and 84% with the systematic uncertainties being generally similar but slightly smaller.

Signal region	Expected events	
	Total background estimates	Multijets estimate
Inclusive	$2.90 \pm 0.40 \pm 0.70$	$0.12 \pm 0.05 \pm 0.06$
GMSB	$0.28 \pm 0.10 \pm 0.22$	$0.06 \pm 0.05 \pm 0.02$
nGM	$3.10 \pm 0.50 \pm 0.90$	$0.07 \pm 0.05 \pm 0.03$
bRPV $m_{1/2}$	$1.09 \pm 0.19 \pm 0.39$	$0.11 \pm 0.05 \pm 0.04$
bRPV m_0	$6.22 \pm 0.91 \pm 1.38$	$0.14 \pm 0.06 \pm 0.20$

Table 6.2: Number of events predicted by the multijets and total background estimates for the different signal regions. For both, the second number gives the statistical, the third the systematic uncertainties uncertainty. Systematic uncertainties comprise all detector and theoretical uncertainties.

6.2 Backgrounds with real tau leptons

Backgrounds with real tau leptons are dominated by events where an electroweak gauge boson decays into a tau. This can happen in direct production of the bosons or in the decay chain of a top quark. Electroweak contributions (including top quark production) can be simulated with high precision and large statistics. Remaining discrepancies between data and MC need to be studied in dedicated control regions (CR). These discrepancies might arise from the particular kinematics studied in this analysis (which is rather untypical for electroweak production due to the hard requirements on $\not{E}_T$ and $p_T^{\mathrm{jet}_1}$) or the mis-modeling of either true or fake taus. Scale factors, obtained from comparing data with simulation in these CRs, are used to correct these background contributions in both the control and signal regions. Ideally, one would construct independent CRs with only one isolated background contribution in each of them. Since this is generally not feasible, other methods have to be employed to treat correlations between the various background sources and control regions correctly. In this analysis, the matrix inversion method is used for this task.

In the following, first the method used to obtain scale factors and their uncertainties in multiple CRs for multiple background sources is presented (Section 6.2.1). Then the choice of the CRs is motivated and validated (Section 6.2.2). The resulting scale factors are presented and discussed (Section 6.2.3), and finally the truth or fake origin of the taus in the different control and signal regions is compared (Section 6.2.4).

6.2.1 The matrix inversion method

Consider a CR relative to background A, where $N_{\mathrm{CR}}^{\mathrm{data}}$ events are observed in data and $N_{\mathrm{CR}}^{\mathrm{A,MC}}$ are expected for background A. Then the prediction for this background in the signal region is obtained as

$$N_{\mathrm{SR}}^{\mathrm{A,predicted}} = \omega_A N_{\mathrm{SR}}^{\mathrm{A,MC}} = \frac{N_{\mathrm{CR}}^{\mathrm{data}} - N_{\mathrm{CR}}^{\mathrm{other,MC}}}{N_{\mathrm{CR}}^{\mathrm{A,MC}}} N_{\mathrm{SR}}^{\mathrm{A,MC}} \tag{6.2}$$

where the prediction from simulation is corrected by a scale factor

$$\omega_A = \frac{N_{\mathrm{CR}}^{\mathrm{data}} - N_{\mathrm{CR}}^{\mathrm{other,MC}}}{N_{\mathrm{CR}}^{\mathrm{A,MC}}} \quad . \tag{6.3}$$

For the discussion of systematic uncertainties resulting from this hypothesis, the above Equation 6.2 for the background prediction can be re-interpreted in a way that defines a purely Monte Carlo based *transfer factor* t_A.

$$t_A = \frac{N_{\mathrm{SR}}^{\mathrm{A,MC}}}{N_{\mathrm{CR}}^{\mathrm{A,MC}}} \tag{6.4}$$

This factor is in turn applied to the observed number of data events in the control region corrected for contaminations from other background sources.

$$N_{\mathrm{SR}}^{\mathrm{A,predicted}} = t_A \left(N_{\mathrm{CR}}^{\mathrm{data}} - N_{\mathrm{CR}}^{\mathrm{other,MC}} \right) = \frac{N_{\mathrm{SR}}^{\mathrm{A,MC}}}{N_{\mathrm{CR}}^{\mathrm{A,MC}}} \left(N_{\mathrm{CR}}^{\mathrm{data}} - N_{\mathrm{CR}}^{\mathrm{other,MC}} \right) \tag{6.5}$$

In practice, scale factors are often needed for several backgrounds. In addition, it is often impossible to construct control regions that are reasonably pure in one background. Generally, all CRs contain contributions from other backgrounds that might be mis-modeled as well. To address this issue, scale factors are to be determined for all studied backgrounds simultaneously. This can e.g. be done using a matrix inversion technique.

Assume three backgrounds A, B and C. Control region A is constructed such that it is dominated by background A, while backgrounds B and C contribute to a lower degree. The same holds analogously for the B and C control regions. Additionally, one can allow for some contamination from other backgrounds that are assumed to be modeled correctly. In this analysis, this is the case for multijets events, which are estimated with a different method but accounted for in this estimation technique, and Dibosons background, which is estimated from simulation only. Equation 6.6 gives a matrix equation that relates the observed data events and the different background predictions in each CR with scale factors applied to correct the A, B and C contributions.

$$\underbrace{\begin{pmatrix} N_1^{\text{data}} - N_1^{\text{QCD,data}} - N_1^{\text{MC,rest}} \\ N_2^{\text{data}} - N_2^{\text{QCD,data}} - N_2^{\text{MC,rest}} \\ N_3^{\text{data}} - N_3^{\text{QCD,data}} - N_3^{\text{MC,rest}} \end{pmatrix}}_{\vec{N}} = \underbrace{\begin{pmatrix} N_1^{\text{A}} & N_1^{\text{B}} & N_1^{\text{C}} \\ N_2^{\text{A}} & N_2^{\text{B}} & N_2^{\text{C}} \\ N_3^{\text{A}} & N_3^{\text{B}} & N_3^{\text{C}} \end{pmatrix}}_{M} \underbrace{\begin{pmatrix} \omega_A \\ \omega_B \\ \omega_C \end{pmatrix}}_{\vec{\omega}} \tag{6.6}$$

In this notation, N_i^{data} is the observed number of data events in the control region i, $N_i^{\text{QCD,data}}$ is the data-driven multijets estimate and $N_i^{\text{MC,rest}}$ is the remaining Monte Carlo contribution from events not being of type A, B or C. In general, these are small and of minor importance in both the CRs and the signal regions. The matrix M is obtained from the Monte Carlo expectation. The vector $\vec{\omega}$ of the scale factors needed to correct all three background types can be obtained by simply inverting the matrix M:

$$\vec{\omega} = M^{-1}\vec{N} \tag{6.7}$$

This technique enables the simultaneous determination of scale factors for N backgrounds, to make predictions and observations agree within N control regions. Moreover, this method allows for an easy determination of the uncertainties on the scale factors, arising from the limited statistics available, and the correlation between them. This is achieved by means of toy Monte Carlo[4]. The scale factors are evaluated multiple times, where in each iteration the input numbers are randomly varied within their respective uncertainties. For simulated events a gaussian probability density function (pdf) is assumed, while data is sampled following a Poisson distribution. By computing the covariance matrix for each iteration, one obtains a measure of the uncertainty on the scaling factors due to the limited statistics available for both data and simulation in the control regions. This automatically takes into account all correlations between and within the control regions.

Finally, the same toy MC method can be used to obtain the background uncertainty in the signal region, now including correlations between control and signal regions. For a given background, yields obtained in the control and signal regions are statistically independent. Thus, together with the input

---

[4] "Toy Monte Carlo" refers to a method often used in statistics in particle physics. It is usually employed when to obtain probability distributions for computations that depend on multiple quantities that are derived from a large simulated dataset in the first place. Instead of repeating the full simulation many times, the quantities resulting from the initial simulation are randomly varied within their uncertainties and the computation is repeated many times with the altered quantities

numbers in the CRs, the MC background prediction in the SR is separately smeared for each iteration, then scaled with the data-driven scalings derived for each iteration. This results in a distribution for the predicted background in the SR, with a width that is determined by the statistical uncertainty of all input values and their correlations.

The entanglement between the scale-factor uncertainties in the CR and the MC statistical uncertainty in the SR can be evaluated by comparing this distribution with and without sampling the pure MC prediction in the signal region.

6.2.2 Control regions

After all cuts, the dominant backgrounds are W+jets, top consisting of $t\bar{t}$ and single top production and Z+jets with the Z boson decaying into two taus. To obtain a data-driven estimate for those backgrounds following the method outlined above, three control regions are defined. Each of these is dominated by one of the backgrounds to be estimated. Depending on the cut on $m_{\mathrm{T}}^{\tau_1} + m_{\mathrm{T}}^{\tau_2}$ employed in the signal region, two of these regions use varying cuts on $m_{\mathrm{T}}^{\tau_1} + m_{\mathrm{T}}^{\tau_2}$ themselves to reproduce the relevant kinematic properties of the signal regions as closely as possible.

Design of the control regions To ensure an optimal similarity between SRs and CRs, all selection cuts up to and including the QCD rejection are applied a priori. Since all signal regions feature a minimal H_T cut of $H_T > 600\,\mathrm{GeV}$, an inverted cut of $H_T < 550\,\mathrm{GeV}$ is applied as a separation cut for all CRs. This cut ensures the orthogonality of control and signal regions and keeps the contamination of the CRs by possible signal events low.

The separation of Z from the other backgrounds by means of a cut on $m_{\mathrm{T}}^{\tau_1} + m_{\mathrm{T}}^{\tau_2}$ comes natural since the cut on this variable has been introduced to reduce Z contamination in the first place. Figure 5.4 in Section 5 shows the distribution of $m_{\mathrm{T}}^{\tau_1} + m_{\mathrm{T}}^{\tau_2}$ used to derived the Z suppression cut. The same distribution suggests that a cut on $m_{\mathrm{T}}^{\tau_1} + m_{\mathrm{T}}^{\tau_2} < 80\,\mathrm{GeV}$ leads to an enrichment of the Z content in the CR.

Also the separation between W and top by means of a b-tag cut is a natural choice, since the production of a W boson in a top decay goes always together with a b quark.

For the W and top CRs, a minimal cut of $m_{\mathrm{T}}^{\tau_1} + m_{\mathrm{T}}^{\tau_2} > 150\,\mathrm{GeV}$ has to be applied to reduce Z contributions as in the SRs.

To ensure the best possible congruence between control and signal regions, cuts on $m_{\mathrm{T}}^{\tau_1} + m_{\mathrm{T}}^{\tau_2}$ and N_{jet} remain to be optimized. In principle, loose CR cuts are desirable to increase the available statistics hence reducing uncertainties on the background estimate. At the same time, it has to be ensured that the difference between control and signal region cuts does not introduce a bias in the estimation technique.

To quantify this, scalings are computed with incremental tightening of the N_{jet} and $m_{\mathrm{T}}^{\tau_1} + m_{\mathrm{T}}^{\tau_2}$ cuts in the W and top CR.

Figure 6.10 (left hand side) shows the values and uncertainties of the computed scale factors with increasingly tighter N_{jet} cuts. The dashed line shows the nominal choice with its statistical uncertainty indicated by the yellow band. Up to and including a cut on at least four jets, all scale factor predictions lie within the uncertainty band on the central scale factor. For higher jet multiplicities, the uncertainty on the scale factors increases strongly, making the use of the corrections obtained that way questionable. Indeed, the distribution of the jet multiplicity is found to be well described in MC (c.f. Figure 6.11).

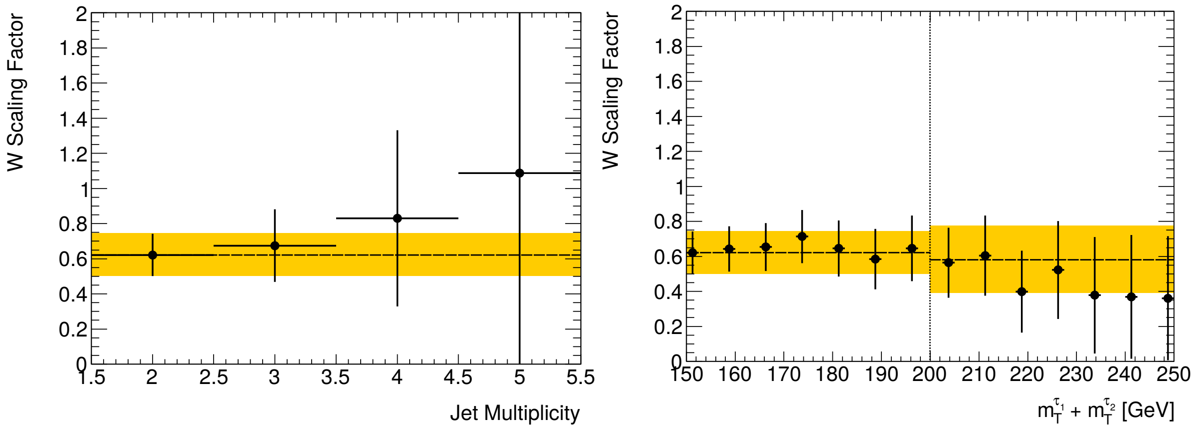

(a) W Scaling

(b) W Scaling

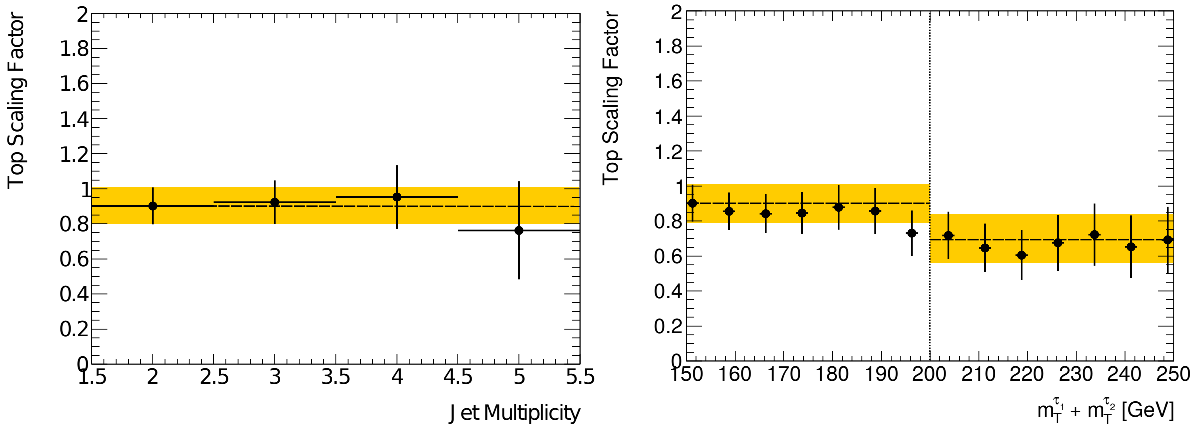

(c) Top Scaling

(d) Top Scaling

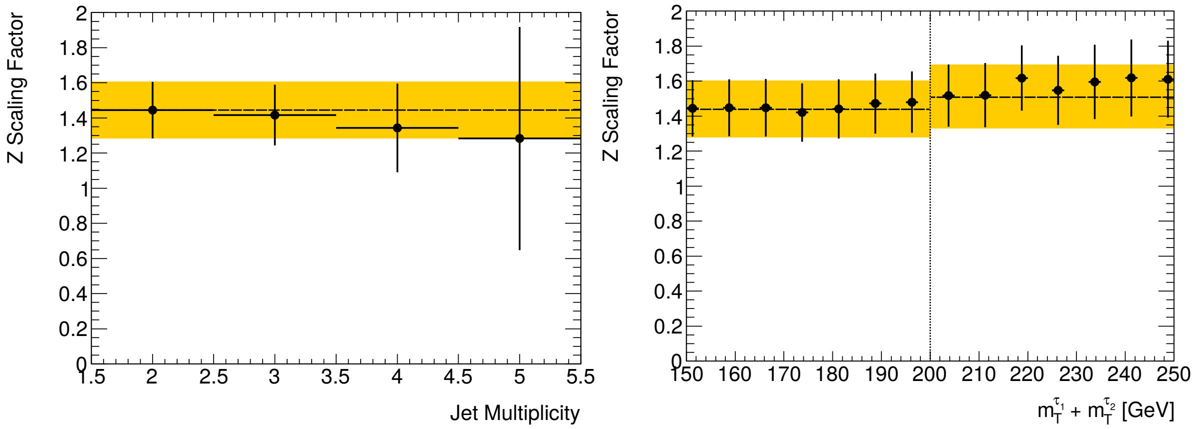

(e) Z Scaling

(f) Z Scaling

Figure 6.10: Change of the computed scaling factor with tighter N_{jet} cuts (left column) and with tighter $m_T^{\tau_1} + m_T^{\tau_2}$ cuts (right column). All other control region cuts are fixed to the nominal values. The final choices are indicated by a dashed line. For the plots showing the dependency on $m_T^{\tau_1} + m_T^{\tau_2}$ the nominal value is shown separately for the regions below and above 200 GeV respectively. The yellow bands show the (statistical) uncertainties on the nominal choices.

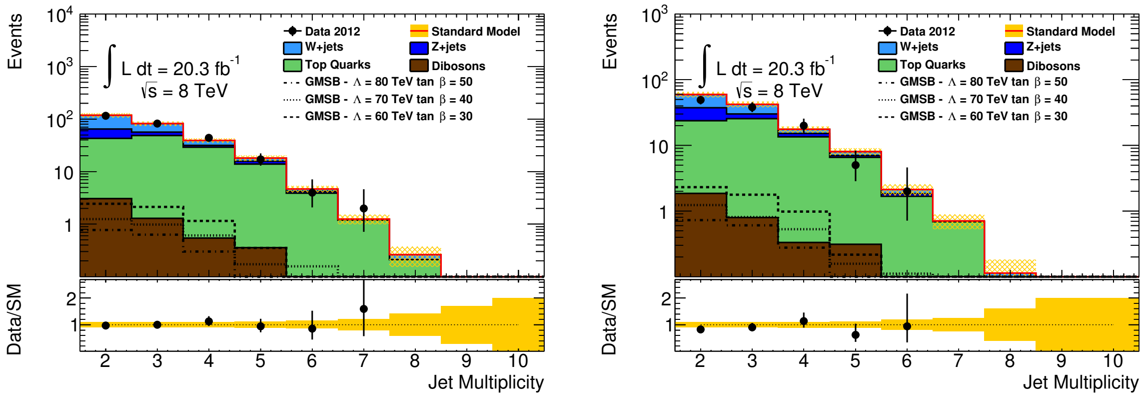

(a) W150/Top150 control region (b) W200/Top200 control region

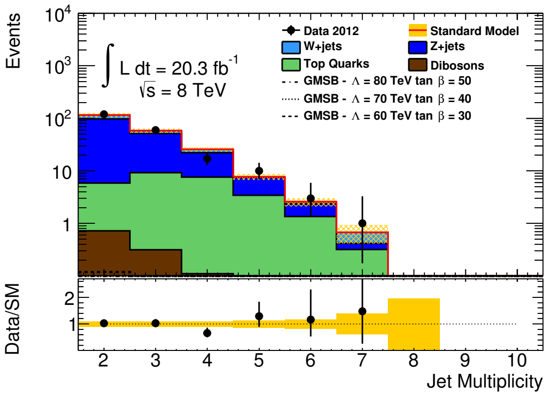

(c) Z control region

Figure 6.11: N_{jet} in the control regions with the computed scaling factors applied. For this comparison the W and the top control regions are unified. Plots are shown for both sets of CRs requiring $m_{\mathrm{T}}^{\tau_1} + m_{\mathrm{T}}^{\tau_2} > 150\,\mathrm{GeV}$ and $m_{\mathrm{T}}^{\tau_1} + m_{\mathrm{T}}^{\tau_2} > 200\,\mathrm{GeV}$, respectively. The jet multiplicity is well described, even up to high multiplicity tails.

A similar scan is displayed in Figure 6.10 (right hand side) for the $m_{\mathrm{T}}^{\tau_1} + m_{\mathrm{T}}^{\tau_2}$ cut. The nominal choice is separated in regions below and above $m_{\mathrm{T}}^{\tau_1} + m_{\mathrm{T}}^{\tau_2} = 200\,\mathrm{GeV}$. The changes of the Z scaling are a result of the correlations between the scale factors, since the Z CR itself is not modified. The W scaling exhibits a good stability across the full range. For cuts above 210 GeV, the uncertainties increase rapidly.

For the top contribution on the other hand, there is a clear drop in the scale factor visible between 190 GeV and 200 GeV. Figure 6.12 shows the underlying $m_{\mathrm{T}}^{\tau_1} + m_{\mathrm{T}}^{\tau_2}$ distribution as well as its constituents' distributions in the top CR. The change in the scale factor coincides with one single bin in the $m_{\mathrm{T}}^{\tau_1} + m_{\mathrm{T}}^{\tau_2}$ distribution, where data fluctuates up above the simulation prediction. Otherwise the data is well described. A cross check in the underlying $m_{\mathrm{T}}^{\tau_1}$ and $m_{\mathrm{T}}^{\tau_2}$ distributions shows no fundamental differences between data and simulation as well. Two bins show slight upward fluctuations, while the overall distribution is well described in MC.

The difference in the top scale factor is most likely the effect of a statistical fluctuation. To remedy this bias, two sets of control regions are defined with $m_{\mathrm{T}}^{\tau_1} + m_{\mathrm{T}}^{\tau_2}$ cuts of 150 GeV and 200 GeV, respectively. In the following, these regions are referred to as W150/Top150 and W200/Top200.

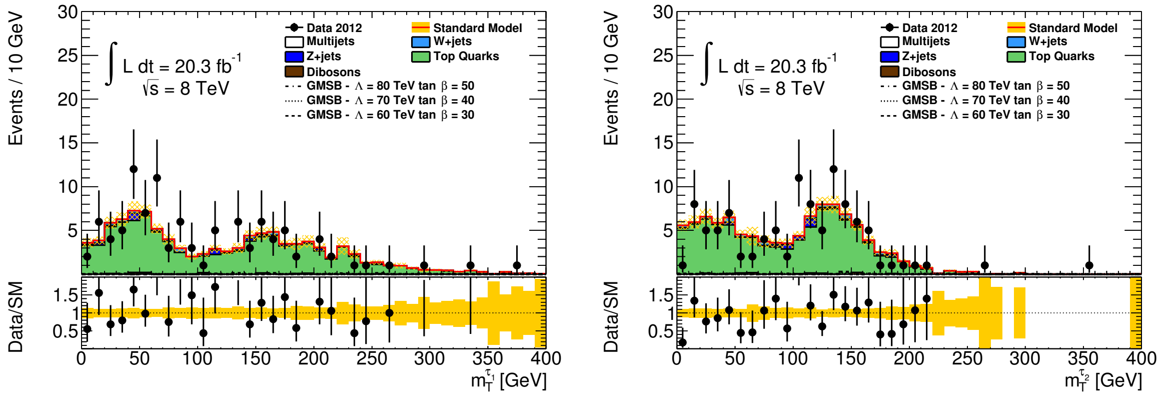

(a) $m_T^{\tau_1}$ (b) $m_T^{\tau_2}$

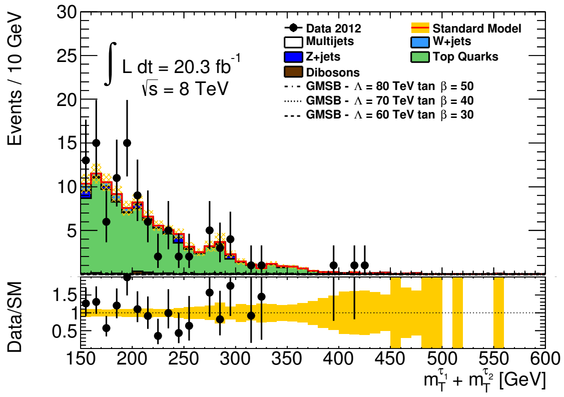

(c) $m_T^{\tau_1} + m_T^{\tau_2}$

Figure 6.12: Distributions of the transverse masses $m_T^{\tau_1}$, $m_T^{\tau_2}$ of the two reconstructed taus and the sum $m_T^{\tau_1} + m_T^{\tau_2}$ in the top control region. Besides the general good agreement, one single bin having a significant over-fluctuation of data is visible in the $m_T^{\tau_1} + m_T^{\tau_2}$ spectrum around 200 GeV.

Control region cuts and yields Figure 6.13 gives an overview of the kinematic cuts of the electroweak control regions. Figure 6.14 shows the definition of the CRs and the SRs in the H_T–$m_T^{\tau_1} + m_T^{\tau_2}$ plane and illustrates the orthogonality between the regions. Figure 6.15 finally displays the leading jet p_T distributions in each of the CRs, demonstrating the dominance of one background contribution as intended.

The yields for the various uncorrected background contributions and their uncertainties together with the observed data events are compiled in Table 6.3. A possible contamination by signal events is studied separately as discussed in section 8.2.

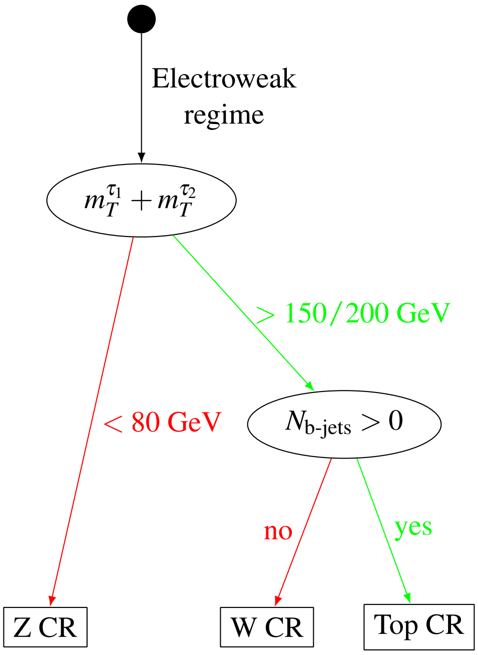

Figure 6.13: Cut flow tree showing the definitions of the electroweak control regions. For the definition of the "electroweak regime" c.f. Figure 6.1.

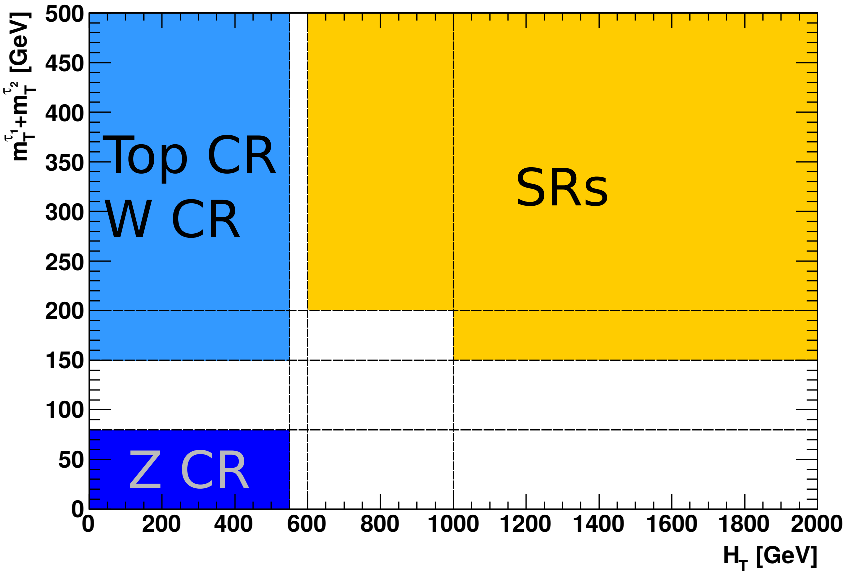

Figure 6.14: Overview of the kinematic definitions of the control and signal regions. The two main kinematic variables employed to separate these are H_T on the x-axis and $m_{\mathrm{T}}^{\tau_1} + m_{\mathrm{T}}^{\tau_2}$ on the y-axis. Multiple SRs are defined by varying cut combinations on these two quantities and additional N_{jet} cuts (c.f. Section 5). CRs for W and top are sub-divided by using b-tagging information.

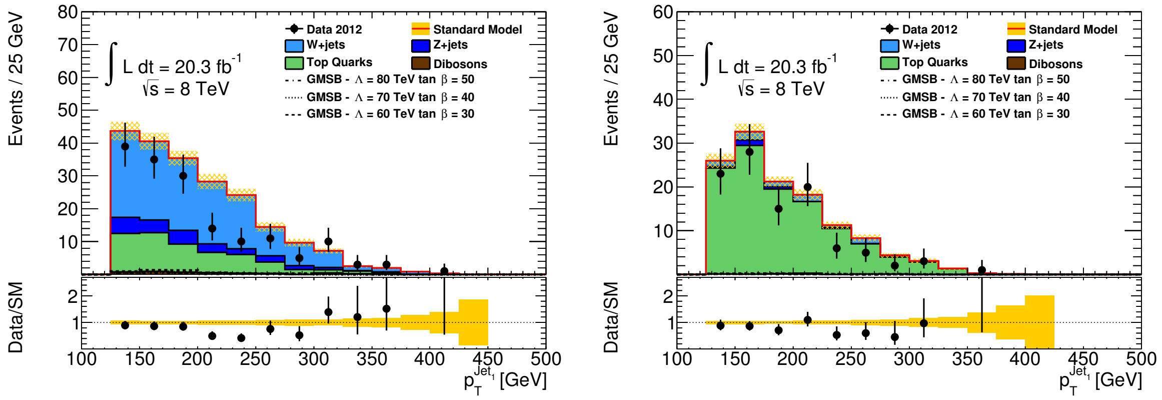

(a) W control region

(b) Top control region

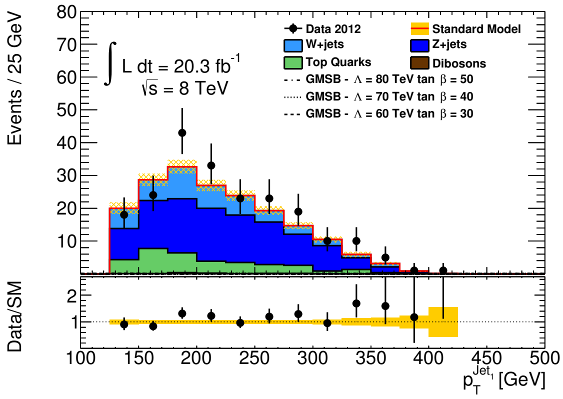

(c) Z control region

Figure 6.15: $p_T^{\text{jet}_1}$ in the three control regions defined for the analysis. The dominance of a single background in each region is clearly visible. All simulated backgrounds are shown uncorrected. The difference between data and simulation demonstrates the need for scaling factors.

Control region	W+jets	Top	Z+jets	Other backgrounds	All MC	Data
W150	132.1 ± 4.9	44.7 ± 2.0	21.6 ± 1.7	7.4 ± 1.6	205.8 ± 5.8	161
Top150	8.5 ± 0.3	102.9 ± 2.9	2.5 ± 0.7	1.3 ± 0.3	115.2 ± 3.0	103
W200	55.8 ± 3.3	21.9 ± 1.5	12.9 ± 1.2	3.7 ± 0.5	94.3 ± 3.9	71
Top200	3.9 ± 0.6	53.6 ± 2.2	1.5 ± 0.4	1.0 ± 0.3	60 ± 2.3	43
Z	45.5 ± 2.9	28.4 ± 1.9	107.2 ± 3.0	1.3 ± 0.3	182.4 ± 4.6	210

Table 6.3: Contributions of different background channels and observed events for the control regions defined for the analysis. “Other backgrounds” comprises the data-driven multijets estimate and Dibosons estimated from simulation. Uncertainties are statistical only. These event numbers are used to calculate the scalings correcting the normalization of the simulation.

6.2.3 Scale factors

For all numbers computed in this section, the data-driven multijets estimate, as described in Section 6.1, is taken into account. It is treated – together with the Dibosons background – as “other backgrounds”. The influence of these additional contributions is found to be negligible as expected and they are hence neglected in all plots.

Background	Scale factor
W+jets	0.62 ± 0.12
Top	0.90 ± 0.11
Z+jets	1.44 ± 0.16

(a) $m_{\mathrm{T}}^{\tau_1} + m_{\mathrm{T}}^{\tau_2} > 150\,\mathrm{GeV}$ Scalings

Background	Scale factor
W+jets	0.58 ± 0.19
Top	0.70 ± 0.13
Z+jets	1.51 ± 0.18

(b) $m_{\mathrm{T}}^{\tau_1} + m_{\mathrm{T}}^{\tau_2} > 200\,\mathrm{GeV}$ Scalings

Table 6.4: Measured scale factors for Standard Model background contributions and their uncertainties arising from limited MC and data statistics in the control regions. For the two sets of CRs with differing $m_{\mathrm{T}}^{\tau_1} + m_{\mathrm{T}}^{\tau_2}$ cuts only the top scaling changes significantly, as expected.

The scaling factors and their uncertainties are obtained by using the matrix inversion method outlined in Section 6.2.1 on the control regions defined in Section 6.2.2. The resulting scale factors are listed in Table 6.4. Histograms showing the distributions are displayed in Figure 6.16.

Correlation factors are listed in Table 6.5. There is a significant anti-correlation between W and top on one hand and W and Z on the other hand, while top and Z are nearly uncorrelated. The reason for this behavior lies in the larger admixtures of both Z+jets and top in the W control region, while the top and Z CRs are much purer themselves. This anti-correlation has to be taken into account when computing the uncertainties on the background expectation due to the limited statistics in the control region and in the signal region. The obtained expected numbers of background events for the different signal regions are compiled in Table 6.6.

	W+jets	Top	Z+jets
W+jets	1	-0.35	-0.44
Top	-0.35	1	-0.08
Z+jets	-0.44	-0.08	1

(a) $m_{\mathrm{T}}^{\tau_1} + m_{\mathrm{T}}^{\tau_2} > 150\,\mathrm{GeV}$ CRs

	W+jets	Top	Z+jets
W+jets	1	-0.33	-0.55
Top	-0.33	1	-0.06
Z+jets	-0.55	-0.06	1

(b) $m_{\mathrm{T}}^{\tau_1} + m_{\mathrm{T}}^{\tau_2} > 200\,\mathrm{GeV}$ CRs

Table 6.5: Correlations between the obtained scale factors. Z and top are uncorrelated while the other combinations of scale factors show significant anti-correlations.

The overall effect of the scalings is visible in Figure 6.17 in which scaled and unscaled $p_T^{\tau_1}$ distributions are shown side by side before any $m_{\mathrm{T}}^{\tau_1} + m_{\mathrm{T}}^{\tau_2}$ cut and with the two cuts applied for the control regions. Independently of the $m_{\mathrm{T}}^{\tau_1} + m_{\mathrm{T}}^{\tau_2}$ cut, the distributions in data are well described by the final background estimates. More comparison plots are displayed in Figures 6.18 to 6.21 showing different kinematic variables in the different control regions. The scaled simulation matches nicely in both shape and normalization the observed data in all cases within the respective statistical uncertainties.

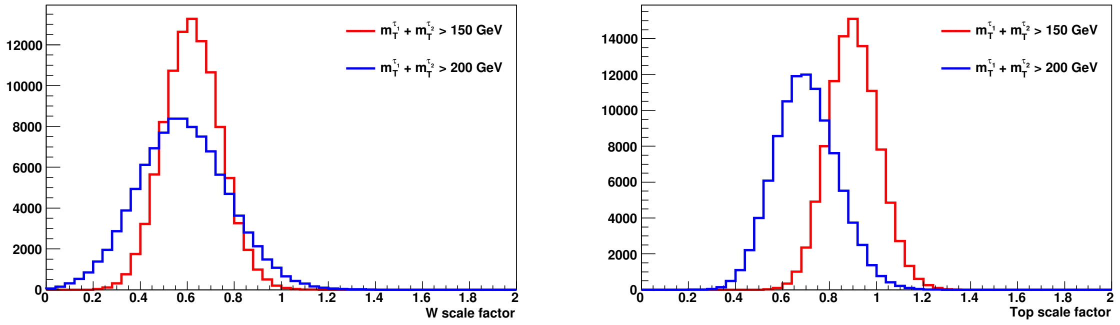

(a) W scale factor (b) Top scale factor

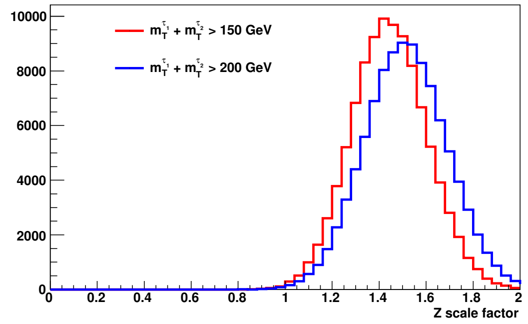

(c) Z scale factor

Figure 6.16: Distributions of the computed scale factors. Each entry corresponds to one iteration of toy Monte Carlo with all input quantities varied randomly within their statistical uncertainties. Shown are the distributions for the cut $m_T^{\tau_1} + m_T^{\tau_2} > 150\,\text{GeV}$ in red and for the cut $m_T^{\tau_1} + m_T^{\tau_2} > 200\,\text{GeV}$ in blue. The change in the central value of the top scaling can be attributed to one single bin showing an upward fluctuation.

Signal region	Background estimates	Top fraction	W fraction	Z fraction
Inclusive	$2.88 \pm 0.34^{\text{stat}} \pm 0.21^{\text{sf}}$	20%	44%	19%
GMSB	$0.28 \pm 0.08^{\text{stat}} \pm 0.04^{\text{sf}}$	18%	47%	13%
nGM	$3.14 \pm 0.39^{\text{stat}} \pm 0.30^{\text{sf}}$	52%	25%	21%
bRPV $m_{1/2}$	$1.09 \pm 0.17^{\text{stat}} \pm 0.08^{\text{sf}}$	29%	44%	17%
bRPV m_0	$6.22 \pm 0.61^{\text{stat}} \pm 0.66^{\text{sf}}$	51%	30%	13%

Table 6.6: Background estimations and their associated uncertainties due to limited MC statistics in the signal region (“stat”) and the statistical uncertainty on the scale factors due to limited data and MC statistics in the control regions (“sf”). Numbers include all backgrounds including multijets from separate estimate and Dibosons from MC. Fractions include all scalings for the respective channels.

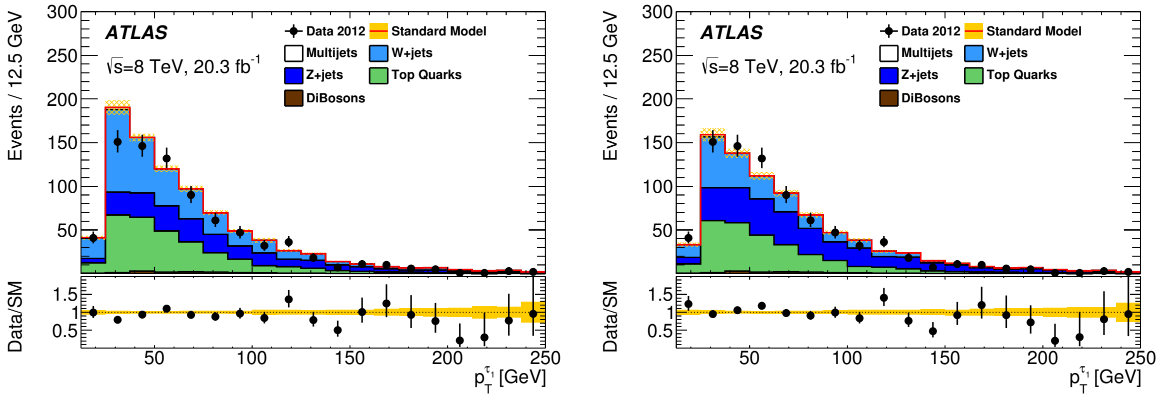

(a) No $m_{\mathrm{T}}^{\tau_1} + m_{\mathrm{T}}^{\tau_2}$ cut, unscaled

(b) No $m_{\mathrm{T}}^{\tau_1} + m_{\mathrm{T}}^{\tau_2}$ cut, scaled

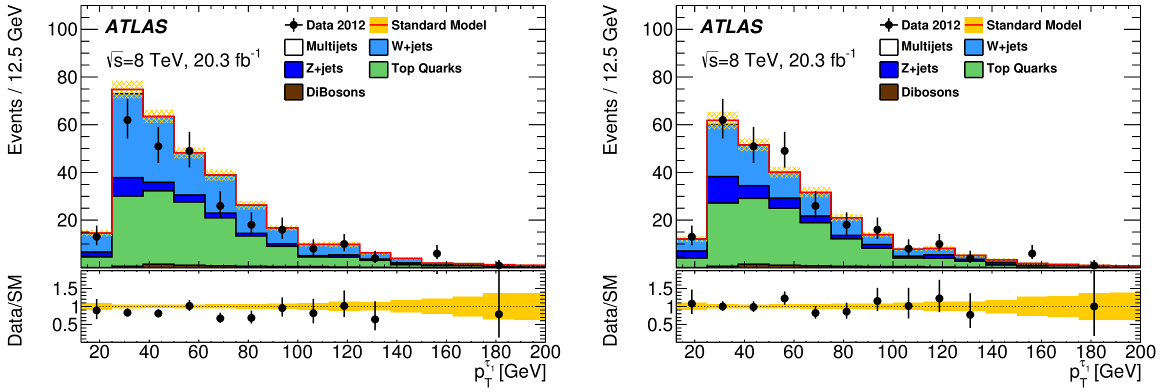

(c) $m_{\mathrm{T}}^{\tau_1} + m_{\mathrm{T}}^{\tau_2} > 150\,\mathrm{GeV}$, unscaled

(d) $m_{\mathrm{T}}^{\tau_1} + m_{\mathrm{T}}^{\tau_2} > 150\,\mathrm{GeV}$, scaled

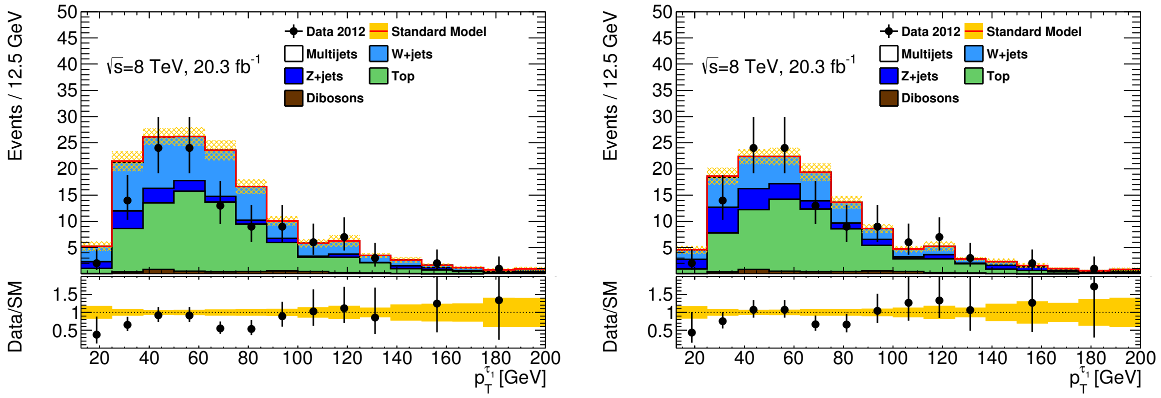

(e) $m_{\mathrm{T}}^{\tau_1} + m_{\mathrm{T}}^{\tau_2} > 200\,\mathrm{GeV}$, unscaled

(f) $m_{\mathrm{T}}^{\tau_1} + m_{\mathrm{T}}^{\tau_2} > 200\,\mathrm{GeV}$, scaled

Figure 6.17: $p_T^{\tau_1}$ after requiring separation between jets and $\not{E}_T$ (first row) and with the two $m_{\mathrm{T}}^{\tau_1} + m_{\mathrm{T}}^{\tau_2}$ cuts applied for the two sets of control regions, respectively, with and without the computed scaling factors applied. An overall improvement of the data/Monte Carlo agreement is visible, under all selections shown.

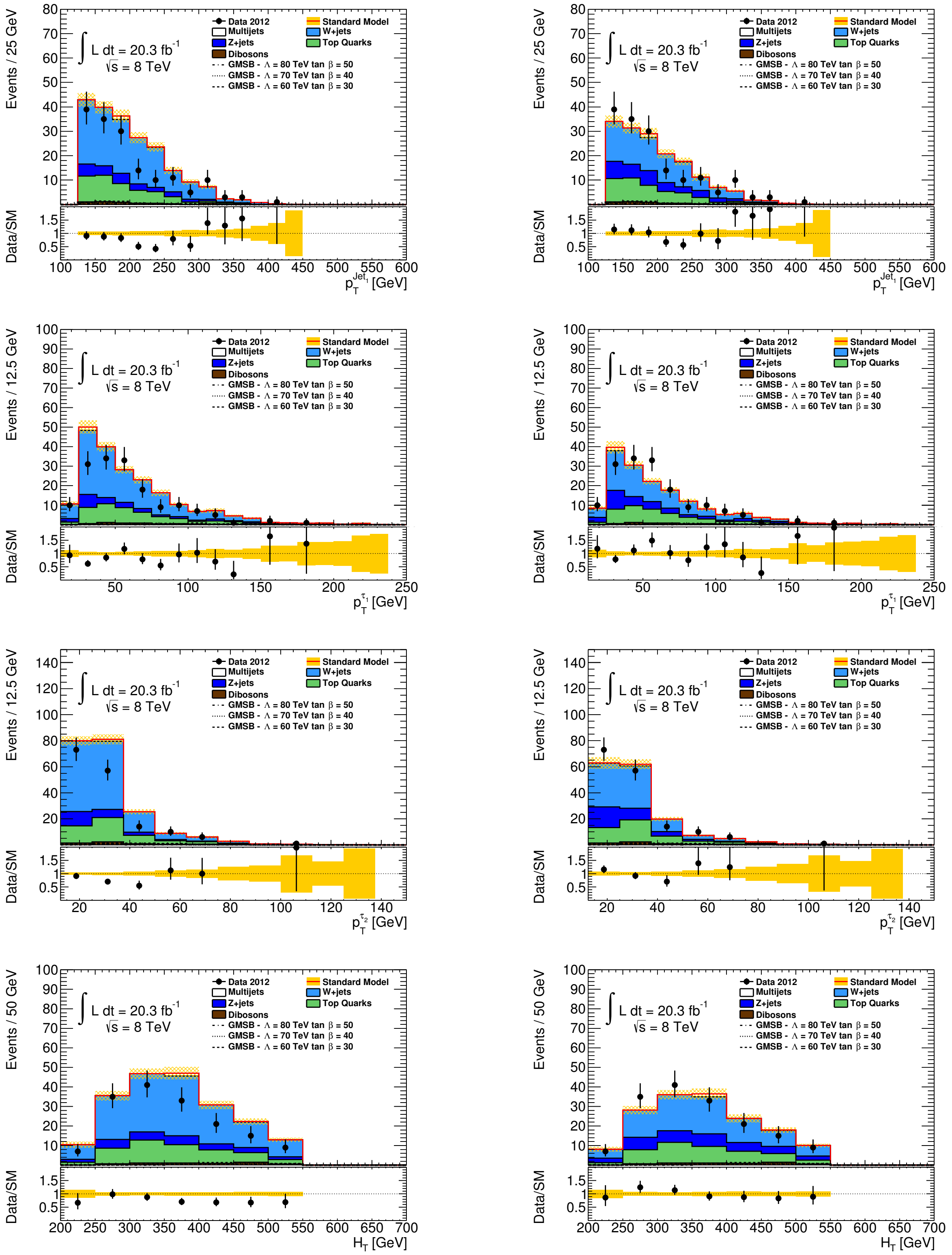

Figure 6.18: Various kinematic variables unscaled (left column) and scaled (right column) in the W control region. An overall improvement of the data/Monte Carlo agreement is clearly visible.

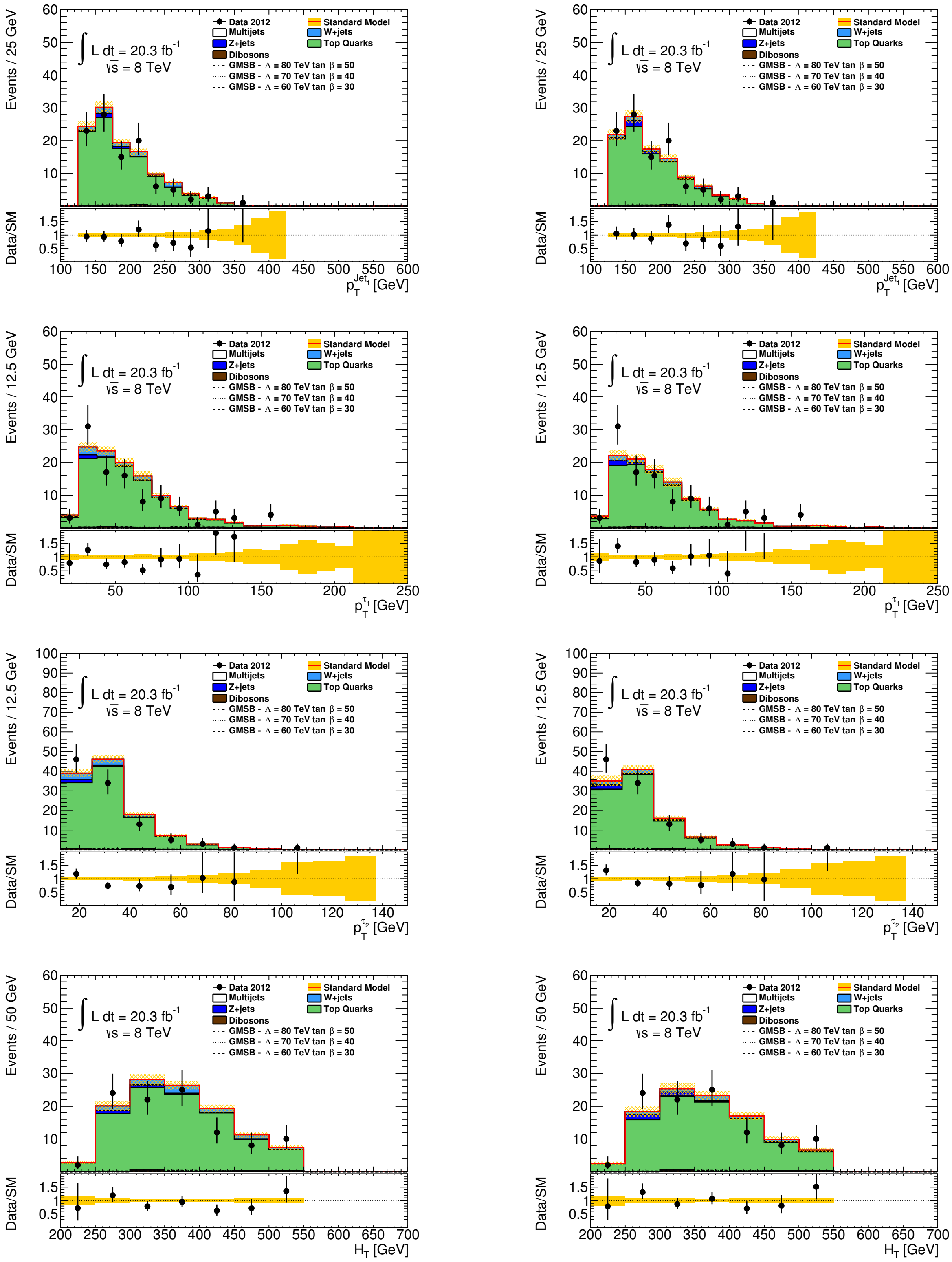

Figure 6.19: Various kinematic variables unscaled (left column) and scaled (right column) in the top control region. An overall improvement of the data/Monte Carlo agreement is clearly visible.

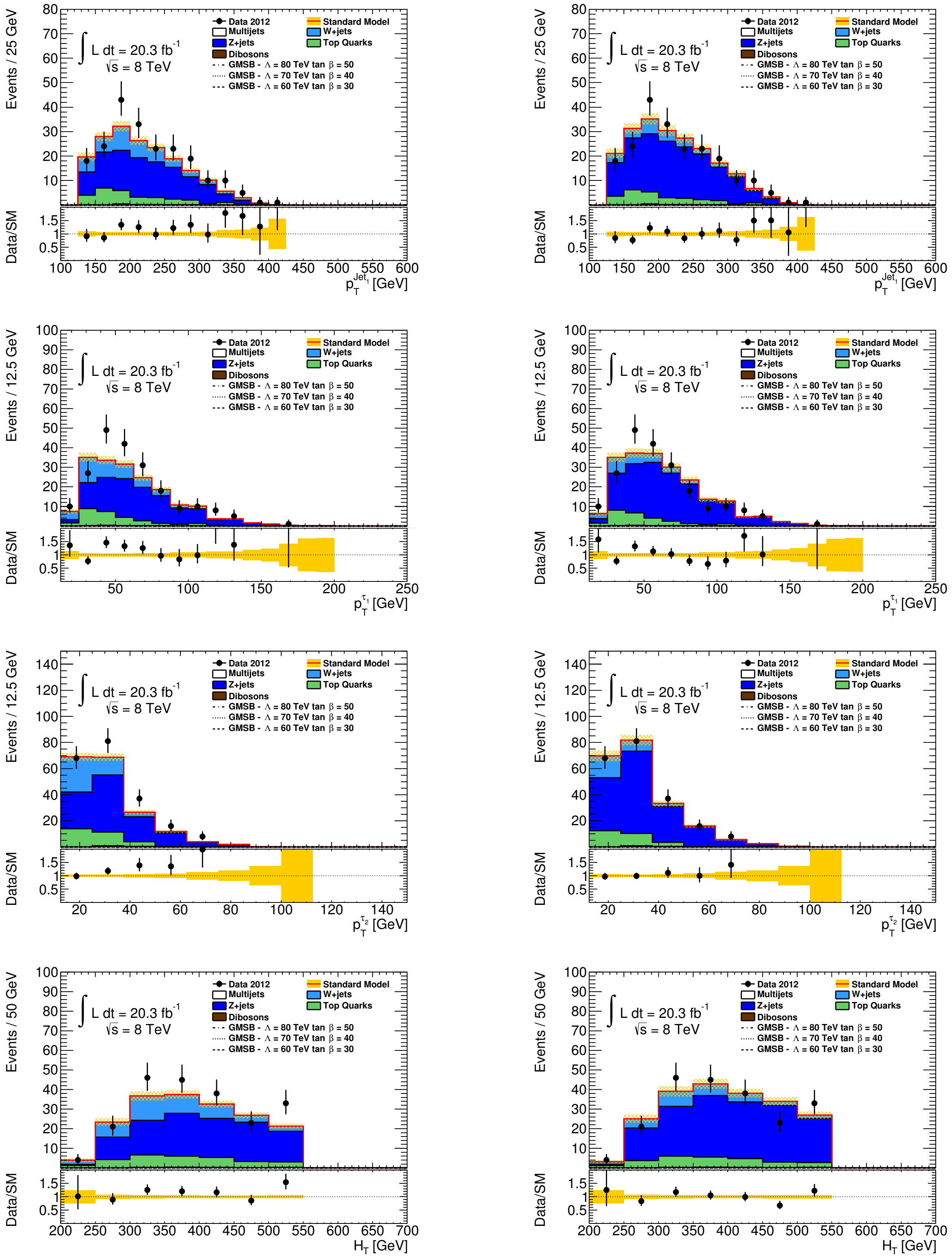

Figure 6.20: Various kinematic variables unscaled (left column) and scaled (right column) in the Z control region. An overall improvement of the data/Monte Carlo agreement is clearly visible.

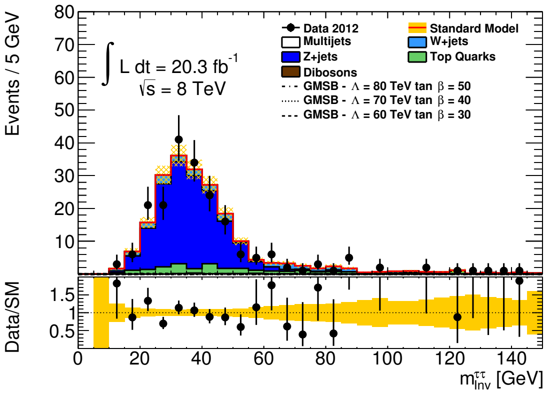

Figure 6.21: Invariant mass of the two tau candidates after applying the scale factors in the Z control region. The expected mass peak together is visible with a good agreement in both data and simulation.

6.2.4 Truth-composition of the control regions

One major issue for all tau-based analyses is the modeling of taus in the simulation. As outlined above, the separation of taus and jets is challenging in itself, and a correct simulation of this difference even more so.

Ideally, one would determine the influence of true taus and fake taus separately. Unfortunately, in this analysis one always has to deal with a mixture of true and fake taus. A separation is not possible without changing the particle types required, which in itself is likely to introduce a bias into the estimate. An attempt for such a separation is attempted in Section 6.3 and employed as a cross check.

Instead of separating true and fake taus, one can also ensure that the composition is similar in the signal and control regions. Since reconstructed true taus are in general much better described in simulation than fake taus, a large difference in this composition would introduce a wrong estimation of the background in the SR.

For this verification, the number of reconstructed true taus per event, i.e. the reconstructed taus that overlap with the visible decay products of a generated tau within a cone of $\Delta R < 0.2$, is evaluated in the various control and signal regions. Figures 6.22 and 6.23 show the distribution of these numbers. It can be seen that for both W+jets and top backgrounds signal and control regions are clearly dominated by events containing one true tau ($\approx$75%). While for top a small number of events with two truth-matched taus is observed in all regions, a small fraction (less than 10%) of W events in the control region contains no truth matched tau.

For Z+jets in the Z control region, the largest fraction of events contain two true taus. This is not the case for the small contributions of Z+jets events in the signal regions. Here, some part of the background has one fake and one true tau. Assuming the same difference between the truth and the fake scale factor as computed for the similar W sample in Section 6.3, this would shift the Z scale factor down towards unity. In the W control region there is a sizable content of Z events which do not have any truth-matched taus. Those contributions originate from $Z \to \nu\nu$ events, where two jets are mis-identified as taus. To assess the effect of including this component in the Z estimation procedure, all scalings are recomputed with taking $Z \to \nu\nu$ directly from MC while only scaling the $Z \to \tau\tau$ component. As expected, top and Z scale factors stay virtually identical, while the correction factor for W is notably larger. It increases

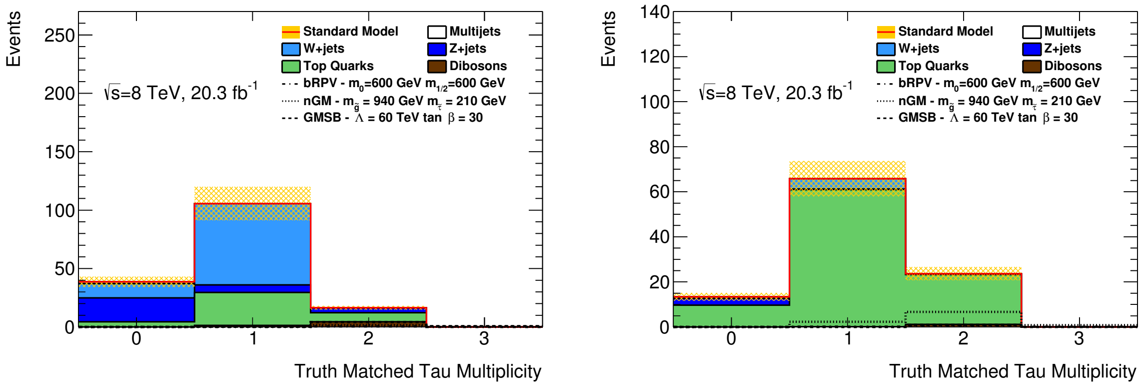

(a) W150 control region (b) Top150 control region

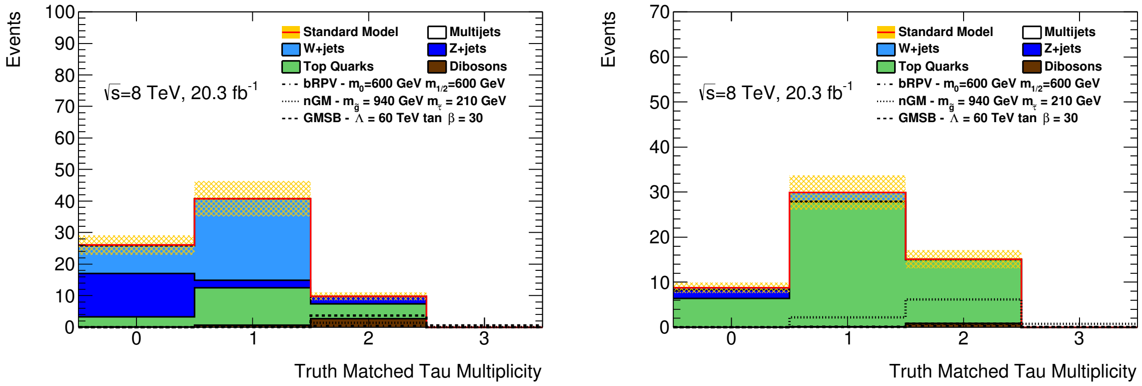

(c) W200 control region (d) Top200 control region

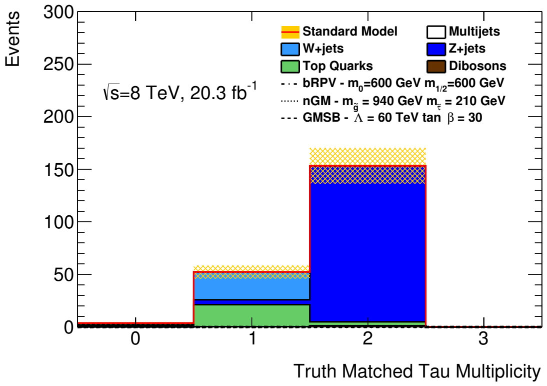

(e) Z control region

Figure 6.22: Number of reconstructed true taus per event in the control regions.

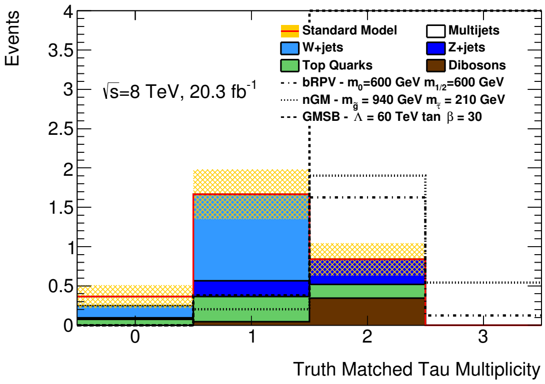

(a) Inclusive signal region

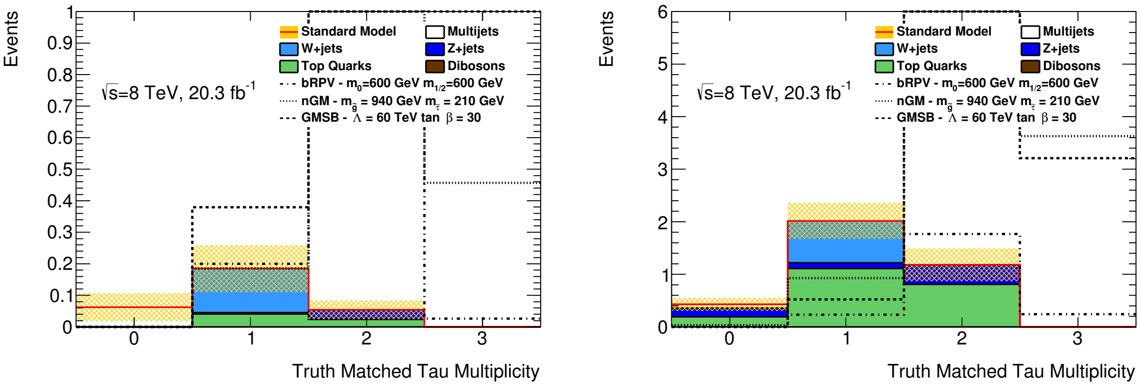

(b) GMSB signal region

(c) nGM signal region

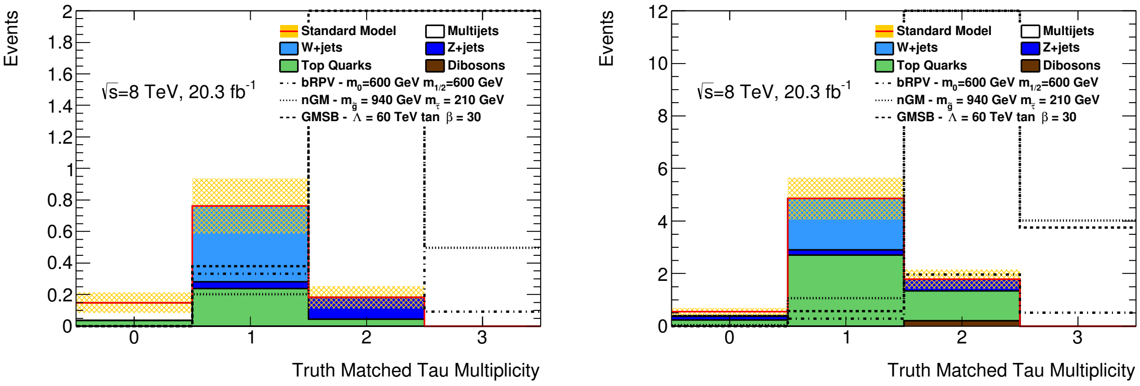

(d) bRPV$m_{1/2}$ signal region

(e) bRPVm_0 signal region

Figure 6.23: Number of reconstructed true taus per event in the signal regions.

from $ditauWScaling$ to 0.77 ± 0.12. The resulting effect on the signal region expectations is very small, however. The largest difference is observed in the GMSB signal region with a relative increase of the background expectation of 19%. The statistical uncertainty on this expectation amounts to 33%, let alone the 79% systematic uncertainty on this number. In all other signal regions, the relative change is below 10%. For this reason it was decided not to assign an extra uncertainty for this effect.

Another aspect in correcting the MC modeling of taus is the actual source of a reconstructed tau. It is well possible that the fake probability might be different for different objects. To determine the true origin of a tau candidate, a multi step matching scheme is applied:

1. If a tau candidate matches within a cone of $\Delta R < 0.2$ to a truth lepton (electron, muon or tau) it is a lepton.
2. If a tau candidate matches within a cone of $\Delta R < 0.2$ to a jet which is tagged as a heavy jet (originating from c or b quark decays) it is a heavy quark fake.
3. If a tau candidate matches within a cone of $\Delta R < 0.2$ to a quark originating directly from a $\mathrm{W} \to \mathrm{q}\bar{\mathrm{q}}$ decay it is a W quark fake.
4. If none of the above applies, the tau candidate is matched to the light quark or gluon in a cone of $\Delta R < 0.4$ around the direction of the reconstructed tau having the largest transverse momentum.

The tau truth de-composition for all control regions and signal regions is shown in Figures 6.24 and 6.25, respectively. The composition for the individual channels is very similar between signal regions and the respective control regions. One of the most striking features is the fact that for fakes in top events a significant fraction originates from heavy quarks, while for W events fakes are entirely dominated by fakes from light quarks and gluons. This might provide some insight in the difference between the scaling factors for W and top events, although a more thorough study on the details is left to the simulation experts and would be much beyond the scope of this thesis.

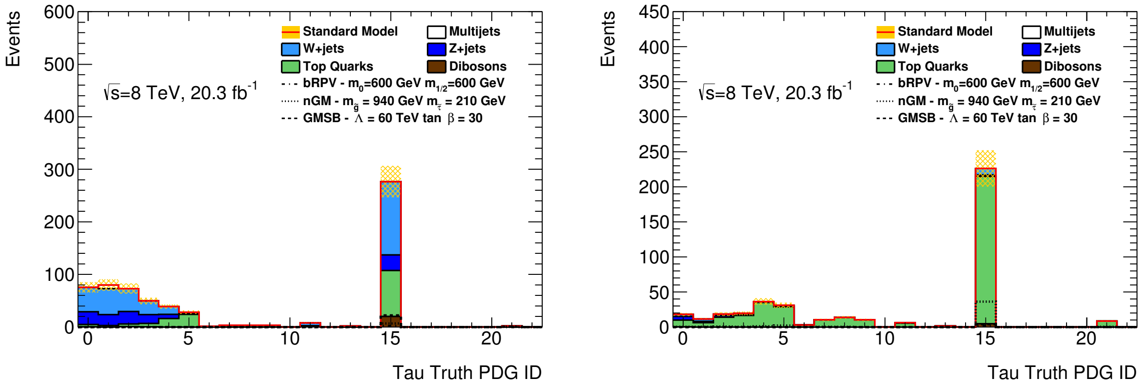

(a) W150 control region

(b) Top150 control region

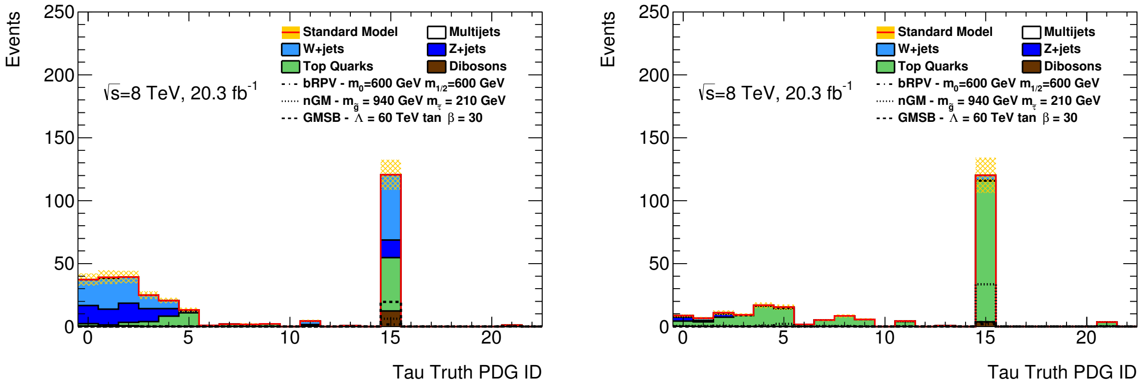

(c) W200 control region

(d) Top200 control region

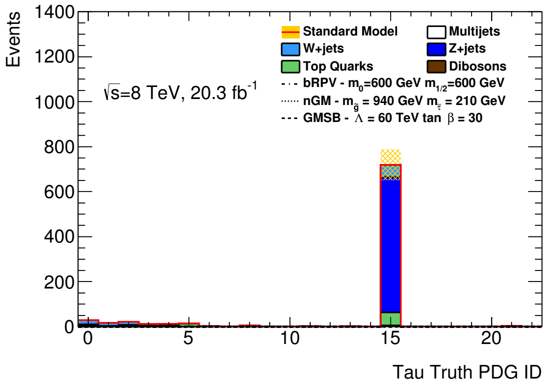

(e) Z control region

Figure 6.24: Truth source of a tau candidate in the control regions. The algorithm used to determine the source is described in Section 6.2.4. Numbers 1-5 correspond to up-bottom quarks, 7-9 to light quarks from W decays, 11, 13 and 15 to electron, muon and tau, respectively, and 21 to gluons.

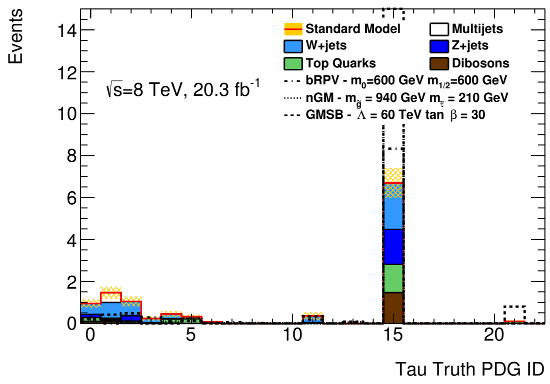

(a) Inclusive signal region

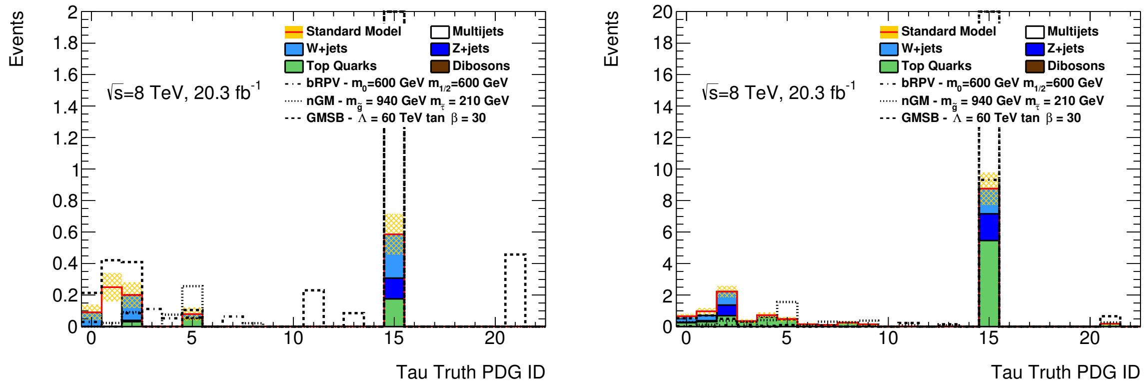

(b) GMSB signal region
(c) nGM signal region

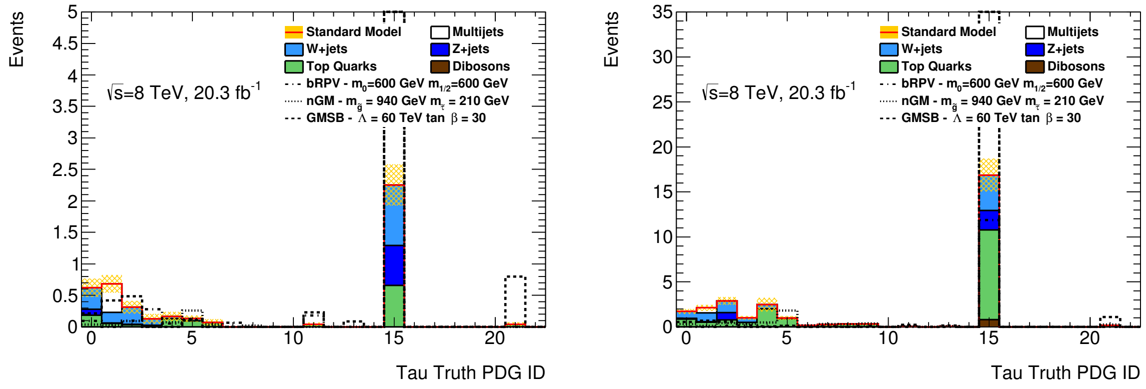

(d) bRPV$m_{1/2}$ signal region
(e) bRPVm_0 signal region

Figure 6.25: Truth source of a tau candidate in the signal regions. The algorithm used to determine the source is described in Section 6.2.4. Numbers 1-5 correspond to up-bottom quarks, 7-9 to light quarks from W decays, 11, 13 and 15 to electron, muon and tau, respectively, and 21 to gluons.

6.3 Validation

The background estimation technique for multijets events is validated in a specific validation region requiring one (fake) tau. This validation shows an excellent agreement (c.f. Section 6.1.4). At the end of Section 6.2.3, the performance of the employed background estimation technique for the dominant electroweak backgrounds is demonstrated within the used control regions. Additional validation checks are compiled in this section. First cross checks in dedicated validation regions are presented in Section 6.3.1. These allow for a consistency check of the scale factors and for a validation of the modeling of the H_T variable. The other main selection variables are validated with a signal-region like selection. It is blinded in the region where signatures of new physics are expected to show up to avoid actual signal contamination (c.f. Section 6.3.2). Finally, the independence of the analysis and the background estimates of the pileup conditions is proven (Section 6.3.3).

6.3.1 Validation with differing particle content

To validate the electroweak background estimate, validation regions (VRs) are designed that differ from the nominal selection in the requested particle content. These regions serve a dual purpose:

In the most general approach, a difference of Monte Carlo to data for this search channel can arise both due the rather specific kinematics and due to mis-modeling of both true and fake taus. In the case where both taus are fake, the single dominant background is multijets production. It is addressed using the Jet Smearing technique to emulate the overall event kinematics and taking the fake taus from data. As argued before, a clear separation of the different effects is nearly impossible for events with real taus, since the selected final state consists of a mixture of true and fake taus in one event for all relevant backgrounds. This can be partially overcome by the use of VRs with differing particle compositions.

These regions can also be used to test the extrapolation of the scale factors. To avoid any effects by possible signal events the H_T distributions can only be checked up to $H_T < 600\,\mathrm{GeV}$ in a nominal two-tau selection. Above that value, the signal regions begin. With a different particle content, one is a priori free of any of the targeted signal. This is not entirely the case for tau rich final states however. Since taus can also decay into muons or be identified as jets, a signal from a two-tau final state can still be present in e.g. a muon-jet selection. The level of contamination is much lower due to the smaller branching ratios, such that the H_T distribution can be evaluated up to higher values.

Design of the validation regions To disentangle the different effects to the best possible level, three additional validation regions are defined[5]. Those validation regions share all kinematic cuts with the nominal regions. Some very small multijets contribution is found in kinematic contributions where the missing transverse momentum is opposite to the leading jet but not aligned to the sub-leading. This is accounted for by additionally rejecting those events. The requirement of one isolated signal muon and one additional jet is imposed to mimic the selection of one true and one fake tau in the kinematic region. In the true tau region, a requirement on one tau and one jet is imposed. Here, the effective tau identification ensures a dominance of true taus over fake taus. To enrich fake taus, one tau and one muon is required. Due to the high efficiency and purity of the muon identification, this requirement selects events where one muon comes from the decay of an electroweak boson and the tau is faked by

---

[5] For the sake of consistency, the same tau identification and overlap removal procedure is applied in all of the regions as in the main selection.

a jet. The three regions are again split into W and top quark dominated parts. The validation of Z+jets backgrounds is not possible in this way, since the Z decays always in two leptons of the same flavor.

All validation regions include a control region by requiring $H_T < 550\,\text{GeV}$ and the sum of the transverse masses of the two defining objects to be larger than $150\,\text{GeV}$[6], thus mirroring the CR cuts in the nominal selection. This technique allows to compare the derived scale factors and checking the H_T distribution up to high levels at the same time. The selection cuts for all VRs and their subsequent CRs are summarized in Table 6.7.

	Kinematic region		True tau region		Fake tau region	
	W	Top	W	Top	W	Top
Trigger plateau	$p_T^{\text{jet}_1} > 130\,\text{GeV}$, $p_T^{\text{jet}_2} > 30\,\text{GeV}$ $\not{E}_T > 150\,\text{GeV}$					
Taus	$N_\tau^{\text{loose}} = 0$		$N_\tau^{\text{loose}} = 1$		$N_\tau^{\text{loose}} = 1$	
Light leptons	$N_\mu^{\text{baseline}} = 1$		$N_\mu^{\text{baseline}} = 0$		$N_\mu^{\text{baseline}} = 1$	
	$N_e^{\text{baseline}} = 0$					
QCD rejection	$\Delta\phi(\text{jet}_{1,2}, \not{E}_T) \geq 0.3$ AND $\Delta\phi(\text{jet}_{1,2}, \not{E}_T) \leq \pi - 0.3$					
W/top separation	$N_{b\text{-jet}} = 0$	$N_{b\text{-jet}} \geq 1$	$N_{b\text{-jet}} = 0$	$N_{b\text{-jet}} \geq 1$	$N_{b\text{-jet}} = 0$	$N_{b\text{-jet}} \geq 1$
VR cuts	$H_T < 1\,200\,\text{GeV}$				$H_T < 800\,\text{GeV}$	
CR cuts	$H_T < 550\,\text{GeV}$					
	$m_\text{T}^\mu + m_\text{T}^{\text{jet}_3} > 150\,\text{GeV}$		$m_\text{T}^{\tau_1} + m_\text{T}^{\text{jet}_3} > 150\,\text{GeV}$		$m_\text{T}^\tau + m_\text{T}^\mu > 150\,\text{GeV}$	

Table 6.7: Overview of the definition validation regions and their respective control regions.

Figures 6.26 and 6.27 show the true and fake tau content in the true and fake tau dominated CRs, respectively. As expected, the regions are largely dominated by the contributions for W+jets. For top quarks, there is a larger admixture of non-desired events. In the true tau region, there is a non-negligible fraction of fake tau events, while in the fake tau region the fraction of events having a true and a fake tau is approximately equal. This has to be considered when interpreting the results. Both regions show a negligible fraction of events with more than one tau candidate.

---

[6] Note that here only the equivalents of the control regions employing a cut on $m_\text{T}^{\tau_1} + m_\text{T}^{\tau_2} > 150\,\text{GeV}$ are documented. Completely analogues studies are performed on regions having an corresponding cut at $200\,\text{GeV}$. While the numbers are slightly different, still all numbers are consistent between the various regions.

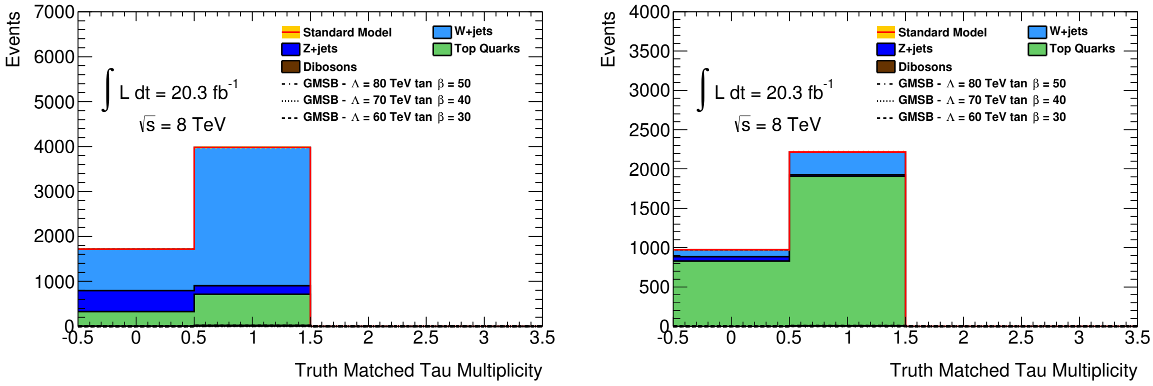

(a) True tau W control region

(b) True tau top control region

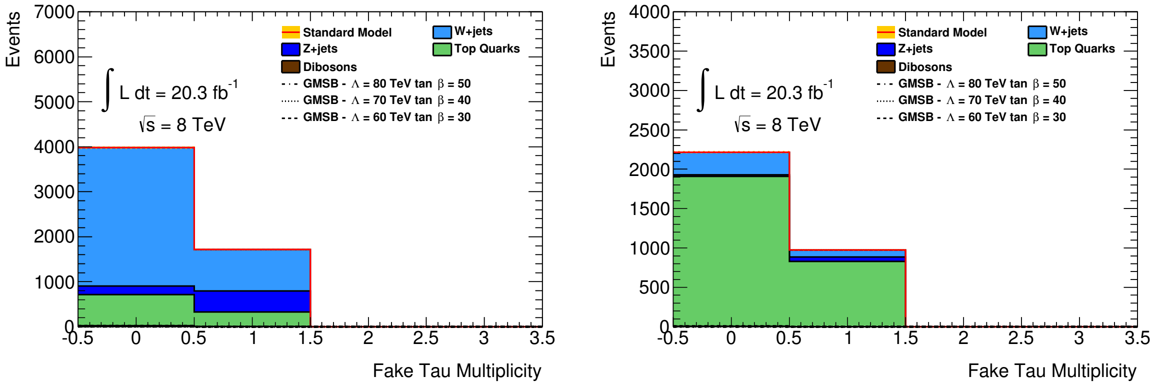

(c) True tau W control region

(d) True tau top control region

Figure 6.26: True tau (top row) and fake tau (bottom row) content of the events in the true tau control region. Both regions are clearly dominated by events containing only one true tau.

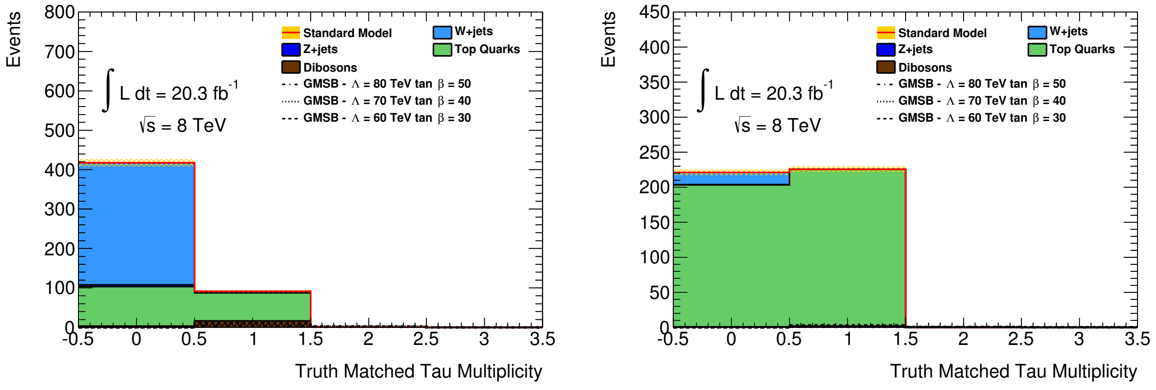

(a) Fake tau W control region (b) Fake tau top control region

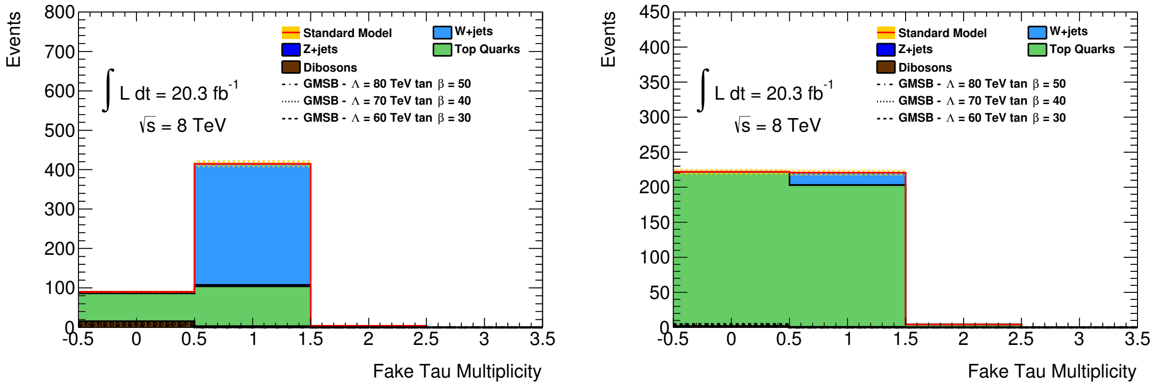

(c) Fake tau W control region (d) Fake tau top control region

Figure 6.27: True tau (top row) and fake tau (bottom row) content of the events in the fake tau control region. The W content in the W validation region consists of nearly 100% fake taus. For top there is a roughly 50% fraction of both true and fake taus.

Computing scale factors For the validation, scale factors are derived from the control regions with a similar method as for the nominal control regions, only reduced to a 2×2 matrix. The correction factors are determined independently for the three regions applying the cuts listed as “CR cuts” in Table 6.7. They are listed in Table 6.8.

	Kinematic CR	True tau CR	Fake tau CR
W+jets Scaling	0.97 ± 0.02	0.85 ± 0.02	0.75 ± 0.07
Top Scaling	0.97 ± 0.02	0.98 ± 0.02	0.87 ± 0.05

Table 6.8: Computed scaling factors and their uncertainties arising from limited MC and data statistics in the validation control regions. The uncertainties are much smaller than for the nominal backgrounds. Top and W show significantly different behaviour.

One finds that the kinematic scalings for both W and top quarks are compatible with unity. The corrections applied (c.f. Section 4) compensate remaining discrepancies in the simulation. For the true tau region, the scaling factor computed in the top dominated region is nearly identical to the kinematic scale factor, while for W+jets it is significantly lower. The reconstruction efficiency for real taus is somewhat over-estimated in the simulation of W+jets events. In the fake region, one finds a value smaller than one in both the W and the top dominated regions. Again, the simulation over-estimates the reconstruction efficiency for fake taus.

Assuming that the different effects of mis-description in the simulation are not correlated, the overall correction factors can be interpreted as the product of three fundamental scaling factors ω_{kin}, ω_{true} and ω_{fake} describing the necessary corrections due to kinematics, true tau modeling and fake tau modeling, respectively. Under this assumption, the scale factor in the kinematic control region would be identical to ω_{kin}. The scale factor in the true and fake tau regions are the product of ω_{kin} with ω_{true} and ω_{fake}, respectively. Vice versa, the fundamental scale factors can be computed from the measured factors in the three regions. They are listed in Table 6.9.

	ω_{kin}	ω_{true}	ω_{fake}
W+jets	0.97 ± 0.02	0.88 ± 0.03	0.77 ± 0.07
Top	0.97 ± 0.02	1.01 ± 0.03	0.89 ± 0.05

Table 6.9: De-composed scale factors for the influence of kinematics, true tau and fake tau description. These component scalings are derived from the validation control regions.

The full scaling factors ω^W and ω^t, measured in the nominal control regions, can be interpreted as being the product $\omega = \omega_{\text{kin}} \times \omega_{\text{true}} \times \omega_{\text{fake}}$ of all three fundamental scalings. For the W CR this approach yields an expected scale factor of $\omega^W_{\text{exp}} = 0.66 \pm 0.07$ (to be compared to the measured $\omega^W = 0.62 \pm 0.12$). For the top control region, one would expect $\omega^t_{\text{exp}} = 0.87 \pm 0.06$ (to be compared to the measured $\omega^t = 0.90 \pm 0.11$). In both cases, the expected and observed scalings agree within their respective uncertainties. This consistence gives a good confidence in the validity of the employed method.

The evaluation of the fundamental scale factors is performed assuming a 100% purity of either true or fake taus in the validation regions. While for W this holds to a good approximation, for top quarks it is not the case. A cross check is done assuming the top fake tau validation region consists of 50% fake and 50% true taus. In this case, the fake scaling factor reduces to $\omega^t_{\text{fake}} = 0.77 \pm 0.11$, while the expected nominal scale factor would reduces to $\omega^t_{\text{exp}} = 0.75 \pm 0.11$. While this is clearly below the observed value, it is still consistent within the statistical uncertainties. Again, this approach neglects that the events in all regions are actually a mixture of true and fake events. For a fully consistent picture, a full simultaneous fit in all control and validation regions separating all backgrounds in truth and fake tau events would be necessary. The good agreement under different simplifying assumptions proves, however, that the chosen method is indeed working as intended and more detailed studies are left for future iterations of this analysis.

Validation of the H_T shape With the correct normalization determined for the three validation regions, the shape of the H_T distribution can be evaluated to higher values as possible in the nominal control regions. Figure 6.28 shows the respective distributions up to a level where signal events could begin to have an effect. All distributions show an excellent agreement between data and simulation.

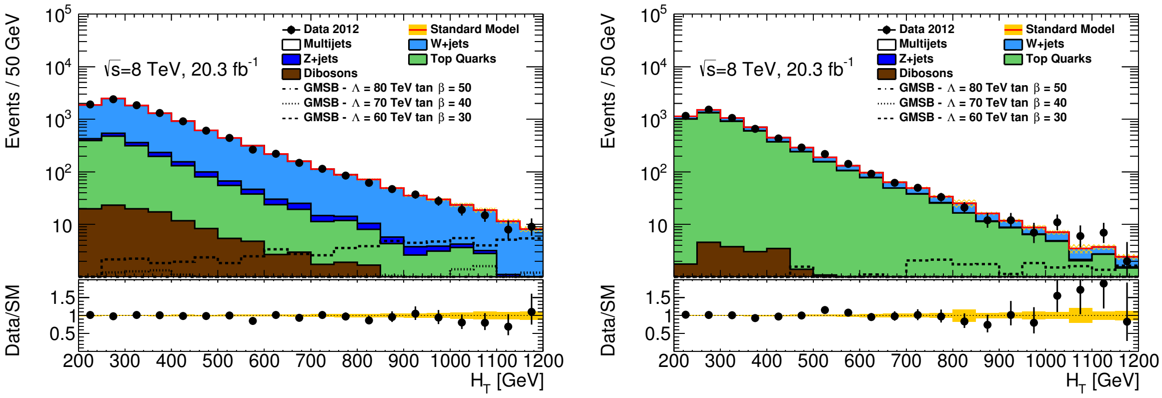

(a) Kinematic VR, W (b) Kinematic VR, top

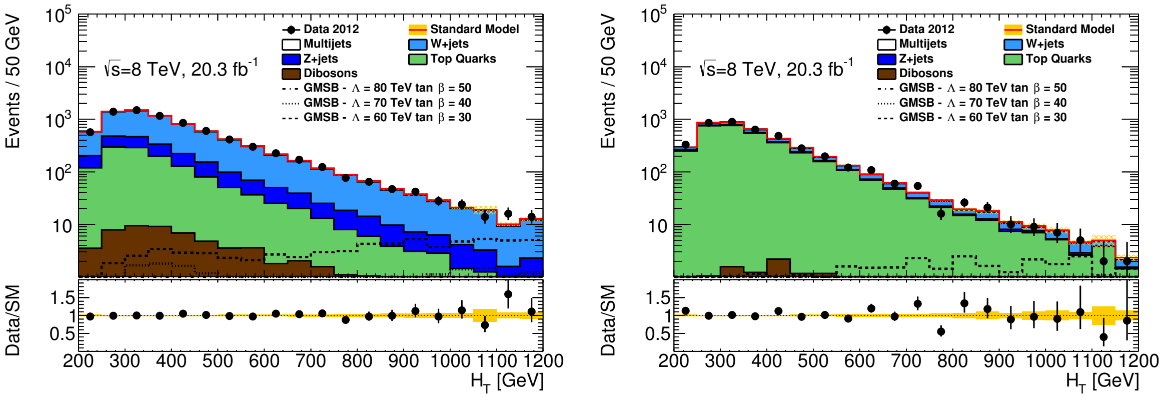

(c) True tau VR, W (d) True tau VR, top

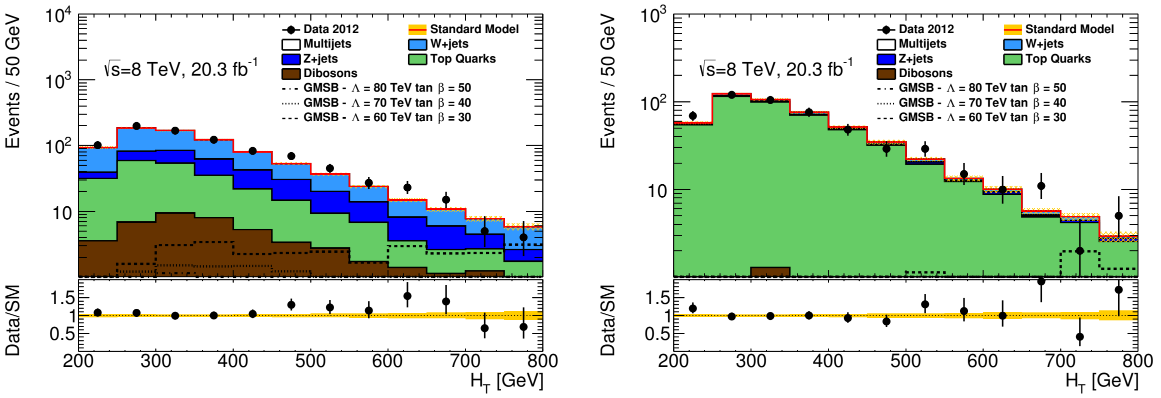

(e) Fake tau VR, W (f) Fake tau VR, top

Figure 6.28: Distributions of the H_T variable in all three validation regions, subdivided for top and W dominated regions. The plots are shown up to a level where possible signal events could begin to play a role. An excellent agreement is achieved. The validation of the $m_{\mathrm{T}}^{\tau_1}+m_{\mathrm{T}}^{\tau_2}$ and N_{jet} distributions is discussed in Section 6.3.2.

6.3.2 Validation with blinded data

While the validation regions presented in Section 6.3.1 offer a conclusive way to check the consistency of the scaling factors and validate the shape of the H_T distribution up to high values, they offer no way to validate the description of the other two main selection variables. For $m_{\mathrm{T}}^{\tau_1} + m_{\mathrm{T}}^{\tau_2}$, two taus are needed, which is not fulfilled in the validation regions. Exchanging a tau for another particle is useful for achieving similar kinematic configurations but it does not help to validate the modeling of $m_{\mathrm{T}}^{\tau_1} + m_{\mathrm{T}}^{\tau_2}$ since the invisible neutrino of the tau decay is missing. For N_{jet}, the validation in the VRs is not conclusive, since additional requirements on the jet multiplicity are made.

For those reasons, $m_{\mathrm{T}}^{\tau_1} + m_{\mathrm{T}}^{\tau_2}$ and N_{jet} is validated with signal region-like cuts. All requirements up to the separation cuts between jets and $\not{E}_T$ are imposed. Additionally, $m_{\mathrm{T}}^{\tau_1} + m_{\mathrm{T}}^{\tau_2} > 150\,\mathrm{GeV}$ is required to suppress Z+jets contributions. The H_T cut is inverted to $H_T < 550\,\mathrm{GeV}$ to avoid any signal influence. The resulting distributions are shown in Figure 6.29. Good agreement between data and simulation is visible over the full range of the distributions.

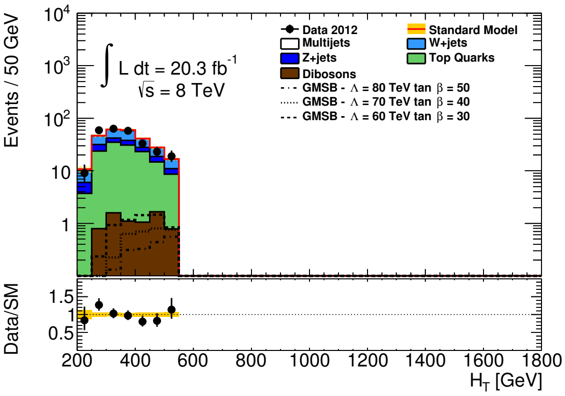

(a) H_T

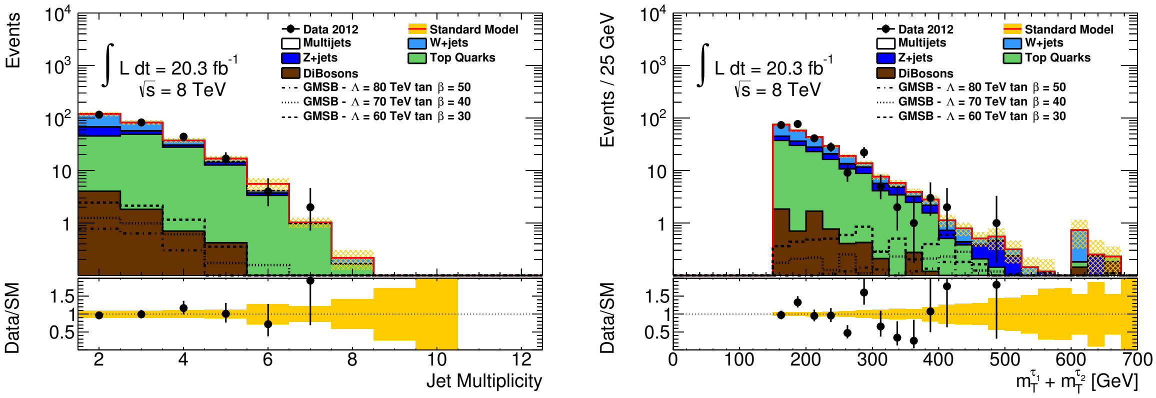

(b) N_{jet}

(c) $m_{\mathrm{T}}^{\tau_1} + m_{\mathrm{T}}^{\tau_2}$

Figure 6.29: Distributions of the main selection variables in a signal-like region. The minimal cut of $m_{\mathrm{T}}^{\tau_1} + m_{\mathrm{T}}^{\tau_2} > 150\,\mathrm{GeV}$ is applied and both data and simulation are blinded above $H_T = 550\,\mathrm{GeV}$ (c.f. figure a)) to avoid any influence by possible signal events. Both the $m_{\mathrm{T}}^{\tau_1} + m_{\mathrm{T}}^{\tau_2}$ and the N_{jet} distribution show an excellent agreement between data and simulation. The validation of the H_T shape is discussed in Section 6.3.1.

6.3.3 Pileup robustness of the background estimate

The pileup, i.e. the influence of spurious collisions and detector activity not associated with the hard interaction, is of paramount importance. This holds even more for searches which focus on the tails of kinematic variables like $\not{E}_T$ or H_T that are by construction sensitive to all activity in the detector. Suitable measures are taken in the object reconstruction to account for pileup and to suppress the effect in the analysis, e.g. by requiring jets to originate from the primary interaction vertex. The agreement between simulation and data is improved by re-weighting the simulated pileup conditions to the observed ones (c.f. Section 4.4.1).

Despite all these efforts, the independence of the employed background estimation techniques of the pileup conditions still has to be evaluated. The most thorough way to achieve this is to prove the independence of the analysis of the pileup conditions. Ideally, this would be done by splitting the analysis for different conditions and comparing the results. A re-computation of scaling factors and background predictions in bins of pileup conditions is however not viable, given the low statistics in the various control regions. Instead, key kinematic distributions are compared in three bins of pileup for low, medium and high activity.

This comparison is performed on the full expected background distributions. It is carried out after requiring all trigger and preselection cuts and the presence of two hadronic taus. Since the comparison is only based on simulation, no measures for signal suppression have to be taken. To obtain a cross check in a less statistic limited region, the same control plots are constructed for the kinematic and true tau validation regions defined in Section 6.3.1 omitting the upper cut on H_T.

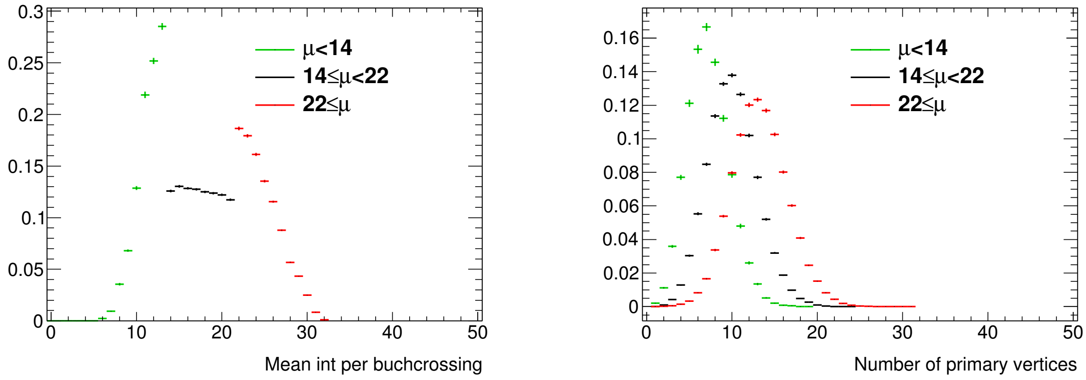

(a) μ (b) N_{vtx}

Figure 6.30: Distributions of the mean interactions per bunchcrossing μ (a) and the number of reconstructed vertices (b) binned in three mean interactions per bunchcrossing bins for the kinematic validation region. The two quantities are clearly correlated yet not identical, but the devised separation yields three configurations of different detector activity.

Figure 6.30 shows the distributions for the mean interactions per bunch crossing and the number of reconstructed primary vertices per event for the three activity bins. All distributions are normalized to unity for each bin. This sanity check proves that the subdivision describes three distinctive activity regions.

Figure 6.31 shows the studied distributions in the nominal control regions. All distributions agree within their statistical uncertainties. Even for the high tails, there is no obvious bias visible.

Figures 6.32 and 6.33 show the same or comparable distributions in the kinematic and true tau validation regions. Again, even with the much higher statistics available here, no bias can be observed.

Since all cuts and estimates rely on the distributions studied here, one can safely conclude that the impact of the pileup on the result of the analysis is negligible. Moreover, to determine the systematic uncertainty on the pileup modeling the distribution is shifted by 5% up and down, which for sure covers all deviations that may still be present.

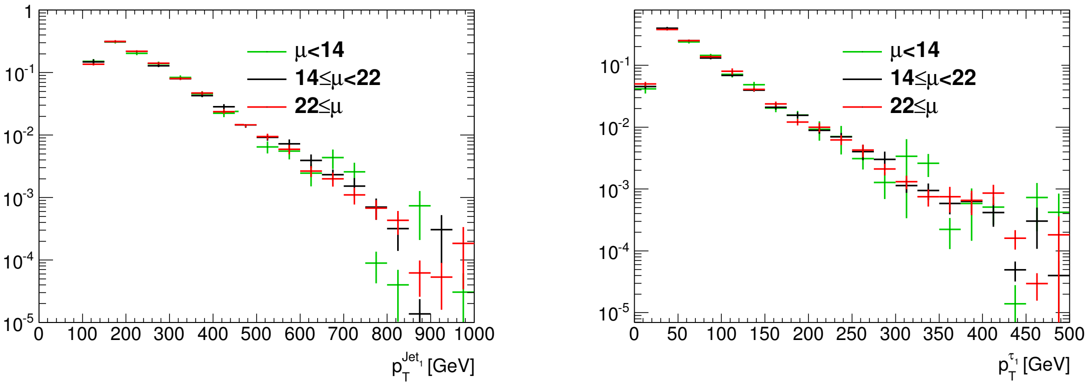

(a) $p_T^{\mathrm{jet}_1}$ (b) $p_T^{\tau_1}$

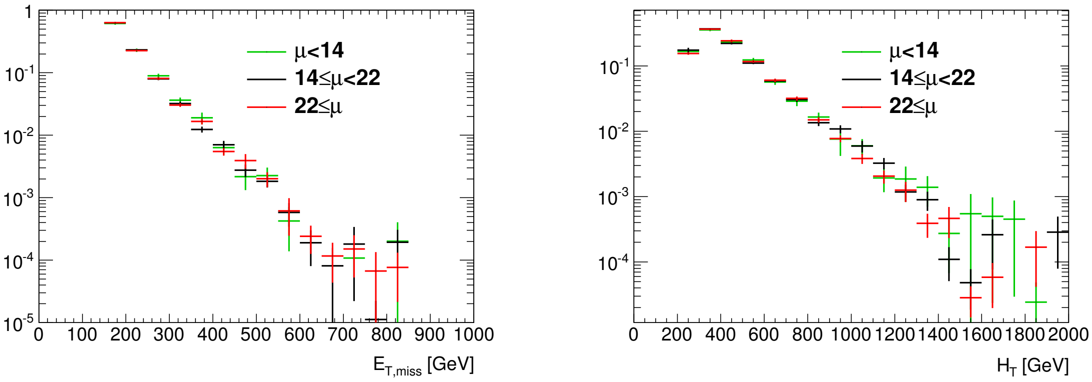

(c) $\not{E}_T$ (d) H_T

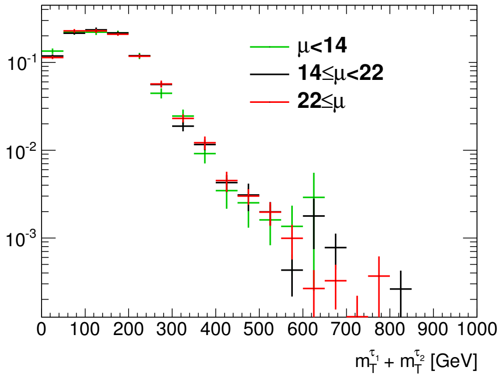

(e) $m_{\mathrm{T}}^{\tau_1} + m_{\mathrm{T}}^{\tau_2}$

Figure 6.31: Distributions of important kinematic variables binned in three mean interactions per bunch crossing bins after requiring two hadronic taus. All distributions agree within their statistical uncertainties.

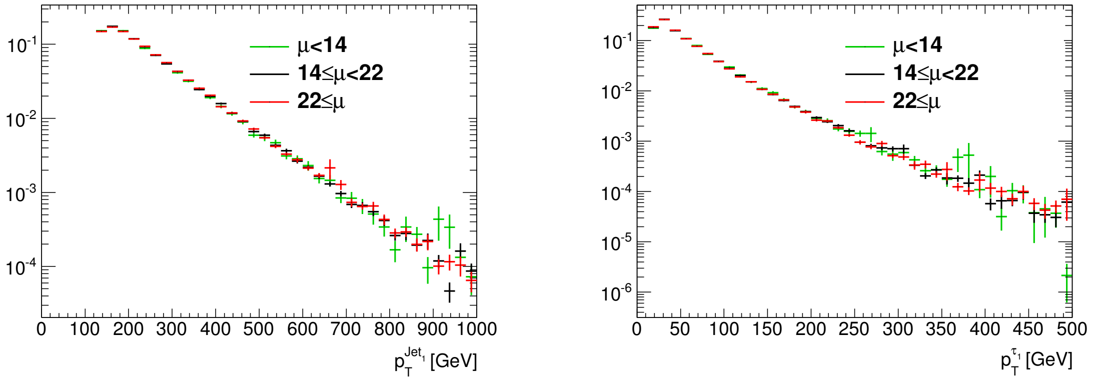

(a) $p_T^{\text{jet}_1}$ (b) $p_T^{\tau_1}$

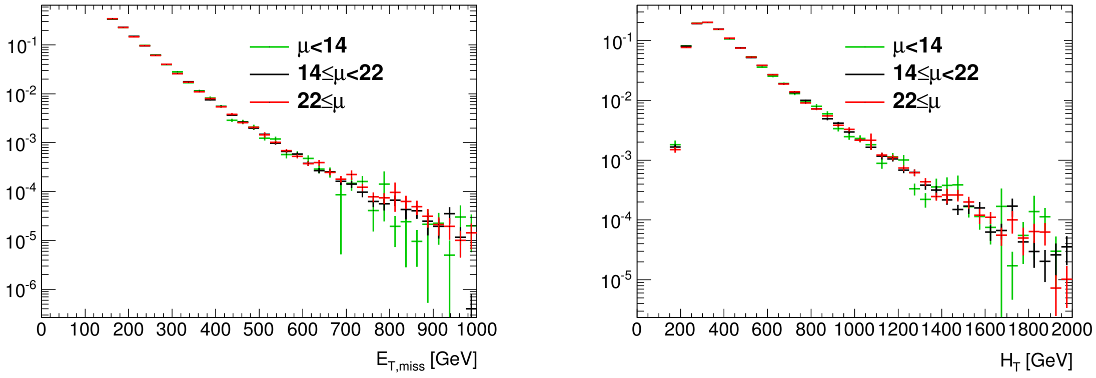

(c) $\not{E}_T$ (d) H_T

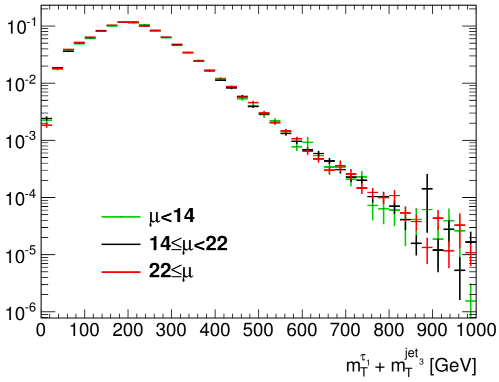

(e) $m_{\mathrm{T}}^{\tau_1} + m_{\mathrm{T}}^{\text{jet}_3}$

Figure 6.32: Distributions of important kinematic variables binned in three mean interactions per bunchcrossing bins for the true-tau validation region. All distributions agree within their statistical uncertainties.

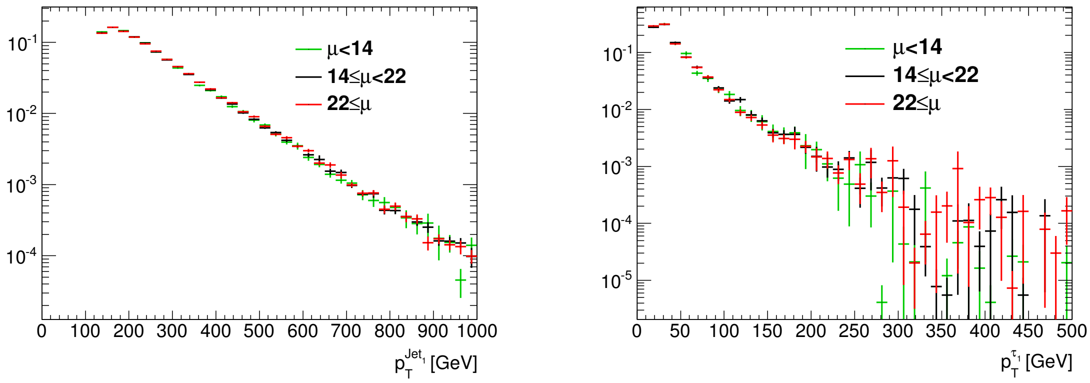

(a) $p_T^{\mathrm{jet}_1}$ (b) $p_T^{\tau_1}$

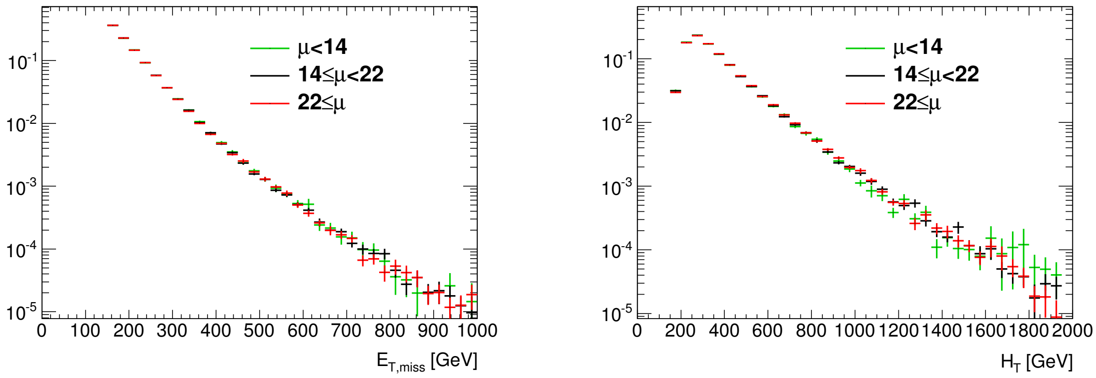

(c) $\not{E}_T$ (d) H_T

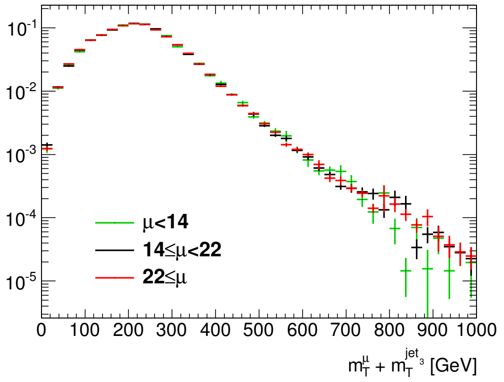

(e) $m_{\mathrm{T}}^{\mu} + m_{\mathrm{T}}^{\mathrm{jet}_3}$

Figure 6.33: Distributions of important kinematic variables binned in three mean interactions per bunchcrossing bins for the kinematic validation region. All distributions agree within their statistical uncertainties.

6.4 Summary

In this chapter, the estimation techniques for the expected backgrounds from SM processes have been presented. Both for multijets and for electroweak backgrounds, methods have been employed to derive or constrain the background estimations from actual data. For all background estimates, a convincing performance and an excellent agreement between data and estimates have been found in different validation studies. The obtained estimates are the basis for the determination of systematic uncertainties and the evaluation of the actual results obtained in the signal regions, presented in the following chapters.

7

Systematic uncertainties

Every measurement is subject to uncertainties. Some are of statistical nature, which means they are limited by the available amount of individual measurements and can be reduced by repeating the experiment. Other errors do not scale with the available statistics. They generally arise from the limited knowledge of the experimental conditions. This kind of uncertainties are referred to as systematic uncertainties.

In this analysis, systematic uncertainties arise predominantly from the estimation of the number of background events in the signal regions, but also from uncertainties in simulating the efficiencies to detect possible signal events. Various sources can lead to a bias in these estimations, such as uncertainty on the luminosity, modeling of the detector response or identification efficiencies for certain objects. Many of these possible sources of uncertainties are studied and quantified, as described in the following.

7.1 Concepts

For the discussion of systematic uncertainties it is more useful to consider the prediction of the number of events in the SR by means of transfer factors as described in Equation 6.4 rather than by scaling simulation to match the data. As demonstrated in Section 6.2.1, these two approaches are equivalent. In the transfer factor interpretation, however, all dependencies on the simulation are absorbed into the transfer factor which is then applied to data, while the scale factors have a mixed dependency on data and MC. Since systematic uncertainties are evaluated by varying the simulation, it comes natural to consider the transfer factors.

The approach of transferring an observed number of events in a control region into the signal region using a transfer factor relies on the assumption that the shape of the observable used to separate the regions is well reproduced in Monte Carlo. This assumption is tested by varying detector parameters that could alter this shape and by studying directly how it depends on the fine tuning of parameters in the event generation process.

Every simulated event is modified according to the studied systematic uncertainty (e.g. rescaling jet energies to study the influence of a possible bias in the energy measurement of jets). The analysis is re-run on all signal and background samples under the same systematic variation. The full background estimation for the background with real taus is repeated on the modified sample yielding a new total background estimate that might differ from the nominal value. To obtain relative uncertainties, the relative difference of the yields on the modified samples to the yields in the nominal samples is computed. The total uncertainty comprising all systematic uncertainties is then computed as the quadratic sum of all individual uncertainties. In cases where uncertainties are provided as up and down variation separately, those are symmetrized, i.e. the average of the absolute values of the two is used.

Due to this approach, the influence of systematic variations on different background contributions can weaken or compensate each other. One example of weakening is the jet energy scale uncertainty in the Inclusive SR (c.f. “JES up” in Table F.2 in Appendix F). On the Z+jets sample this variation leads to a 23% increase of the expected number of events in the SR. Since Z+jets contributes only about 20% of the total and the effect of increasing the jet energy scale on the other backgrounds is only small, the effect on the total background expectation is only about 8%. An example of compensation effects can e.g. be observed for the Z generator uncertainties. Exchanging the generator for Z leads to a large decrease of the expected yield. However Z and W are strongly anti-correlated by the background estimation technique, hence the W expectation increases. These two effects partially cancel so the net effect on the total background expectation is much larger than the effect on the individual channels.

Since these cancellations are only effective when taking all background channels into account, the total number for the systematic uncertainty is much larger for the individual channel than for the combined total background yield.

Many of the predicted cross sections for the Standard Model backgrounds have very large theoretical uncertainties in the extreme kinematic region studied by this analysis. Their influence on the analysis is removed by measuring the background expectation on the data as described in the various chapters on background estimates in this note. Instead, the statistical error of the data sample in the control region and secondary effects such as the uncertainty associated to the extrapolation from a control region into the signal region enter the analysis.

7.2 Uncertainties from machine and detector performance

All uncertainties here relate to uncertainties on the detector response or the reconstruction performance for a certain object. These are derived and quantified by the various performance groups that also study and provide the reconstruction algorithms. For reference, the software packages used for the individual sources of uncertainties and their versions are listed in Table F.1 in Appendix F.1.

Jet energy scale The relation between a calorimeter signal and the corresponding jet energy is not known precisely. This uncertainty on the jet energy scale (JES) is determined in MC studies, where nominal results are compared to samples with varied hadronic shower and physics models, alternative detector configurations and by a data vs. MC comparison of the jet response as function of η. Additional corrections are taken into account for close-by jets in the region $|\eta| < 2.9$ where a sufficiently good double jet resolution is provided. All techniques are documented in [221], while the actual size of the uncertainties has been updated to match the data taking performance in the 2012 8 TeV measurements.

Changes in the jet energies are propagated to $\not{E}_T$ by the following relation:

$$E_{x,y}^{\text{miss,new}} = E_{x,y}^{\text{miss,old}} + \sum_{\text{jets}} p_{x,y}^{\text{old}} - \sum_{\text{jets}} p_{x,y}^{\text{new}} \,. \tag{7.1}$$

These variations are applied before the jet-tau overlap removal step, i.e. also to all objects that are later identified as taus. This is important since taus are treated as jets for the computation of the missing transverse momentum.

Furthermore, jet energy scale and tau energy scale are treated as uncorrelated, because the methods and measurement employed to derive and constrain the energy scale calibrations are very different and no significant overlap is expected.

Jet energy resolution The jet energy resolution (JER) can only be simulated with finite precision by the GEANT4 detector simulation. The agreement between the jet energy resolution in data and simulation has been studied using the spread of the p_T imbalance in di-jet events and with different in-situ techniques. Methods are described in [221], while again the individual numbers have been updated. Deviations have been found to be in the order of 10% depending on p_T and η of the jet. All jets in an event are smeared uncorrelated and randomly with a Gaussian of mean one and a standard deviation according to the jet resolution measurements.

The modified jet energies are propagated to the $\not{E}_T$ calculation following Equation 7.1. These corrections are applied before the jet-tau overlap removal, so these uncertainties are applied to the tau candidates as well as far as the $\not{E}_T$ measurement is considered.

Tau energy scale Systematic uncertainties for the tau energy scale (TES) are determined in Monte Carlo truth studies varying parameters affecting the tau energy reconstruction and evaluating the influence on the energy scale. Largest uncertainties are found to come from the hadronic shower model and the data-simulation difference. These results are documented in [160]. A few examples of tau performance studies are also documented in Section 3.3.4. The uncertainty depends on p_T, η and the number of associated tracks of the tau candidate and is ranging from 2% up to 4%.

The systematic influence of the tau energy scale is evaluated in the same way as described for the jet energy scale. Scaling of the taus is not propagated to the missing transverse energy since the definition of $\not{E}_T$ does not include a tau term; since all selected taus are seeded by jets, the influence of varying energy scales is already covered in the jet energy scale studies.

Tau identification Systematic uncertainties on the tau identification (Tau ID) efficiency for the 2012 dataset, in general, depend on the tau identification algorithm, the kinematics of the τ sample, and the number of associated tracks. Several studies are performed using tag and probe methods, one of them using $Z \rightarrow \tau\tau$ events while the other one uses $W \rightarrow \tau\nu$ events. They are documented in [160]; a short overview is also compiled in Section 3.3.4. In a similar way, also the uncertainty on the electron-tau separation is derived.

To evaluate the resulting systematic effects on the analysis, the MC samples are re-weighted. The total event weight is increased or decreased by the measured uncertainty for each selected tau object. When performing this efficiency re-weighting, only τ candidates are considered that can be matched to simulated real taus or electrons, respectively. The modeling of fake taus from jets is addressed by the various background estimation techniques.

In general, the effect of mis-modeled tau identification in MC is largely compensated by the applied background scaling methods. The uncertainties described above are only effective in the background contributions estimated from Monte Carlo only. In data-driven estimates they cancel to a large extent.

Missing transverse energy The missing transverse energy is affected by all kinds of fluctuations in the energy measurement of objects in the ATLAS detector. Variations of the jet and tau energies are hence propagated to the $\not{E}_T$ calculation as described in the respective sections. Those contributions are the main uncertainties on the $\not{E}_T$ measurement.

Additionally, the influence of uncertainties on “soft terms” (ST), related to objects below the reconstruction thresholds and energy depositions in the calorimeter which cannot be related to physical objects, is quantified. For those terms, a scale uncertainty is evaluated varying the individual magnitudes. Also a resolution uncertainty is included by applying a smearing depending on the total deposited energy in the calorimeter.

Pileup influence The influence depends on the model assumed for the determination of the pileup conditions in the data. To quantify this effect, the analysis is repeated with changing the nominal value for the average interactions per bunch crossing in data by 10% and the relative deviations from the nominal analysis has been taken as the influence of systematic uncertainties related to the pileup.

The analysis additionally requires a JVF cut for the definition of signal jets. This cut is source of an individual uncertainty which directly affects the ability to separate activity from pileup events from activity from hard interactions. To evaluate this uncertainty, the nominal cut value for the JVF cut is varied to emulate the uncertainty on the cut definition.

B-tag efficiencies Since in the analysis b-tagging is used to separate top and W contributions in the control regions, the uncertainties on the b quark identification techniques has to be evaluated. For the b-tagging, uncertainties based on the efficiencies for tagging jets from c quarks and from b quarks as well as the mis-tag rate are studied. The three sources on uncertainties are treated as statistically independent and have all been varied both up and down.

Trigger efficiencies For the Jet + $\not{E}_T$ trigger used, no special treatment of trigger systematic uncertainties is necessary. As described in Section 5, trigger plateau cuts on both the leading jet p_T and $\not{E}_T$ ensure a 100% efficiency of the trigger in data in selected events. In Monte Carlo, no trigger requirement is made but the plateau cuts are applied directly to ensure direct comparability between data and MC.

Luminosity Uncertainties on the luminosity measurement are neglected for background simulation, but is included for signal samples. The Dibosons contribution is the only background estimated directly from Monte Carlo and is thus affected by luminosity uncertainties. Since other systematic uncertainties on this channel are much larger than the uncertainty on the luminosity, this part is neglected.

7.3 Theory uncertainties

Besides uncertainties on the measurements itself and the modeling of detector effects in the simulation, the process of simulating the physics can be subject to uncertainties. Indeed, many choices in the generation process are at least partially arbitrary. While the effect of varying these choices is generally small, it might lead to larger effects in certain kinematic configurations.

Other inputs like the values of the strong coupling α_s or the parton density function of the proton do have an intrinsic uncertainty themselves. For the PDFs moreover, various competing fits from different groups are available.

Finally, details of the later steps in the simulation chain can influence the prediction of the backgrounds as well. Typical examples are the choice of the showering algorithm or the interface between event generation and showering.

The evaluation of this kind of uncertainties is described in the following, separately for signal and background simulation.

7.3.1 Uncertainties on the background

A consistent way to evaluate the influence of the sources of uncertainties mentioned above would be to change one parameter at a time, re-simulate the full sample and then evaluate the effect on the background estimation. While in principle this is possible and has been done for numerous other analysis, there are some drawbacks on this approach for this work. Many of the available comparison samples focus on one flavor of light leptons assuming the difference between electron and muon reconstruction is negligible compared to the differences in the theory settings. Often those samples are only available without the detector simulation and reconstruction applied. One of the most important sources of uncertainties in this analysis is the modeling of taus and especially of objects that fake taus. For this reason these samples are not useful in this context.

Instead of having many millions of simulation events being produced only for the purpose of assessing the uncertainty for one analysis, one can instead compare existing, different simulations of the same process. Ideally, the comparison sample should be as different from the nominal sample as possible. This approach is also motivated by the differences between different generators that have been found when identifying the optimal background sample for $t\bar{t}$ (c.f. Appendix D.1).

The three dominant backgrounds (W, $t\bar{t}$ and Z) have thus been recomputed using different generators. For $t\bar{t}$, POWHEG interfaced to PYTHIA is compared to ALPGEN interfaced to HERWIG (c.f. Table A.2). Indeed, this comparison between the nominal and the alternative sample comprises many of the possible features discussed above:

- Two different generators (POWHEG vs. ALPGEN) with very different approaches (NLO vs. sliced final state parton multiplicities)
- Two different shower algorithms (PYTHIA vs. HERWIG)
- Two different detector simulations (AFII vs. GEANT4)

Similarly for W+jets, SHERPA is compared to ALPGEN interfaced to HERWIG (c.f. Table A.7). Here the integrated approach of SHERPA faces the sliced generation approach of ALPGEN that is chosen with focus on higher additional jet multiplicities. Using samples that are filtered at generator level to exhibit hard jets and high $\not{E}_T$ the available MC statistics in the studied kinematic range can be increased. For Z, SHERPA is compared to ALPGEN interfaced to PYTHIA for the charged lepton decays of the Z (c.f. Table A.9) and ALPGEN interfaced to HERWIG for the neutrino decays (c.f. Table A.11).

For Dibosons, which is taken directly from simulation without any data-driven corrections, SHERPA is compared to POWHEG +PYTHIA 8 (c.f. Table A.13). In cases where no Dibosons background was observed with the nominal but with the alternative sample, this is accounted for in the total uncertainty (10% uncertainty on the Dibosons generator in the nGM SR). For the limit setting, a conservative approach is taken for the channels where the nominal generator predicts no Dibosons content in the signal region: If any of the studied systematic variations yields some Dibosons contribution to a specific SR, the highest expectation under any systematic is taken as central value with a 100% uncertainty.

For all comparisons, the difference between the estimated background of one type between the two generators compared is evaluated. Due to the correlation between samples through the background estimation procedure, the estimates for other backgrounds change as well by a small amount. The result is a one-sided variation in the total background prediction, which is added in quadrature to a second contribution arising from the limited statistical precision of the comparison generator.

This second contribution has to be evaluated carefully. The total statistical uncertainty of the background estimate includes uncertainties in the control regions on all MC samples (not only the one studied) and the data. This uncertainty, however, is already included in the uncertainty on the central estimate. Hence taking the full statistical uncertainty would yield significant double counting. For this reason, only the statistical uncertainty on the uncorrected simulation prediction of the channel in study in the respective signal region is considered as additional statistic factor in the generator comparison.

The relevant variables that are used in defining the signal and control regions and which are extrapolated over are H_T, $m_{\mathrm{T}}^{\tau_1}+m_{\mathrm{T}}^{\tau_2}$ and N_{jet}. Figure 7.1 shows for example the different shapes for the nominal and the comparison generator in the H_T variable. For this comparison, all samples are normalized in the respective control regions. For H_T this is roughly equivalent to the region below 550 GeV, however, the different cuts on $m_{\mathrm{T}}^{\tau_1}+m_{\mathrm{T}}^{\tau_2}$ also do have an effect which is not visible in this figure. While the general trend is quite similar in all distributions, they differ especially in the high tails. This is most striking for Z+jets where ALPGEN virtually runs out of statistics for values above $H_T > 1400\,\mathrm{GeV}$, while SHERPA continues way beyond. More comparison plots for all three variables and all backgrounds are compiled in Appendix F.2.

Additional deviations that are not covered in the generator comparisons could arise e.g. from the simulation of initial and final state radiation (ISR/FSR). To evaluate this, two samples produced with ACER MC are available which are identical except for the simulated phase space for ISR/FSR. Figure 7.2 shows the main kinematic distributions for the phase space comparison and for the nominal $t\bar{t}$ sample after requiring two taus. The samples are again normalized in the top control region.

Clearly in the signal region of high H_T, the tails in the systematic samples run out of statistics. This makes it hard to evaluate the effect at all. Moreover, in the region which is sufficiently populated, the difference between the two phase space configurations is smaller than the difference between the two $t\bar{t}$ samples. Conclusively, this uncertainty has been neglected.

In the same way, the effect of exchanging the showering algorithm is studied by comparing the same set of POWHEG generated events, once with PYTHIA showering and once with HERWIG showering. Respective plots are also collected in Appendix F.2. As expected the difference between the two showering algorithms is much smaller than the total difference between ALPGEN and POWHEG.

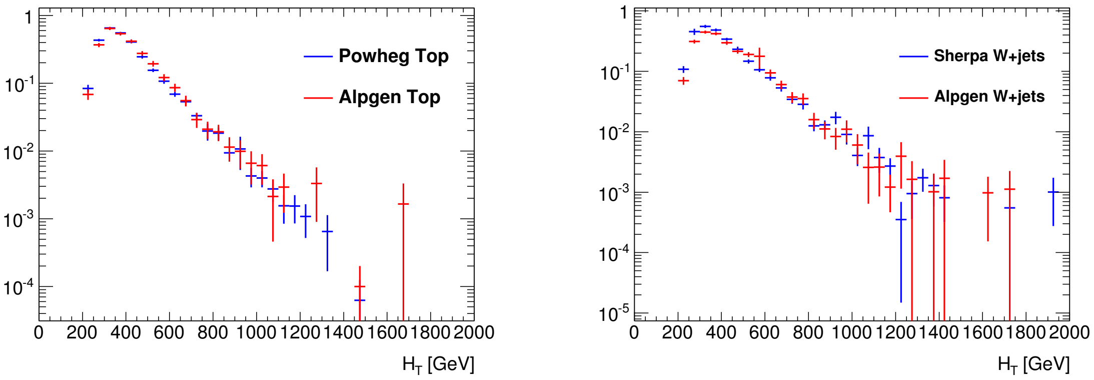

(a) $t\bar{t}$

(b) W+jets

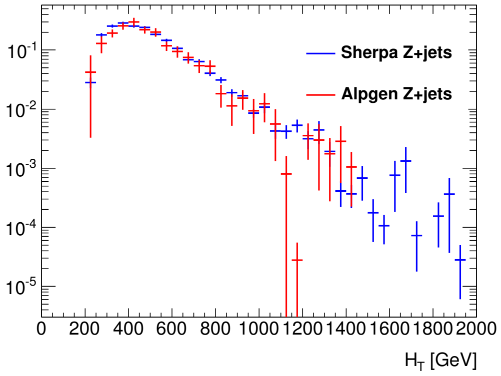

(c) Z+jets

Figure 7.1: H_T-shape comparison for the three main backgrounds. All plots are made after requiring all objects selected in the analysis. All samples are normalized in the respective control region matching the samples compared.

7.3.2 Uncertainties on the predicted signal

In contrast to the Standard Model backgrounds, for the SUSY signals there is no external constraint on the total production cross section available. Hence the total cross section uncertainty is of great importance. The calculation of the SUSY cross section depends on the process and is performed at NLO accuracy for electroweak and mixed production and at NLO+NLL accuracy for strong production (c.f. Section 4.3). In the computation, uncertainties due to the choices of parameters in the generation process, the PDF uncertainties and the uncertainties on the strong coupling constant are evaluated by re-computing the cross section under different parameters. The resulting cross section values form an envelope where the median is taken as nominal value and the upper and lower extremes are symmetrized to yield one uncertainty as described in [209].

The cross section uncertainty is not combined with other uncertainties, but treated as separate source. This results in three exclusion lines presented in the final plots, one for the nominal value of the cross section and one for the $\pm 1\sigma$ values. This allows to disentangle the effect of systematic uncertainties that are unavoidable from external uncertainties that come with the definition of the signal models.

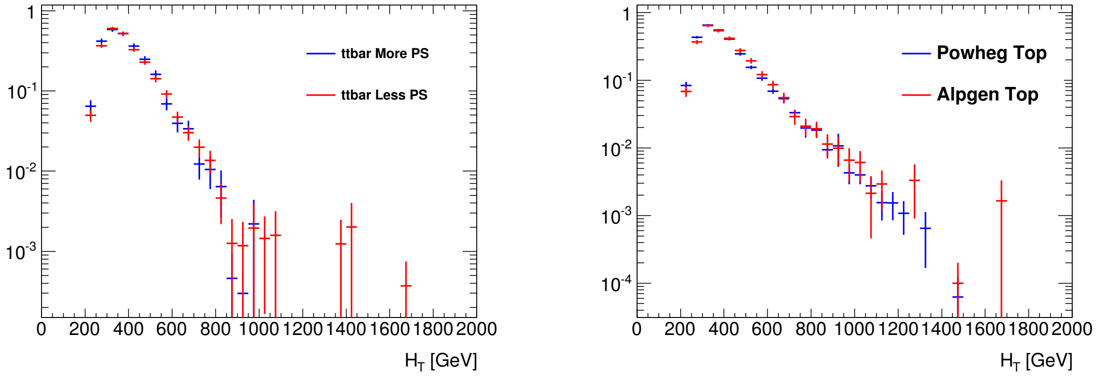

(a) H_T Phase-space

(b) H_T Generator

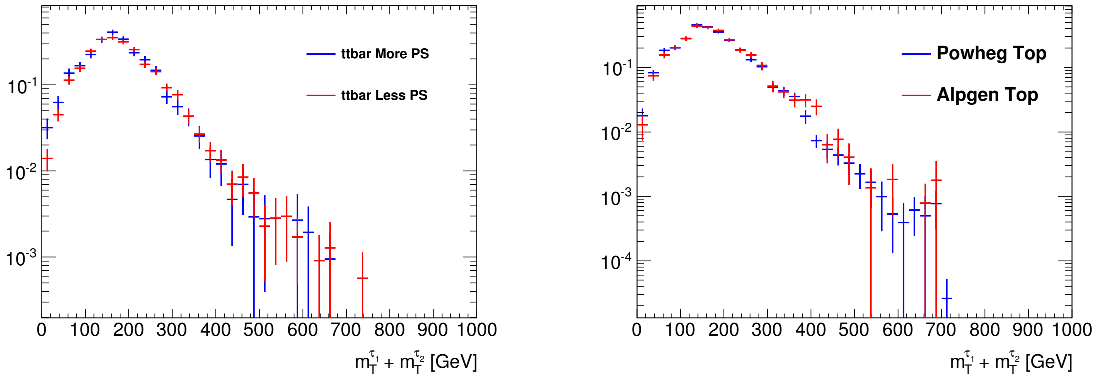

(c) $m_{\mathrm{T}}^{\tau_1} + m_{\mathrm{T}}^{\tau_2}$ Phase-space

(d) $m_{\mathrm{T}}^{\tau_1} + m_{\mathrm{T}}^{\tau_2}$ Generator

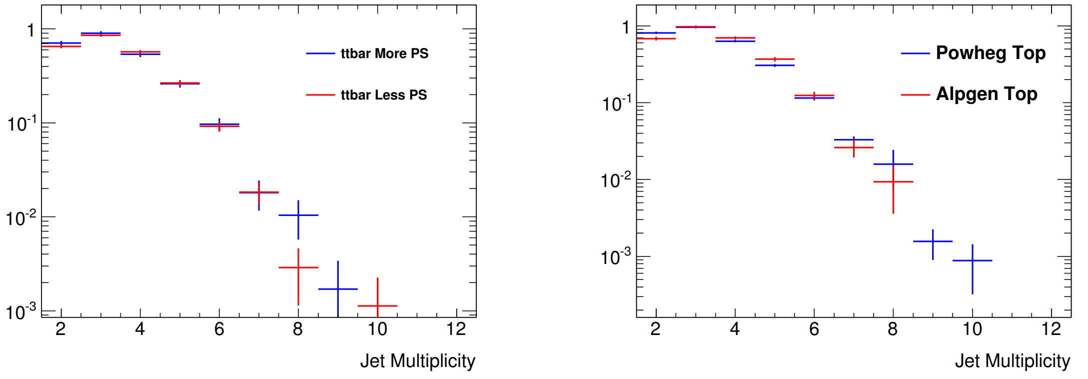

(e) N_{jet} Phase-space

(f) N_{jet} Generator

Figure 7.2: Comparison between the phase-space uncertainty and the overall generator uncertainty for the main kinematic variables. All plots are made after requiring all objects selected in the analysis. All samples are normalized in the respective control region matching the samples compared. Note that the shapes for the phase-space comparison cannot be compared to the shapes of the overall comparison since the underlying generators are different. In general a much larger difference between the different generators than between the different phase-space configurations is observed.

7.4 Uncertainties on external corrections

Both the vector boson and the top backgrounds are re-weighted with scalings that have been derived outside this analysis. For both backgrounds, the re-weighting is applied to remedy trends and discrepancies observed in certain control regions. In that sense it is not a “blind” modification of the background simulation but a well defined and specific correction.

Nevertheless, in case of the $t\bar{t}$ sample the effect of the weighting on the signal region estimates and the systematic uncertainties has been studied in detail. It is found that by applying the weights both the signal region estimates and the absolute difference between nominal and comparison generator (i.e. generator systematic) decrease. Especially the latter implies a higher level of consistency being achieved by applying the weights. Moreover, it is verified that the difference between re-weighted and original MC is covered by the generator uncertainty on the original MC.

For all those reasons it is justified to apply the weighting without assigning an extra uncertainty to the procedure but refrain to the (anyhow conservative) uncertainties in place already.

7.5 Uncertainties on the data-driven estimate of the multijets background

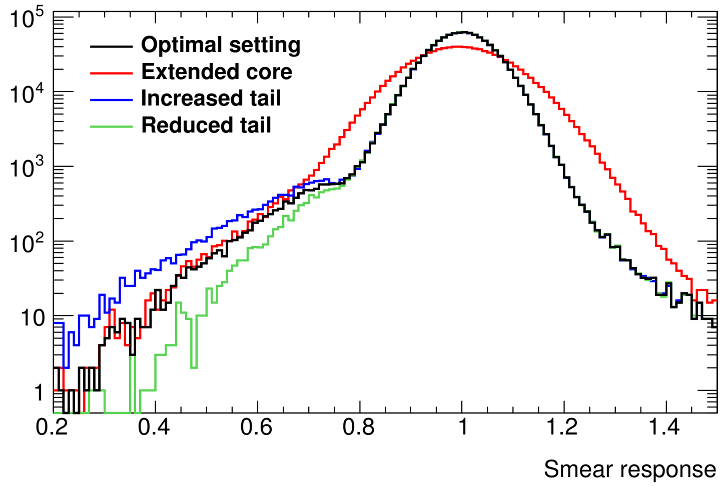

Figure 7.3: Response shapes for the jet smearing in the multijets estimate. Shown are the response shape to yield optimal results in dedicated studies as well as modified response shapes which are employed for deriving systematic uncertainties on the multijets estimate.

Since the multijets background is not estimated using any simulation, the aforementioned detector and generator uncertainties do not apply here. There are however uncertainties on the JetSmearing method used to estimate the uncertainties. As described in Section 6.1, the detector response of a jet hitting the calorimeters is modeled and parametrized. This response is then constraint in dedicated measurements of the jet response using di-jet and so called “Mercedes” (tri-jet) events. The general shape of the response is a gaussian core with tails to low energies.

For both the tail contributions and the width of the gaussian core, the measured constraints still leave quite a large uncertainty. To evaluate systematic uncertainties on the multijets estimate, the tail contributions are varied up and down and the width of the core is increased. Figure 7.3 gives response shapes for the leading jet in one example seed event for the optimal smearing configuration and the three systematic configurations. The difference is clearly visible.

To estimate the influence of the different response shapes, the multijets background is re-computed using the different smearing settings and is compared to the optimal settings.

7.6 Resulting uncertainties

Tables F.2 to F.6 in Appendix F.3 give a full breakdown of all systematic uncertainties for all backgrounds and all signal regions. For nearly all signal regions the generator uncertainties dominate the total uncertainty. In fact, except for the bRPV$m_{1/2}$ region, the generator uncertainties amount to at least twice the value as the next higher uncertainty.

Among the detector systematic uncertainties, the jet and tau energy related ones dominate. For the bRPV$m_{1/2}$ selection they are nearly as large as the generator uncertainties. In contrast to that, tau identification related uncertainties are negligible due to the background estimation technique which is specifically designed to account for deficits in the description of taus in MC. Also the pileup related uncertainties are very small in accordance with what is found in the specific pileup studies.

In all signal regions, the total uncertainty is dominated by the systematic uncertainty with the statistical uncertainty being considerably smaller. Hereby the statistical uncertainty is not only the uncertainty arising from the limited amount of Monte Carlo events available in the signal region, but contains also the uncertainties due to limited statistics of both data and Monte Carlo in the control regions. In this case, the statistical uncertainty of the total expected background is driven by the uncertainty on the Monte Carlo statistics in the signal regions and not on the scaling factors.

For the signal simulation, all sources of “detector systematic uncertainties” (i.e. those that affect the object and event reconstruction) are evaluated as well, besides the cross uncertainties as described in Section 7.6.

Figure F.5 in Appendix F.4 shows statistical, systematic and cross section uncertainties for the GMSB and nGM signal region in the respective grid. Figure F.6 holds the same plots for the bRPV signal regions. All detector uncertainties are summed up for this plot.

While for GMSB systematic and statistical uncertainties are roughly equal, the nGM grid is clearly dominated by systematic uncertainties. This grid also shows a smooth behavior of the cross section uncertainty. This is due to the fact that in the nGM grid only one production process is evaluated, hence the uncertainty is independent of the actual events in the signal region. For GMSB on the other hand, both the cross section and its uncertainty is evaluated per production process. Hence the observed total uncertainty in the signal region depends on the admixture of different production processes that enter the signal region for one given signal point. Note that the theory uncertainty does not enter the limit calculation but is treated as an extra and completely uncorrelated uncertainty on the actual limit position in the grid. The same behavior is seen in the bRPV grid. Moreover the larger statistical uncertainty in the $m_{1/2}$ signal region due to the tighter cuts is clearly visible.

8

Results

In the previous chapters, a selection has been established, background simulation has been validated and corrected in control regions and uncertainties have been computed. In this chapter, finally, the focus lies on the signal region and the observed data.

The background expectations with all their uncertainties are compiled in Section 8.1 and are compared to the actual observations. In Section 8.2, the predictions of the various signal models together with their uncertainties is compiled. Finally, in Section 8.3, all predictions and observations are combined into limits and exclusions, using statistical interpretations.

8.1 Background predictions and observations in the signal regions

Table 8.1 gives the cut flow of all individual background contributions for all cut steps after the trigger plateau requirement up to the various signal regions. The expected number of electroweak background events comprising W, t and Z is scaled to data in dedicated control regions (c.f. Section 6.2). Dibosons production is estimated purely from Monte Carlo simulations and multijets events are estimated using the Jet Smearing method (c.f. Section 6.1). The numbers for the electroweak backgrounds include data-driven scalings appropriate to the given cut. Table 8.2 compares the sum of all expected backgrounds to the actual data observed after each cut. To reduce data to a reasonable amount, minimal kinematic selections are applied to all data and simulation a priori. Unfortunately, it is not possible to use identical data reduction schemes in data and simulation. In the present event selection, only after the first tau requirement those differences are expected to be small. Indeed, starting with the $N_\tau \geq 2$ requirement a very nice agreement between data and background expectation is observed.

For the Inclusive signal region, a total background of $2.88 \pm 0.34^{\text{stat}} \pm 0.21^{\text{sf}} \pm 0.67^{\text{syst}} = 2.88 \pm 0.77$ events is expected. For the GMSB SR, the total background is estimated to be $0.28 \pm 0.08^{\text{stat}} \pm 0.04^{\text{sf}} \pm 0.22^{\text{syst}} = 0.28 \pm 0.24$ events. For bRPV$m_{1/2}$, the estimate is $1.09 \pm 0.17^{\text{stat}} \pm 0.08^{\text{sf}} \pm 0.39^{\text{syst}} = 1.09 \pm 0.44$ events. A background of $3.14 \pm 0.39^{\text{stat}} \pm 0.30^{\text{sf}} \pm 0.93^{\text{syst}} = 3.14 \pm 1.06$ events is expected for

	Expected events by background contribution				
	Dibosons	Multijets	Top	W+jets	Z+jets
Trigger Cuts	2394 ± 13	$(1.350 \pm 0.009) \times 10^5$	68435 ± 1415	$3.39 \times 10^5 \pm 6.99 \times 10^3$	62355 ± 116
$p_T^{jet2} > 30\,\text{GeV}$	1477 ± 10	$1.34 \times 10^5 \pm 9.13 \times 10^2$	64615 ± 1336	$1.83 \times 10^5 \pm 3.78 \times 10^3$	34189 ± 71
Lepton Veto	375 ± 5	$1.34 \times 10^5 \pm 9.13 \times 10^2$	28172 ± 585	88597 ± 1833	31058 ± 67
$N_\tau \geq 1$	140 ± 3	1740 ± 72	8341 ± 174	21340 ± 500	3800 ± 22
$N_\tau \geq 2$	17 ± 1	10 ± 2	287 ± 35	231 ± 45	319 ± 36
$\Delta\Phi(\text{jet}_{1/2}, \not{p}_T) > 0.3$	16 ± 1	2.69 ± 1.49	266 ± 33	221 ± 43	304 ± 34
$H_T > 1000\,\text{GeV}$	0.78 ± 0.27	0.14 ± 0.06	1.09 ± 0.22	2.12 ± 0.55	5.98 ± 0.91
$m_{\text{T}}^{\tau_1} + m_{\text{T}}^{\tau_2} > 150\,\text{GeV}$	$0.39 \pm 0.19 \pm 0.30$	$0.12 \pm 0.05 \pm 0.06$	$0.57 \pm 0.14 \pm 0.32$	$1.26 \pm 0.33 \pm 0.54$	$0.54 \pm 0.15 \pm 0.64$
$H_T > 1000\,\text{GeV}$	0.78 ± 0.27	0.14 ± 0.06	1.09 ± 0.22	2.12 ± 0.55	5.98 ± 0.91
$N_{\text{jet}} \geq 4$	0	0.13 ± 0.06	0.64 ± 0.16	0.73 ± 0.21	1.56 ± 0.32
$m_{\text{T}}^{\tau_1} + m_{\text{T}}^{\tau_2} > 150\,\text{GeV}$	0 ± 0	$0.11 \pm 0.05 \pm 0.04$	$0.32 \pm 0.10 \pm 0.19$	$0.48 \pm 0.15 \pm 0.31$	$0.18 \pm 0.07 \pm 0.21$
$m_{\text{T}}^{\tau_1} + m_{\text{T}}^{\tau_2} > 250\,\text{GeV}$	0 ± 0	$0.062 \pm 0.045 \pm 0.021$	$0.050 \pm 0.031 \pm 0.053$	$0.14 \pm 0.07 \pm 0.18$	$0.037 \pm 0.020 \pm 0.042$
$H_T > 600\,\text{GeV}$	3.49 ± 0.56	0.84 ± 0.26	21 ± 3	22 ± 4	61 ± 7
$N_{\text{jet}} \geq 4$	0.46 ± 0.17	0.29 ± 0.07	12 ± 2	6.26 ± 1.36	14 ± 2
$m_{\text{T}}^{\tau_1} + m_{\text{T}}^{\tau_2} > 200\,\text{GeV}$	$0.20 \pm 0.13 \pm 0.14$	$0.14 \pm 0.06 \pm 0.20$	$3.18 \pm 0.75 \pm 1.10$	$1.87 \pm 0.67 \pm 1.05$	$0.82 \pm 0.31 \pm 1.18$
$m_{\text{T}}^{\tau_1} + m_{\text{T}}^{\tau_2} > 250\,\text{GeV}$	0 ± 0	$0.066 \pm 0.045 \pm 0.032$	$1.65 \pm 0.38 \pm 0.65$	$0.78 \pm 0.31 \pm 0.47$	$0.65 \pm 0.28 \pm 0.94$

Table 8.1: Cut-flow table for the individual background components expected to contribute to the signal regions. For all cuts up to the one tau cut only the kinematic scale factors are applied. For the one tau cut the true tau scale factors are applied. For all following cuts the full scaling is applied. Uncertainties quoted gives the uncertainty due to both the limited available mc statistics at the respective cut and the uncertainty due to the scaling where applied. For the final cut additionally the systematic uncertainty for all channels are given.

		Data	Background estimate
	Trigger Cuts	1.65×10^6	$6.07\times10^5\pm7.19\times10^3$
	$p_T^{jet2} > 30\,\text{GeV}$	6.84×10^5	$4.17\times10^5\pm4.11\times10^3$
	Lepton Veto	5.34×10^5	$2.82\times10^5\pm2.13\times10^3$
	$N_\tau \geq 1$	37504	35362 ± 535
	$N_\tau \geq 2$	859	865 ± 68
	$\Delta\Phi(\text{jet}_{1/2}, \not{p}_T) > 0.3$	804	810 ± 64
	$H_T > 1\,000\,\text{GeV}$	7	10 ± 1
Inclusive SR	$m_\text{T}^{\tau_1}+m_\text{T}^{\tau_2} > 150\,\text{GeV}$	3	$2.88\pm0.40\pm0.67$
	$H_T > 1\,000\,\text{GeV}$	7	10 ± 1
	$N_\text{jet} \geq 4$	4	3.06 ± 0.42
bRPV$m_{1/2}$ SR	$m_\text{T}^{\tau_1}+m_\text{T}^{\tau_2} > 150\,\text{GeV}$	1	$1.09\pm0.19\pm0.39$
GMSB SR	$m_\text{T}^{\tau_1}+m_\text{T}^{\tau_2} > 250\,\text{GeV}$	0	$0.28\pm0.10\pm0.22$
	$H_T > 600\,\text{GeV}$	105	109 ± 9
	$N_\text{jet} \geq 4$	42	34 ± 3
bRPVm_0 SR	$m_\text{T}^{\tau_1}+m_\text{T}^{\tau_2} > 200\,\text{GeV}$	5	$6.22\pm0.91\pm1.38$
nGM SR	$m_\text{T}^{\tau_1}+m_\text{T}^{\tau_2} > 250\,\text{GeV}$	1	$3.14\pm0.50\pm0.93$

Table 8.2: Cut-flow table for data and the sum of all expected background events. For all cuts up to the one tau cut only the kinematic scale factors are applied. For the one tau cut the true tau scale factors are applied. For all following cuts the full scaling is applied. Uncertainties quoted give the uncertainty due to both the limited available MC statistics at the respective cut stepand the uncertainty due to the scaling where applied. For the final cut additionally the systematic uncertainty is given. The total background prediction for the final cuts is computed taking into account correlations between the different channels. Hence, the uncertainties are different from the quadratic sum of the individual uncertainties from Table 8.1. Note due to technical reasons of the data processing, agreement is not expected before the single tau requirement.

the nGM SR, while the bRPVm_0 SR has the largest background expectation of all regions, namely $6.22\pm0.61^\text{stat}\pm0.66^\text{sf}\pm1.38^\text{syst} = 6.22\pm1.65$ events.

At all cut steps a reasonable agreement between the expected and observed number of events is observed. The only significant exception is the $N_\text{jet}\geq 4$ cut after the $H_T > 600\,\text{GeV}$ requirement, where 42 events are observed compared to $34\pm3^\text{(stat)}$ expected. Unfortunately, the method employed to calculate the systematic uncertainties does not allow for a computation at this cut step. Since the bRPVm_0 SR is reasonably similar to the considered selection, however, one can consider the systematic uncertainty from this cut step. This amounts to an additional uncertainty of 7.5 events and hence to a total uncertainty of 8 events, which covers the observed difference.

Table 8.3 lists cut flows for two example points from each signal model. These points are chosen to be close to the expected exclusion line. The yields at these points are compared to the expected number of background events for all Standard Model processes. An enrichment of the signal with respect to the background with each cut step is visible.

After looking in data, unfortunately a good agreement between the observed number of events and the prediction from the background estimates is found. In the nGM signal region, there is a small downward fluctuation exceeding the computed uncertainties. However, the observation is still within two standard deviations of the expected background level.

	Background estimate	GMSB		bRPV		nGM	
		$\Lambda = 70\,\text{TeV}$ $\tan\beta = 40$	$\Lambda = 80\,\text{TeV}$ $\tan\beta = 50$	$m_0 = 1\,000\,\text{GeV}$ $m_{1/2} = 500\,\text{GeV}$	$m_0 = 600\,\text{GeV}$ $m_{1/2} = 750\,\text{GeV}$	$m_{\tilde{\tau}} = 210$ $m_{\tilde{g}} = 1020$	$m_{\tilde{\tau}} = 210$ $m_{\tilde{g}} = 1180$
$N_\tau \geq 2$	865 ± 68	14 ± 1	6.10 ± 0.28	9.16 ± 1.05	3.99 ± 0.19	22 ± 1	5.39 ± 0.16
$\Delta\phi(E_T^{miss}, \text{jet}1,2) > 0.3$	810 ± 64	13 ± 1	5.76 ± 0.27	8.14 ± 1.00	3.67 ± 0.19	20 ± 1	5.13 ± 0.15
$H_T > 600\,\text{GeV}$	109 ± 9	9.07 ± 0.51	3.34 ± 0.22	4.88 ± 0.85	2.47 ± 0.16	13 ± 1	3.98 ± 0.14
$H_T > 1\,000\,\text{GeV}$	10 ± 1	6.25 ± 0.44	1.72 ± 0.17	1.59 ± 0.47	1.47 ± 0.13	1.92 ± 0.19	0.88 ± 0.06
$m_{\text{T}}^{\tau_1} + m_{\text{T}}^{\tau_2} > 150\,\text{GeV}$	2.88 ± 0.77	5.29 ± 0.40	1.56 ± 0.16	1.19 ± 0.35	1.29 ± 0.12	1.82 ± 0.18	0.83 ± 0.06
$N_{\text{jet}} \geq 4$	34 ± 3	6.40 ± 0.45	1.96 ± 0.18	4.88 ± 0.85	1.99 ± 0.15	13 ± 1	3.94 ± 0.14
$m_{\text{T}}^{\tau_1} + m_{\text{T}}^{\tau_2} > 200\,\text{GeV}$	6.22 ± 1.65	4.86 ± 0.39	1.70 ± 0.17	2.49 ± 0.61	1.58 ± 0.13	11 ± 0	3.41 ± 0.13
$m_{\text{T}}^{\tau_1} + m_{\text{T}}^{\tau_2} > 250\,\text{GeV}$	3.14 ± 1.06	4.25 ± 0.36	1.51 ± 0.16	2.29 ± 0.60	1.41 ± 0.12	9.94 ± 0.43	3.07 ± 0.12
$H_T > 1\,000\,\text{GeV}$	10 ± 1	6.25 ± 0.44	1.72 ± 0.17	1.59 ± 0.47	1.47 ± 0.13	1.92 ± 0.19	0.88 ± 0.06
$N_{\text{jet}} \geq 4$	3.06 ± 0.42	4.88 ± 0.41	1.33 ± 0.16	1.59 ± 0.47	1.33 ± 0.12	1.83 ± 0.18	0.86 ± 0.06
$m_{\text{T}}^{\tau_1} + m_{\text{T}}^{\tau_2} > 150\,\text{GeV}$	1.09 ± 0.44	4.10 ± 0.37	1.19 ± 0.15	1.19 ± 0.35	1.16 ± 0.12	1.73 ± 0.18	0.80 ± 0.06
$m_{\text{T}}^{\tau_1} + m_{\text{T}}^{\tau_2} > 250\,\text{GeV}$	0.28 ± 0.24	3.28 ± 0.33	0.98 ± 0.14	0.78 ± 0.29	0.94 ± 0.10	1.51 ± 0.16	0.68 ± 0.06

Table 8.3: Cut flow table for all signal regions comparing event yields at example points to the sum of expected SM background events. For all cuts the full scaling is applied according to the control region matching the respective $m_{\text{T}}^{\tau_1} + m_{\text{T}}^{\tau_2}$ cut. Uncertainties quoted comprise statistical and scale uncertainties. For the numbers in the signal regions, the total uncertainties including systematic uncertainties are given for the SM expectation.

Run	Event	SR	$p_T^{\text{jet}_1}$	$p_T^{\text{jet}_2}$	N_{jet}	$\not{E}_T$	$p_T^{\tau_1}$	$p_T^{\tau_2}$	$m_{\text{T}}^{\tau_1} + m_{\text{T}}^{\tau_2}$	H_T
200987	2347305	Inclusive	760 GeV	619 GeV	2	246 GeV	48 GeV	39 GeV	190 GeV	1 466 GeV
201006	49494410	Inclusive / bRPV $m_{1/2}$	634 GeV	374 GeV	4	370 GeV	109 GeV	22 GeV	154 GeV	1 138 GeV
201257	105423728	bRPV m_0	465 GeV	280 GeV	4	213 GeV	33 GeV	26 GeV	222 GeV	805 GeV
204857	15371783	Inclusive	675 GeV	270 GeV	3	224 GeV	220 GeV	26 GeV	161 GeV	1 191 GeV
208781	17455496	bRPV m_0	444 GeV	114 GeV	4	306 GeV	48 GeV	36 GeV	207 GeV	643 GeV
208189	17862563	bRPV m_0	194 GeV	150 GeV	4	208 GeV	226 GeV	31 GeV	207 GeV	601 GeV
213964	15937747	bRPV m_0 / nGM	483 GeV	100 GeV	4	378 GeV	105 GeV	32 GeV	300 GeV	720 GeV
214680	165560353	bRPV m_0	389 GeV	149 GeV	4	349 GeV	74 GeV	31 GeV	222 GeV	643 GeV

Table 8.4: Events from the 2012 p–p collisions at $\sqrt{s} = 8\,\text{TeV}$ selected in the analysis with their kinematic properties.

The run and event numbers of the data events passing the full selection as well as their basic kinematic properties are listed in Table 8.4. Detector displays of these events are compiled in Appendix G.

Figure 8.1 shows some data-to-simulation comparison for the main kinematic variables used for selecting the signal regions. The agreement in all quantities, both before and after cutting on $m_{\mathrm{T}}^{\tau_1} + m_{\mathrm{T}}^{\tau_2}$, is very good. For very high values in $m_{\mathrm{T}}^{\tau_1} + m_{\mathrm{T}}^{\tau_2}$ the simulation predicts overall slightly higher levels than observed in the data, which leads to the under-fluctuation in the nGM SR (low H_T, high $m_{\mathrm{T}}^{\tau_1} + m_{\mathrm{T}}^{\tau_2}$ cut).

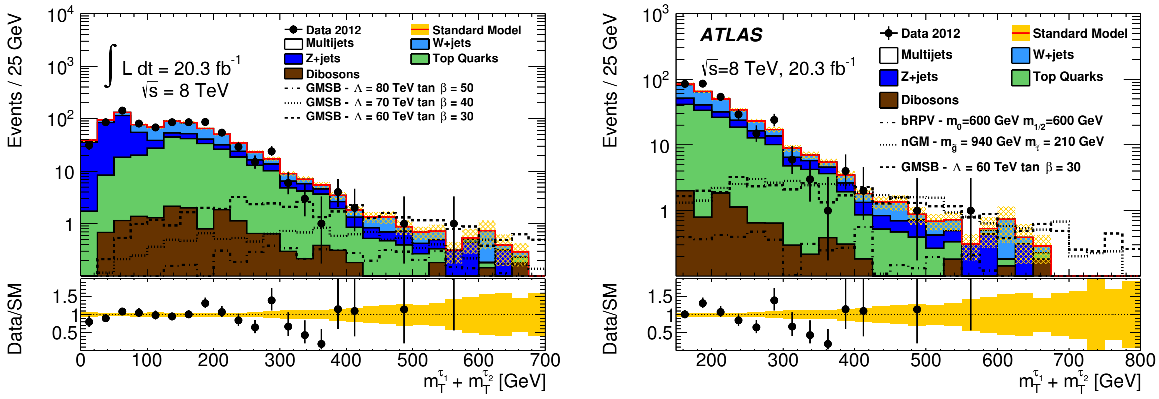

(a) $m_{\mathrm{T}}^{\tau_1} + m_{\mathrm{T}}^{\tau_2}$ after QCD supression

(b) $m_{\mathrm{T}}^{\tau_1} + m_{\mathrm{T}}^{\tau_2}$ after $m_{\mathrm{T}}^{\tau_1} + m_{\mathrm{T}}^{\tau_2} > 150\,\mathrm{GeV}$ cut

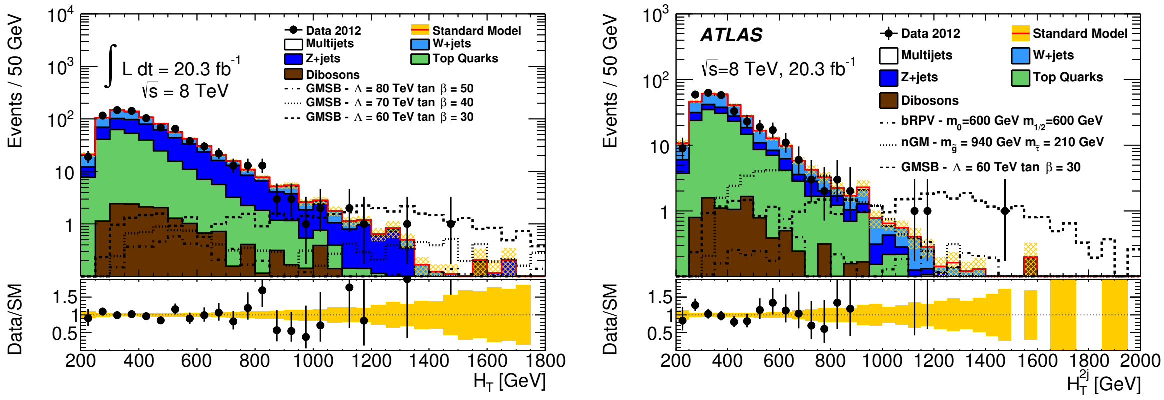

(c) H_T after QCD supression

(d) H_T after $m_{\mathrm{T}}^{\tau_1} + m_{\mathrm{T}}^{\tau_2} > 150\,\mathrm{GeV}$ cut

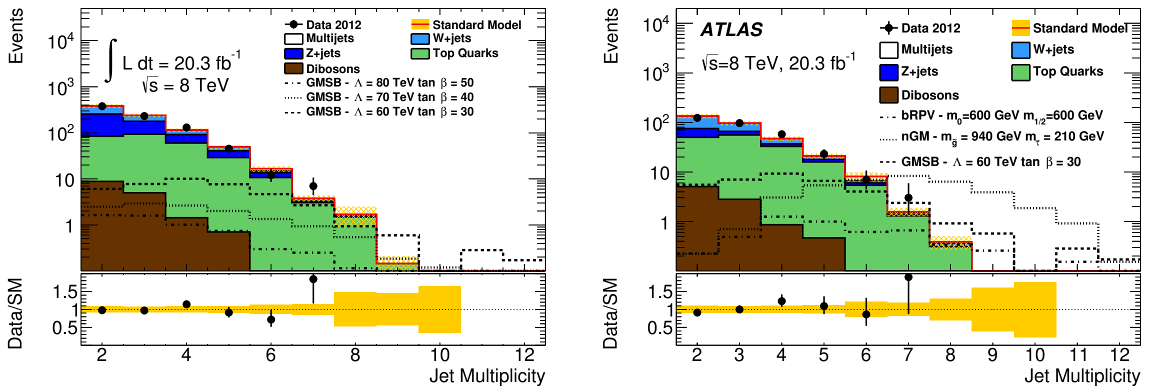

(e) N_{jet} after QCD supression

(f) N_{jet} after $m_{\mathrm{T}}^{\tau_1} + m_{\mathrm{T}}^{\tau_2} > 150\,\mathrm{GeV}$ cut

Figure 8.1: Distribution of the the kinematic selection variables $m_{\mathrm{T}}^{\tau_1} + m_{\mathrm{T}}^{\tau_2}$, H_T and N_{jet} after the QCD suppression cuts (left column) and after the soft $m_{\mathrm{T}}^{\tau_1} + m_{\mathrm{T}}^{\tau_2}$ cut on 150 GeV (right column). All uncertainties are statistical only.

8.2 Details on the studied signal grids

Figure 8.2 a)-b) show the expected number of events for the various points in the nGM grid as well as their combined uncertainties due to limited statistics and systematic uncertainties. As expected, the number of events and statistical uncertainty drop rather steeply with the gluino mass as the cross section does. At the same time the uncertainty on the cross section increases. Uncertainties are rather flat over the grid amounting to about 10% to 15% for most of the studied parameter space. Those numbers enter the exclusion and combination procedure as individual signal hypotheses. Correlations between signal and background in the individual uncertainties are taken care of.

Subfigure c)-e) show acceptance (the fraction of generated events that have generator-level properties that would in general allow the detection in the employed selection), efficiency (the fraction of generated events within the acceptance that are actually selected based on the reconstructed particles) and the product of those numbers. The acceptance is rather high at 15% for large gluino masses and drops with $m_{\tilde{g}}$ below the percent level. The efficiency shows the reverse trend, dropping from more than 50% to below 25% as the gluino mass increases. Subfigure f) shows the signal contamination in the control region. In the area of high gluino masses – where the limit is set – a small contamination is observed. For low gluino masses there is a significant leakage.

If there was signal present in the CR, it would manifest as an overshoot of data over the simulated backgrounds. Considering the observed event numbers in the CRs, there is no sign of any excess, however. On the contrary, significantly less data than expected is observed, which results in the low scale factor of 0.58 ± 0.19. A large signal contamination is hence highly unlikely.

For low gluino masses, the expected number of signal events exceeds the observed number of events by far, allowing for an exclusion using the control region alone. For regions above 1 000 GeV gluino mass, where the limit is set, the leakage in the control region is small, but not negligible.

Figure 8.3 shows the fraction of signal events in the W and top control regions for all grid points in the region of interest. Clearly, the dominant part of the contamination ends up in the top control region while the fraction of events in the W region is negligible.

To assess the effect, the background estimates are recomputed assuming a 16% signal contamination (average at $m_{\tilde{g}} = 960\,\text{GeV}$ well below the lowest uncertainty border of the final exclusion contour) and a 1% contamination (average at $m_{\tilde{g}} = 1\,180\,\text{GeV}$ above the highest uncertainty border). The expected background drops from 3.14 ± 0.50 to 3.12 ± 0.50 (1% contamination) to 2.90 ± 0.48 (16% contamination). These numbers include 0.06 events from multijets background, which is not affected by the contamination.

With these modified background expectations the limit is recomputed. As a simplification, the systematic uncertainties are kept the same since the effect of contamination is expected to be the same for both the nominal and the varied sample.

Figure 8.4 shows the expected and observed limits for the different signal contamination hypotheses. For 1% contamination, no difference to the nominal limit (c.f. Figure 8.9) is visible. For 16% contamination there is a small difference. However, it is completely negligible compared to the uncertainties on the limits. For the purpose of the limit calculation it can hence be neglected.

Figure 8.5 shows the same plots for the GMSB signal grid and the GMSB SR. Uncertainties vary between 10% in the center of the grid and 30% for high Λ and small $\tan\beta$ where the grid runs out of statistics. The acceptance varies between 2% and 0.2% while the efficiency is rather uniformly scattered around 25%. Contamination of signal events in the control region is well below 5%.

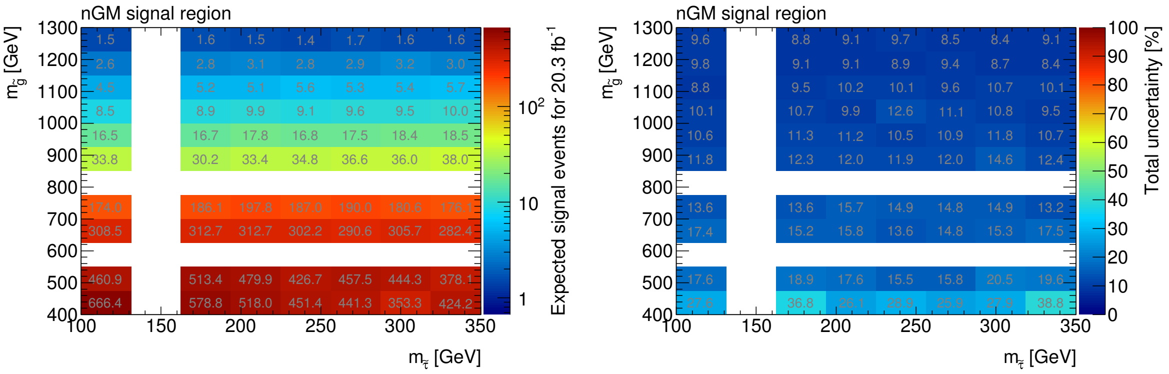

(a) Expected events (b) Total uncertainty

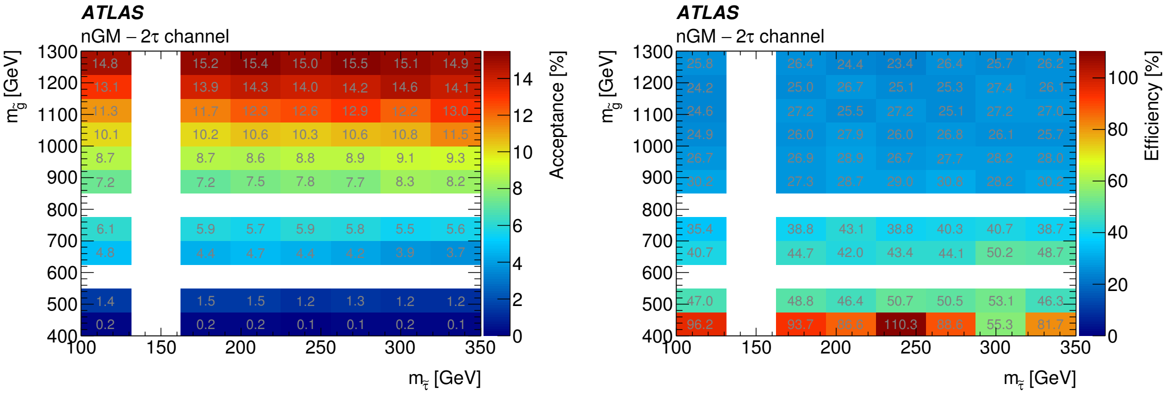

(c) Acceptance (d) Efficiency

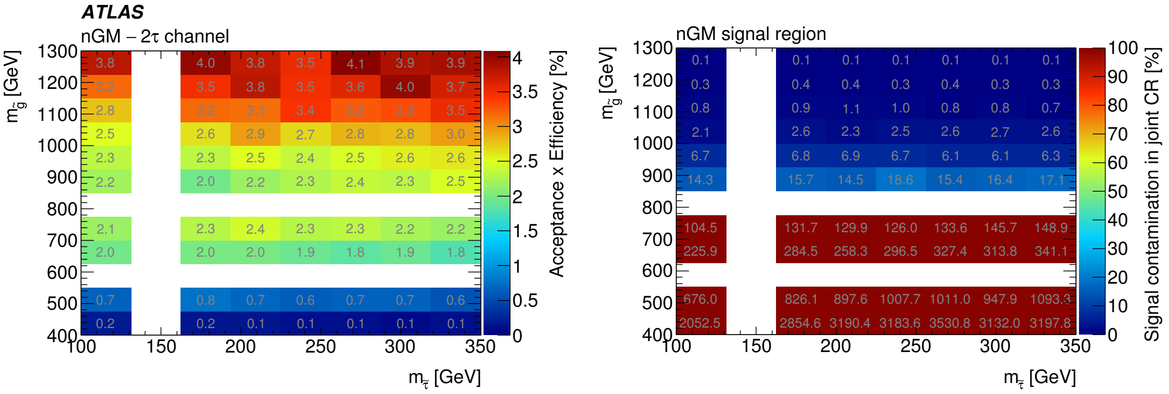

(e) Acceptance × Efficiency (f) Signal contamination in CR

Figure 8.2: Details on the results for the nGM SR in the nGM signal grid. Empty columns and rows are due to the non-regular spacing of the grid.

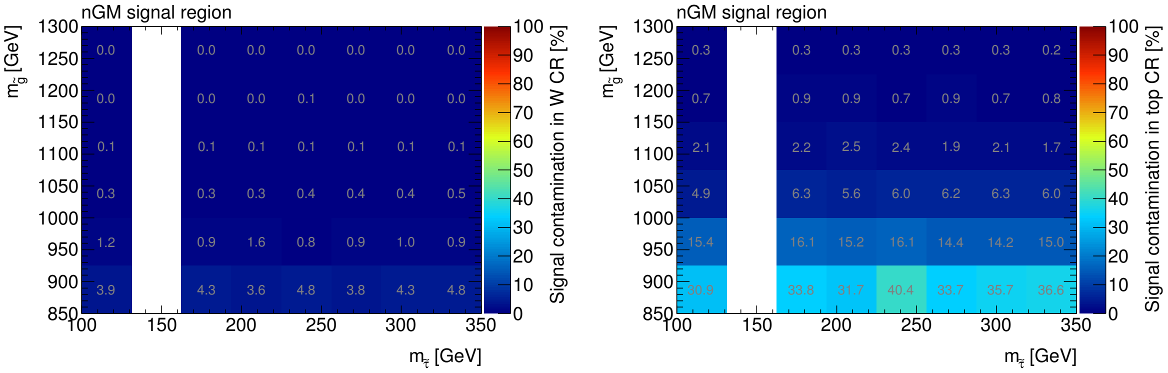

(a) Signal contamination in W CR

(b) Signal contamination in Top CR

Figure 8.3: Fraction of signal events of the nGM grid on the total expectation in the W and Top control region. The dominant contamination is located in the Top CR while the contamination in the W CR is negligible.

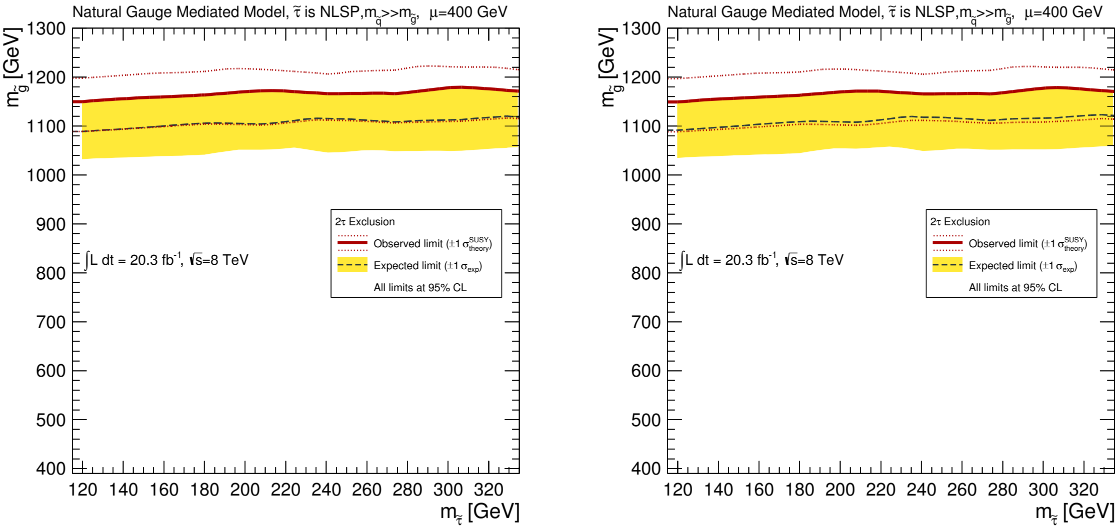

(a) 1% signal contamination

(b) 16% signal contamination

Figure 8.4: Expected and observed limits in the nGM grid for various hypothetical levels of signal contamination in the top control region. No significant effect on the limits is observed.

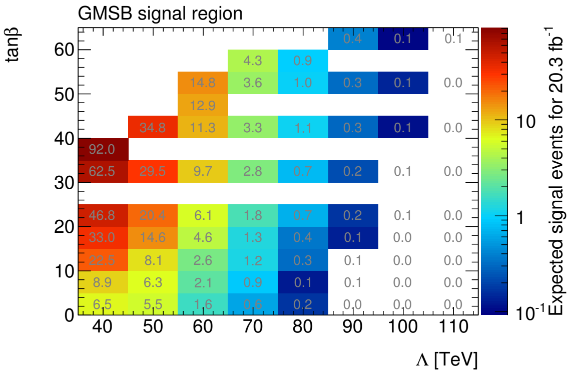

(a) Expected events

(b) Total uncertainty

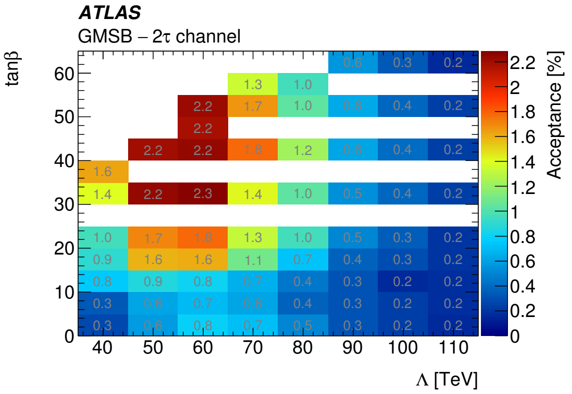

(c) Acceptance

(d) Efficiency

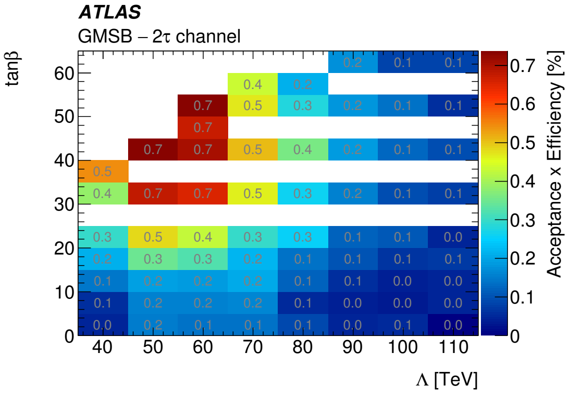

(e) Acceptance × Efficiency

(f) Signal contamination in CR

Figure 8.5: Details on the results for the GMSB SR in the GMSB signal grid. Empty columns and rows are due to the non-regular spacing of the grid.

For the bRPV grid, two signal regions are employed. Figures 8.7 and 8.6 give an overview of the performance of the bRPV$m_{1/2}$ and the bRPVm_0 SRs respectively. Both exhibit comparable acceptance and uncertainties with neither showing any significant signal contamination in the respective control regions. The uncertainties are around 12% at the most sensitive areas and rapidly rise to larger numbers at the outer parts of the grid. In the same way the acceptance drops from around 5% to below 0.1%. Efficiencies are again rather uniform in the order of 25% to 30%.

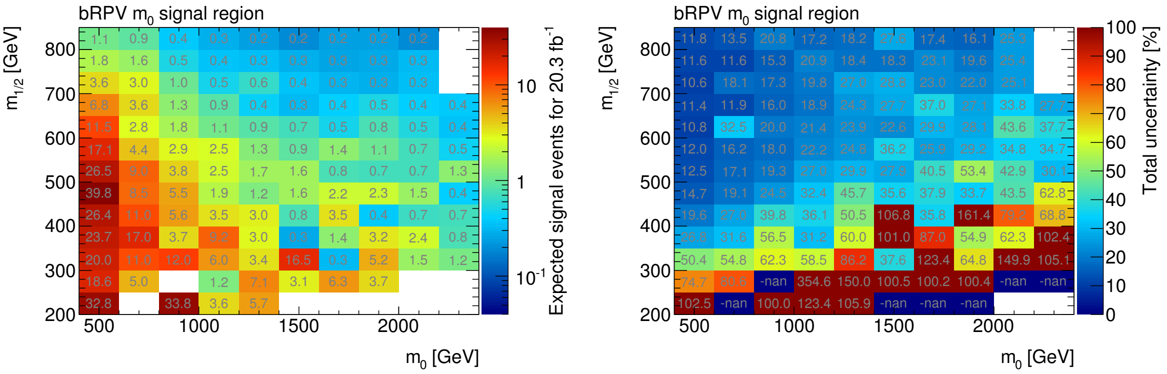

(a) Expected events (b) Total uncertainty

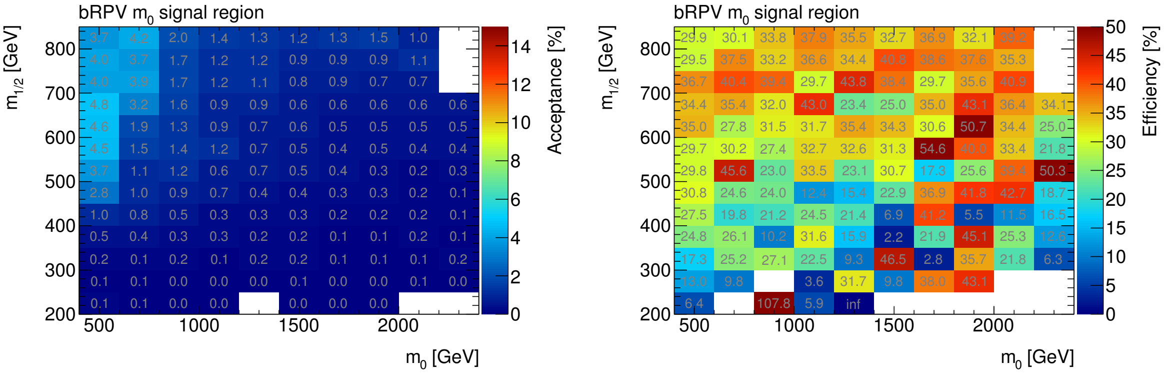

(c) Acceptance (d) Efficiency

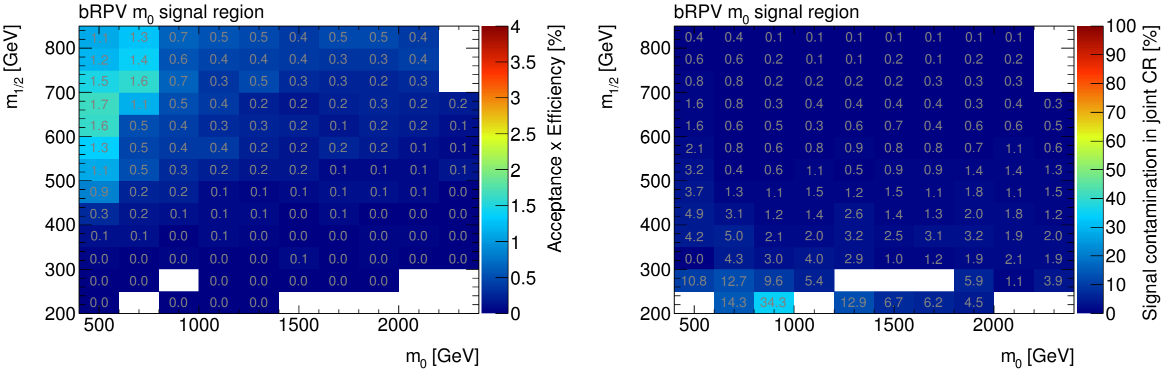

(e) Acceptance × Efficiency (f) Signal contamination in CR

Figure 8.6: Details on the results for the bPRVm_0 SR in the bRPV signal grid.

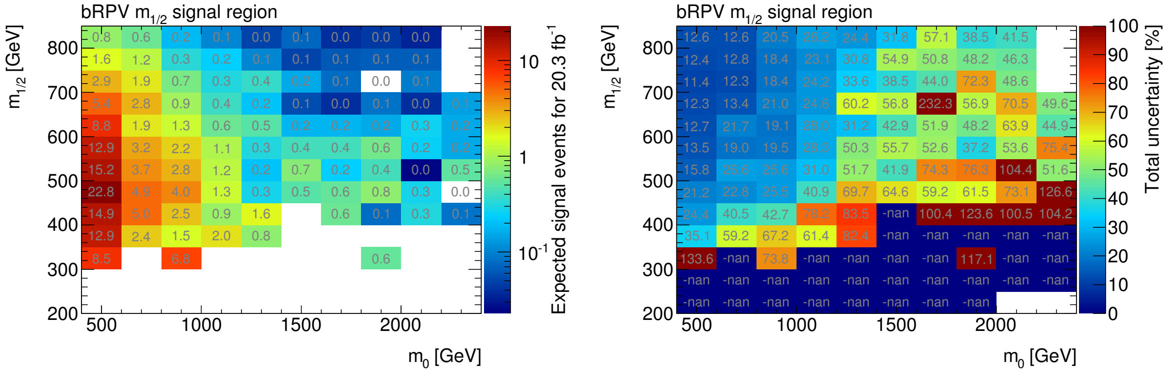

(a) Expected events

(b) Total uncertainty

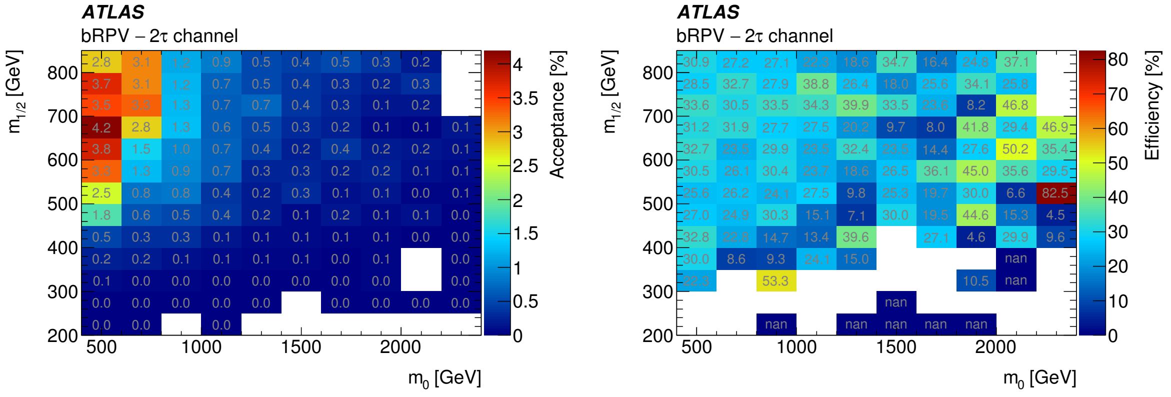

(c) Acceptance

(d) Efficiency

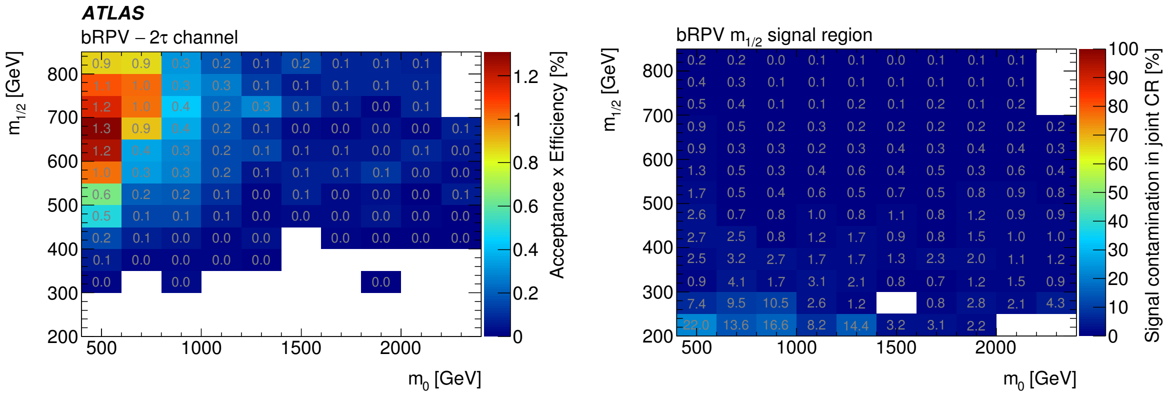

(e) Acceptance × Efficiency

(f) Signal contamination in CR

Figure 8.7: Details on the results for the bRPV$m_{1/2}$ SR in the bRPV signal grid.

8.3 Interpretation and limits

The non-observation of any excess of observed events over the expected background events in all signal regions is clearly a null-result. This null-result provides valuable information nevertheless, since it allows to exclude a certain level of non-SM events in the signal regions and certain parameter values for individual models. While often exclusions are intuitive, they nevertheless have to be formalized to achieve an objective way to exclude certain theories. This is done using hypothesis testing, where the compatibility of an observation with a prediction over defined hypotheses – in this case “background-only” and “signal + background” – is quantified. In the following, the statistical method used in this analysis is briefly summarized and then the interpretation of the results is presented.

8.3.1 Statistical method

The statistical methods to quantify the results of LHC searches has been developed by and agreed upon between experts of both major experiments. They are summarized in [222]. Below a condensed summary is given.

A probability distribution of some variable x that depends on some external parameter μ can be described by a joint function $p(x,\mu)$. Interpreting this function as a $p(x|\mu)$ yields the probability density function (pdf). However, for a typical particle physics analysis one does not have access to a full distribution but has to rely on a single observation and faces a large variety of possible parameters. Hence, we are more interested in the likelihood $\mathscr{L}(\mu) = p(\mu|x)$.

In the case of a counting experiment, the likelihood is essentially described by a Poisson distribution that describe the probability to observe n events given the prediction of b background and s signal events, where the latter is scaled by a strength parameter μ:

$$\mathscr{L}(\mu) = P_{\text{Poisson}}(n, b+\mu s) = e^{-(b+\mu s)} \frac{(b+\mu s)^n}{n!}$$

This likelihood can be extended to incorporate the effect of systematic uncertainties. For this purpose, the signal and background expectations are re-defined as

$$s \to s\left(\vec{\theta}\right) = s \prod_k \left(1+\theta_k \sigma_k^s\right) \quad \text{and} \quad b \to b\left(\vec{\theta}\right) = b \prod_k \left(1+\theta_k \sigma_k^b\right)$$

where the $\sigma_k^{s/b}$ describe the relative uncertainty due to the k^{th} systematic uncertainty on the signal and background prediction, respectively. Each of these uncertainties is scaled by a nuisance parameter θ_k. The nuisance parameters themselves are constrained by an additional term in $\mathscr{L}$

$$P_{\text{syst}}(\theta) = \prod_k \frac{1}{\sqrt{2\pi}} e^{-\frac{\theta_k^2}{2}},$$

a gaussian pdf with unity width, centered around zero. Correlations between uncertainties on signal and background can be modeled by assigning to them one common (correlated) or different (uncorrelated) nuisance parameters.

The full likelihood is thus:

$$\mathscr{L}\left(\mu,\vec{\theta}\right) = P_{\text{Poisson}}\left(n, b\left(\vec{\theta}\right) + \mu s\left(\vec{\theta}\right)\right) \times P_{\text{syst}}(\theta).$$

Based on the likelihood, the compatibility of the observed data with different hypotheses (predicted signal, no signal, etc.) can be quantified using hypothesis testing [223]. For this purpose, the profile likelihood ratio $\lambda(\mu)$ is constructed as

$$\lambda(\mu) = \frac{\mathscr{L}\left(\mu, \hat{\hat{\vec{\theta}}}_\mu\right)}{\mathscr{L}\left(\hat{\mu}, \hat{\vec{\theta}}\right)}.$$

Here $\hat{\hat{\vec{\theta}}}_\mu$ is the set of nuisance parameters that maximize the likelihood for a given signal strength μ while $\hat{\mu}$ and $\hat{\vec{\theta}}$ denote the strength and the corresponding set of parameters that maximize the likelihood globally. $\hat{\mu}$ may only assume values in a physically meaningful range, e.g. negative signal strength parameters are excluded. Moreover, $\hat{\mu}$ is bound from above by μ to avoid the exclusion of small parameters in the presence of a large signal.

To obtain a test statistics $\tilde{q}_\mu$ [217] for a given signal strength parameter μ, which increases as the compatibility with the data decreases, λ is slightly redefined as

$$\tilde{q}_\mu = -2\ln(\lambda(\mu)), \qquad \text{with } 0 \leq \hat{\mu} \leq \mu.$$

For a given signal under study and a real observation, the observed value of the test statistics $\tilde{q}_\mu^{\text{obs}}$ can be computed. To quantify the level of agreement, however, the pdf of the test statistics for the signal case $f\left(\tilde{q}_\mu|\mu, \hat{\hat{\vec{\theta}}}_\mu\right)$ and the background-only case $f\left(\tilde{q}_\mu|0, \hat{\hat{\vec{\theta}}}_0\right)$ are needed. To obtain these, pseudo-data is generated using toy Monte Carlo experiments from the expected number of events in each case. The nuisance parameters are fixed to the values obtained by minimizing $\tilde{q}$ under the real observation for the generation of the pseudo-data, but are fitted for the evaluation of the test statistics for each toy MC event [224].

From these distributions the *p-values* that quantify the level of agreement between the observed value of the test statistics and the signal + background and background-only hypothesis can be computed by evaluating in which fraction of the pseudo-data events a value is obtained that is at least as incompatible with the hypothesis as the observation:

$$p_\mu = P\left(\tilde{q}_\mu \geq \tilde{q}_\mu^{\text{obs}}|\text{signal + background}\right) = \int_{\tilde{q}_\mu^{\text{obs}}}^{\infty} f\left(\tilde{q}_\mu|\mu, \hat{\hat{\vec{\theta}}}_\mu\right) \mathrm{d}\tilde{q}_\mu$$

$$1 - p_b = P\left(\tilde{q}_\mu \geq \tilde{q}_\mu^{\text{obs}}|\text{background-only}\right) = \int_{\tilde{q}_\mu^{\text{obs}}}^{\infty} f\left(\tilde{q}_\mu|0, \hat{\hat{\vec{\theta}}}_0\right) \mathrm{d}\tilde{q}_\mu.$$

p_μ directly quantifies the probability of the observed number of events under the signal + background hypothesis. A low p_μ value is however not sufficient alone to exclude a scenario. In the case of a serious downward fluctuation in the number of observed events it would allow to exclude models which one is by construction not sensitive to. To prevent this, the CL_s method is employed. From the two p-values defined above, the confidence level for the signal hypothesis is finally computed as (c.f. [225])

$$\mathrm{CL}_s = \frac{p_\mu}{1 - p_b}.$$

A signal hypothesis is excluded at 95% confidence level if $\mathrm{CL}_s < 0.05$. Similarly, an upper limit on μ can be derived by varying μ until reaching $\mathrm{CL}_s = 0.05$. This construction of CL_s prevents an exclusion of a possible signal if the observation is incompatible with both the signal + background and the background-only hypothesis.

To obtain an expected exclusion and its uncertainty, the same procedure as above is performed only with replacing the one observation by a large set of background-only pseudo-data. This results in a distribution of upper limits of which the 50% quantile gives the central expected limit and the 16% and 84% quantiles give the $\pm 1\sigma$ uncertainties, respectively.

This process of obtaining the pdf of the test statistics from toy Monte Carlo is computationally rather expensive. To effectively deal with a high number of hypothesis tests, as e.g. needed when computing expected and observed limits on a grid of signal points, effective approximation methods have been developed [217]. They rely on analytical approximations of the profile likelihood ratio ("Asimov approximation") that yield exact results in the case of large sample sets. A special dataset where all observed values are set to their expectations is used to evaluate p-values which otherwise would need the full pdf to be generated from toy datasets. Although being exact only in the limit of infinite datasets, the method has been proven to yield good results down to small sample sizes, e.g. for an expected background of five events the pdf for the null-hypothesis shows very good agreement even in the tails (c.f. [217]).

All statistical operations are implemented in the HISTFITTER [226] package, which was used for all limits in this analysis. It relies on components of the RooStats software package [227] for the calculation of the CL_s and p-values.

In HISTFITTER, no fits in control regions or extrapolations are performed. All backgrounds are provided as they result from the various background estimation techniques described above. HISTFITTER is then only used to model the likelihoods and perform the statistical tests to obtain model independent limits and exclusion contours.

8.3.2 Model independent limits

For all five signal regions, model independent exclusions are computed using only the expected background and its uncertainty, as well as the observed number of events in the signal regions. Technically, the number of expected signal events is set to one and all uncertainties on the prediction are set to zero. The numbers for the background prediction is left unaltered. This way the 95% CL on the value of the signal strength parameter μ can directly be interpreted as a model independent limit on the number of bsm signal events. All limits are computed using HISTFITTER by running over 5000 events of toy MC. The excluded number of events has also been converted in a limit on the visible cross section using the integrated luminosity employed for this analysis. The limits are listed in Table 8.5.

Signal channel	$\langle\epsilon\sigma\rangle^{95}_{\mathrm{obs}}$[fb]	S^{95}_{obs}	S^{95}_{exp}	CL_B	$p(s=0)$
Inclusive	0.28	5.6	$5.3^{+1.9}_{-1.3}$	0.58	0.48
GMSB	0.17	3.5	$3.5^{+0.6}_{-0.1}$	0.36	0.50
nGM	0.18	3.7	$5.1^{+2.0}_{-1.2}$	0.12	0.50
bRPV$m_{1/2}$	0.20	4.0	$4.0^{+1.6}_{-0.4}$	0.52	0.50
bRPVm_0	0.31	6.2	$7.0^{+2.6}_{-2.0}$	0.36	0.50

Table 8.5: Left to right: 95% CL upper limits on the visible cross section ($\langle\epsilon\sigma\rangle^{95}_{\mathrm{obs}}$) and on the number of signal events (S^{95}_{obs}). The third column (S^{95}_{exp}) shows the 95% CL upper limit on the number of signal events, given the expected number (and $\pm1\sigma$ excursions on the expectation) of background events. The last two columns indicate the CL_B value, i.e. the confidence level observed for the background-only hypothesis and the discovery p-value ($p(s=0)$). The last value is bound from above to a value of 0.5 in cases where the observation is below the background prediction.

8.3.3 Signal model exclusions

Besides model independent limits, also exclusions are computed. Again HISTFITTER is used albeit not running on toy MC but using the Asimov approximation. It is verified that the use of the approximation is justified and working well by re-computing the model independent limits with the approximation method. A good level of agreement within the expected statistical uncertainty is observed.

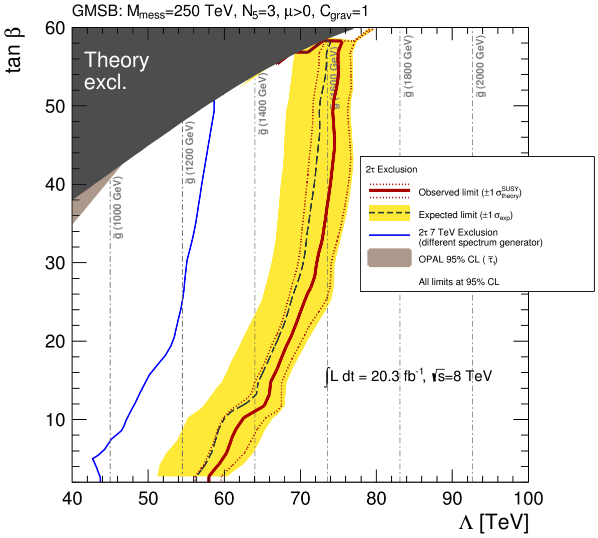

Figure 8.8: Expected and observed 95 % CL limits on the minimal GMSB model parameters Λ and $\tan\beta$. The dark grey area indicates the region which is theoretically excluded due to unphysical sparticle mass values. Additional model parameters are $M_{mess} = 250\,\mathrm{TeV}$, $N_5 = 3$, $\mu > 0$ and $C_{grav} = 1$.

The exclusion plot obtained in this analysis for the GMSB grid using the aforementioned expectation and observation can be seen in Figure 8.8. Due to the smaller uncertainties and the more aggressive selection, the limit is significantly stronger than any previously achieved exclusion with tau final states in this model. It now extends up to values of $\Lambda = 75\,\text{TeV}$ for large $\tan\beta$, which corresponds to gluino masses of $m_{\tilde{g}} \approx 1\,600\,\text{GeV}$.

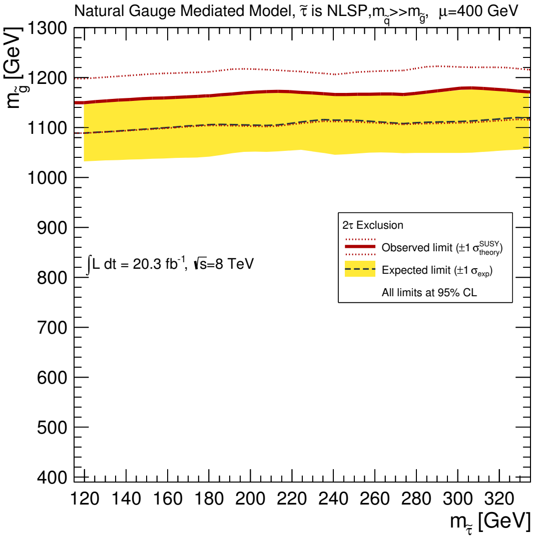

Figure 8.9: Expected and observed 95 % CL limits on the nGM model parameters $m_{\tilde{g}}$ and $m_{\tilde{\tau}}$. Additional model parameters are $\mu = 400\,\text{GeV}$ while all particles not involved in the modeled decay chain are set to very high masses $> 4\,\text{TeV}$.

Figure 8.9 shows an exclusion for the nGM region. Gluino masses of about $m_{\tilde{g}} = 1\,150\,\text{GeV}$ can be excluded regardless of the stau mass. The nGM signal hypothesis yields a significant signal contamination in the control regions of this analysis. The effect of a possible contamination on the limit has been studied and found to be negligible (c.f. Section 8.2).

Finally, Figure 8.10 displays exclusions for the bRPV signal grid. As intended, each of the two signal regions has its strength in a different part of the grid. To exploit the exclusion power of both SRs, a combination by best expected significance is performed. For every point in the signal grid the one result from the signal region which yields the highest expected exclusion significance is considered. This way one does not have to worry about orthogonality of signal regions but can still exploit the varying phenomenologies across the bRPV grid. The combined limit is basically the union of the individual limit with some additionally excluded region. The additional exclusion is mainly due to the interpolation done across the significance plane between the individual signal points.

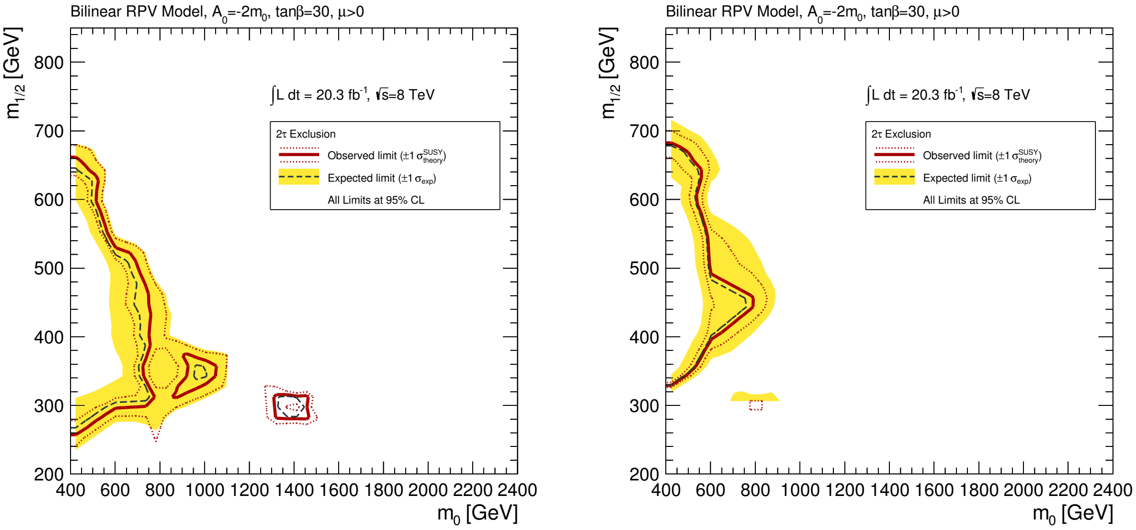

(a) bRPVm_0

(b) bRPV$m_{1/2}$

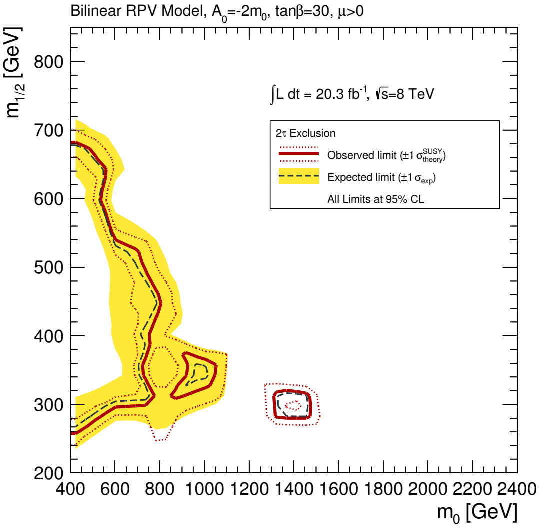

(c) bRPV 2τ Combined

Figure 8.10: Expected and observed 95 % CL limits on the bRPV model parameters m_0 and $m_{1/2}$. Figures a) and b) give the individual exclusion for each signal region while figure c) gives an combined exclusion taking for every signal point the one signal region with the best expected significance. Additional model parameters are $A_0 = 2m_0$, $\tan\beta = 30$ and $\mu > 0$.

8.3.4 Combination with other search channels

As stated in the introduction already, the analysis in this thesis is designed to be a part of a larger effort covering multiple search channels. Indeed, the published version [6] comprises four combined channels. The presented “two-tau” analysis, however, has a strong influence on the achieved results. This is clearly visible from Figure 8.11, which displays the exclusions from this thesis together with the published combined exclusions. The combination is performed by the same method as the individual limits, only formulating one likelihood covering all search channels as the product of the individual likelihoods. Correlations between the channels are considered in the modeling of the systematic uncertainties with common nuisance parameters. This combination method is possible since the search channels are orthogonal to each other by construction.

For GMSB, the limit in the high $\tan\beta$ region is clearly driven by the two-tau analysis. In the lower $\tan\beta$ regions, the search channels for a light lepton together with a tau lepton can add some extra reach. Here the mass splitting between the stau and the selectron/smuon is small so that decay chains comprising light leptons have a higher relevance. In the nGM scenario, the other search channels do not play a significant role. The observed combined limit follows the two-tau exclusion due to the small under-fluctuation of data observed. In the bRPV setting, the two-tau limit pushes the combined exclusion up to higher $m_{1/2}$ values for very low m_0. While the combined limit is significantly stronger than the limit obtained from the bRPV $m_{1/2}$ signal region alone, the combination of the $m_{1/2}$ and the m_0 region can compete with the combination over a large area. However, the combination is much smoother, resulting from the large statistical fluctuations the two-tau bRPV m_0 signal region suffers for large areas of the grid.

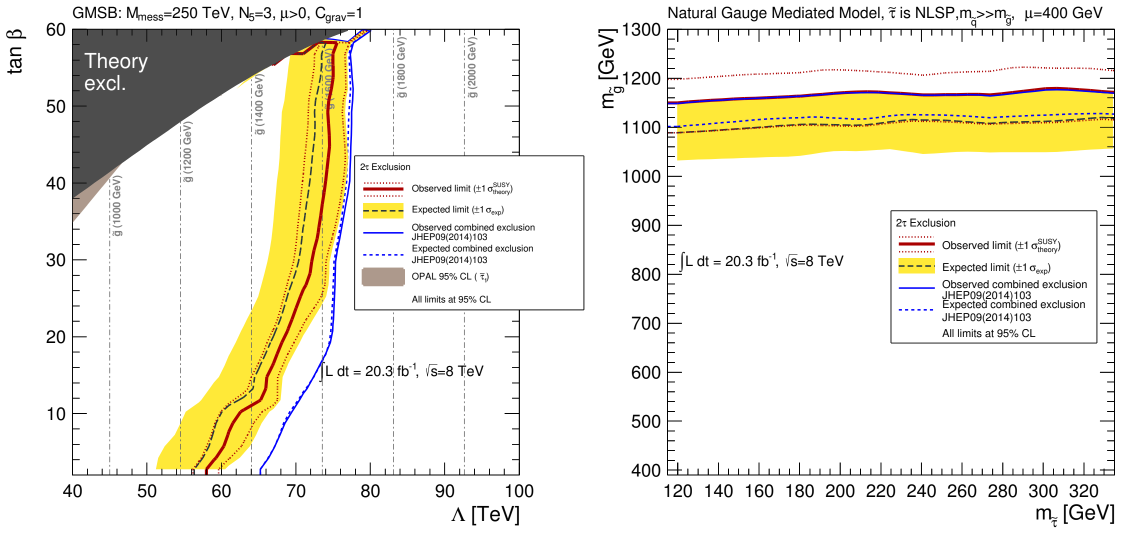

(a) GMSB
(b) nGM

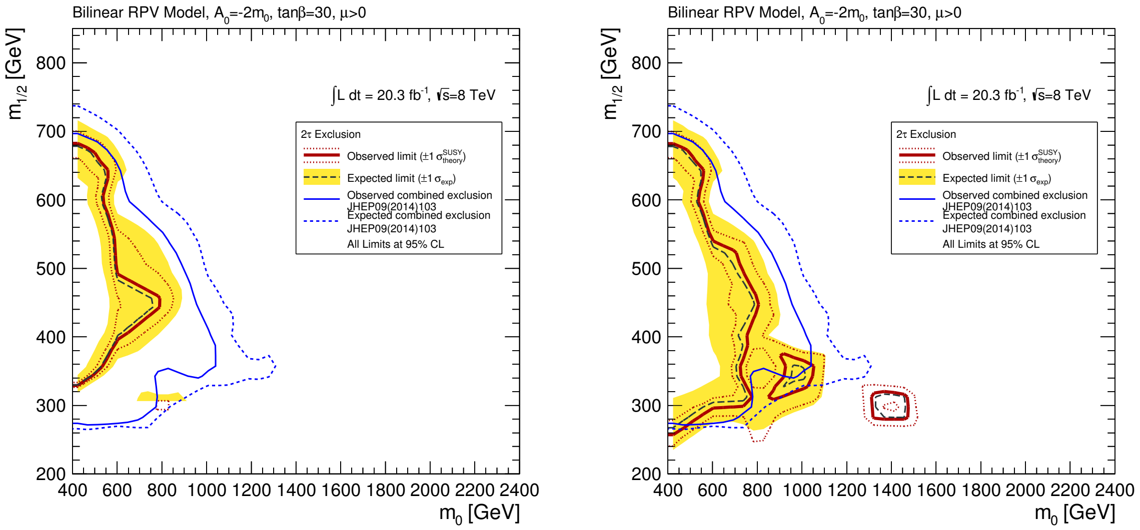

(c) bRPV$m_{1/2}$
(d) bRPV 2τ Combined

Figure 8.11: Comparison between the exclusions obtained in this analysis (red lines) and the published combined exclusions (blue lines). For the bRPV model only the bRPV $m_{1/2}$ signal region is included in the combination since the bRPV m_0 exclusion is superseded by exclusions from other channels.

8.4 Summary

No excess of observed events over the predicted number of background events has been found in any of the signal regions. Instead, a good agreement between prediction and observation has been found both in absolute values and in the distribution of all important kinematic variables. The non-observation of any excess has been interpreted as a limit on the possible number of extra events in each signal region. Moreover, exclusions have been set in the parameter planes for the signal models studied. The achieved exclusions contribute significantly to the published results obtained by combining four independent search channels in all models studied.

9

Conclusion

The Standard Model of particle physics is a tremendously successful theory. However, many indications point toward it not being the “final theory”, but an effective low-energy approximation of a more fundamental, “larger” theory. One of the best motivated candidates for such a theory is Supersymmetry.

In the search for signs of possible physics beyond the Standard Model, signatures with multiple tau leptons, jets and missing transverse momentum are promising candidates for a discovery. A search in this final state has been performed using $20.3\,\mathrm{fb}^{-1}$ integrated luminosity of 8 TeV proton–proton collision data recorded with the ATLAS detector at the LHC in 2012. Five search regions are considered, four of them targeted at specific theory predictions from assumed models of SUSY breaking. The expected backgrounds are estimated from data for pure multijets production and from Monte Carlo simulation for electroweak backgrounds and top quark production. The simulated estimates are normalized in control regions, correcting mainly for a mis-modeling of the fake probability of a tau lepton from a quark or gluon jet. The uncertainty on the expected backgrounds is dominated by uncertainties on the shapes of the kinematic variables which are used to separate the control from the the signal regions. In the end, an excellent agreement between the predictions and the observed data is achieved.

Unfortunately, this also implies no excess is found and the recorded number of events is consistent with the prediction of the Standard Model in all search regions.

The lack of any excess above the predicted backgrounds is translated into model independent exclusions of event numbers from any possible new physics scenario for the five search regions. Those limits range from 3.5 to 6.2 events at 95% confidence level. At the same time, exclusions are computed in various hypothetical scenarios of SUSY breaking. In GMSB, values of $\Lambda \lesssim 64\,\mathrm{TeV}$ are excluded for $\tan\beta \gtrsim 10$. The limit increases with $\tan\beta$, leading to an exclusion of $\Lambda \lesssim 74\,\mathrm{TeV}$ for $\tan\beta \gtrsim 30$. These values correspond to gluino masses of $m_{\tilde{g}} \lesssim 1.4\,\mathrm{TeV}$ and $m_{\tilde{g}} \lesssim 1.6\,\mathrm{TeV}$, respectively, making this analysis competitive to the strongest ATLAS SUSY limits published to date (c.f. Figure 9.1).

In the nGM scenario, gluino masses of $m_{\tilde{g}} \lesssim 1.15\,\mathrm{TeV}$ can be excluded over the full range of stau masses considered. The excluded mass range is lower in this approach than in GMSB since only one production channel and a very limited set of decay possibilities are considered. The model and the

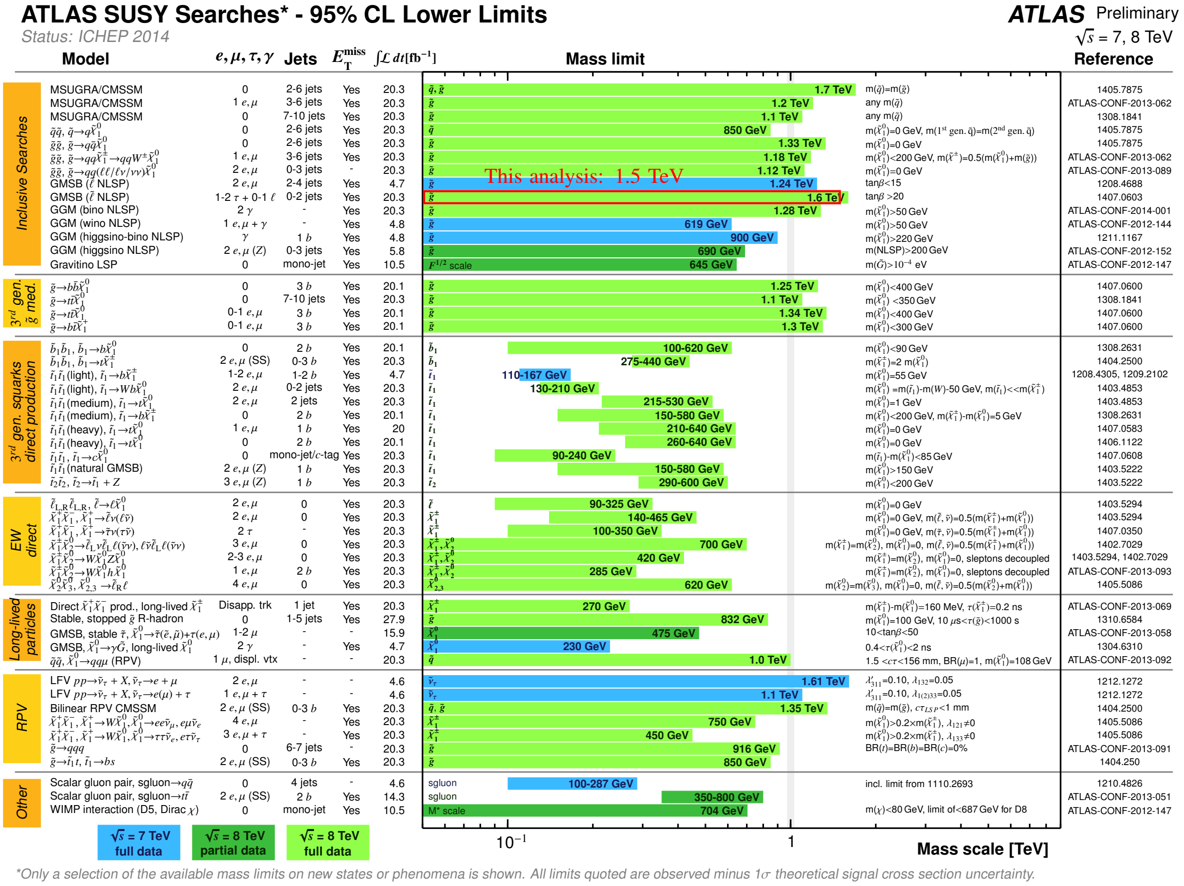

Figure 9.1: Comparison of the reaches of all ATLAS SUSY exclusions to date [228]. The red box indicates the exclusion reach of the analysis presented in this thesis. It is overlayed with the exclusion obtained by combining this analysis with the other three search channels as published in [6].

obtained limit are of high interest nevertheless. Comprising only a very limited set of particles and couplings between those, the exclusion can directly be translated into other models which feature a similar mass hierarchy and branching ratios – independent of all other SUSY particles not considered in the nGM model.

In the bRPV mSUGRA scenario, finally, an area of parameters at lower m_0 values can be excluded. The exclusion range peaks at $m_{1/2} \lesssim 700\,\text{GeV}$ for $m_0 = 400\,\text{GeV}$.

Limiting factors

A large limiting factor is the mis-modeling of the probabilities for fake taus in the Monte Carlo simulation. Although this is efficiently corrected for, the method employed comes at a high cost. It requires an extrapolation of normalization factors from a H_T region below 550 GeV to a region above 1 000 GeV for some signal regions. This approach is highly susceptible to mis-modelings of the shapes of various kinematic quantities. Together with the large corrections, this leads to sizable uncertainties in the final prediction.

One way of improving the whole analysis is the improvement of the fake tau modeling in the simulation. This proves, however, very difficult since the process is very sensitive to highly complex QCD phenomena like the color flow between the partons produced in the hard interaction and the proton remnant. A large-scale effort between tau experts, simulation experts and people that actually use taus in their analyses is needed. Alternatively, methods could be investigated to separate the tau modeling more efficiently from the non tau-related corrections in the data-driven estimate of the backgrounds.

Another limiting factor, especially for the GMSB scenario, is the design of this analysis to be sensitive nearly exclusively to the production of squarks and gluinos. For increasing Λ, the mass of the colored sparticles increases until the direct production of electroweak gauginos and even sleptons dominates. At $\Lambda = 90\,\mathrm{TeV}$, 96% of the total cross section consists of electroweak production processes. There are multiple ways to improve on this. First one could include triggers that are not relying on hard jets or large $\not{E}_T$, especially two-tau triggers. These suffer a low efficiency, limiting the sensitivity of the analysis. A dedicated analysis for electroweak SUSY production with tau final states using a two-tau trigger is already performed within the ATLAS SUSY group [214]. This analysis has not been interpreted in the GMSB scenario yet. Also a search for final states with multiple light leptons targets the GMSB scenario, but has not been published yet. Although these signatures are only sparsely produced in GMSB (from tau decays), the expected backgrounds from Standard Model physics are very low and these signatures can be triggered very efficiently and independently of any other kinematic constraints. One published result comes from the search for final states with two same-sign light leptons [229]. In this analysis, a comparable reach in Λ is achieved for large $\tan\beta$ while it performs better for low $\tan\beta$ where signatures with light leptons occur in higher abundance.

Outlook

In many searches for new physics, as in this work, no hint for SUSY in the LHC Run-I data has been found. As a result, together with the observation of the Higgs boson at a mass of approximately 125 GeV, many “high scale” SUSY benchmark models like mSUGRA or GMSB are under severe stress. However, these models represent only a tiny fraction of the possibilities in the MSSM. In other scenarios there is still a lot of room for SUSY to be realized in nature.

Despite the signal regions of the current analysis being tailored towards specific physics scenarios, at least some of them exhibit fairly generic properties. A natural extension of this work is hence a re-interpretation of the obtained results in the context of other, less constrained signal models. Indeed, re-interpretations of this search will be included in two upcoming ATLAS publications that summarize the concerted efforts within the collaboration during Run-I.

In one of these publications [8], a large scan over the parameter space within the pMSSM is presented (c.f. Section 2.2.7). For this study, more than 100 000 signal points have been considered. Points that are either highly unlikely or highly likely to be excluded by any ATLAS analysis based on the cross section and generator level acceptance studies are not considered any further. The remaining models are simulated on full reconstruction level and are studied by the analyses which are most promising to exclude these individual signal points. For the tau analyses, this amounts to 171 signal models, of which 11(26) can be excluded based on the expected (observed) exclusion of any of the signal regions in this analysis.

The other publication [7] will summarize all efforts for finding SUSY in strong production events. In this publication, special emphasis will be put on simplified models. This class of models circumvents external constraints by not assuming any full model at all but focusing on single decay topologies. This way, limits can be set directly on the mass of the involved particles in this one decay chain. This approach has the advantage that the resulting limits are easily adoptable for a wide range of theories and scenarios by simply comparing the mass and branching ratio predictions of a given theory with the model independent mass limits. For the tau strong production analyses, two grids are considered where either gluinos or squarks are produced which decay via a gaugino and a stau into a tau and a neutralino. All other SUSY particles are put to arbitrarily high mass, while all branching ratios and couplings are assumed to be the same. The mass of the initial particle and the neutralino are treated as free parameters while the mass of the two intermediate particles is fixed to a mass halfway down their decay. Figure 9.2 shows the resulting limits.

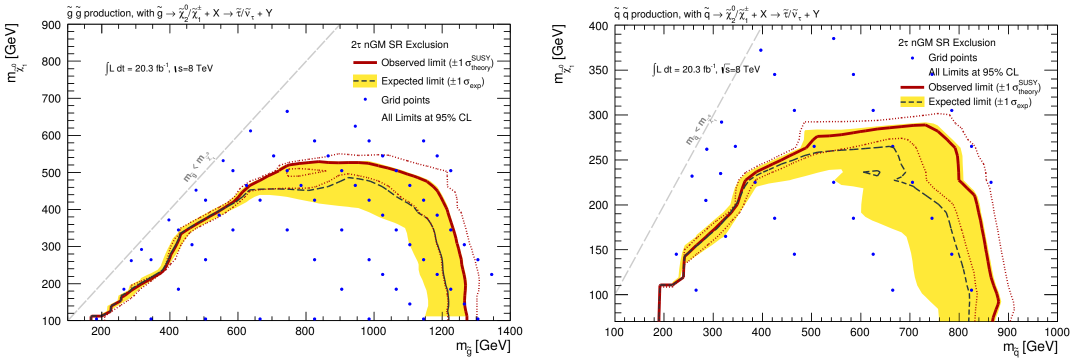

(a) Gluino grid

(b) Squark grid

Figure 9.2: Limits on simplified model grids with gluinos (a) and squarks (b) as initially produced particles. The limits are based on nGM SR however a different limit setting approach has to be used due to non-negligible signal contamination in the CRs. Details will be included in [7]

These limits are based on the results obtained for the nGM SR. The limit setting procedure is however different, owing to the fact that a non-negligible signal contamination in the control regions is observed for these signal models. Details on the limit setting and refined results performing a combination with the single tau search channel will be documented in [7].

The simplified model grids used in the aforementioned summary publication have relatively strong and somewhat arbitrary constraints. In the future, new simplified models tailored towards analyses using tau final states will be available. First studies within the master thesis of Oliver Ricken [230] show that some of the ad-hoc assumptions in the existing grids are not necessarily ideal and more suitable simplifications should be attempted.

The limited reach for strong production will naturally be boosted dramatically with the increase of the center of mass energy of the LHC in Run II. A study on the impact on the analysis in this thesis has been performed within a bachelor thesis [231]. An enormous gain was observed. For $\Lambda = 90\,\mathrm{TeV}$ e.g. a strong production fraction of the leading-order cross section of 45% was found at $\sqrt{s} = 14\,\mathrm{TeV}$, compared to 4% at $\sqrt{s} = 8\,\mathrm{TeV}$. With some optimization the exclusion reach should be easily expendable in the $\Lambda = 90\,\mathrm{TeV}$ region with an initial 13 TeV dataset.

Also the limit setting holds optimization potential. Instead of computing background expectations from discrete control regions for discrete signal regions one could perform a global fit of all background and signal contributions to one or multiple kinematic variables over a larger number of bins. This way one could possibly limit the sensitivity to the modeling by limiting the extrapolation distance and at the same time increase the sensitivity by exploiting the differences between signal and background in more detail. While being promising, this approach is also very challenging. It requires a deep understanding of not only the statistics behind the approach but also of the properties of the involved simulation, data and the various kinematic distributions. With the understanding and experience gained during this iteration of the analysis, this approach is now an attractive option for further improvements.

A

Simulated backgrounds

Sample ID	Name	Generator	xsec [pb]	k-factor	filter eff.	No. of events
117050	ttbar NoAllHad	PowhegPythia+AFII	253	1.00	0.543	74947917
108343	SingleTopSChanWenu	McAtNloJimmy	0.560	1.07	1.00	169183
108344	SingleTopSChanWmunu	McAtNloJimmy	0.560	1.07	1.00	169100
108345	SingleTopSChanWtaunu	McAtNloJimmy	0.560	1.07	1.00	169061
108346	SingleTopWtChanIncl	McAtNloJimmy	20.6	1.08	1.00	1766958
117360	t-channel $t \to e\nu$	AcerMCPythia	8.60	1.10	1.00	256853
117361	t-channel $t \to \mu\nu$	AcerMCPythia	8.60	1.10	1.00	256914
117362	t-channel $t \to \tau\nu$	AcerMCPythia	8.60	1.10	1.00	251341

Table A.1: Used $t\bar{t}$ and single t MC samples with their corresponding sample ID, event generator, cross section [232], k-factor, filter efficiency and number of generated events.

Sample ID	Name	Generator	LO [pb]	k-factor	No. of events
164440	ttbarlnlnNp0_baseline	AlpgenJimmy	4.79	1.74	799897
164441	ttbarlnlnNp1_baseline	AlpgenJimmy	5.07	1.74	808897
164442	ttbarlnlnNp2_baseline	AlpgenJimmy	3.26	1.74	529996
164444	ttbarlnlnNp3_baseline	AlpgenJimmy	1.52	1.74	410000
164445	ttbarlnlnNp4p_baseline	AlpgenJimmy	0.771	1.74	187997
164450	ttbarlnqqNp0_baseline	AlpgenJimmy	19.2	1.81	3359080
164451	ttbarlnqqNp1_baseline	AlpgenJimmy	20.3	1.81	3398787
164452	ttbarlnqqNp2_baseline	AlpgenJimmy	13.1	1.81	2209980
164454	ttbarlnqqNp3_baseline	AlpgenJimmy	6.08	1.81	1499794
164455	ttbarlnqqNp4p_baseline	AlpgenJimmy	3.08	1.81	556989
116108	ttbbincl	AlpgenJimmy	1.43	1.69	299998
116109	ttccincl	AlpgenJimmy	2.72	1.69	499997

Table A.2: Additional $t\bar{t}$ samples with their corresponding sample ID, event generator, LO cross section and number of generated events. Applying the k-factor yields the NNLO cross sections.Those samples have helped validating the analyses and are used to compare to the prediction from the baseline $t\bar{t}$ sample in order to estimate the size of systematic uncertainty of the MC generator.

Sample ID	Name	p_T^{low} [GeV]	p_T^{high} [GeV]	Flavor Filter	AFII/FS	NLO [pb]	k-factor	filter eff.	No. of events
167749	Zee	0		BFilter	AFII	1 110	1.12	0.0280	3999000
167750	Zee	0		CFilterBVeto	AFII	1 110	1.12	0.283	2999995
167751	Zee	0		CVetoBVeto	AFII	1 110	1.12	0.686	4978999
167752	Zmumu	0		BFilter	AFII	1 110	1.12	0.0280	3997997
167753	Zmumu	0		CFilterBVeto	AFII	1 110	1.12	0.283	2987995
167754	Zmumu	0		CVetoBVeto	AFII	1 110	1.12	0.690	4413999
167755	Ztautau	0		BFilter	AFII	1 110	1.12	0.0278	3997994
167756	Ztautau	0		CFilterBVeto	AFII	1 110	1.12	0.284	2998998
167757	Ztautau	0		CVetoBVeto	AFII	1 110	1.12	0.689	4979999
167758	Znunu	0		BFilter	AFII	5 990	1.12	0.0294	24992972
167759	Znunu	0		CFilterBVeto	AFII	5 990	1.12	0.280	19957480
167760	Znunu	0		CVetoBVeto	AFII	5 990	1.12	0.690	23359980
180543	Zee	40	70	BFilter	AFII	70.5	1.12	0.0706	600000
180544	Zee	40	70	CFilterBVeto	AFII	70.5	1.12	0.342	600000
180545	Zee	40	70	CVetoBVeto	AFII	70.4	1.12	0.588	1049998
180546	Zmumu	40	70	BFilter	AFII	70.5	1.12	0.0707	599000
180547	Zmumu	40	70	CFilterBVeto	AFII	70.5	1.12	0.341	599000
180548	Zmumu	40	70	CVetoBVeto	AFII	70.5	1.12	0.588	1398999
180549	Ztautau	40	70	BFilter	AFII	70.4	1.12	0.0709	598999
180550	Ztautau	40	70	CFilterBVeto	AFII	70.5	1.12	0.342	600000
180551	Ztautau	40	70	CVetoBVeto	AFII	70.5	1.12	0.588	1399996
167797	Zee	70	140	BFilter	AFII	29.5	1.12	0.0825	1396999
167798	Zee	70	140	CFilterBVeto	AFII	29.5	1.12	0.355	999999
167799	Zee	70	140	CVetoBVeto	AFII	29.5	1.12	0.563	1999998
167800	Zmumu	70	140	BFilter	AFII	29.5	1.12	0.0826	1159000
167801	Zmumu	70	140	CFilterBVeto	AFII	29.4	1.12	0.355	1000000
167802	Zmumu	70	140	CVetoBVeto	AFII	29.5	1.12	0.562	1996998
167803	Ztautau	70	140	BFilter	FS	29.5	1.12	0.0826	1199396
167804	Ztautau	70	140	CFilterBVeto	FS	29.5	1.12	0.355	979998
167805	Ztautau	70	140	CVetoBVeto	FS	29.5	1.12	0.562	1999693
167806	Znunu	70	140	BFilter	AFII	167	1.12	0.0841	5078993
167807	Znunu	70	140	CFilterBVeto	AFII	167	1.12	0.352	2998998
167808	Znunu	70	140	CVetoBVeto	AFII	167	1.12	0.564	4999996

Table A.3: Used Sherpa Z+jets MC samples with their corresponding sample ID, event generator, p_T slices, flavor filter, detector simulation, NLO cross section, k-factor, filter efficiency and number of generated events. These simulated with massive c and b quarks and massless light quarks. Moreover they are binned in the p_T of the Z boson. (continued in Table A.4)

Sample ID	Name	p_T^{low} [GeV]	p_T^{high} [GeV]	Flavor Filter	AFII/FS	NLO [pb]	k-factor	filter eff.	No. of events
167809	Zee	140	280	BFilter	AFII	3.99	1.12	0.0952	200000
167810	Zee	140	280	CFilterBVeto	AFII	3.98	1.12	0.369	399999
167811	Zee	140	280	CVetoBVeto	AFII	3.99	1.12	0.534	600000
167812	Zmumu	140	280	BFilter	AFII	3.98	1.12	0.0954	200000
167813	Zmumu	140	280	CFilterBVeto	AFII	3.99	1.12	0.370	389000
167814	Zmumu	140	280	CVetoBVeto	AFII	3.98	1.12	0.534	599500
167815	Ztautau	140	280	BFilter	FS	3.99	1.12	0.0958	199900
167816	Ztautau	140	280	CFilterBVeto	FS	3.99	1.12	0.370	399999
167817	Ztautau	140	280	CVetoBVeto	FS	3.99	1.12	0.533	598897
167818	Znunu	140	280	BFilter	AFII	22.5	1.12	0.0969	1000000
167819	Znunu	140	280	CFilterBVeto	AFII	22.5	1.12	0.368	1989998
167820	Znunu	140	280	CVetoBVeto	AFII	22.5	1.12	0.535	2979999
167821	Zee	280	500	BFilter	FS	0.242	1.12	0.109	20000
167822	Zee	280	500	CFilterBVeto	FS	0.241	1.12	0.387	49899
167823	Zee	280	500	CVetoBVeto	FS	0.242	1.12	0.506	39999
167824	Zmumu	280	500	BFilter	FS	0.242	1.12	0.108	19900
167825	Zmumu	280	500	CFilterBVeto	FS	0.242	1.12	0.386	50000
167826	Zmumu	280	500	CVetoBVeto	FS	0.243	1.12	0.505	50000
167827	Ztautau	280	500	BFilter	FS	0.241	1.12	0.107	19999
167828	Ztautau	280	500	CFilterBVeto	FS	0.241	1.12	0.385	50000
167829	Ztautau	280	500	CVetoBVeto	FS	0.241	1.12	0.507	49899
167830	Znunu	280	500	BFilter	FS	1.35	1.12	0.109	199999
167831	Znunu	280	500	CFilterBVeto	FS	1.36	1.12	0.384	239999
167832	Znunu	280	500	CVetoBVeto	FS	1.35	1.12	0.507	999892
167833	Zee	500		Bfilter	FS	0.0132	1.12	0.116	9600
167834	Zee	500		CFilterBVeto	FS	0.0135	1.12	0.398	10000
167835	Zee	500		CVetoBVeto	FS	0.0133	1.12	0.485	50000
167836	Zmumu	500		BFilter	FS	0.0132	1.12	0.114	10000
167837	Zmumu	500		CfilterBVeto	FS	0.0135	1.12	0.399	10000
167838	Zmumu	500		CVetoBVeto	FS	0.0133	1.12	0.487	10000
167839	Ztautau	500		BFilter	FS	0.0132	1.12	0.115	10000
167840	Ztautau	500		CFilterBVeto	FS	0.0133	1.12	0.393	10000
167841	Ztautau	500		CvetoBVeto	FS	0.0133	1.12	0.486	50000
167842	Znunu	500		BFilter	FS	0.0731	1.12	0.118	49999
167843	Znunu	500		CFilterBVeto	FS	0.0733	1.12	0.396	50000
167844	Znunu	500		CVetoBVeto	FS	0.0733	1.12	0.484	199699

Table A.4: Used Sherpa *Z*+jets MC samples continued from Table A.3.

Sample ID	Name	p_T^{low} [GeV]	p_T^{high} [GeV]	Flavor Filter	AFII/FS	NLO [pb]	k-factor	filter eff.	No. of events
167740	Wenu	0		BFilter	AFII	11 000	1.11	0.0128	14977980
167741	Wenu	0		CFilterBVeto	AFII	11 000	1.11	0.0490	9998989
167742	Wenu	0		CVetoBVeto	AFII	11 000	1.11	0.938	48415976
167743	Wmunu	0		BFilter	AFII	11 000	1.11	0.0128	14989485
167744	Wmunu	0		CFilterBVeto	AFII	11 000	1.11	0.0425	9872485
167745	Wmunu	0		CVetoBVeto	AFII	11 000	1.11	0.945	48856968
167746	Wtaunu	0		BFilter	AFII	11 000	1.11	0.0128	14850862
167747	Wtaunu	0		CFilterBVeto	AFII	11 000	1.11	0.0461	9993984
167748	Wtaunu	0		CVetoBVeto	AFII	11 000	1.11	0.941	49640972
180534	Wenu	40	70	BFilter	AFII	653	1.11	0.0345	1100000
180535	Wenu	40	70	CFilterBVeto	AFII	653	1.11	0.171	899999
180536	Wenu	40	70	CVetoBVeto	AFII	653	1.11	0.793	16947492
180537	Wmunu	40	70	BFilter	AFII	653	1.11	0.0346	1097999
180538	Wmunu	40	70	CFilterBVeto	AFII	653	1.11	0.166	900000
180539	Wmunu	40	70	CVetoBVeto	AFII	653	1.11	0.800	16978984
180540	Wtaunu	40	70	BFilter	AFII	653	1.11	0.0346	1099999
180541	Wtaunu	40	70	CFilterBVeto	AFII	653	1.11	0.169	889999
180542	Wtaunu	40	70	CVetoBVeto	AFII	653	1.11	0.796	15166494
167761	Wenu	70	140	BFilter	AFII	251	1.11	0.0459	2000000
167762	Wenu	70	140	CFilterBVeto	AFII	251	1.11	0.201	2996497
167763	Wenu	70	140	CVetoBVeto	AFII	250	1.11	0.753	14908986
167764	Wmunu	70	140	BFilter	AFII	251	1.11	0.0459	1988999
167765	Wmunu	70	140	CFilterBVeto	AFII	251	1.11	0.199	2995999
167766	Wmunu	70	140	CVetoBVeto	AFII	251	1.11	0.759	14931984
167767	Wtaunu	70	140	BFilter	FS	251	1.11	0.0459	1999893
167768	Wtaunu	70	140	CFilterBVeto	FS	251	1.11	0.199	2999890
167769	Wtaunu	70	140	CVetoBVeto	FS	251	1.11	0.755	14928649

Table A.5: Used Sherpa W+jets MC samples with their corresponding sample ID, event generator, p_T slices, flavor filter, detector simulation, NLO cross section, k-factor, filter efficiency and number of generated events. These simulated with massive c and b quarks and massless light quarks. Moreover they are binned in the p_T of the W boson. (continued in Table A.6)

Sample ID	Name	p_T^{low} [GeV]	p_T^{high} [GeV]	Flavor Filter	AFII/FS	NLO [pb]	k-factor	filter eff.	No. of events
167770	Wenu	140	280	BFilter	AFII	31.2	1.11	0.0632	999999
167771	Wenu	140	280	CFilterBVeto	AFII	31.2	1.11	0.222	1999997
167772	Wenu	140	280	CVetoBVeto	AFII	31.1	1.11	0.715	2000000
167773	Wmunu	140	280	BFilter	AFII	31.2	1.11	0.0631	997497
167774	Wmunu	140	280	CFilterBVeto	AFII	31.2	1.11	0.216	1985998
167775	Wmunu	140	280	CVetoBVeto	AFII	31.2	1.11	0.720	1993999
167776	Wtaunu	140	280	BFilter	FS	31.2	1.11	0.0631	989797
167777	Wtaunu	140	280	CFilterBVeto	FS	31.2	1.11	0.220	1998688
167778	Wtaunu	140	280	CVetoBVeto	FS	31.2	1.11	0.716	1999994
167779	Wenu	280	500	BFilter	FS	1.84	1.11	0.0829	99998
167780	Wenu	280	500	CFilterBVeto	FS	1.84	1.11	0.235	199898
167781	Wenu	280	500	CVetoBVeto	FS	1.84	1.11	0.682	499891
167782	Wmunu	280	500	BFilter	FS	1.84	1.11	0.0829	100000
167783	Wmunu	280	500	CFilterBVeto	FS	1.84	1.11	0.228	199998
167784	Wmunu	280	500	CVetoBVeto	FS	1.84	1.11	0.688	499698
167785	Wtaunu	280	500	BFilter	FS	1.84	1.11	0.0830	100000
167786	Wtaunu	280	500	CFilterBVeto	FS	1.84	1.11	0.233	199998
167787	Wtaunu	280	500	CVetoBVeto	FS	1.84	1.11	0.684	499998
167788	Wenu	500		BFilter	FS	0.102	1.11	0.0997	10000
167789	Wenu	500		CFilterBVeto	FS	0.101	1.11	0.244	10000
167790	Wenu	500		CVetoBVeto	FS	0.101	1.11	0.657	10000
167791	Wmunu	500		BFilter	FS	0.102	1.11	0.100	10000
167792	Wmunu	500		CFilterBVeto	FS	0.102	1.11	0.239	10000
167793	Wmunu	500		CVetoBVeto	FS	0.102	1.11	0.658	49700
167794	Wtaunu	500		BFilter	FS	0.102	1.11	0.0997	10000
167795	Wtaunu	500		CFilterBVeto	FS	0.101	1.11	0.242	10000
167796	Wtaunu	500		CVetoBVeto	FS	0.102	1.11	0.660	49998

Table A.6: Used Sherpa *W*+jets MC samples continued from Table A.5.

Sample ID	Name	Generator	LO [pb]	k-factor	No. of events
107680	WenuNp0	AlpgenJimmy	8 040	1.19	3459718
107681	WenuNp1	AlpgenJimmy	1 580	1.19	2499797
107682	WenuNp2	AlpgenJimmy	477	1.19	3769889
107683	WenuNp3	AlpgenJimmy	134	1.19	1009965
107684	WenuNp4	AlpgenJimmy	35.6	1.19	249999
107685	WenuNp5	AlpgenJimmy	10.5	1.19	70000
107690	WmunuNp0	AlpgenJimmy	8 040	1.19	3469591
107691	WmunuNp1	AlpgenJimmy	1 580	1.19	2499893
107692	WmunuNp2	AlpgenJimmy	478	1.19	3769890
107693	WmunuNp3	AlpgenJimmy	134	1.19	1009896
107694	WmunuNp4	AlpgenJimmy	35.6	1.19	255000
107695	WmunuNp5	AlpgenJimmy	10.5	1.19	20000
107700	WtaunuNp0	AlpgenJimmy	8 040	1.19	3364789
107701	WtaunuNp1	AlpgenJimmy	1 580	1.19	2449991
107702	WtaunuNp2	AlpgenJimmy	478	1.19	3719888
107703	WtaunuNp3	AlpgenJimmy	134	1.19	1009993
107704	WtaunuNp4	AlpgenJimmy	35.5	1.19	249898
107705	WtaunuNp5	AlpgenJimmy	10.5	1.19	65000
117284	WccNp0	AlpgenJimmy	150	1.19	1274998
117285	WccNp1	AlpgenJimmy	133	1.19	1049997
117286	WccNp2	AlpgenJimmy	71.8	1.19	552899
117287	WccNp3	AlpgenJimmy	30.3	1.19	170000
117293	WcNp0	AlpgenJimmy	808	1.19	6489181
117294	WcNp1	AlpgenJimmy	268	1.19	2069695
117295	WcNp2	AlpgenJimmy	69.8	1.19	519999
117296	WcNp3	AlpgenJimmy	20.5	1.19	110000
117297	WcNp4	AlpgenJimmy	4.30	1.19	20000
107280	WbbNp0	AlpgenJimmy	55.7	1.19	474999
107281	WbbNp1	AlpgenJimmy	45.2	1.19	359999
107282	WbbNp2	AlpgenJimmy	23.2	1.19	174999
107283	WbbNp3	AlpgenJimmy	11.1	1.19	50000

Table A.7: Additional W+jets MC samples with their corresponding sample ID, event generator, LO cross section, k-factor, and number of generated events. The overlap between nominal and heavy flavor samples is removed using the heavy flavor overlap prescription (HFOR).

Sample ID	Name	Generator	LO [pb]	k-factor	filter eff.	No. of events
172001	WenuNp1_susyfilt	AlpgenJimmy	12.7	1.19	1.00	1999991
172002	WenuNp2_susyfilt	AlpgenJimmy	8.95	1.19	1.00	1492993
172003	WenuNp3_susyfilt	AlpgenJimmy	4.33	1.19	1.00	1249989
172004	WenuNp4_susyfilt	AlpgenJimmy	1.70	1.19	1.00	399498
172005	WenuNp5_susyfilt	AlpgenJimmy	0.550	1.19	1.00	109899
172006	WenuNp6_susyfilt	AlpgenJimmy	0.190	1.19	1.00	20000
172011	WmunuNp1_susyfilt	AlpgenJimmy	12.7	1.19	1.00	1999795
172012	WmunuNp2_susyfilt	AlpgenJimmy	8.96	1.19	1.00	1499993
172013	WmunuNp3_susyfilt	AlpgenJimmy	4.33	1.19	1.00	1249296
172014	WmunuNp4_susyfilt	AlpgenJimmy	1.70	1.19	1.00	399898
172015	WmunuNp5_susyfilt	AlpgenJimmy	0.560	1.19	1.00	109998
172016	WmunuNp6_susyfilt	AlpgenJimmy	0.190	1.19	1.00	20000
172021	WtaunuNp1_susyfilt	AlpgenJimmy	46.4	1.19	0.348	3994886
172022	WtaunuNp2_susyfilt	AlpgenJimmy	34.3	1.19	0.335	2794687
172023	WtaunuNp3_susyfilt	AlpgenJimmy	17.1	1.19	0.327	1234793
172024	WtaunuNp4_susyfilt	AlpgenJimmy	6.55	1.19	0.336	549496
172025	WtaunuNp5_susyfilt	AlpgenJimmy	2.04	1.19	0.354	150000
172026	WtaunuNp6_susyfilt	AlpgenJimmy	0.660	1.19	0.381	30000

Table A.8: Additional W+jets MC samples with their corresponding sample ID, event generator, LO cross section, k-factor, and number of generated events. These “susyfilt” samples have been produced with a truth level filter requiring one jet of at least 80 GeV p_T and at least 100 GeV of missing transverse energy. Overlap between those and the inclusive samples is removed by applying corresponding veto cuts to the inclusive samples.

Sample ID	Name	Generator	LO [pb]	k-factor	No. of events
147105	ZeeNp0	AlpgenPythia	719	1.18	6298988
147106	ZeeNp1	AlpgenPythia	176	1.18	8199476
147107	ZeeNp2	AlpgenPythia	58.9	1.18	3175991
147108	ZeeNp3	AlpgenPythia	15.6	1.18	814995
147109	ZeeNp4	AlpgenPythia	4.01	1.18	348597
147110	ZeeNp5Incl	AlpgenPythia	1.26	1.18	219700
147113	ZmumuNp0	AlpgenPythia	719	1.18	6288796
147114	ZmumuNp1	AlpgenPythia	176	1.18	8088384
147115	ZmumuNp2	AlpgenPythia	58.9	1.18	3175488
147116	ZmumuNp3	AlpgenPythia	15.7	1.18	844799
147117	ZmumuNp4	AlpgenPythia	4.01	1.18	378200
147118	ZmumuNp5Incl	AlpgenPythia	1.25	1.18	179200
147121	ZtautauNp0	AlpgenPythia	719	1.18	16797868
147122	ZtautauNp1	AlpgenPythia	176	1.18	10679582
147123	ZtautauNp2	AlpgenPythia	58.9	1.18	3740893
147124	ZtautauNp3	AlpgenPythia	15.7	1.18	1011994
147125	ZtautauNp4	AlpgenPythia	4.01	1.18	378798
147126	ZtautauNp5Incl	AlpgenPythia	1.26	1.18	209799

Table A.9: Additional Z+jets MC samples for Z decaying to charged leptons listed with their corresponding sample ID, event generator, LO cross section, k-factor and number of generated events.

Sample ID	Name	Generator	LO [pb]	k-factor	No. of events
200332	ZeebbNp0	AlpgenPythia	0.460	1.18	1629895
200333	ZeebbNp1	AlpgenPythia	0.331	1.18	619997
200334	ZeebbNp2	AlpgenPythia	0.148	1.18	170000
200335	ZeebbNp3Incl	AlpgenPythia	0.0796	1.18	109997
200340	ZmuumbbNp0	AlpgenPythia	0.459	1.18	1529994
200341	ZmumubbNp1	AlpgenPythia	0.330	1.18	449700
200342	ZmumubbNp2	AlpgenPythia	0.149	1.18	219999
200343	ZmumubbNp3Incl	AlpgenPythia	0.0798	1.18	109499
200348	ZtautaubbNp0	AlpgenPythia	0.459	1.18	259999
200349	ZtautaubbNp1	AlpgenPythia	0.330	1.18	90000
200350	ZtautaubbNp2	AlpgenPythia	0.148	1.18	50000
200351	ZtautaubbNp3Incl	AlpgenPythia	0.0799	1.18	50000
200432	ZeeccNp0	AlpgenPythia	0.412	1.18	279998
200433	ZeeccNp1	AlpgenPythia	0.298	1.18	169499
200434	ZeeccNp2	AlpgenPythia	0.137	1.18	100000
200435	ZeeccNp3Incl	AlpgenPythia	0.0764	1.18	50000
200440	ZmuumccNp0	AlpgenPythia	0.411	1.18	289798
200441	ZmumuccNp1	AlpgenPythia	0.298	1.18	190000
200442	ZmumuccNp2	AlpgenPythia	0.137	1.18	90000
200443	ZmumuccNp3Incl	AlpgenPythia	0.0764	1.18	40000
200448	ZtautauccNp0	AlpgenPythia	0.412	1.18	269999
200449	ZtautauccNp1	AlpgenPythia	0.298	1.18	159900
200450	ZtautauccNp2	AlpgenPythia	0.137	1.18	100000
200451	ZtautauccNp3Incl	AlpgenPythia	0.0766	1.18	49999

Table A.10: Additional Z+jets MC samples for Z decaying to charged leptons in production with heavy flavor quarks listed with their corresponding sample ID, event generator, LO cross section, k-factor and number of generated events. The overlap between nominal and heavy flavor samples is removed using the heavy flavor overlap prescription (HFOR).

Sample ID	Name (event generator: AlpgenJimmy)	LO [pb]	k-factor	filter eff.	No. of events
156803	ZnunuNp0_filt1jet	4150	1.23	0.00646	5000
156804	ZnunuNp1_filt1jet	892	1.23	0.455	85000
156808	ZnunuNp1_met70_filt1jet	69.5	1.00	0.999	75000
156805	ZnunuNp1_met140_filt1jet	6.03	1.00	1.00	95000
156806	ZnunuNp1_met280_filt1jet	0.243	1.00	1.00	25000
156807	ZnunuNp1_met500_filt1jet	0.00895	1.00	1.00	5000
156809	ZnunuNp2_filt1jet	282	1.23	0.761	40000
156813	ZnunuNp2_met70_filt1jet	61.0	1.00	0.991	100000
156810	ZnunuNp2_met140_filt1jet	8.00	1.00	1.00	150000
156811	ZnunuNp2_met280_filt1jet	0.460	1.00	1.00	50000
156812	ZnunuNp2_met500_filt1jet	0.0229	1.00	1.00	13000
156814	ZnunuNp3_filt1jet	82.0	1.23	0.906	15000
156818	ZnunuNp3_met70_filt1jet	27.5	1.00	0.986	75000
156815	ZnunuNp3_met140_filt1jet	5.24	1.00	1.00	110000
156816	ZnunuNp3_met280_filt1jet	0.392	1.00	1.00	50000
156817	ZnunuNp3_met500_filt1jet	0.0227	1.00	1.00	13000
156819	ZnunuNp4_filt1jet	21.6	1.23	0.965	4000
156823	ZnunuNp4_met70_filt1jet	9.43	1.00	0.993	25000
156820	ZnunuNp4_met140_filt1jet	2.35	1.00	1.00	120000
156821	ZnunuNp4_met280_filt1jet	0.220	1.00	1.00	45000
156822	ZnunuNp4_met500_filt1jet	0.0142	1.00	1.00	10000
156824	ZnunuNp5_filt1jet	6.60	1.23	0.989	8000
156828	ZnunuNp5_met70_filt1jet	3.35	1.00	0.998	19000
156825	ZnunuNp5_met140_filt1jet	1.04	1.00	1.00	30000
156826	ZnunuNp5_met280_filt1jet	0.121	1.00	1.00	17000
156827	ZnunuNp5_met500_filt1jet	0.00876	1.00	1.00	4000

Table A.11: Additional Z+jets MC samples with the Z decaying to neutrino pairs, generated with AlpgenJimmy and listed with their corresponding sample ID, LO cross section, k-factor, filter efficiency, NNLO cross section,and number of generated events. The event generator version corresponds to the ATLAS release (tag E1601), which has the meson energy deposits correctly simulated. They are filtered for the presence of at least one jet and various levels of $\not{E}_T$ from 0 to 500 GeV. Double counting of cross section is prevented by excluding from a given sample the $\not{E}_T$ filtered range of all higher filters.

Sample ID	Generator	Final state	NLO [pb]	k-factor	No. of events
126892	Sherpa	$W^+W^- \to \ell\nu\ell\nu$	5.50	1.06	2699994
126893	Sherpa	$W^\pm Z \to \ell\ell\ell\nu$	9.75	1.05	2699893
126894	Sherpa	$ZZ \to \ell\ell\ell\ell$	8.74	1.00	3799491
126895	Sherpa	$ZZ \to \ell\ell\nu\ell\nu$	0.496	1.05	899899

Table A.12: Used Dibosons MC samples with their corresponding sample ID, event generator, final state, NLO cross section, k-factor and number of generated events.

Sample ID	Name (event generator: Powheg+Pythia8)	NLO [pb]	k-factor	filter eff.	No. of events
126928	WpWm_ee	0.598	1.08	1.00	599700
126929	WpWm_me	0.597	1.08	1.00	600000
126930	WpWm_te	0.598	1.08	1.00	580000
126931	WpWm_em	0.598	1.08	1.00	589999
126932	WpWm_mm	0.597	1.08	1.00	600000
126933	WpWm_tm	0.597	1.08	1.00	599798
126934	WpWm_et	0.597	1.08	1.00	580000
126935	WpWm_mt	0.598	1.08	1.00	599999
126936	WpWm_tt	0.598	1.08	1.00	580000
126937	ZZ_4e_mll4_2pt5	0.0770	1.00	0.908	1099997
126938	ZZ_2e2mu_mll4_2pt5	0.176	1.00	0.827	1599696
126939	ZZ_2e2tau_mll4_2pt5	0.175	1.00	0.583	1079798
126940	ZZ_4mu_mll4_2pt5	0.0770	1.00	0.912	1099798
126941	ZZ_2mu2tau_mll4_2pt5	0.175	1.00	0.587	1069799
126942	ZZ_4tau_mll4_2pt5	0.0770	1.00	0.106	299999
126949	ZZllnunu_ee_mll4	0.0540	3.00	1.00	299400
126950	ZZllnunu_mm_mll4	0.0540	3.00	1.00	300000
126951	ZZllnunu_tt_mll4	0.0540	3.00	1.00	299999
129477	WZ_Wm11Z11_mll0p250d0_2LeptonFilter5	1.41	1.12	0.295	190000
129478	WZ_Wm11Z13_mll0p4614d0_2LeptonFilter5	0.938	1.12	0.352	190000
129479	WZ_Wm11Z15_mll3p804d0_2LeptonFilter5	0.175	1.12	0.167	75999
129480	WZ_Wm13Z11_mll0p250d0_2LeptonFilter5	1.40	1.12	0.294	159999
129481	WZ_Wm13Z13_mll0p4614d0_2LeptonFilter5	0.954	1.12	0.351	190000
129482	WZ_Wm13Z15_mll3p804d0_2LeptonFilter5	0.175	1.12	0.169	76000
129483	WZ_Wm15Z11_mll0p250d0_2LeptonFilter5	1.40	1.12	0.143	70000
129484	WZ_Wm15Z13_mll0p4614d0_2LeptonFilter5	0.938	1.12	0.183	76000
129485	WZ_Wm15Z15_mll3p804d0_2LeptonFilter5	0.172	1.12	0.0590	9000
129486	WZ_W11Z11_mll0p250d0_2LeptonFilter5	0.980	1.14	0.297	189899
129487	WZ_W11Z13_mll0p4614d0_2LeptonFilter5	0.639	1.14	0.353	190000
129488	WZ_W11Z15_mll3p804d0_2LeptonFilter5	0.113	1.14	0.160	76000
129489	WZ_W13Z11_mll0p250d0_2LeptonFilter5	0.936	1.14	0.298	190000
129490	WZ_W13Z13_mll0p4614d0_2LeptonFilter5	0.649	1.14	0.354	190000
129491	WZ_W13Z15_mll3p804d0_2LeptonFilter5	0.113	1.14	0.160	76000
129492	WZ_W15Z11_mll0p250d0_2LeptonFilter5	0.936	1.14	0.148	76000
129493	WZ_W15Z13_mll0p4614d0_2LeptonFilter5	0.639	1.14	0.187	75999
129494	WZ_W15Z15_mll3p804d0_2LeptonFilter5	0.111	1.14	0.0570	19000
178411	ZZ_2e2tau_mll4_taufilter	0.175	1.00	0.0840	100000
178412	ZZ_2mu2tau_mll4_taufilter	0.175	1.00	0.0820	100000
178413	ZZ_4tau_mll4_taufilter	0.0770	1.00	0.324	299998

Table A.13: Additional Powheg+Pythia8 Dibosons MC samples with their corresponding sample ID, final state, NLO cross section, k-factor filter efficiency and number of generated events. These samples are used for computing generator systematic uncertainties on the Dibosons prediction in the hadronic channels.

Sample ID	Name (event generator: Powheg+Pythia8)	NLO [pb]	k-factor	filter eff.	No. of events
179385	WZ_Wm11Z15_mll3p80d40_taufilter	0.175	1.12	0.163	76000
179386	WZ_Wm13Z15_mll3p80d40_taufilter	0.175	1.12	0.164	66000
179387	WZ_Wm15Z11_mll0p250d0_taufilter	1.40	1.12	0.0530	19000
179388	WZ_Wm15Z13_mll0p4614d0_taufilter	0.938	1.12	0.0580	19000
179389	WZ_Wm15Z15_mll3p804d0_taufilter	0.172	1.12	0.198	19000
179390	WZ_W11Z15_mll3p80d40_taufilter	0.113	1.14	0.151	75999
179391	WZ_W13Z15_mll3p80d40_taufilter	0.113	1.14	0.152	76000
179392	WZ_W15Z11_mll0p250d0_taufilter	0.936	1.14	0.0570	19000
179393	WZ_W15Z13_mll0p4614d0_taufilter	0.639	1.14	0.0660	19000
179394	WZ_W15Z15_mll3p804d0_taufilter	0.111	1.14	0.183	19000

Table A.14: Additional Powheg+Pythia8 Dibosons MC samples continued from Table A.13

B

Simulated signals

Sample ID	Λ [TeV]	$\tan\beta$	σ [pb]
175821	40	2	0.71
175822	40	5	0.76
175823	40	10	0.77
175824	40	15	0.77
175825	40	20	0.78
175826	40	30	0.80
175827	40	36	0.84
175828	40	37	0.85
175829	50	2	0.18
175830	50	5	0.20
175831	50	10	0.21
175832	50	15	0.21
175833	50	20	0.21
175834	50	30	0.21
175835	50	40	0.23
175836	50	43	0.25
175837	50	44	0.26
175838	60	2	0.057
175839	60	5	0.067
175840	60	10	0.070
175841	60	15	0.070
175842	60	20	0.071
175843	60	30	0.073
175844	60	40	0.079
175845	60	49	0.095
175846	60	50	0.099
175847	70	2	0.021
175848	70	5	0.026
175849	70	10	0.028
175850	70	15	0.028
175851	70	20	0.029
175852	70	30	0.030
175853	70	40	0.032
175854	70	50	0.038
175855	70	57	0.049
175856	70	58	0.051
175857	80	2	0.0093
175858	80	5	0.012
175859	80	10	0.013
175860	80	15	0.013
175861	80	20	0.013
175862	80	30	0.014
175863	80	40	0.015
175864	80	50	0.017
175865	80	58	0.022
175866	80	59	0.023
175867	90	2	0.0045
175868	90	5	0.0061
175869	90	10	0.0067
175870	90	15	0.0068
175871	90	20	0.0069
175872	90	30	0.0072
175873	90	40	0.0078
175874	90	50	0.0089
175875	90	60	0.011
175876	90	61	0.012
175877	90	62	0.012
175878	100	2	0.0024
175879	100	5	0.0033
175880	100	10	0.0037
175881	100	15	0.0038
175882	100	20	0.0039
175883	100	30	0.0040
175884	100	40	0.0043
175885	100	50	0.0049
175886	100	60	0.0061
175887	100	61	0.0063
175888	100	62	0.0065
175889	110	2	0.0014
175890	110	5	0.0019
175891	110	10	0.0022
175892	110	15	0.0022
175893	110	20	0.0023
175894	110	30	0.0024
175895	110	40	0.0026
175896	110	50	0.0029
175897	110	60	0.0035
175898	110	61	0.0036
175899	110	62	0.0037

Table B.1: List of MC signal samples for various points in the SUSY GMSB parameter grid. All samples are generated using Herwig++. Four out of six parameters defining the GMSB points are the same for all samples: $\langle S\rangle = 250\,\mathrm{TeV}$, $N_5 = 3$, $\mathrm{sign}(\mu) = +$ and $C_{\tilde{G}} = 1$. The parameters Λ and $\tan\beta$ are varied as shown in the table. The leading-order cross section is also given. Note that the samples are re-weighted using the NLO cross section per process.

Sample ID	Λ [TeV]	$\tan\beta$	σ [pb]
174170	117	700	0.36
174171	117	860	0.068
174172	117	940	0.031
174173	117	1020	0.015
174174	117	1100	0.0071
174175	117	1180	0.0035
174176	117	400	17
174177	117	520	3.1
174178	117	640	0.71
174179	179	700	0.36
174180	179	860	0.068
174181	179	940	0.031
174182	179	1020	0.015
174183	179	1100	0.0071
174184	179	1180	0.0035
174185	179	400	17
174186	179	520	3.1
174187	179	640	0.71
174188	210	700	0.36
174189	210	860	0.068
174190	210	940	0.031
174191	210	1020	0.015
174192	210	1100	0.0071
174193	210	1180	0.0035
174194	210	400	17
174195	210	520	3.1
174196	210	640	0.71
174197	242	700	0.36
174198	242	860	0.068
174199	242	940	0.031
174200	242	1020	0.015
174201	242	1100	0.0071
174202	242	1180	0.0035
174203	242	400	17
174204	242	520	3.1
174205	242	640	0.71
174206	274	700	0.36
174207	274	860	0.068
174208	274	940	0.031
174209	274	1020	0.015
174210	274	1100	0.0071
174211	274	1180	0.0035
174212	274	400	17
174213	274	520	3.1
174214	274	640	0.71
174215	305	700	0.36
174216	305	860	0.068
174217	305	940	0.031
174218	305	1020	0.015
174219	305	1100	0.0071
174220	305	1180	0.0035
174221	305	400	17
174222	305	520	3.1
174223	305	640	0.71
174224	337	700	0.36
174225	337	860	0.068
174226	337	940	0.031
174227	337	1020	0.015
174228	337	1100	0.0071
174229	337	1180	0.0035
174230	337	400	17
174231	337	520	3.1
174232	337	640	0.71
177275	117	1260	0.0020
177276	179	1260	0.0020
177277	210	1260	0.0020
177278	242	1260	0.0020
177279	274	1260	0.0020
177280	305	1260	0.0020
177281	337	1260	0.0020

Table B.2: List of MC samples for the SUSY signal in the nGM model. Masses are quoted in GeV. All samples are generated using Herwig++. The next-to-leading-order cross section is also given.

Sample ID	Λ [TeV]	$\tan\beta$	σ [pb]
174053	400	250	6.1
174054	400	300	2.3
174055	400	350	1.00
174056	400	400	0.46
174057	400	450	0.23
174058	400	500	0.12
174059	400	550	0.063
174060	400	600	0.035
174061	400	650	0.020
174062	400	700	0.012
174063	400	750	0.0075
174064	400	800	0.0048
174065	600	250	4.6
174066	600	300	1.7
174067	600	350	0.72
174068	600	400	0.34
174069	600	450	0.17
174070	600	500	0.088
174071	600	550	0.048
174072	600	600	0.027
174073	600	650	0.016
174074	600	700	0.0092
174075	600	750	0.0056
174076	600	800	0.0035
174077	800	250	3.9
174078	800	300	1.4
174079	800	350	0.56
174080	800	400	0.26
174081	800	450	0.13
174082	800	500	0.069
174083	800	550	0.038
174084	800	600	0.022
174085	800	650	0.013
174086	800	700	0.0076
174087	800	750	0.0047
174088	800	800	0.0029
174089	1000	250	3.4
174090	1000	300	1.2
174091	1000	350	0.48
174092	1000	400	0.22
174093	1000	450	0.11
174094	1000	500	0.059
174095	1000	550	0.033
174096	1000	600	0.019
174097	1000	650	0.011
174098	1000	700	0.0067
174099	1000	750	0.0042
174100	1000	800	0.0026
174101	1200	250	2.9
174102	1200	300	1.1
174103	1200	350	0.44
174104	1200	400	0.20
174105	1200	450	0.10
174106	1200	500	0.053
174107	1200	550	0.030
174108	1200	600	0.017
174109	1200	650	0.010
174110	1200	700	0.0063
174111	1200	750	0.0039
174112	1200	800	0.0025
174113	1400	250	2.4
174114	1400	300	0.92
174115	1400	350	0.40
174116	1400	400	0.19
174117	1400	450	0.095
174118	1400	500	0.051
174119	1400	550	0.028
174120	1400	600	0.017
174121	1400	650	0.0099
174122	1400	700	0.0061
174123	1400	750	0.0039
174124	1400	800	0.0025
174125	1600	250	1.9
174126	1600	300	0.81
174127	1600	350	0.37
174128	1600	400	0.18
174129	1600	450	0.091
174130	1600	500	0.049
174131	1600	550	0.028
174132	1600	600	0.016
174133	1600	650	0.0098
174134	1600	700	0.0061
174135	1600	750	0.0038
174136	1600	800	0.0025

Table B.3: List of MC samples for the SUSY signal in the bRPV model (part 1). Masses are quoted in GeV. All samples are generated using PYTHIA6. Common parameters are $A_0 = -2m_0$, $\tan\beta = 30$ and sign $\mu = +1$. The leading-order cross section is also given. Note that the samples are re-weighted using the NLO cross section per process.

Sample ID	Λ [TeV]	$\tan\beta$	σ [pb]
174137	1800	250	1.6
174138	1800	300	0.70
174139	1800	350	0.33
174140	1800	400	0.17
174141	1800	450	0.087
174142	1800	500	0.048
174143	1800	550	0.028
174144	1800	600	0.016
174145	1800	650	0.0098
174146	1800	700	0.0061
174147	1800	750	0.0039
174148	1800	800	0.0025
174149	2000	250	1.4
174150	2000	300	0.62
174151	2000	350	0.30
174152	2000	400	0.15
174153	2000	450	0.083
174154	2000	500	0.047
174155	2000	550	0.027
174156	2000	600	0.016
174157	2000	650	0.0098
174158	2000	700	0.0061
174159	2000	750	0.0039
174160	2000	800	0.0025
174161	2200	250	1.3
174162	2200	300	0.56
174163	2200	350	0.27
174164	2200	400	0.14
174165	2200	450	0.079
174166	2200	500	0.045
174167	2200	550	0.026
174168	2200	600	0.016
174169	2200	650	0.0098
174980	400	200	20
174981	600	200	17
174982	800	200	16
174983	1000	200	13
174984	1200	200	9.2
174985	1400	200	6.6
174986	1600	200	5.1
174987	1800	200	4.3

Table B.4: List of MC samples for the SUSY signal in the bRPV model continued from Table B.3.

C

Computation of missing energy

In contrast to particle objects, “Missing Energy” has no unambiguous physical definition. It is computed by building the balance of all energy measurements in one event. By this approach it is susceptible to energy calibrations and definitions in all underlying object. For the tau based searches, especially the difference between taus and jets is of particular interest.

The default $\not{E}_T$ definition “MET RefFinal” comprises a tau term which is build from all taus fulfilling “medium” tau identification criteria. However for most SUSY analyses, a different kind of $\not{E}_T$ (“MET Egamma10NoTau”) computation which treats all hadronic objects as jets, independent of any tau identification has emerged as most widespread approach. The difference between these two flavors boils down to the choice of calibration for some hadronic object. In MET RefFinal, it is calibrated as a tau if it fulfills medium tau identification criteria and as jet otherwise while in MET Egamma10NoTau it is calibrated as a jet in any case.

The following studies are based on the p1328 SUSYD3PD production. It compares the two aforementioned $\not{E}_T$ flavors for both a $t\bar{t}$ sample (sample id 117809, Sherpa, $t\bar{t} \to \tau\tau$) and one Z+jets sample (sample id 147772, Sherpa, $Z \to \tau\tau$). These samples are not used in the main analysis, however the findings are general and also applicable for the nominal samples, since neither the computational approach nor the basic definitions have changed. These samples are chosen to represent different kinematic extremes. $t\bar{t}$ events tend to have a high level of general activity with multiple sources of $\not{E}_T$ from the decay of the W. On the contrary, in Z+jets one expects events where the neutrinos of the tau decays are the only source of $\not{E}_T$.

In general, there are two approaches for the computation of “$\not{E}_T$”. All flavors of missing energy are computed centrally and stored in the data files. One can also compute this quantity at analysis level based on all identified objects in the event. However, even the latter approach relies on a priory information since it employs “weight maps” which are computed centrally. It is only possible to change the energy calibration of a given object at analysis level but not the association to a given class of physics objects. Figure C.1 shows a closure test between the centrally computed and the custom computed $\not{E}_T$. It also gives some impression of the influence of the tau term in the $\not{E}_T$ computation.

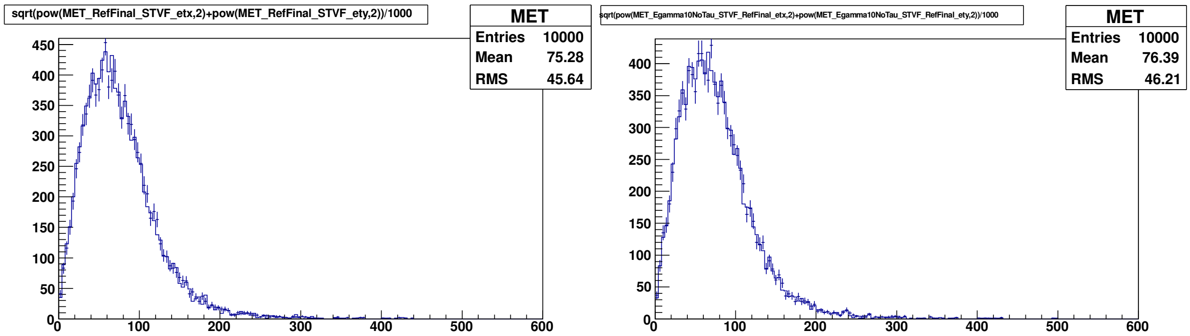

(a) MET RefFinal (b) MET Egamma10NoTau

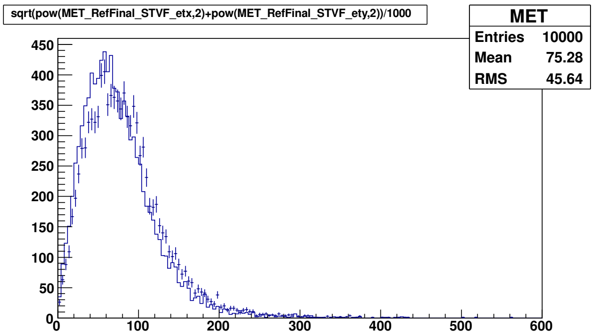

(c) MET RefFinal w/o tau term

Figure C.1: Closure test for the re-computation of $\not\!\!E_T$ terms from analysis objects. The solid line shows the distributions obtained from precomputed information stored in the data files while the points show the distributions obtained from analysis objects. A very good agreement is obtained for both flavors of $\not\!\!E_T$ considered (a and b). Note the effect of omitting the tau term in the generally tau-aware MET RefFinal flavor (c).

Additional complication arises due to the choice of identification strength of the tau candidates. For the analyses "loose" taus are considered, while MET RefFinal relies on medium taus. However, there is no easy way to recompute $\not\!\!E_T$ for different tau ID levels due to the weight map. The influence of a discrepancy between object ID level and $\not\!\!E_T$ ID level has also to be evaluated.

Figure C.2 shows comparisons for the different $\not\!\!E_T$ flavors on the $t\bar{t}$ sample at one and two tau cut stages both for medium and loose taus. Note that MET RefFinal is computed from medium taus in all cases. While at one tau level, no difference is visible some difference seem to arise at two tau level. This difference is well covered by the statistical uncertainty on the samples alone.

Figure C.3 shows the same comparisons for the Z+jets sample. Here, a clear difference is visible at both one tau and two tau cut stage. Note that the difference is significantly more pronounced for medium taus in the cut than for loose taus.

These comparisons show that one is sensitive to the $\not\!\!E_T$ definition only in cases where the invisible part of the tau decay contributed significantly to the physical missing energy. This is easily understood since in such a topology the $\not\!\!E_T$ vector is expected to point in the direction of the taus. Hence, a difference of the calibration of the tau object (what the different $\not\!\!E_T$ flavors boil down to) translates directly in a difference in the $\not\!\!E_T$ magnitude. In $t\bar{t}$ events on the other hand, the neutrinos from the W decays contribute probably more to the physical $\not\!\!E_T$. Hence the direction of the taus and the $\not\!\!E_T$ are

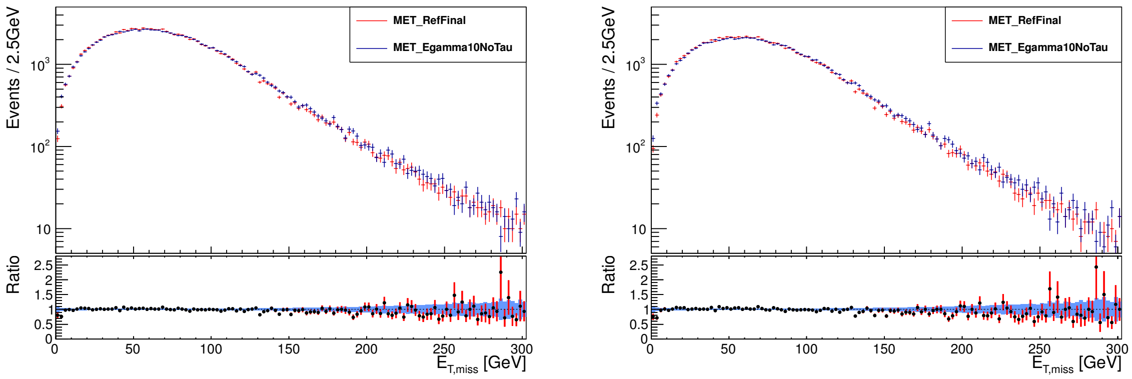

(a) 1τ cut, loose τ

(b) 1τ cut, medium τ

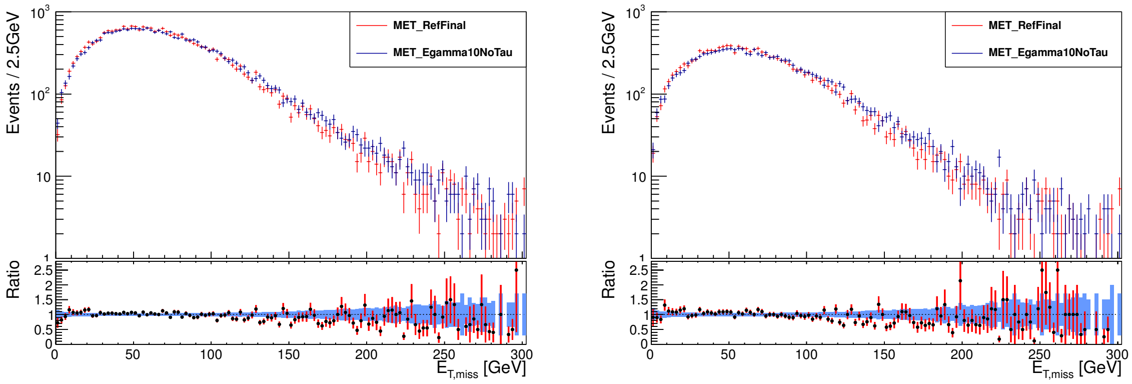

(c) 2τ cut, loose τ

(d) 2τ cut, medium τ

Figure C.2: Comparison of the $\not{E}_T$ distribution for both $\not{E}_T$ flavors for the $t\bar{t}$ sample. Comparisons are made after requiring one or two taus with both medium and loose tau ID criteria. MET RefFinal is computed using medium taus in all cases.

more or less uncorrelated.

Given that the aim of these searches are SUSY scenarios with invisible particles, the expected topology is much more $t\bar{t}$ like than Z like. In fact, the analysis employs some cuts that explicitly suppress topologies where the $\not{E}_T$ vector and the tau direction are aligned (e.g. the $m_{\mathrm{T}}^{\tau_1} + m_{\mathrm{T}}^{\tau_2}$ cuts). Moreover these studies show that care has to be taken when employing different identification strengths to tau objects in analysis and $\not{E}_T$ level so ideally one would have to have a different $\not{E}_T$ flavor for each tau identification strength.

Concluding, it was decided to choose the standard SUSY MET Egamma10NoTau computation to be independent of the tau ID applied and since effects of SUSY-like topologies are expected to be small.

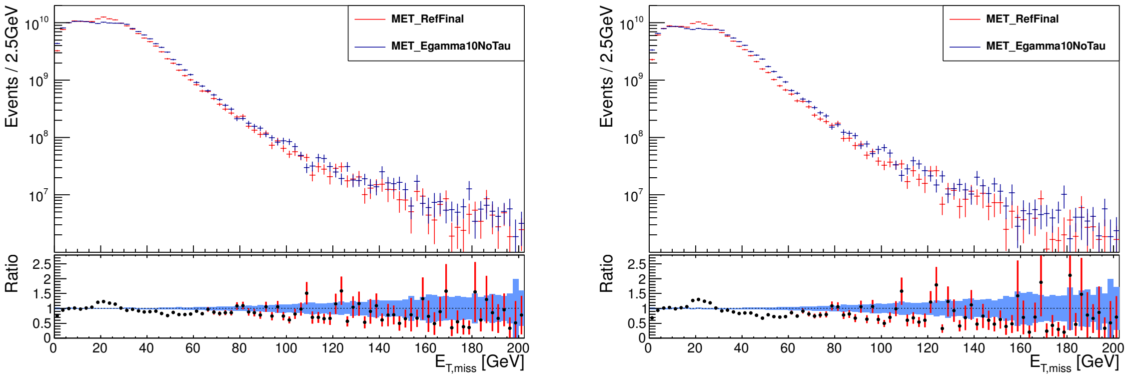

(a) 1τ cut, loose τ

(b) 1τ cut, medium τ

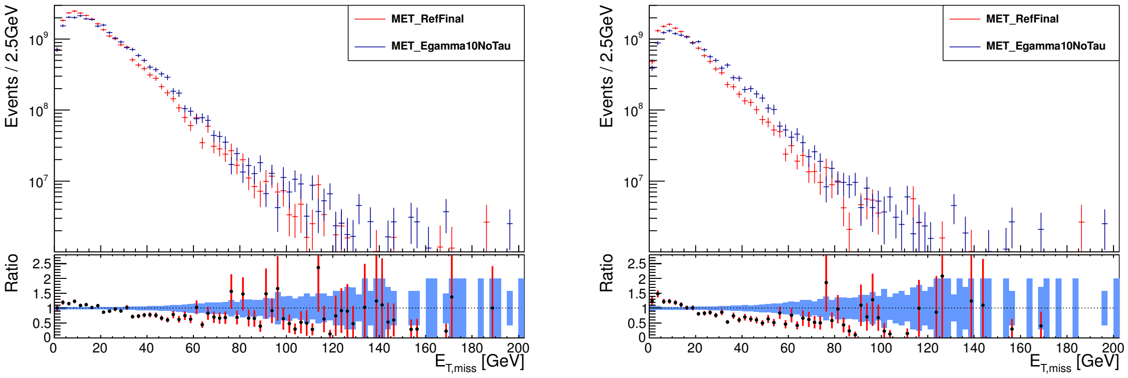

(c) 2τ cut, loose τ

(d) 2τ cut, medium τ

Figure C.3: Comparison of the $\not\!\!E_T$ distribution for both $\not\!\!E_T$ flavors for the Z+jets sample. Comparisons are made after requiring one or two taus with both medium and loose tau ID criteria. MET RefFinal is computed using medium taus in all cases.

D

Studies on background simulations

D.1 Choice of a $t\bar{t}$ generator

In earlier production campaigns, a mis-modeling of the $m_{\mathrm{T}}^{\tau_1} + m_{\mathrm{T}}^{\tau_2}$-shape in the SHERPA $t\bar{t}$ samples has been observed. This mis-modeling is clearly visible in Figure D.1 a). Figure D.1 b)-e) shows the same distribution with the same kinematic selection in the production p1512 used for this thesis. Clearly, the bias is reduced or even vanished. The tau ID has undergone significant improvements between the two production releases which obviously cured the problem observed before.

In the current production there are four different samples available, all containing a similar number of simulated events. Looking at the shapes for the four available generators, no clear preference for any of them is striking. This is cross-checked with various others kinematic distributions (c.f. Figures D.2-D.7). While in some one generator may outperform the others there is no clear “winner”.

Since for POWHEG there is a large extension with the fast simulation AFII available (c.f. Section D.2), it was chosen as baseline generator. For deriving systematic uncertainties, ALPGEN is chosen as comparison generator. This decision was driven by the fact that the ALPGEN sample is different from the POWHEG in nearly all aspects so an uncertainty derived from this comparison is expected to cover many possible sources of differences.

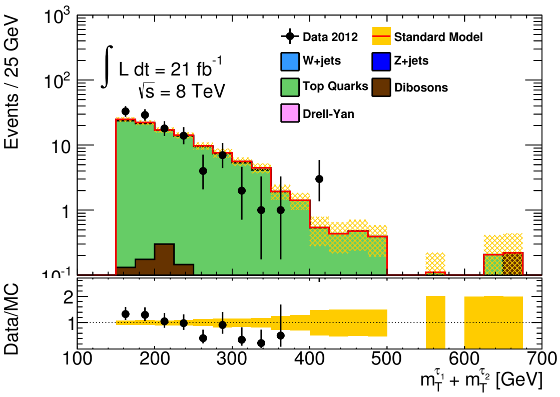

(a) Sherpa in p1318

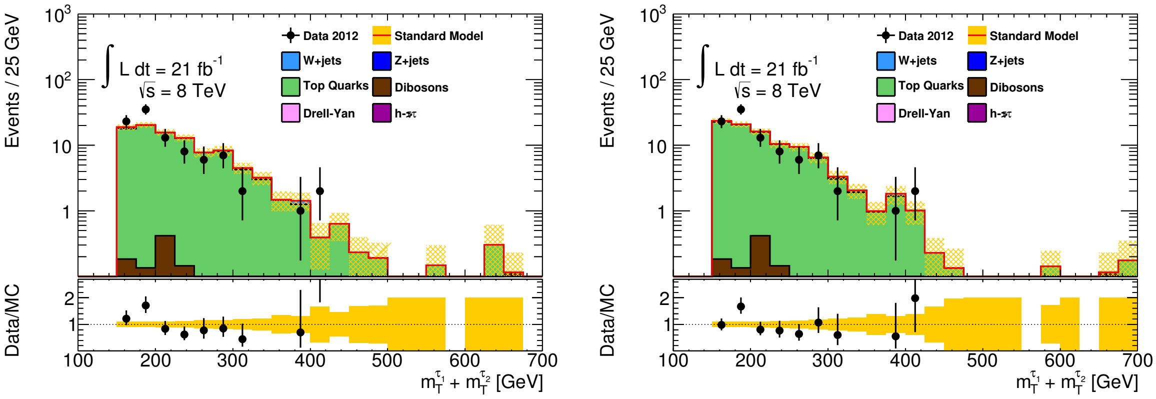

(b) Sherpa in p1512 (c) Alpgen in p1512

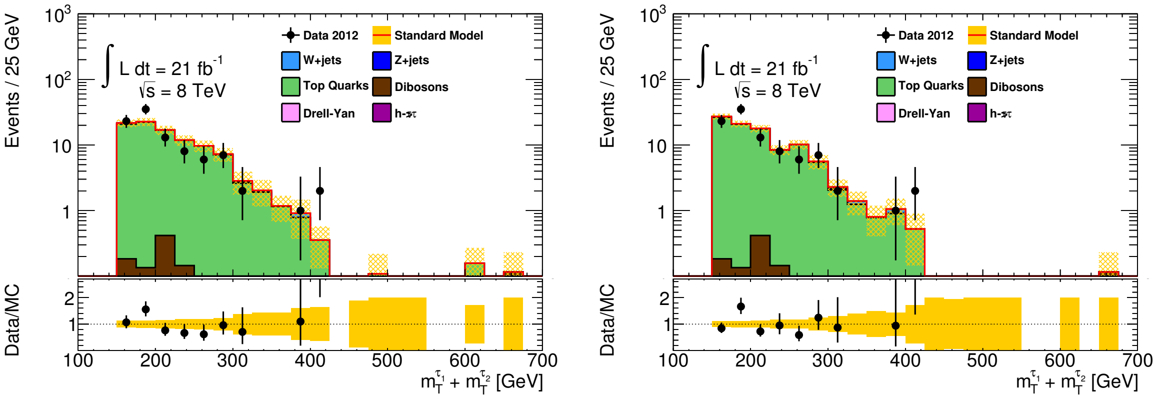

(d) MC@NLO in p1512 (e) Powheg in p1512

Figure D.1: $m_T^{\tau_1} + m_T^{\tau_2}$ shape comparison in the top CR in p1318 usingSHERPA (a) and in p1512 for four different generators (b-e). The observer bias in p1318 is largely cured with the new tau ID in p1512. All four generators show a reasonable agreement.

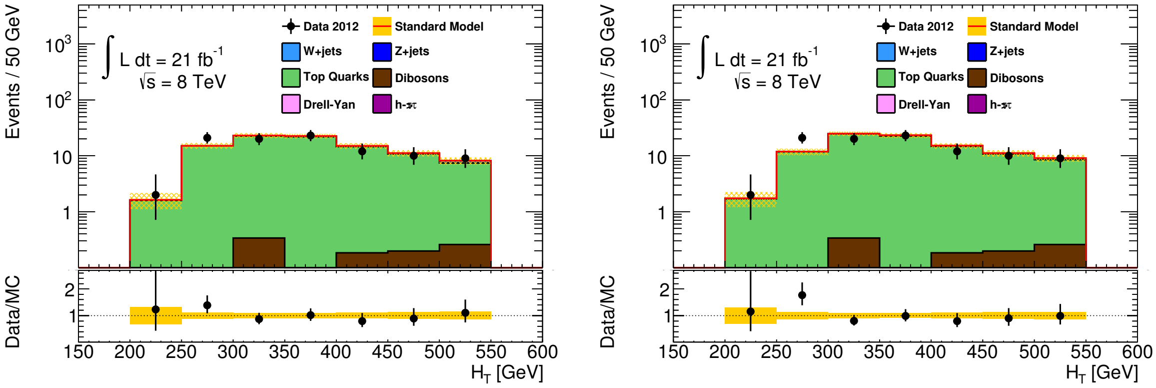

(a) H_T in SHERPA

(b) H_T in ALPGEN

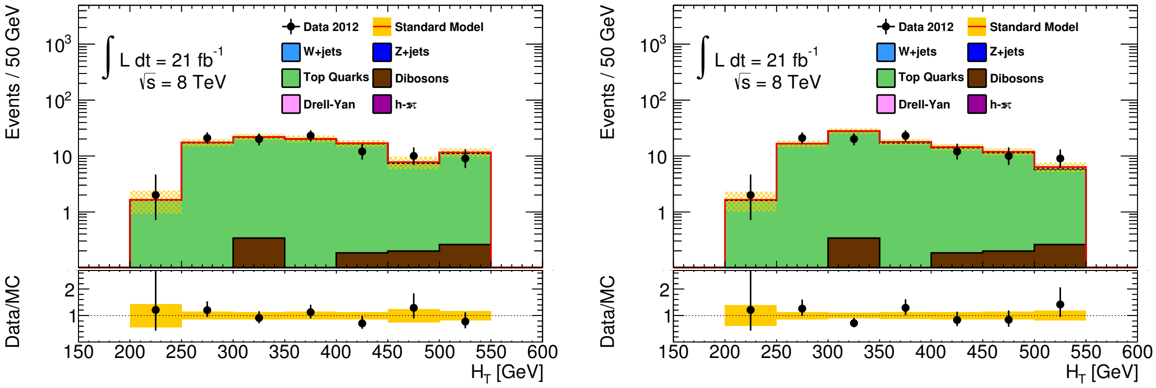

(c) H_T in MC@NLO

(d) H_T in POWHEG

Figure D.2: H_T shape comparison in the top CR for four different generators. All four generators show a reasonable agreement.

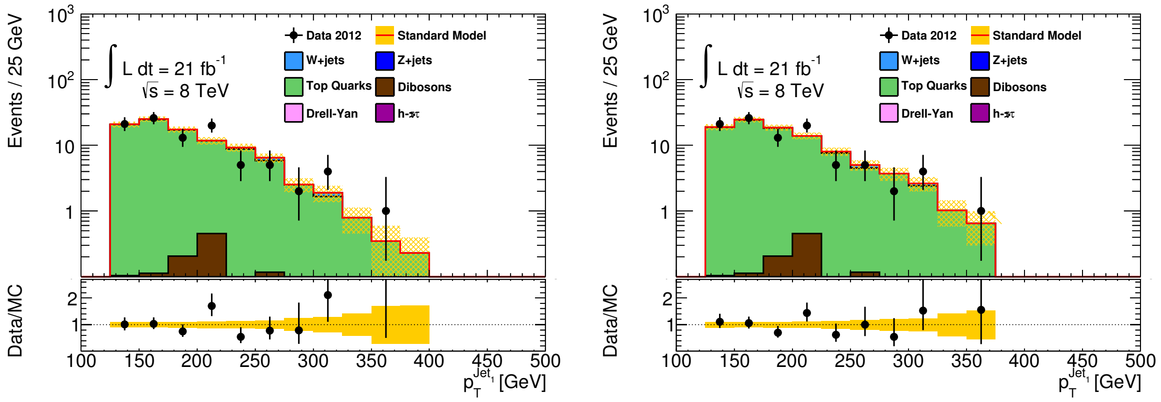

(a) $p_T^{\mathrm{jet}_1}$ in SHERPA
(b) $p_T^{\mathrm{jet}_1}$ in ALPGEN

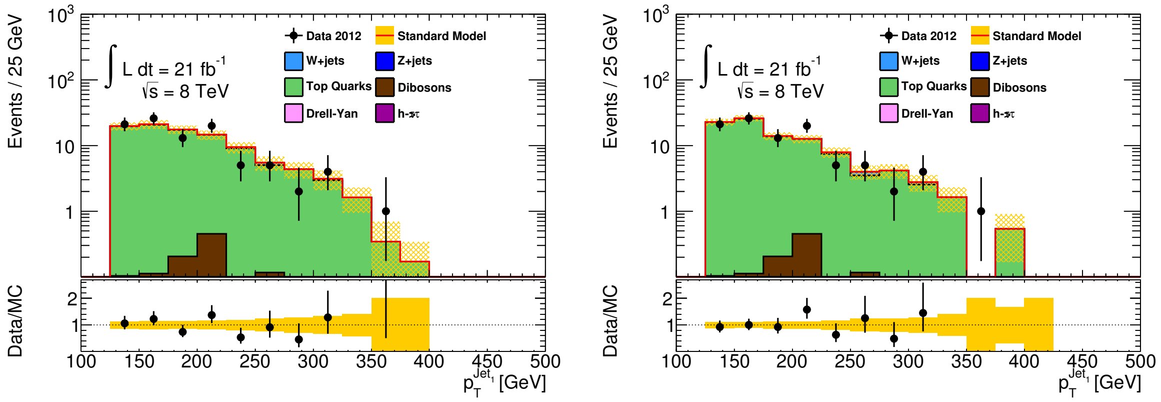

(c) $p_T^{\mathrm{jet}_1}$ in MC@NLO
(d) $p_T^{\mathrm{jet}_1}$ in POWHEG

Figure D.3: $p_T^{\mathrm{jet}_1}$ shape comparison in the top CR for four different generators. All four generators show a reasonable agreement.

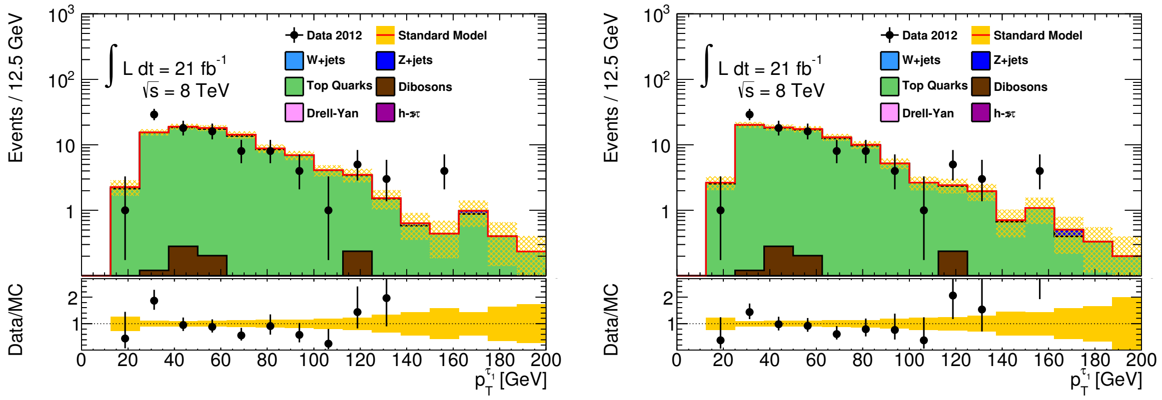

(a) $p_T^{\tau_1}$ in SHERPA (b) $p_T^{\tau_1}$ in ALPGEN

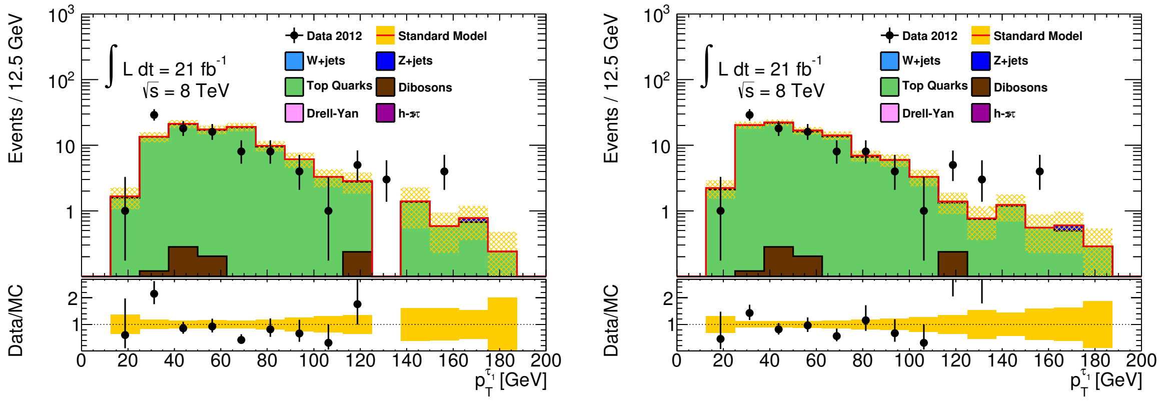

(c) $p_T^{\tau_1}$ in MC@NLO (d) $p_T^{\tau_1}$ in POWHEG

Figure D.4: $p_T^{\tau_1}$ shape comparison in the top CR for four different generators. All four generators show a reasonable agreement.

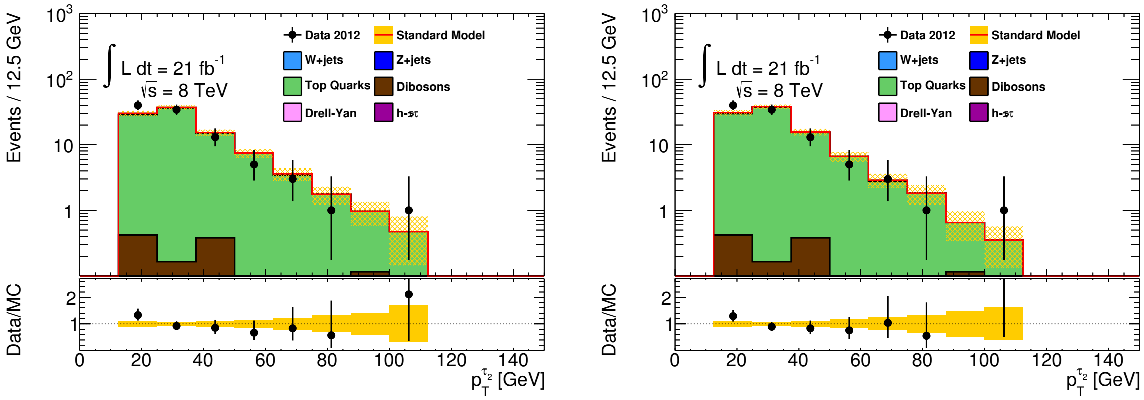

(a) $p_T^{\tau_2}$ in SHERPA

(b) $p_T^{\tau_2}$ in ALPGEN

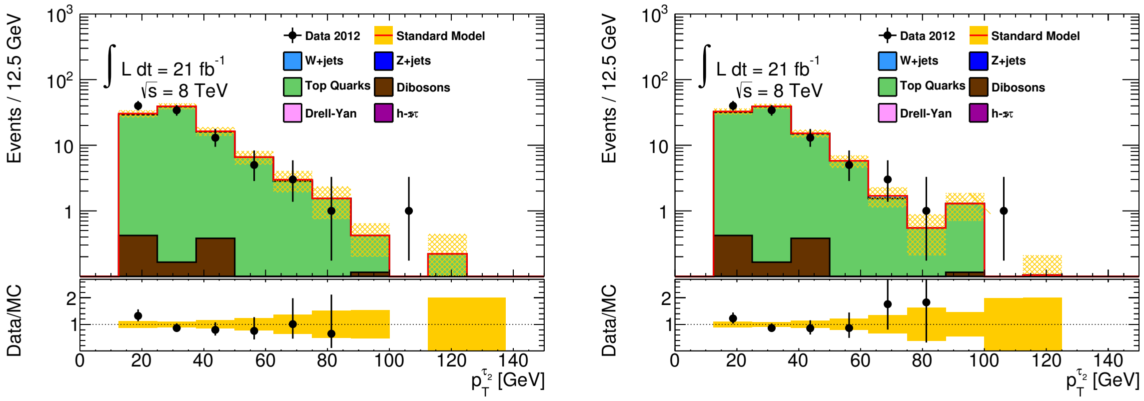

(c) $p_T^{\tau_2}$ in MC@NLO

(d) $p_T^{\tau_2}$ in POWHEG

Figure D.5: $p_T^{\tau_2}$ shape comparison in the top CR for four different generators. All four generators show a reasonable agreement.

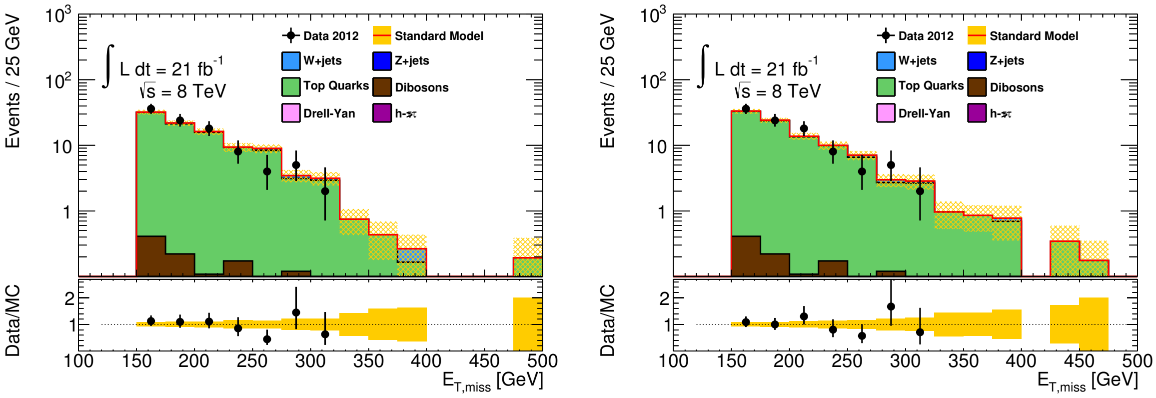

(a) $\not{E}_T$ in SHERPA (b) $\not{E}_T$ in ALPGEN

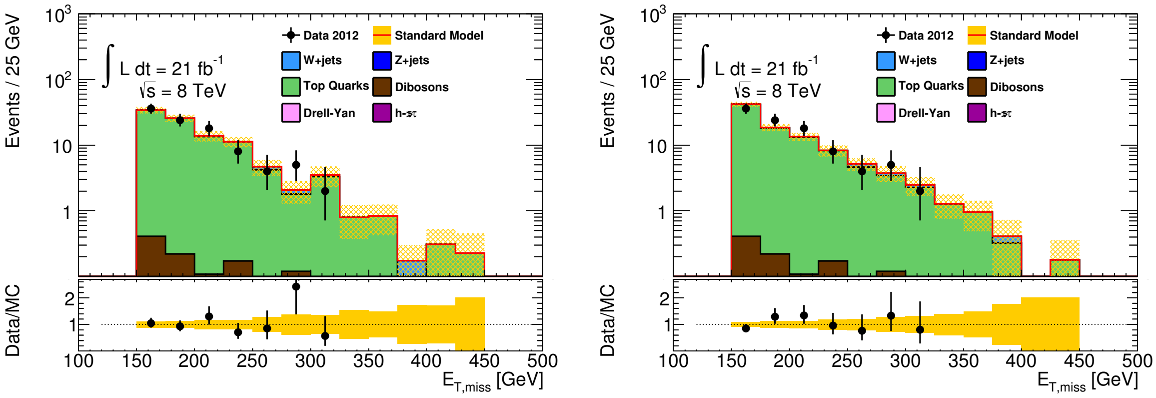

(c) $\not{E}_T$ in MC@NLO (d) $\not{E}_T$ in POWHEG

Figure D.6: $\not{E}_T$ shape comparison in the top CR for four different generators. All four generators show a reasonable agreement.

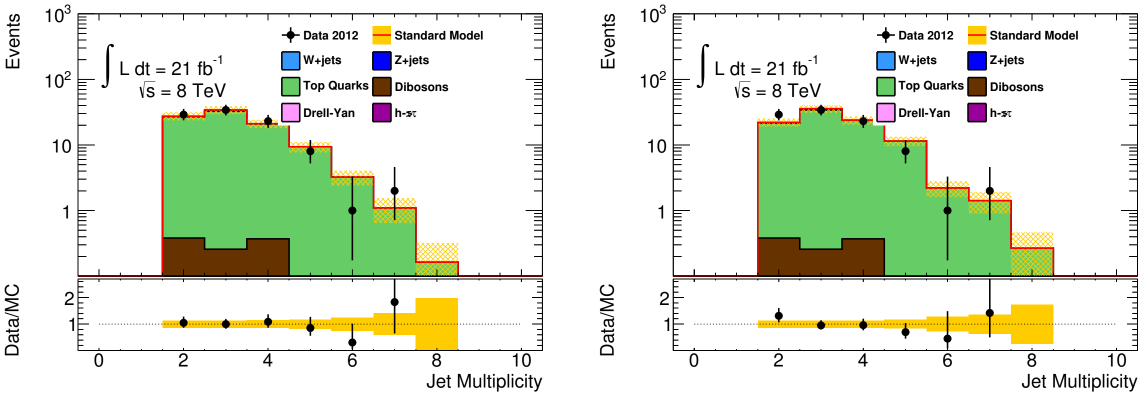

(a) N_{jet} in SHERPA (b) N_{jet} in ALPGEN

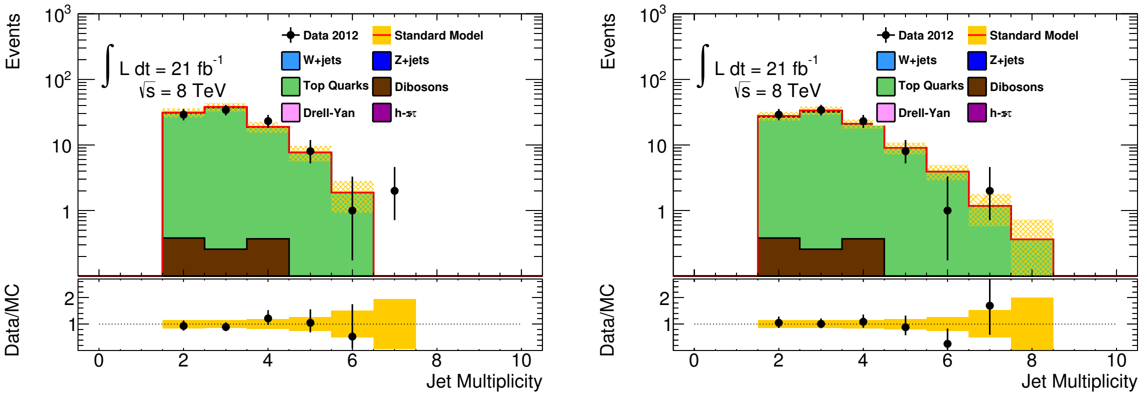

(c) N_{jet} in MC@NLO (d) N_{jet} in POWHEG

Figure D.7: N_{jet} shape comparison in the top CR for four different generators. All four generators show a reasonable agreement.

D.2 Validation of fast simulation samples

As shown before, there is no clear preference on the choice of a particular generator for $t\bar{t}$ from initial physics studies. However, the available number of simulated events for $t\bar{t}$ production simulated with POWHEG and AFII exceeds the number of events generated with full simulation (FS) by a factor of five. It is highly desirable to use this sample to decrease statistical uncertainties. The use of fast simulation for jets and light leptons is validated centrally by the respective performance groups and needed corrections are implemented in the respective reconstruction.

In former studies, results of varying quality are found when using AFII, depending on the generator and the studies kinematics. An individual evaluation is required for each analysis. This affects only true taus since fake taus are generally found to be unreliably described in simulation and have to be constraint from data anyway.

To account for possible mis-modeling of the taus in AFII, two corrections are provided by the Tau working group: One correction for the efficiency in terms of a kinematic dependent scaling factor and one correction for a p_T mis-modeling in terms of a p_T shift. In principle, both corrections are intended to be applied at the same time. However, some studies suggest that certain samples require the use of only one of the corrections while others don't require any treatment.

Also for the nominal *W/Z*+jets samples, some samples are only available in fast simulation depending on the vector boson p_T and the decay channels. For the decay of the W/Z to light lepton this comprises all samples with $p_T^{W/Z} < 280\,\text{GeV}$. Since those simulations contain only fake taus and are more or less negligible for the analysis due to the applied veto on light leptons, no further investigations are made. For those samples with bosons decaying into tau leptons, only samples with $p_T^{W/Z} < 70\,\text{GeV}$ are simulated in fast simulation. Studies show that events with these relatively low boson momenta are highly unlikely to end up in any signal region due to the $p_T^{\text{jet}_1}$ cut that requires a hard recoiling object in vector boson production events. Hence, the validation is focused on $t\bar{t}$.

A first comparison is made between full simulation, fast simulation and fast simulation including both tau specific corrections. Results for this are collected in Figure D.8. Obviously the agreement in the overall normalization and hence the efficiency of the tau ID is far better when not applying any correction to the AFII taus. The shape of the tau kinematic variables is well modeled both with and without corrections. No significant shape deviations are visible between corrected and uncorrected taus.

The correction on the tau efficiency actually lowers the tau ID performance in the AFII samples. A second comparison is made between FS, AFII and AFII using only the p_T correction. Special attention is given to subtle shape differences that might arise by correcting the tau candidates momentum. Figure D.9 shows a display of cutflows for different control and signal regions used in the analysis. Figure D.10 shows comparisons for different tau related kinematic variables used in the analysis for all events in the top control region. Figures D.11-D.12 show tau kinematics for various subsets of tau candidates in the same region. All comparisons show an excellent agreement between AFII and FS on the level of statistical uncertainties. No significant effect of the p_T correction on the quality of the shape agreement can be observed.

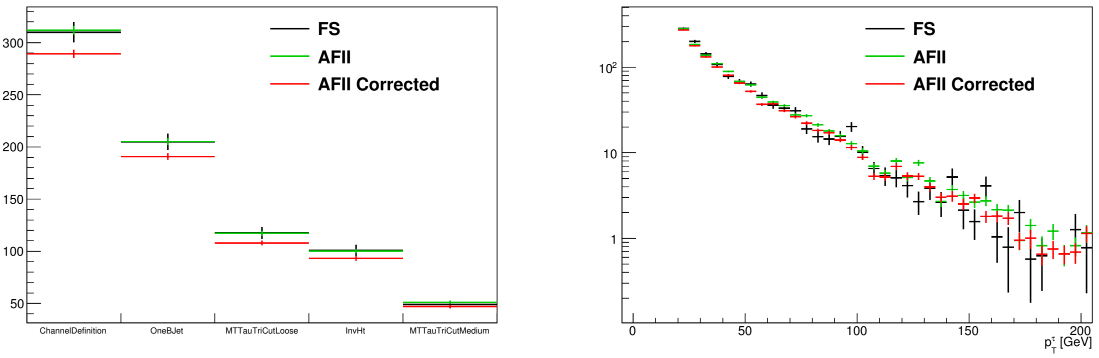

(a) Cutflow (b) τ p_T

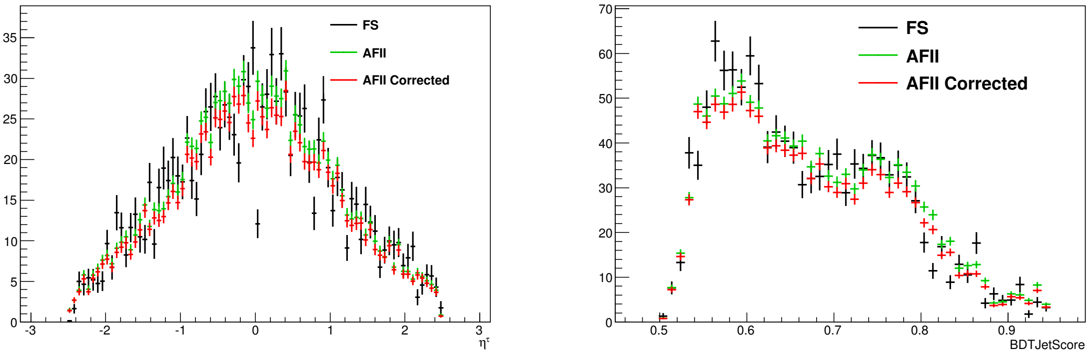

(c) τ η (d) Jet BDT

Figure D.8: Comparison of various tau kinematic distributions and the cut flow in the top control region for Full Simulation (FS), Fast Simulation (AFII) and Fast Simulation including full tau corrections (AFII Corrected). A good agreement between FS and AFII is observed while the tau corrections clearly underestimate the efficiency of the tau ID.

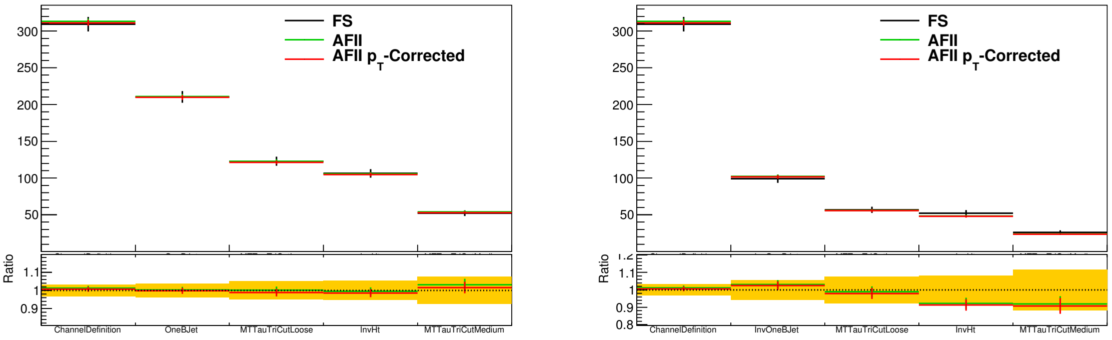

(a) Cutflow in top CR

(b) Cutflow in W CR

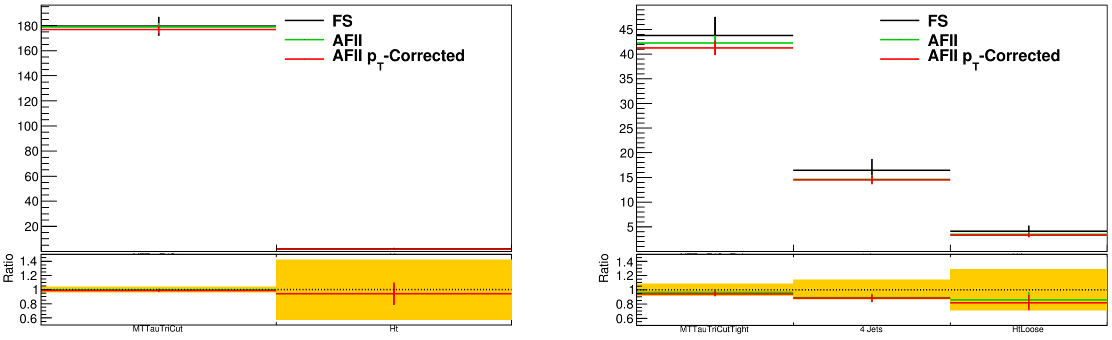

(c) Cutflow in Inclusive SR

(d) Cutflow in nGM SR

Figure D.9: Comparison of cutflows in different regions for Full Simulation (FS), Fast Simulation (AFII) and Fast Simulation including tau p_T corrections (AFII p_T-Corrected). A good agreement between FS and AFII is observed while the tau p_T corrections have only a very small effect.

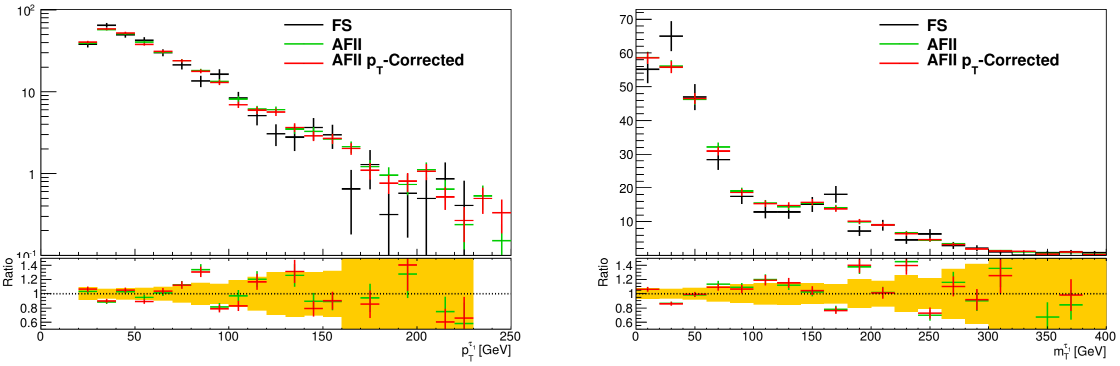

(a) $p_T^{\tau_1}$ (b) $m_\mathrm{T}^{\tau_1}$

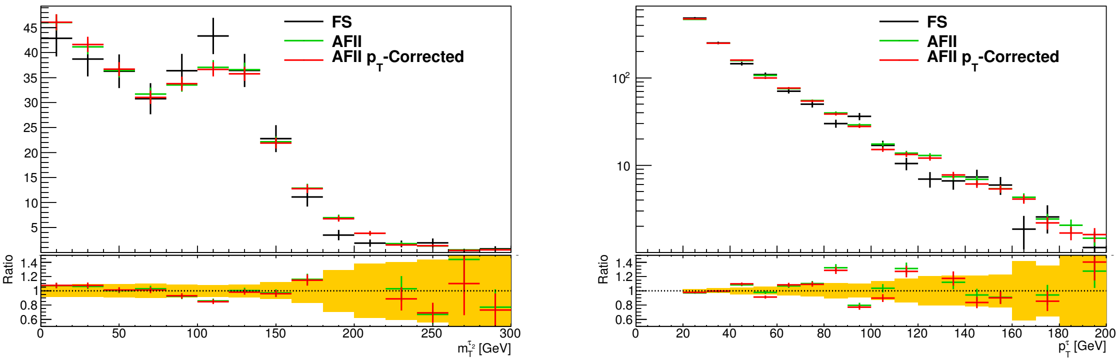

(c) $m_\mathrm{T}^{\tau_2}$ (d) τ p_T

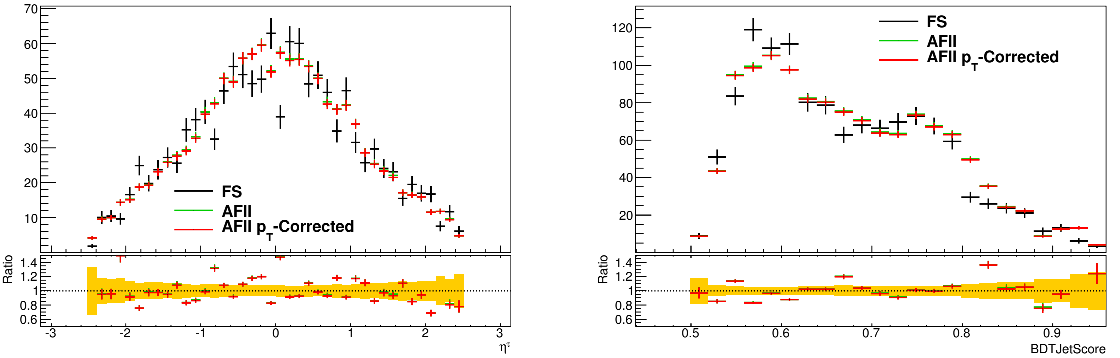

(e) τ η (f) Jet BDT

Figure D.10: Comparison of various kinematic distributions in different regions for Full Simulation (FS), Fast Simulation (AFII) and Fast Simulation including tau p_T corrections (AFII p_T-Corrected). A good agreement between FS and AFII is observed while the tau p_T corrections have only a very small effect.

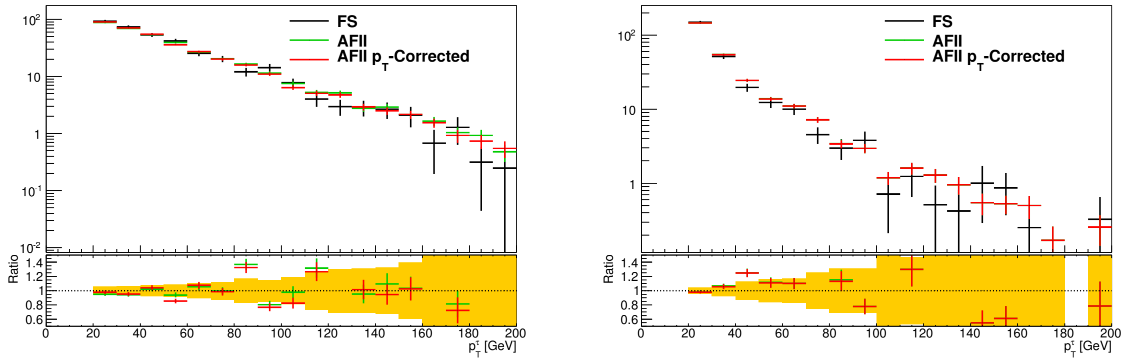

(a) τ p_T true taus

(b) τ p_T fake taus

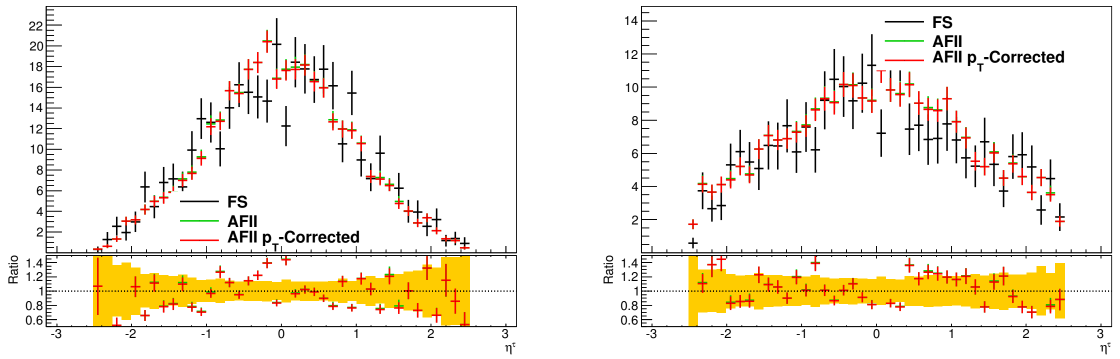

(c) τ η true taus

(d) τ η fake taus

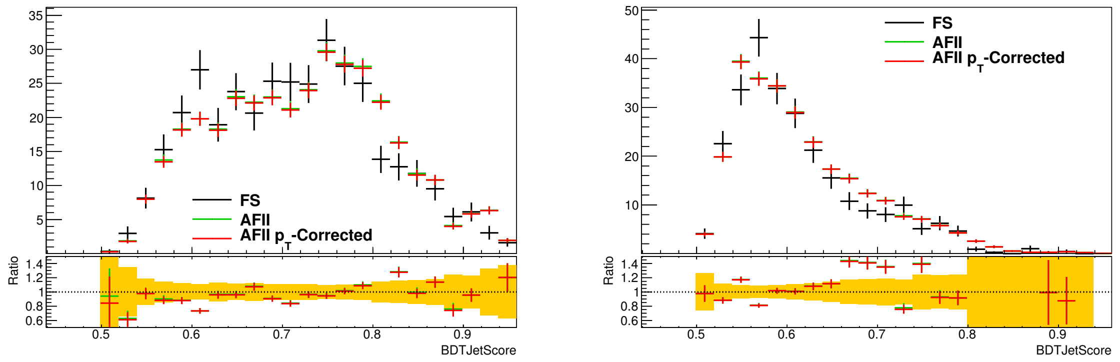

(e) Jet BDT true taus

(f) Jet BDT fake taus

Figure D.11: Comparison of various kinematic distributions for true and fake taus in different regions for Full Simulation (FS), Fast Simulation (AFII) and Fast Simulation including tau p_T corrections (AFII p_T-Corrected). A good agreement between FS and AFII is observed while the tau p_T corrections have only a very small effect.

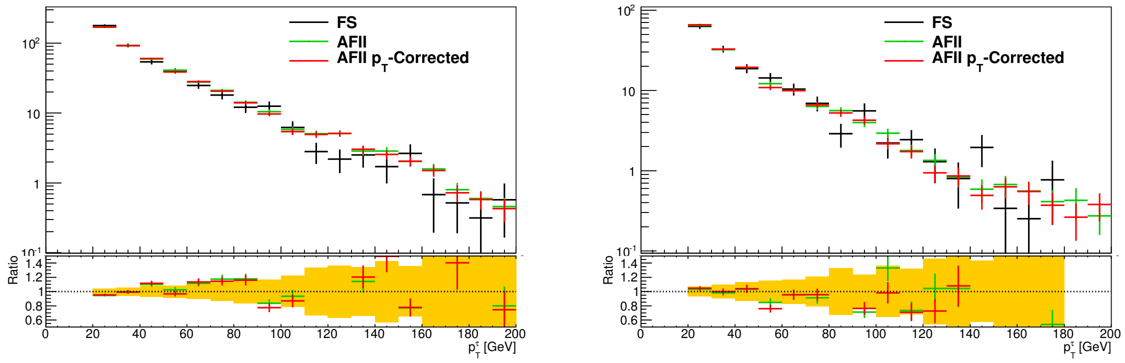

(a) τ p_T 1-prong taus

(b) τ p_T 3-prong taus

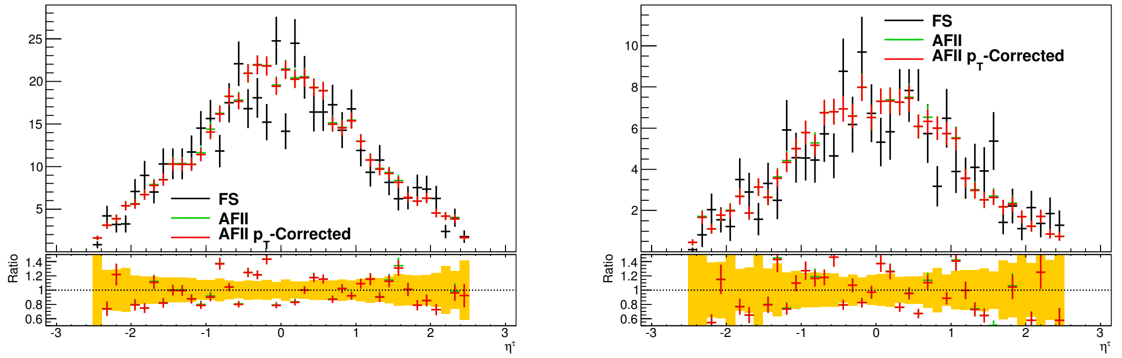

(c) τ η 1-prong taus

(d) τ η 3-prong taus

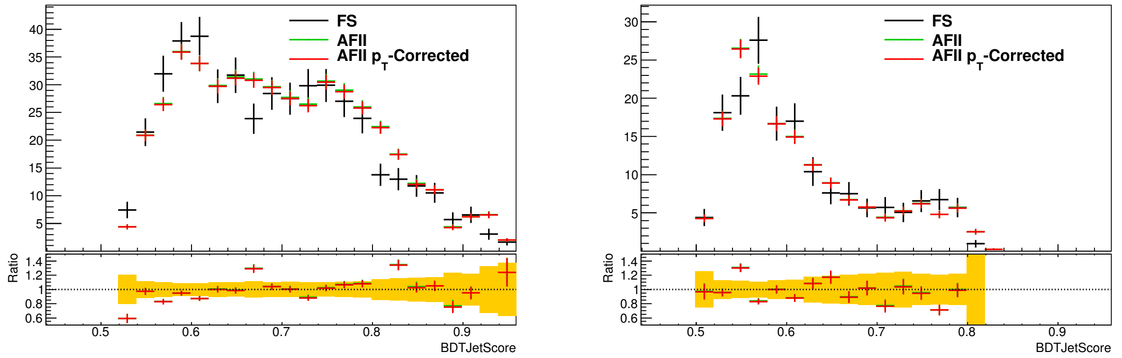

(e) Jet BDT 1-prong taus

(f) Jet BDT 3-prong taus

Figure D.12: Comparison of various kinematic distributions for 1-prong and 3-prong taus in different regions for Full Simulation (FS), Fast Simulation (AFII) and Fast Simulation including tau p_T corrections (AFII p_T-Corrected). A good agreement between FS and AFII is observed while the tau p_T corrections have only a very small effect.

In the light of these studies, it was decided together with the tau combined performance working group that the use of the large AFII $t\bar{t}$ sample is safe for the purpose of the analysis. Deviations observed are minimal and are on the level of the statistical uncertainty. Any overall normalization difference will be caught by the background estimation procedure and no notable shape difference can be found. An estimate of any possible normalization difference can be drawn from the distributions of the Jet-BDT score displayed for all tau candidates in a subset of the samples in study shown in Figure D.13. The very small shift between full simulation and AFII shape manifests in form of slight differences in the identification efficiency. Shifts are at a level of percent, while uncertainties of the choice of $t\bar{t}$ generators alone are typically in the order of few ten percents. Note that these plots include all tau candidates regardless of the event kinematics. For this reason, no further uncertainty is assigned to the use of fast simulation for taus.

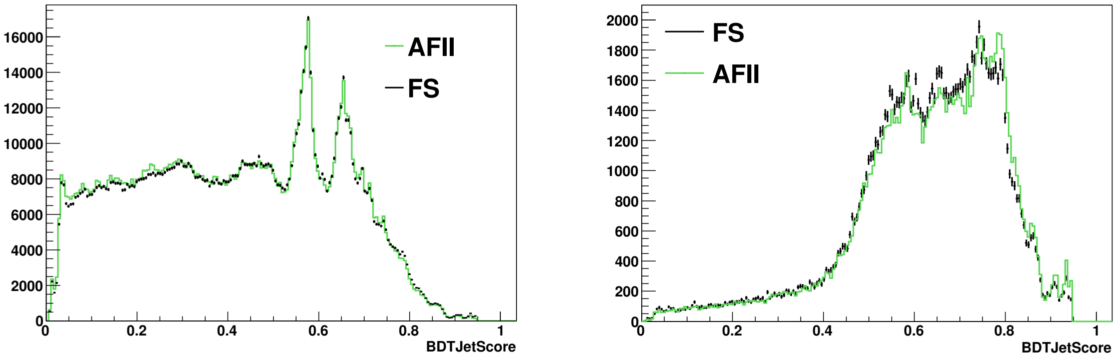

(a) Jet BDT

(b) Jet BDT for true taus

Figure D.13: Comparison of the shape of the tau ID BDT for all candidates (a) and only truth matched candidates (b) in a subset of the sample studied. The small shift observed between Full Simulation (FS) and Fast Simulation (AFII) is the source of any remaining difference in the tau ID efficiency.

D.3 Differential cross section re-weighting on POWHEG $t\bar{t}$ sample

As explained in Section 4, the used $t\bar{t}$ sample generated with POWHEG exhibits a deviation compared to data. This is remedied by applying a re-weighting procedure that is based on an ATLAS differential $t\bar{t}$ cross section measurement [212, 213].

Although in the main selections no obvious deviations are observed, a validation region can easily be constructed to find such deviations. To do so, the kinematic control region introduced in Section 6.3.1 is extended by dropping the H_T and the $m_{\mathrm{T}}^{\mu} + m_{\mathrm{T}}^{\mathrm{jet}_3}$ cut. In this region, a clear trend is observable in many kinematic variables.

After applying the correction however the trend vanishes and an excellent agreement between data and simulation is achieved. This is nicely displayed in Figure D.14 that compiles various kinematic distributions with and without re-weighting in the specific validation region.

In the nominal control regions the effect on shapes is barely visible. However, the re-weighting influences the scaling factors derived in Section 6.2.3 bringing them closer to unity.

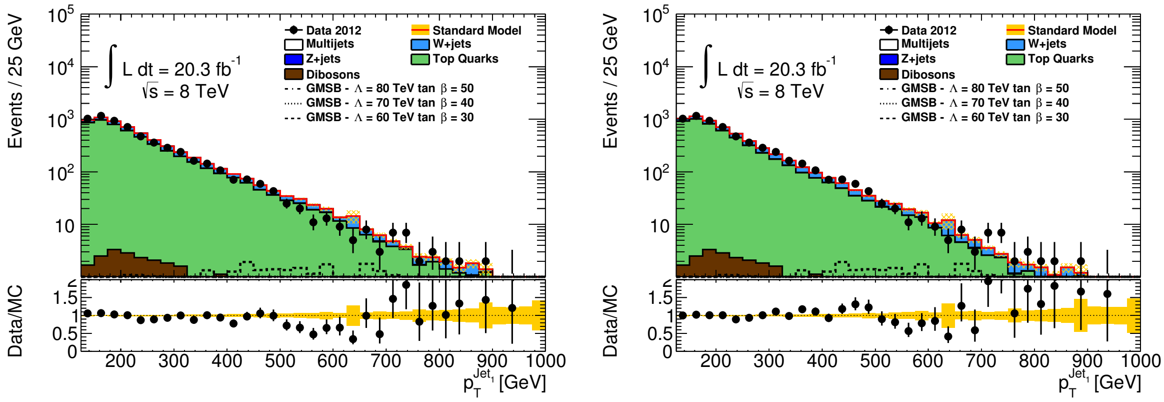

(a) $p_T^{\mathrm{jet}_1}$ Nominal (b) $p_T^{\mathrm{jet}_1}$ Re-weighted

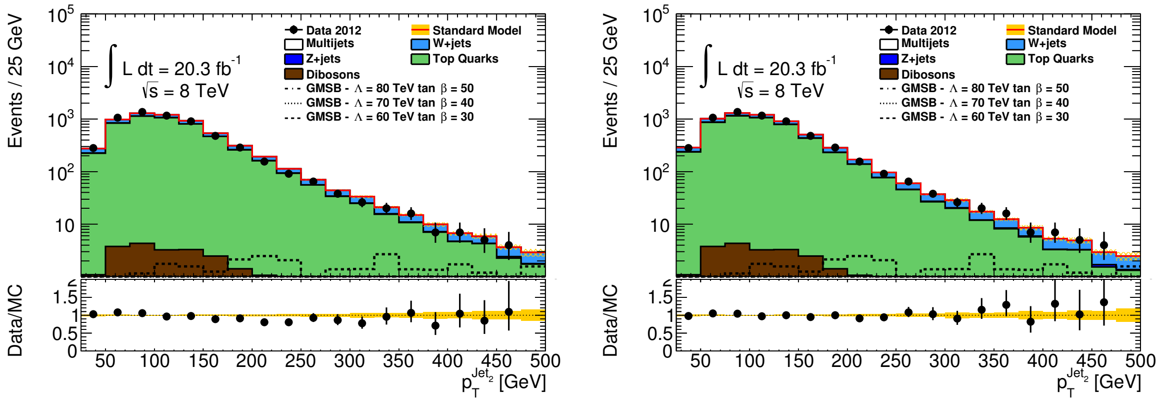

(c) $p_T^{\mathrm{jet}_2}$ Nominal (d) $p_T^{\mathrm{jet}_2}$ Re-weighted

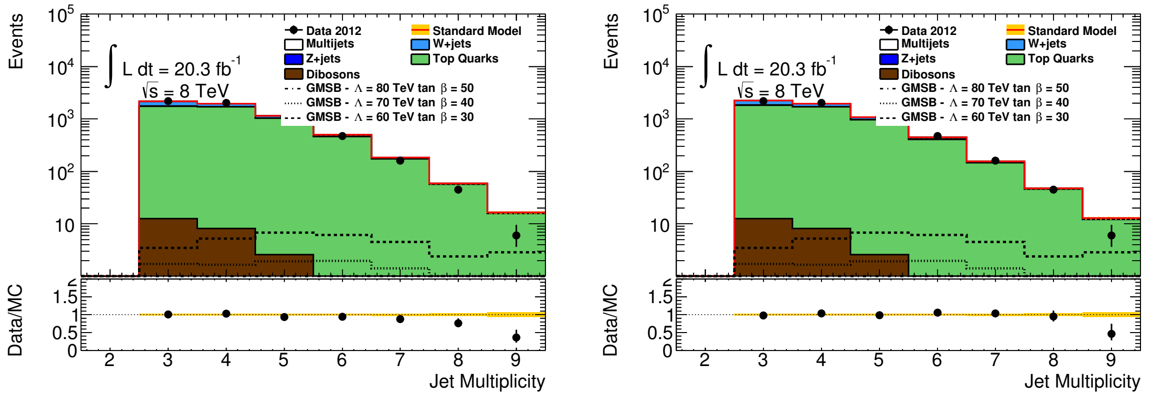

(e) N_{jet} Nominal (f) N_{jet} Re-weighted

Figure D.14: Shape comparison for various kinematic variables with and without cross section re-weighting for the $t\bar{t}$ background. Plots are made in a specific validation region that is susceptible to this kind of problems. The re-weighting clearly improves the agreement between data and simulation.

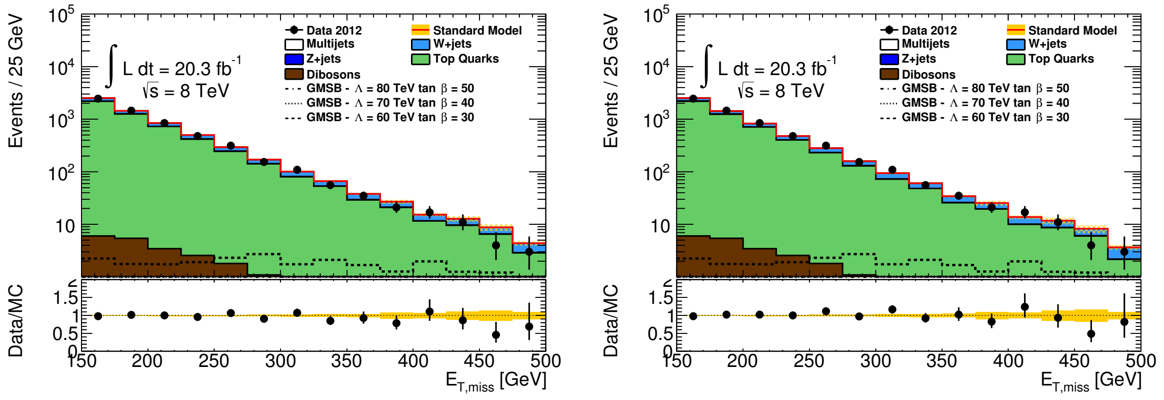

(a) $\not{E}_T$ Nominal

(b) $\not{E}_T$ Re-weighted

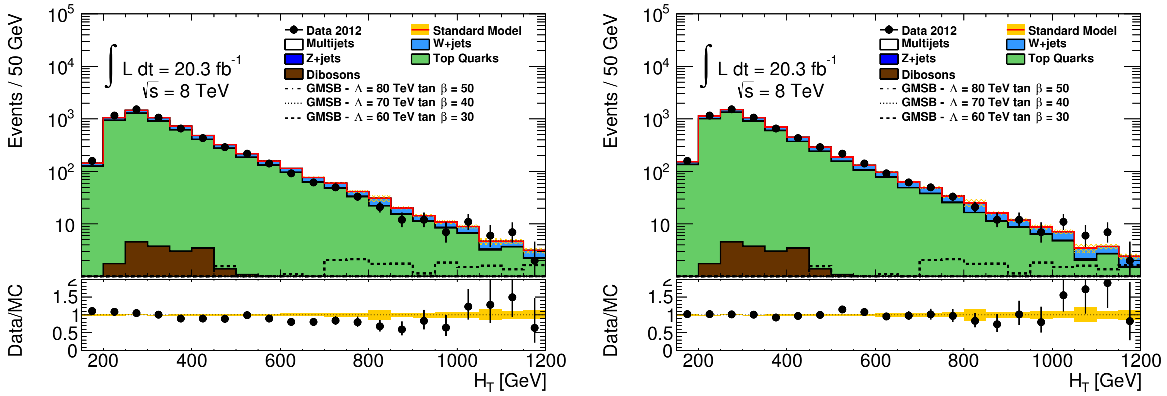

(c) H_T Nominal

(d) H_T Re-weighted

Figure D.15: Further shape comparison for various kinematic variables with and without cross section re-weighting for the $t\bar{t}$ background. Plots are made in a specific validation region that is susceptible to this kind of problems. The re-weighting clearly improves the agreement between data and simulation.

For the final background estimate, the expected level of background is slightly decreased with the difference being covered by the generator uncertainties on the nominal $t\bar{t}$ prediction. Systematic uncertainties evaluated by comparing ALPGEN to POWHEG also decrease.

D.4 Boson p_T re-weighting on SHERPA *W*+jets/*Z*+jets samples

For the central *W*+jets and *Z*+jets samples, previous studies have shown that the p_T of the boson is not correctly modeled in kinematic regions with high $\not{E}_T$ and hard jet p_T. This is however exactly the configuration enforced by the trigger employed in the analysis. A correction factor in several bins of the true p_T of the boson is derived in the context of the stop-charm search (section 8.1 of [233]). These corrections are derived in control regions that exhibit kinematic properties very similar to the ones of this search. Indeed, studies in the kinematic control regions (c.f. definition in Section 6.3.1) show a slope in the data/MC ratio for distributions sensitive to boson p_T mis-modeling. This bias is cured by applying the re-weighting factors (c.f. Figure D.16).

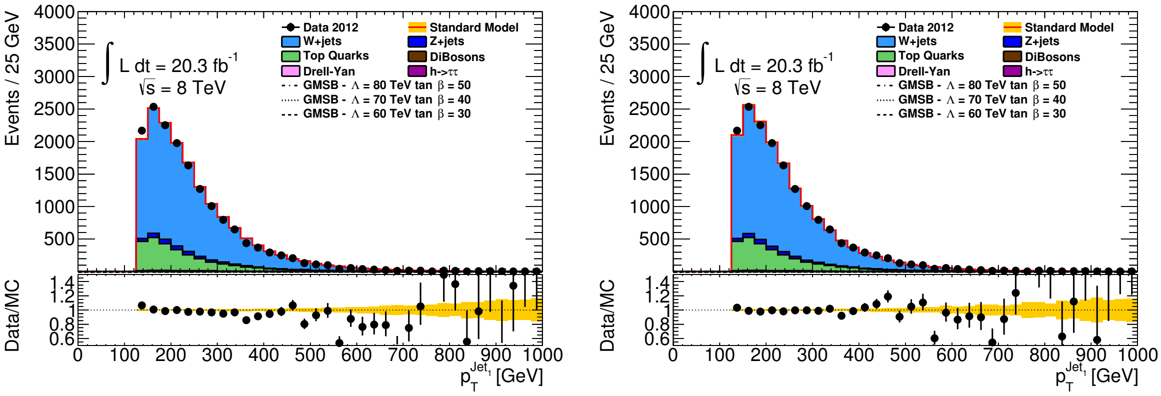

(a) $p_T^{\mathrm{jet}_1}$ w/o boson p_T re-weighting (b) $p_T^{\mathrm{jet}_1}$ w/ boson p_T re-weighting

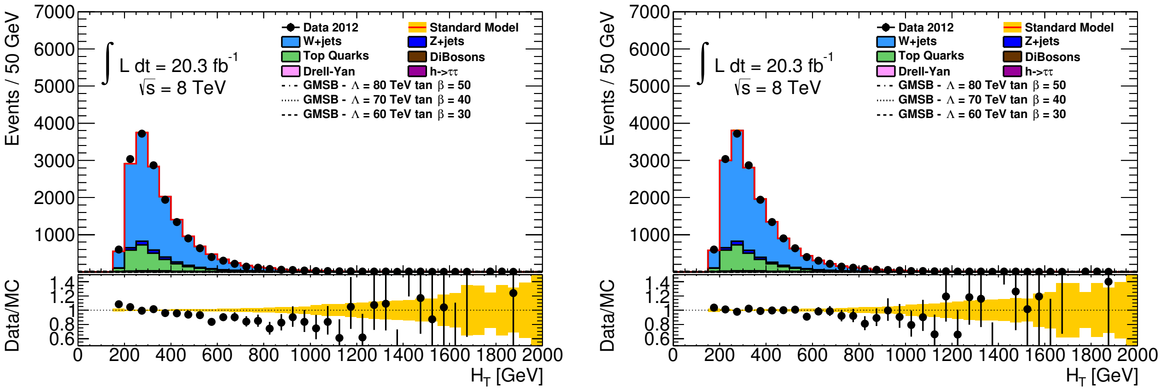

(c) H_T w/o boson p_T re-weighting (d) H_T w/ boson p_T re-weighting

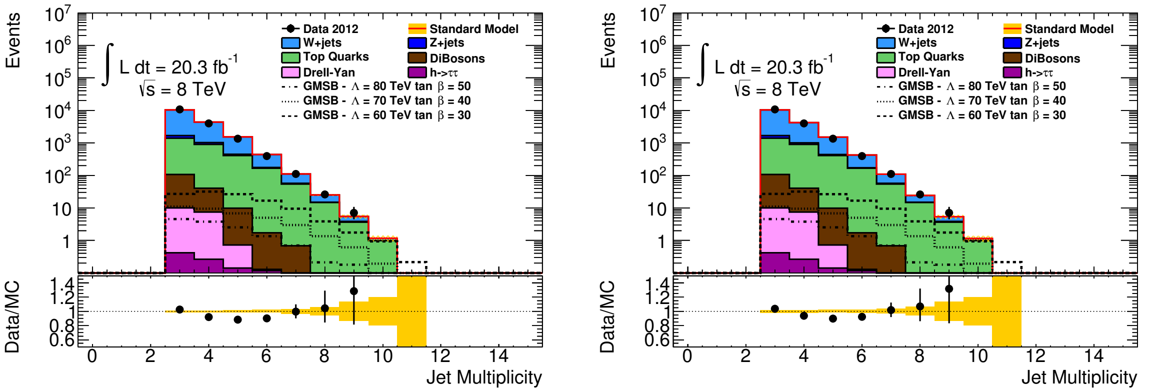

(e) N_{jet} w/o boson p_T re-weighting (f) N_{jet} w/ boson p_T re-weighting

Figure D.16: Comparison of $p_T^{\mathrm{jet}_1}$, H_T and N_{jet} in a $W \to \mu\nu$ enriched W kinematic control region with and without the boson p_T re-weighting procedure for theSHERPA W and Z samples. A clear improvement of the agreement between data and MC is observed after applying the re-weighting.

The re-weighting of the vector boson samples according to the p_T of the boson is derived in a region with a fixed jet multiplicity cut. To validate the applicability to other multiplicities, the effect of the re-weighting on $p_T^{\text{jet}_1}$ is studied for different jet multiplicities in the W kinematic control region. The jet p_T is chosen since it should be directly correlated to the boson p_T under the assumption that most of the recoil is absorbed by one jet. The said control region was chosen since it allowed for independent variations of the jet multiplicity cut and has been shown to be sensitive to the boson p_T mis-modeling before.

Figures D.17 and D.18 show these distributions. Clearly, the re-weighting improves the data-MC agreement regardless of the selected jet multiplicity.

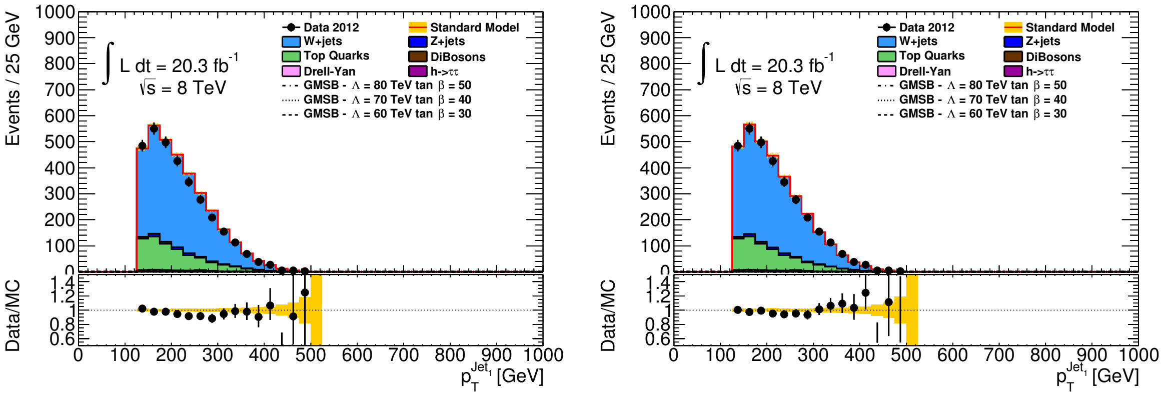

(a) $p_T^{\text{jet}_1}$ after 1 μ, 3 jets and CR kinematic w/o re-weighting (b) $p_T^{\text{jet}_1}$ after 1 μ, 3 jets and CR kinematic w/ re-weighting

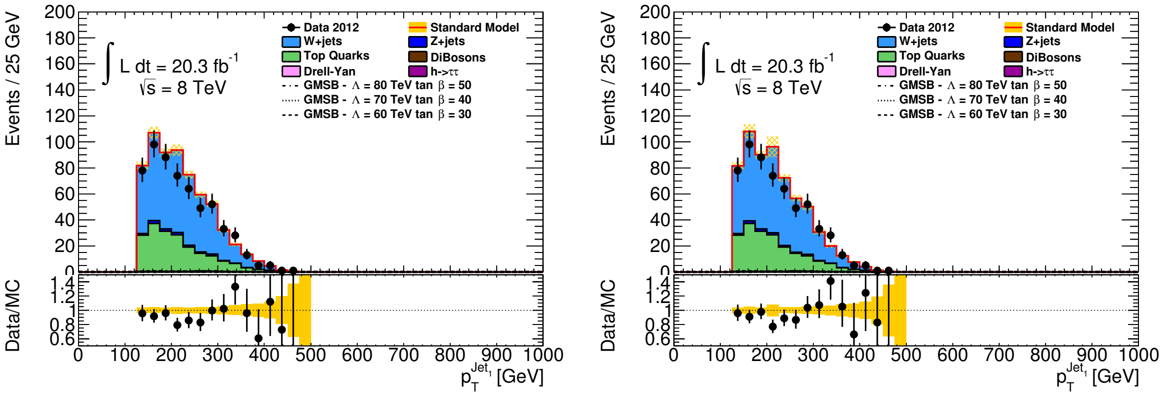

(c) $p_T^{\text{jet}_1}$ after 1 μ, 5 jets and CR kinematic w/o re-weighting (d) $p_T^{\text{jet}_1}$ after 1 μ, 5 jets and CR kinematic w/ re-weighting

Figure D.17: $p_T^{\text{jet}_1}$ without and with the boson p_T re-weighting applied for different jet multiplicity cuts in the kinematic W control region.

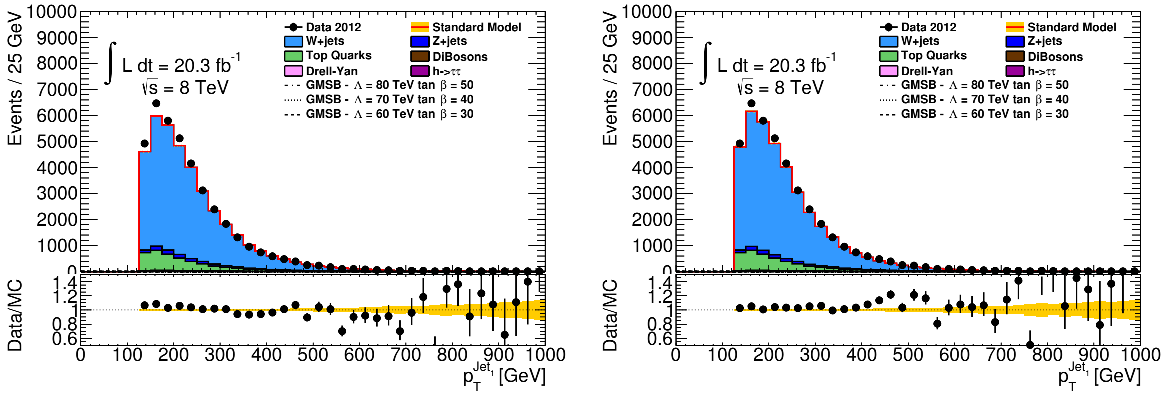

(a) $p_T^{\text{jet}_1}$ after 1 μ, 2 jets w/o re-weighting (b) $p_T^{\text{jet}_1}$ after 1 μ, 2 jets w/ re-weighting

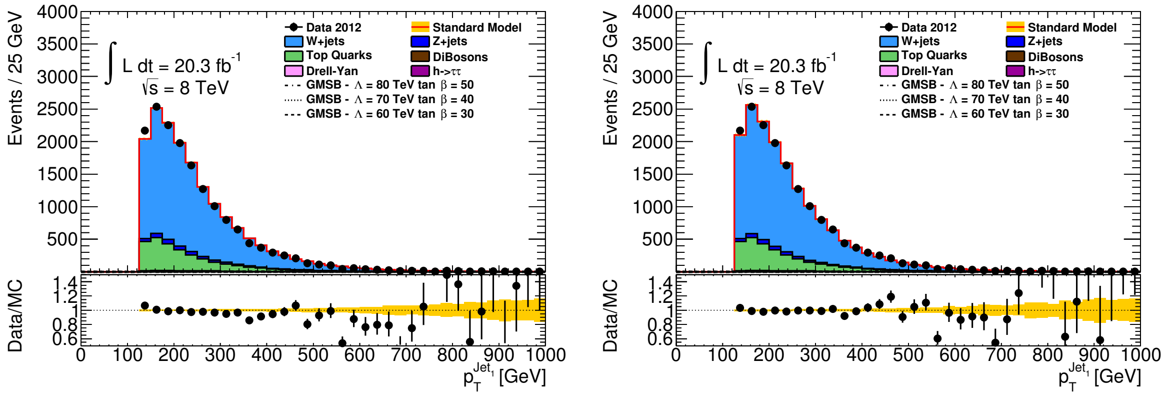

(c) $p_T^{\text{jet}_1}$ after 1 μ, 3 jets w/o re-weighting (d) $p_T^{\text{jet}_1}$ after 1 μ, 3 jets w/ re-weighting

Figure D.18: $p_T^{\text{jet}_1}$ without and with the boson p_T re-weighting applied for different jet multiplicity cuts in the kinematic W control region (cont'd).

E

Additional plots on the event selection

E.1 GMSB

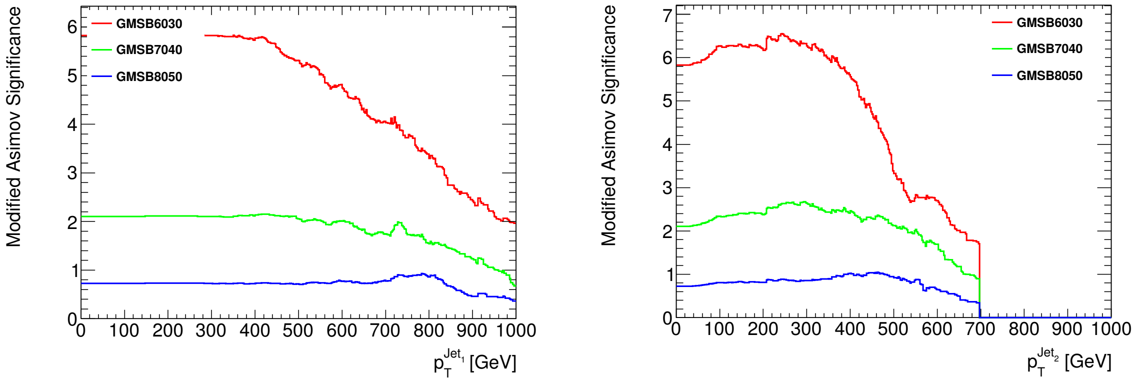

(a) $p_T^{\text{jet}_1}$ (b) $p_T^{\text{jet}_2}$

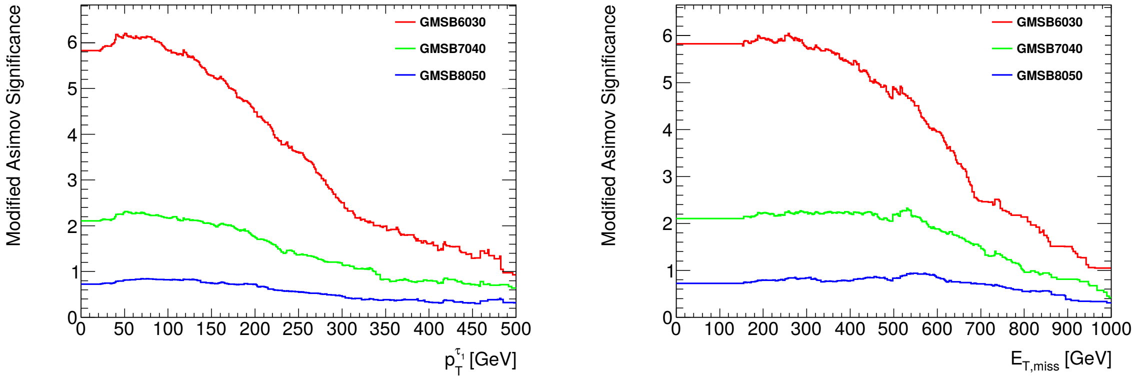

(c) $p_T^{\tau_1}$ (d) $\not{E}_T$

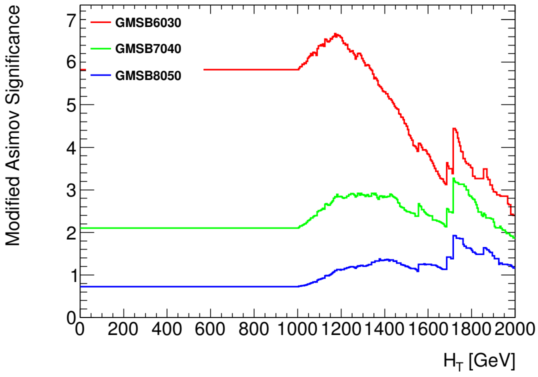

(e) H_T

Figure E.1: Significance scans for optimization of the GMSB signal region starting from the Inclusive signal region. All backgrounds are scaled with their respective scale factors.

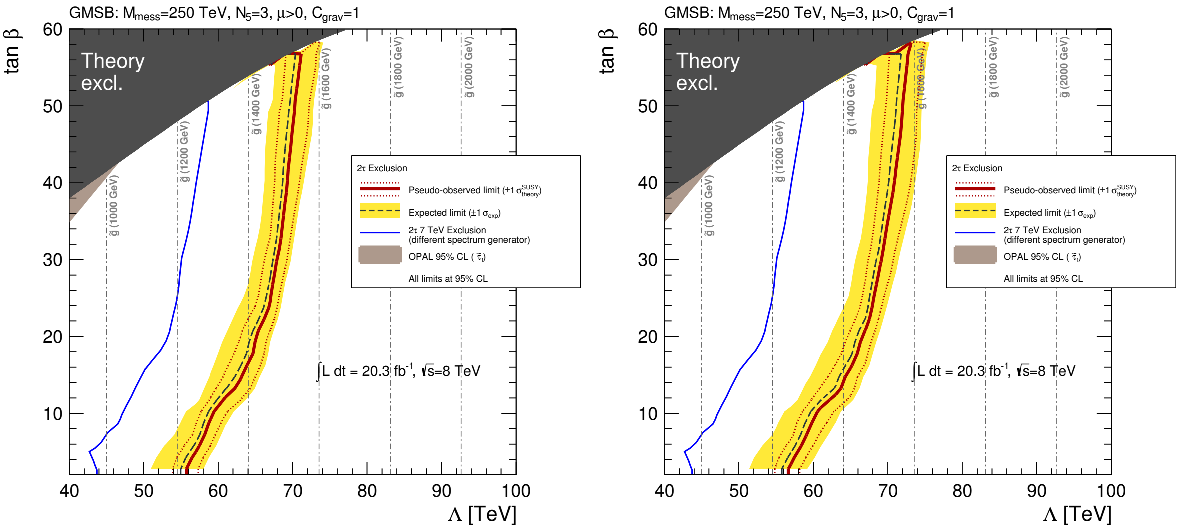

(a) $H_T > 900\,\text{GeV}$ (b) $H_T > 1\,000\,\text{GeV}$

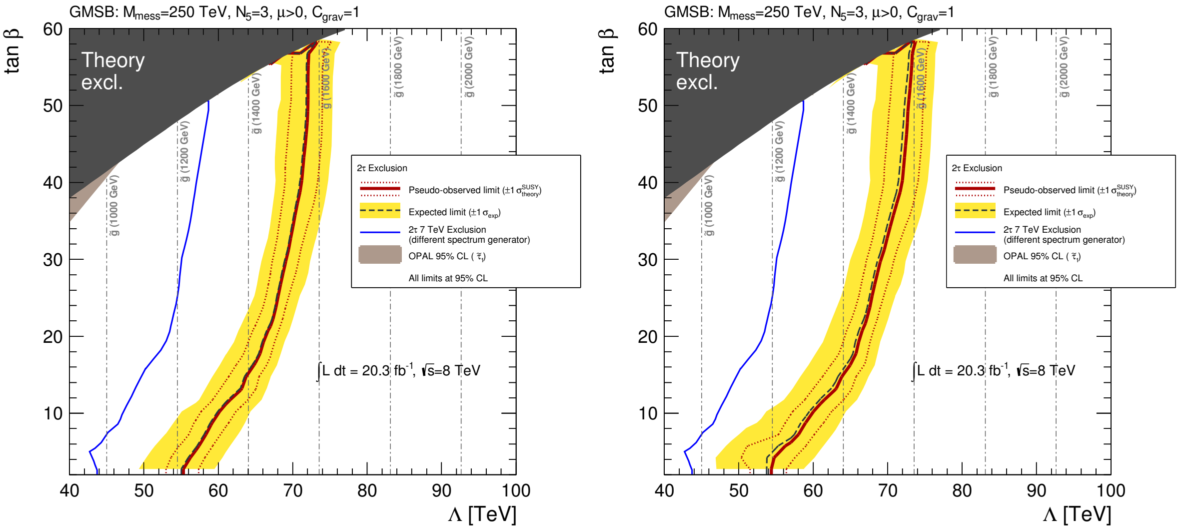

(c) $H_T > 1\,100\,\text{GeV}$ (d) $H_T > 1\,200\,\text{GeV}$

Figure E.2: GMSB exclusion plots for different H_T cuts. All exclusions are computed employing a $m_{\mathrm{T}}^{\tau_1} + m_{\mathrm{T}}^{\tau_2} > 150\,\text{GeV}$ cut. Systematic uncertainties are re-computed for the chosen cut value for each plot. The “observed” line gives the exclusion achieved by assuming the closest integer to the expected number of events as “observed” number of events.

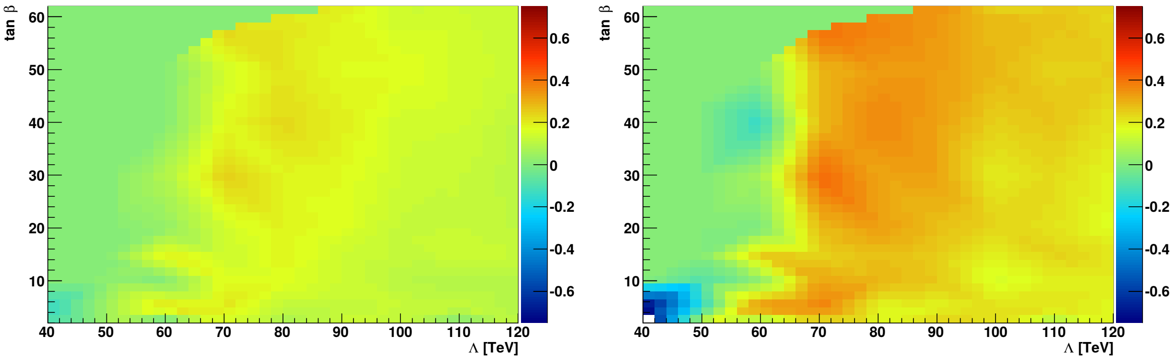

(a) $m_{\mathrm{T}}^{\tau_1} + m_{\mathrm{T}}^{\tau_2} > 200\,\mathrm{GeV}$, no N_{jet} cut

(b) $m_{\mathrm{T}}^{\tau_1} + m_{\mathrm{T}}^{\tau_2} > 250\,\mathrm{GeV}$, no N_{jet} cut

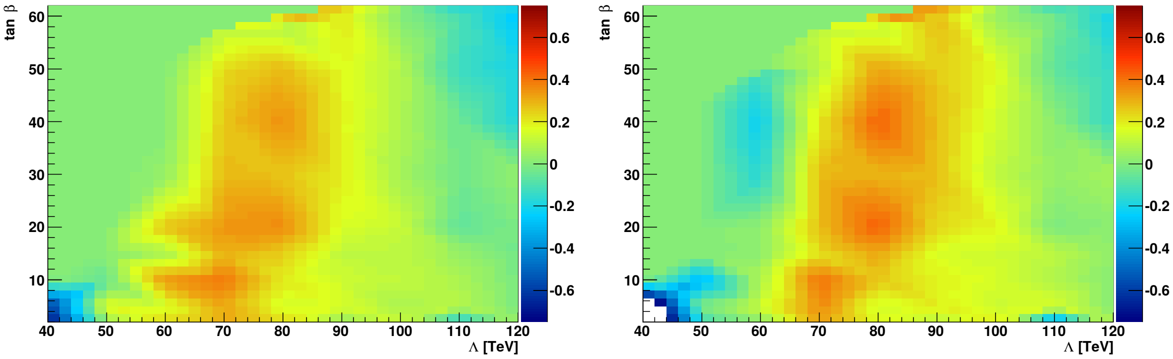

(c) $m_{\mathrm{T}}^{\tau_1} + m_{\mathrm{T}}^{\tau_2} > 150\,\mathrm{GeV}$, $N_{\mathrm{jet}} \geq 4$

(d) $m_{\mathrm{T}}^{\tau_1} + m_{\mathrm{T}}^{\tau_2} > 200\,\mathrm{GeV}$, $N_{\mathrm{jet}} \geq 4$

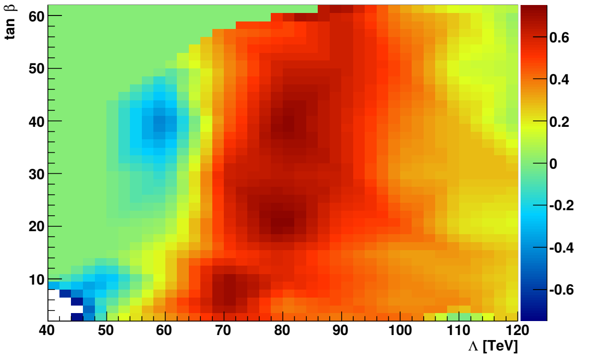

(e) $m_{\mathrm{T}}^{\tau_1} + m_{\mathrm{T}}^{\tau_2} > 250\,\mathrm{GeV}$, $N_{\mathrm{jet}} \geq 4$

Figure E.3: Difference in significance between various hypothetical signal regions and the Inclusive SR for the GMSB grid.

E.2 nGM

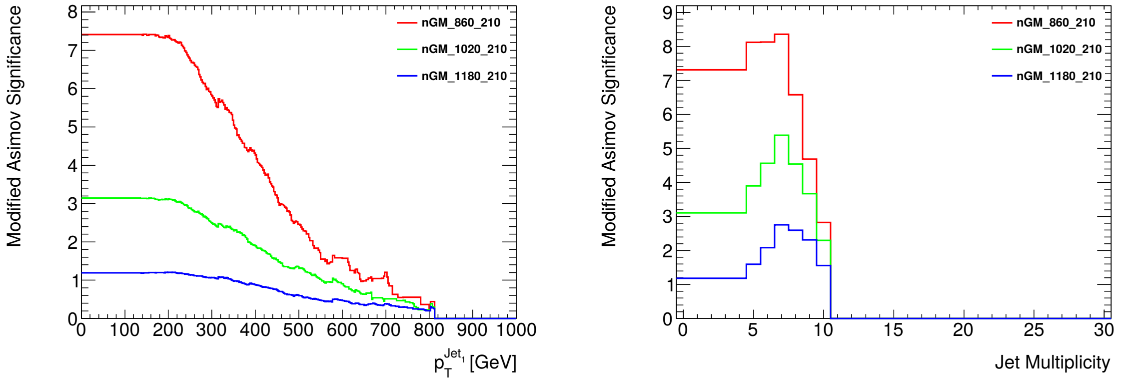

(a) $p_T^{\text{jet}_1}$ (b) N_{jet}

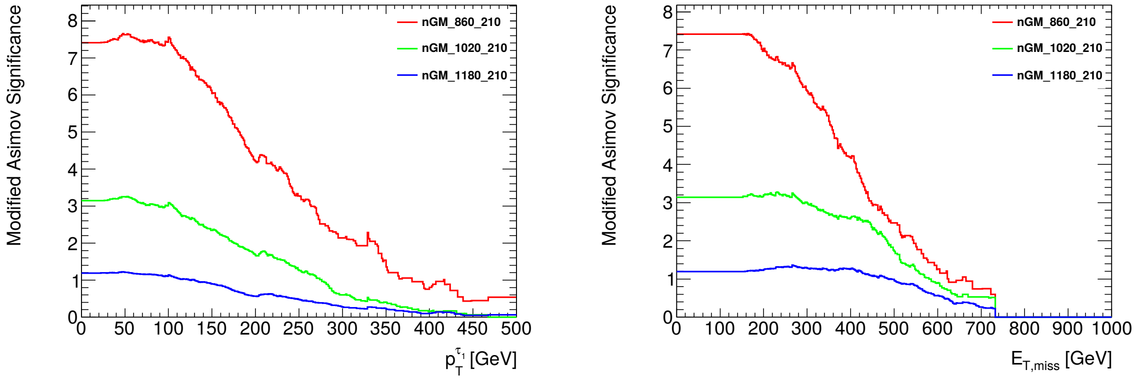

(c) $p_T^{\tau_1}$ (d) $\not{E}_T$

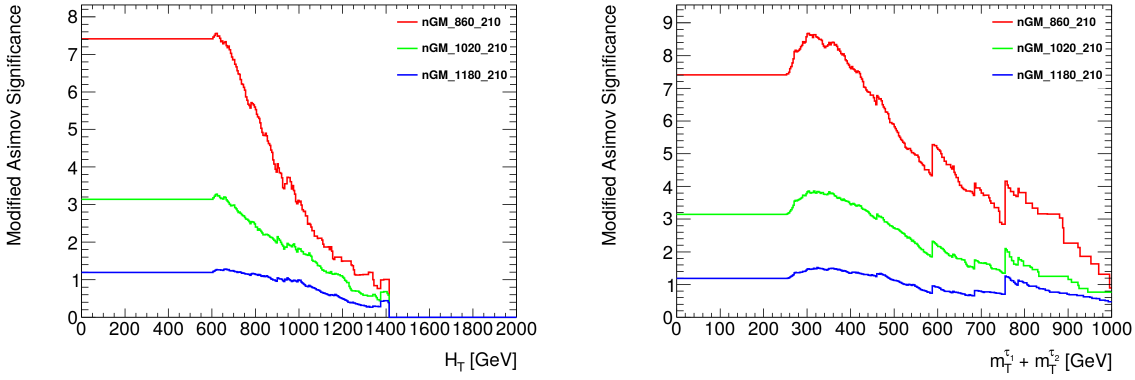

(e) H_T (f) $m_{\text{T}}^{\tau_1} + m_{\text{T}}^{\tau_2}$

Figure E.4: Significance scans for optimization of the nGM signal region starting from the nGM signal rsegion. All backgrounds are scaled with their respective scale factors.

E.3 bRPV

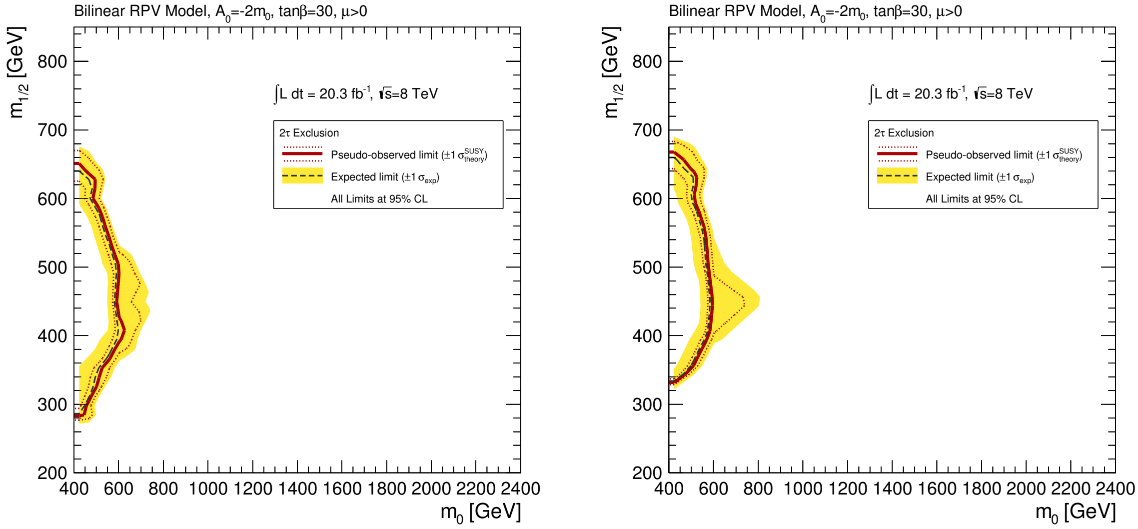

(a) $H_T > 900\,\text{GeV}$

(b) $H_T > 1\,000\,\text{GeV}$

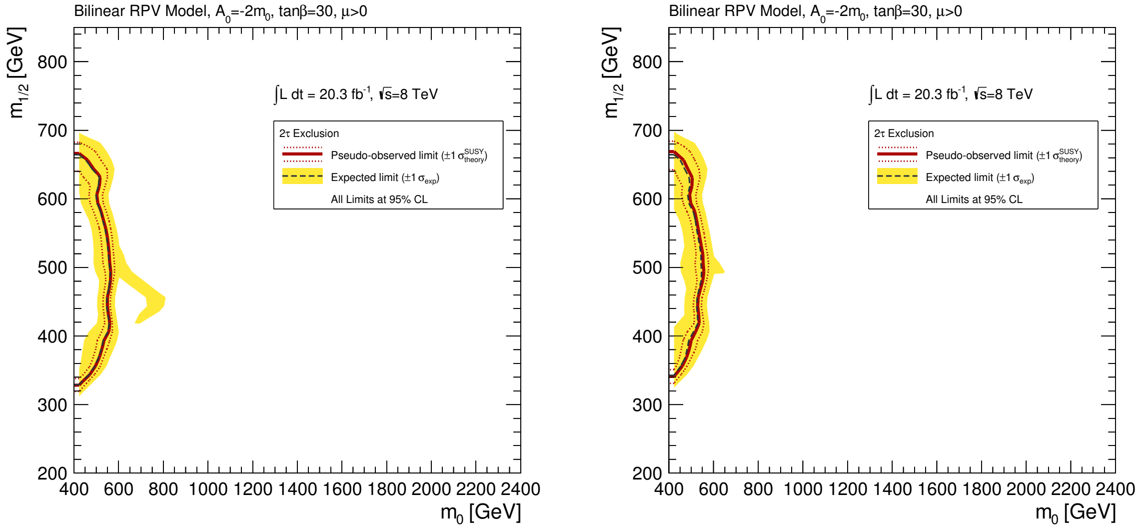

(c) $H_T > 1\,100\,\text{GeV}$

(d) $H_T > 1\,200\,\text{GeV}$

Figure E.5: bRPV exclusion plots for different H_T cuts. All exclusions are computed employing a $m_T^{\tau_1} + m_T^{\tau_2} > 150\,\text{GeV}$ cut. Systematic uncertainties are re-computed for the chosen cut value for each plot. The “observed” line gives the exclusion achieved by assuming the closest integer to the expected number of events as “observed” number of events.

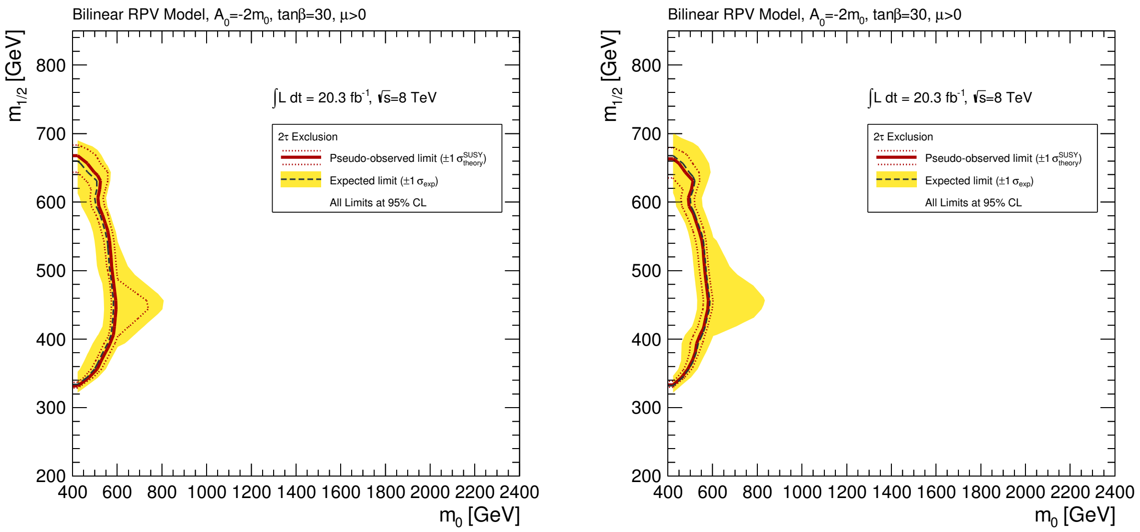

(a) $m_{\mathrm{T}}^{\tau_1} + m_{\mathrm{T}}^{\tau_2} > 150\,\mathrm{GeV}$

(b) $m_{\mathrm{T}}^{\tau_1} + m_{\mathrm{T}}^{\tau_2} > 200\,\mathrm{GeV}$

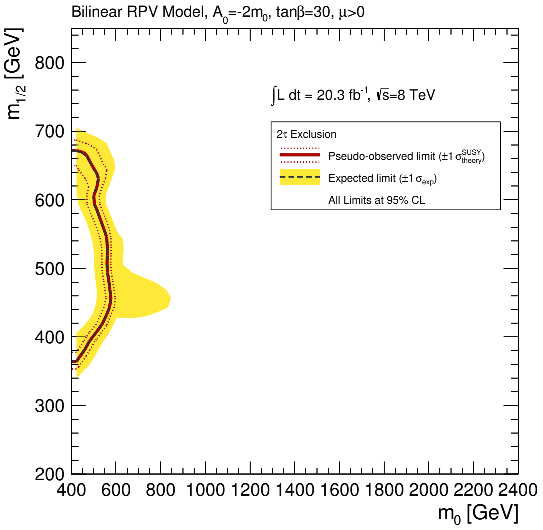

(c) $m_{\mathrm{T}}^{\tau_1} + m_{\mathrm{T}}^{\tau_2} > 250\,\mathrm{GeV}$

Figure E.6: bRPV exclusion plots for different $m_{\mathrm{T}}^{\tau_1} + m_{\mathrm{T}}^{\tau_2}$ cuts. All exclusions are computed employing a $H_T > 1\,000\,\mathrm{GeV}$ cut. Systematic uncertainties are re-computed for the chosen cut value for each plot. The “observed” line gives the exclusion achieved by assuming the closest integer to the expected number of events as “observed” number of events.

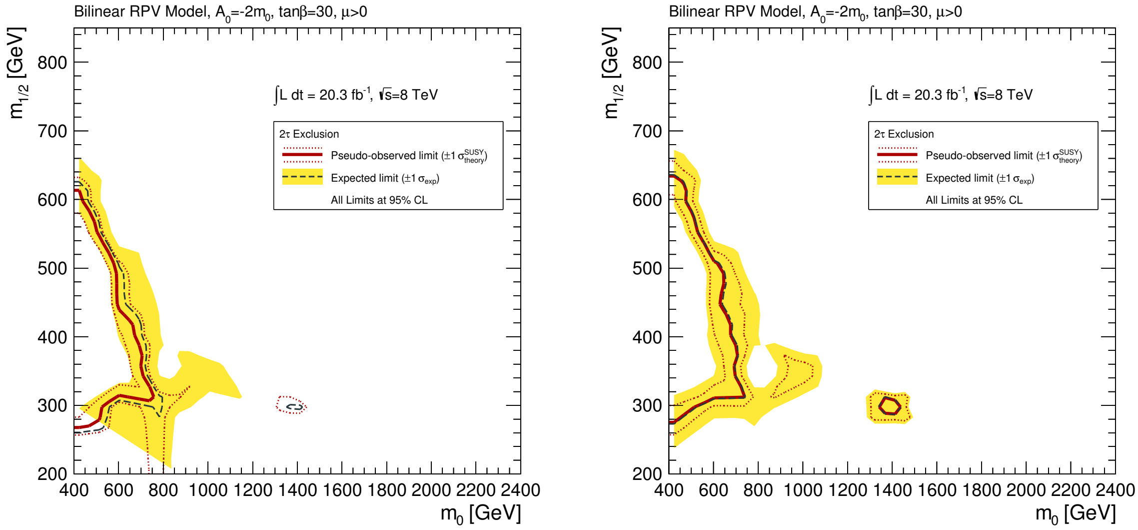

(a) $m_T^{\tau_1} + m_T^{\tau_2} > 150\,\text{GeV}$

(b) $m_T^{\tau_1} + m_T^{\tau_2} > 200\,\text{GeV}$

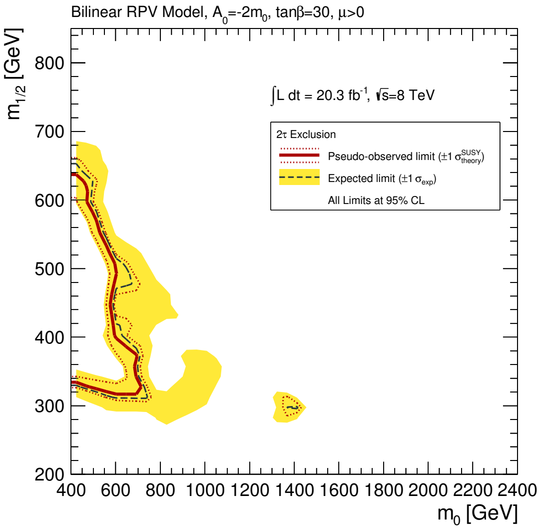

(c) $m_T^{\tau_1} + m_T^{\tau_2} > 250\,\text{GeV}$

Figure E.7: bRPV exclusion plots for different $m_T^{\tau_1} + m_T^{\tau_2}$ cuts. All exclusions are computed employing a $H_T > 600\,\text{GeV}$ and a $N_{\text{jet}} \geq 4$ cut. Systematic uncertainties are re-computed for the chosen cut value for each plot. The “observed” line gives the exclusion achieved by assuming the closest integer to the expected number of events as “observed” number of events.

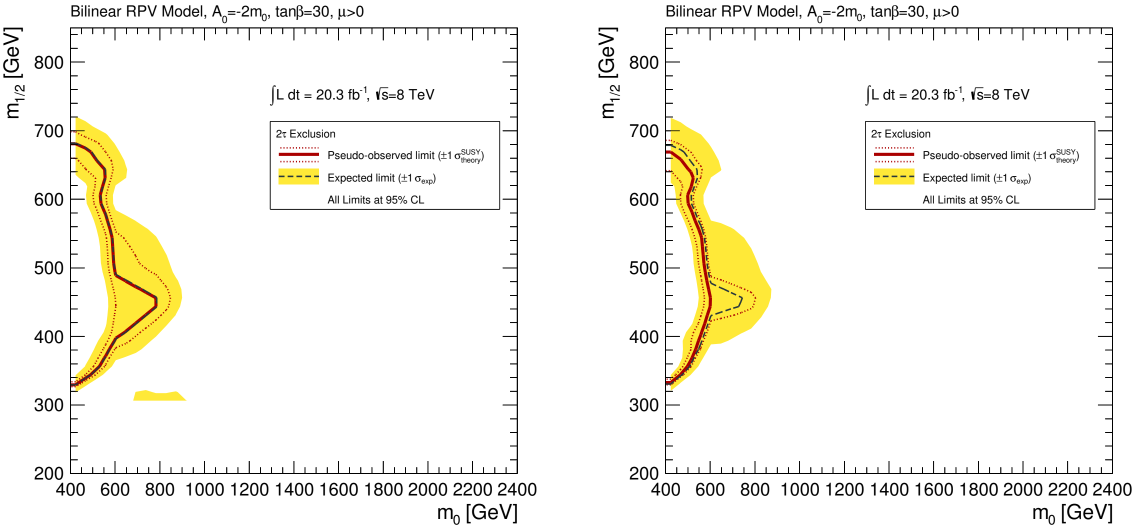

(a) $m_{\mathrm{T}}^{\tau_1} + m_{\mathrm{T}}^{\tau_2} > 150\,\mathrm{GeV}$

(b) $m_{\mathrm{T}}^{\tau_1} + m_{\mathrm{T}}^{\tau_2} > 200\,\mathrm{GeV}$

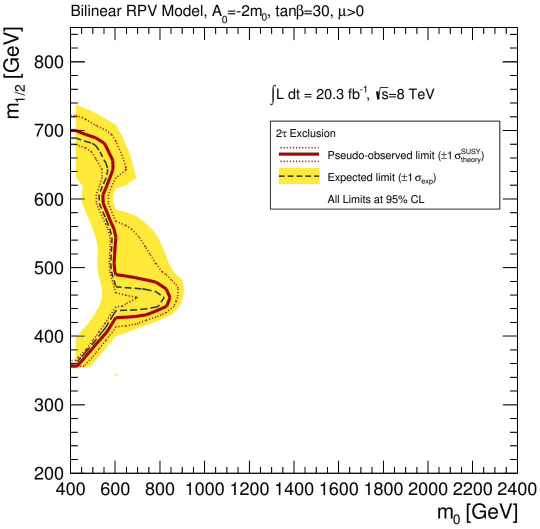

(c) $m_{\mathrm{T}}^{\tau_1} + m_{\mathrm{T}}^{\tau_2} > 250\,\mathrm{GeV}$

Figure E.8: bRPV exclusion plots for different $m_{\mathrm{T}}^{\tau_1} + m_{\mathrm{T}}^{\tau_2}$ cuts. All exclusions are computed employing a $H_T >$ 1 000 GeV and a $N_{\mathrm{jet}} \geq 4$ cut. Systematic uncertainties are re-computed for the chosen cut value for each plot. The “observed” line gives the exclusion achieved by assuming the closest integer to the expected number of events as “observed” number of events.

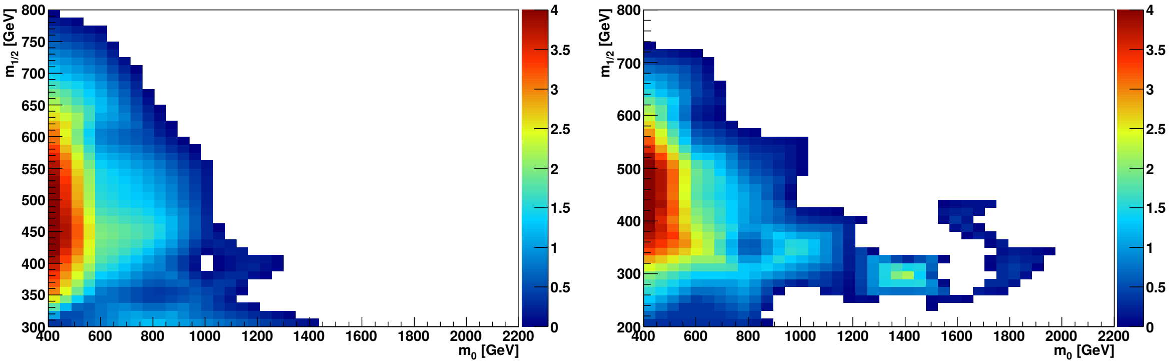

(a) bRPV $m_{1/2}$ Significance Map

(b) bRPV m_0 Significance Map

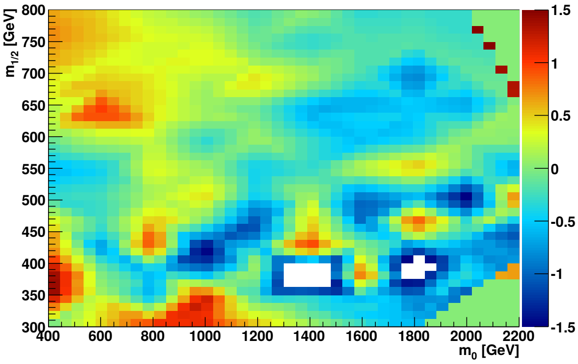

(c) Significance Difference Map

Figure E.9: Significance maps for the two bRPV signal regions (a and b). The shape of the excluded regions is reflected in the shape of the significance landscape. (c) shows the difference between the two maps. Depending on the position in the grid the performance of the two SRs changes rapidly.

F

Additional information on systematic uncertainties

F.1 Software packages used for the computation of systematic uncertainties

Uncertainty	Package	Version
Jet energy scale	JETUNCERTAINTIES	00-08-06
Jet energy resolution	JETENERGYRESOLUTIONPROVIDER	02-00-02
Tau energy scale	TAUCORRUNCERTPROVIDER	00-00-07
Tau identification	TAUCORRUNCERTPROVIDER	00-00-07
Missing transverse momentum	MISSINGETUTILITY	01-02-06
Pileup re-weighting	PILEUPREWEIGHTING	00-02-11
B-tag efficiency	CALIBRATIONDATAINTERFACE	00-03-06
Jet-vertex-fraction	JVFUNCERTAINTYTOOL	00-00-04

Table F.1: Overview of the software packages used to compute the various systematic uncertainties considered.

F.2 Generator comparisons

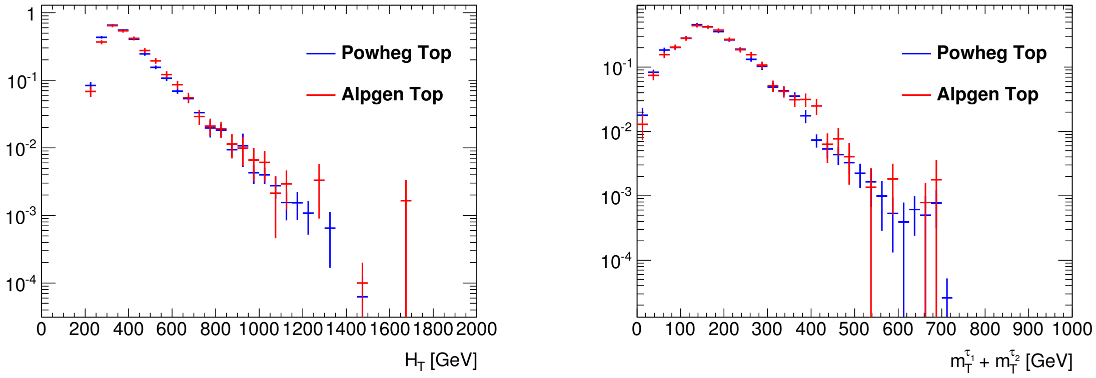

(a) H_T (b) $m_{\mathrm{T}}^{\tau_1} + m_{\mathrm{T}}^{\tau_2}$

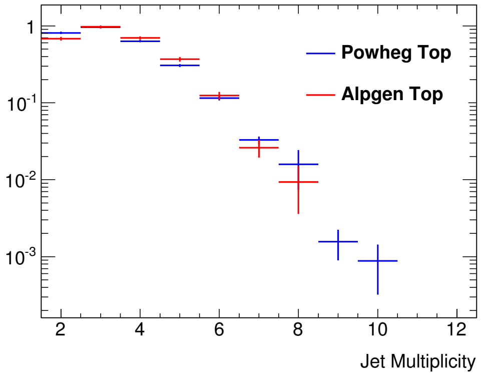

(c) N_{jet}

Figure F.1: Shape comparison for the main kinematic variables. Compared are the $t\bar{t}$ generators POWHEG and ALPGEN. All plots are made after requiring all objects selected in the analysis. All samples are normalized in the respective control region matching the samples compared.

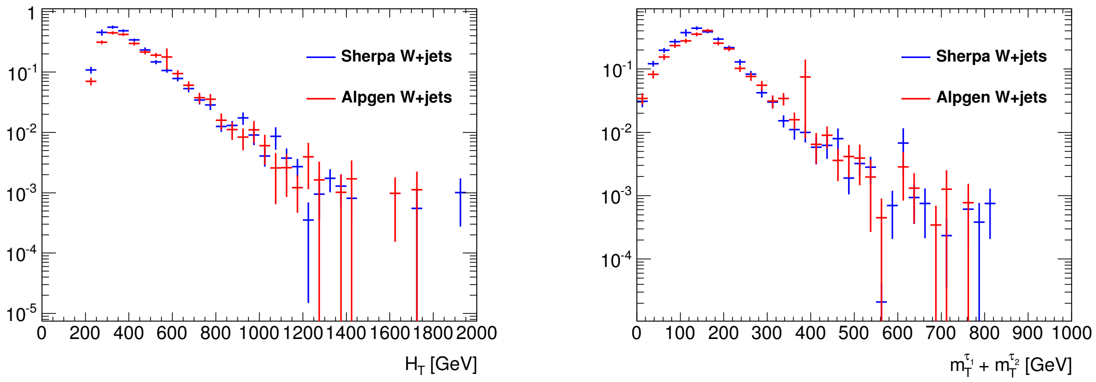

(a) H_T

(b) $m_{\mathrm{T}}^{\tau_1} + m_{\mathrm{T}}^{\tau_2}$

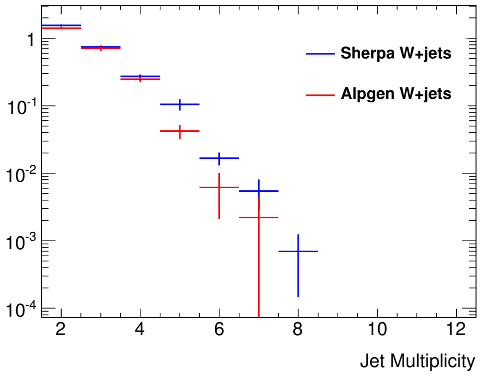

(c) N_{jet}

Figure F.2: Shape comparison for the main kinematic variables. Compared are the W+jets generators SHERPA and ALPGEN. All plots are made after requiring all objects selected in the analysis. All samples are normalized in the respective control region matching the samples compared.

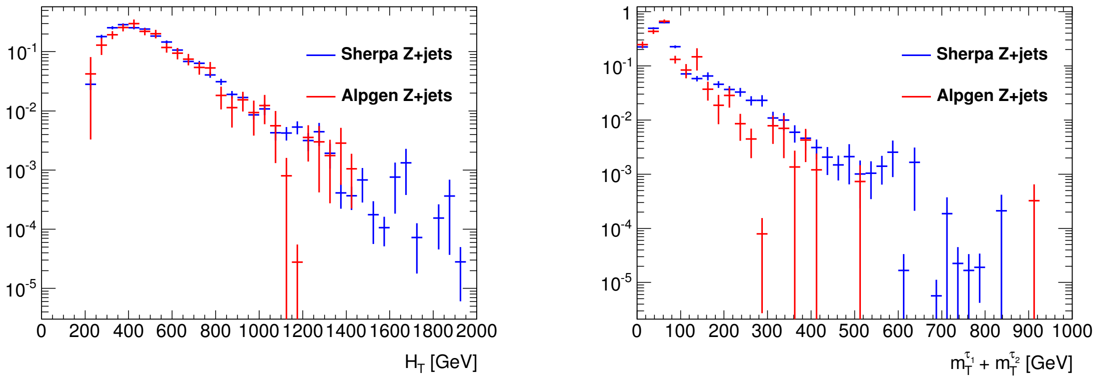

(a) H_T (b) $m_{\mathrm{T}}^{\tau_1} + m_{\mathrm{T}}^{\tau_2}$

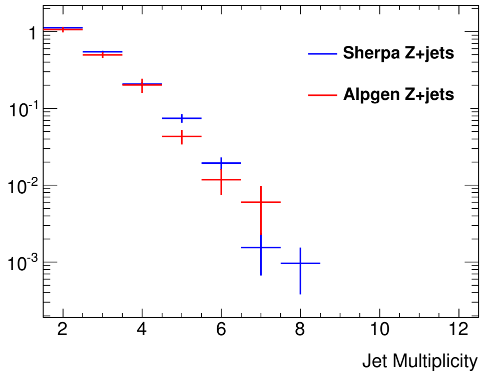

(c) N_{jet}

Figure F.3: Shape comparison for the main kinematic variables. Compared are the Z+jets generators SHERPA and ALPGEN. All plots are made after requiring all objects selected in the analysis. All samples are normalized in the respective control region matching the samples compared.

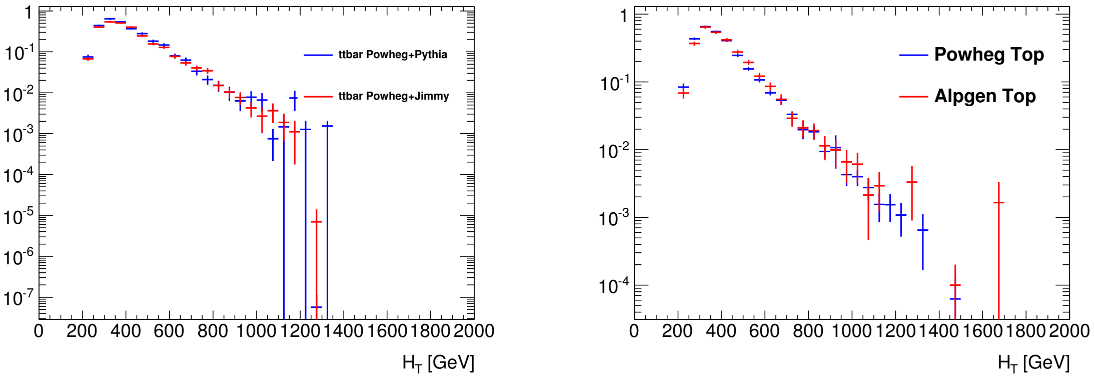

(a) H_T Showering (b) H_T Generator

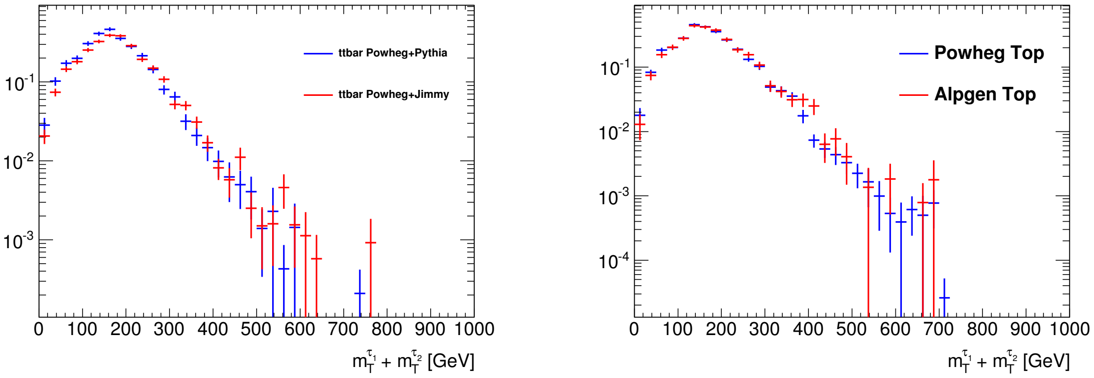

(c) $m_{\mathrm{T}}^{\tau_1} + m_{\mathrm{T}}^{\tau_2}$ Showering (d) $m_{\mathrm{T}}^{\tau_1} + m_{\mathrm{T}}^{\tau_2}$ Generator

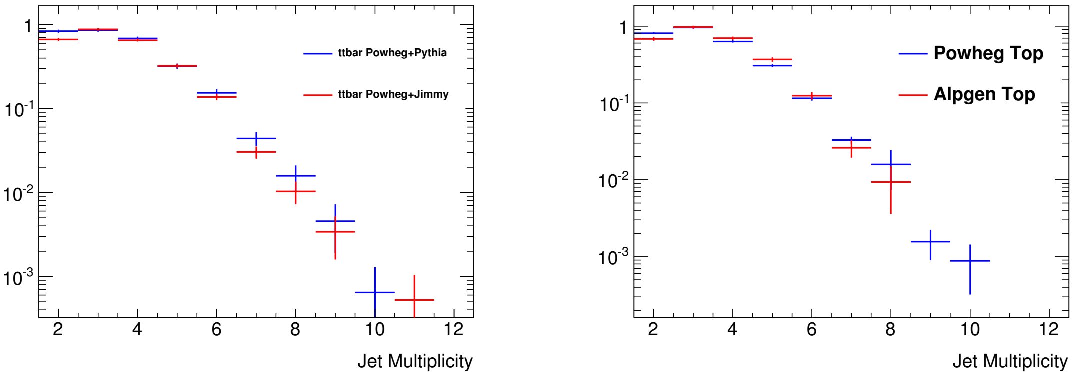

(e) N_{jet} Showering (f) N_{jet} Generator

Figure F.4: Comparison between the uncertainty due to the choice of the showering algortihm and the overall generator uncertainty for the main kinematic variables. All plots are made after requiring all objects selected in the analysis. All samples are normalized in the respective control region matching the samples compared. Note that the shapes for the showering comparison cannot directly be compared to the shapes of the overall comparison. In general a much larger difference between the different generators than between the different phase-space configurations is observed.

F.3 Detailed tables of background uncertainties

Systematic	Total	Dibosons	Multijets	W	Top	Z
JER	−0.021	0.	-	−0.043	−0.0020	−0.012
JES up	0.071	0.	-	0.025	0.083	0.23
JES down	0.034	−0.036	-	0.12	0.0060	−0.087
TES up	−0.028	0.	-	−0.067	−0.045	0.052
TES down	−0.018	0.	-	0.021	0.073	−0.22
Tau ID up	0.0070	0.041	-	0.0070	0.0010	−0.010
Tau ID down	−0.0070	−0.040	-	−0.0080	−0.0010	0.011
Tau EVETO up	0.016	0.	-	0.022	0.033	0.0010
Tau EVETO down	−0.016	0.	-	−0.023	−0.030	−0.0010
BTag down	0.019	0.	-	0.018	0.074	−0.015
BTag up	−0.017	0.	-	−0.014	−0.068	0.014
$\not{E}_T$ resolution	0.0090	0.	-	−0.023	−0.061	0.17
$\not{E}_T$ scale down	−0.011	0.	-	−0.018	−0.049	0.034
$\not{E}_T$ scale up	0.010	0.	-	0.0010	0.083	−0.037
Pileup up	−0.015	−0.19	-	0.028	−0.039	0.034
Pileup down	0.013	0.16	-	−0.016	0.026	−0.038
Top Generator	0.11	-	-	0.066	0.34	0.045
Top Generator Stat	0.087	-	-	-	0.43	-
W Generator	0.026	-	-	0.090	0.031	0.040
W Generator Stat	0.14	-	-	0.34	-	-
Z Generator	0.056	-	-	0.21	0.023	0.82
Z Generator Stat	0.029	-	-	-	-	0.82
Dibosons Generator	0.065	0.53	-	0.010	0.011	0.0030
Dibosons Generator Stat	0.035	0.51	-	-	-	-
JVF up	0.0030	0.	-	0.0050	0.0030	0.
JVF down	−0.0020	0.	-	−0.0030	−0.0010	−0.0010
QCD Tails up	0.0020	-	−0.12	0.016	−0.0010	−0.0030
QCD Tails down	0.040	-	0.78	0.022	−0.0010	−0.0040
QCD Gauss	0.0020	-	0.29	−0.023	−0.0040	0.0050
Total systematic uncertainty	0.23	0.75	0.54	0.43	0.57	1.2
Statistical uncertainty	0.13	0.50	0.47	0.26	0.25	0.27
Total uncertainty	0.27	0.90	0.72	0.50	0.62	1.2

Table F.2: Breakdown of all systematic and statistical uncertainties for the Inclusive signal region. Acronyms are introduced in Section 7.2. Systematic uncertainties are evaluated as relative changes in the background prediction for the signal region including changes in the data-driven background prediction due to changes in the transfer factors.

Systematic	Total	Multijets	W	Top	Z
JER	-0.047	-	-0.037	-0.015	-0.20
JES up	-0.020	-	-0.12	-0.10	0.41
JES down	-0.028	-	0.024	0.11	-0.45
TES up	-0.024	-	-0.031	-0.064	0.011
TES down	-0.15	-	-0.23	0.10	-0.46
Tau ID up	0.0080	-	0.023	-0.0070	-0.0070
Tau ID down	-0.0090	-	-0.025	0.0070	0.0070
Tau EVETO up	-0.0030	-	-0.0050	-0.0070	0.0010
Tau EVETO down	0.0040	-	0.0050	0.0070	-0.0010
BTag down	0.022	-	0.020	0.079	-0.013
BTag up	-0.019	-	-0.016	-0.072	0.012
$\not\!\!E_T$ resolution	-0.012	-	-0.030	0.	0.015
$\not\!\!E_T$ scale down	-0.022	-	-0.068	0.014	0.050
$\not\!\!E_T$ scale up	-0.083	-	-0.16	-0.012	-0.044
Pileup up	0.023	-	0.026	0.010	0.067
Pileup down	0.0070	-	0.050	-0.061	-0.042
Top Generator	0.10	-	0.057	0.46	0.039
Top Generator Stat	0.32	-	-	0.94	-
W Generator	0.52	-	1.1	0.033	0.043
W Generator Stat	0.46	-	0.71	-	-
Z Generator	0.061	-	0.40	0.028	1.0
Z Generator Stat	0.	-	-	-	0.
Dibosons Generator	0.013	-	0.021	0.023	0.0060
Dibosons Generator Stat	0.	-	-	-	-
JVF up	0.0020	-	0.0010	0.0070	0.
JVF down	-0.0030	-	-0.0050	-0.0020	0.
QCD Tails up	-0.15	-0.66	-0.0030	0.	0.0010
QCD Tails down	0.0020	-0.0050	0.0080	0.	-0.0010
QCD gauss	0.0060	0.017	0.010	-0.014	0.
Total systematic uncertainty	0.79	0.33	1.4	1.1	1.1
Statistical uncertainty	0.33	0.72	0.55	0.62	0.54
Total uncertainty	0.85	0.79	1.5	1.2	1.3

Table F.3: Breakdown of all systematic and statistical uncertainties for the GMSB signal region. Acronyms are introduced in Section 7.2. Systematic uncertainties are evaluated as relative changes in the background prediction for the signal region including changes in the data-driven background prediction due to changes in the transfer factors.

Systematic	Total	Multijets	W	Top	Z
JER	0.021	-	0.028	−0.0060	−0.16
JES up	0.049	-	−0.19	0.064	0.13
JES down	−0.048	-	0.043	−0.0050	−0.27
TES up	0.031	-	−0.15	0.062	0.18
TES down	0.028	-	0.052	0.043	−0.037
Tau ID up	0.0020	-	0.024	0.0010	−0.022
Tau ID down	−0.0020	-	−0.026	−0.0010	0.025
Tau EVETO up	−0.0040	-	−0.0050	−0.0060	0.0010
Tau EVETO down	0.0040	-	0.0050	0.0060	−0.0010
BTag down	0.044	-	0.020	0.079	−0.013
BTag up	−0.040	-	−0.016	−0.072	0.012
$\not{E}_T$ resolution	−0.014	-	−0.040	−0.014	0.015
$\not{E}_T$ scale down	0.010	-	−0.068	0.031	0.050
$\not{E}_T$ scale up	−0.031	-	0.012	−0.027	−0.092
Pileup up	−0.013	-	−0.032	−0.018	0.018
Pileup down	0.018	-	0.048	0.021	−0.024
Top Generator	0.17	-	0.057	0.28	0.039
Top Generator Stat	0.13	-	-	0.25	-
W Generator	0.081	-	0.22	0.033	0.043
W Generator Stat	0.099	-	0.35	-	-
Z Generator	0.093	-	0.40	0.028	1.0
Z Generator Stat	0.	-	-	-	1.0
Dibosons Generator	0.096	-	0.021	0.023	0.0060
Dibosons Generator Stat	0.032	-	-	-	-
JVF up	0.0010	-	−0.012	0.0070	0.
JVF down	−0.0010	-	−0.0050	0.	0.
QCD Tails up	−0.012	−0.53	−0.0030	0.	0.0010
QCD Tails down	0.0030	0.078	0.0080	0.	−0.0010
QCD gauss	0.0040	0.39	0.010	−0.014	0.
Total systematic uncertainty	0.30	0.50	0.61	0.39	1.4
Statistical uncertainty	0.16	0.68	0.40	0.23	0.43
Total uncertainty	0.34	0.84	0.73	0.46	1.5

Table F.4: Breakdown of all systematic and statistical uncertainties for the nGM signal region. Acronyms are introduced in Section 7.2. Systematic uncertainties are evaluated as relative changes in the background prediction for the signal region including changes in the data-driven background prediction due to changes in the transfer factors.

Systematic	Total	Multijets	W	Top	Z
JER	0.094	-	0.019	0.099	0.34
JES up	0.12	-	−0.11	0.22	0.65
JES down	0.032	-	0.11	0.036	−0.17
TES up	0.015	-	0.037	−0.012	0.012
TES down	−0.041	-	−0.071	0.073	−0.19
Tau ID up	0.0010	-	0.0080	−0.0040	−0.012
Tau ID down	−0.0010	-	−0.010	0.0040	0.013
Tau EVETO up	0.016	-	−0.0050	0.063	0.0010
Tau EVETO down	−0.015	-	0.0050	−0.058	−0.0010
BTag down	0.027	-	0.018	0.074	−0.015
BTag up	−0.024	-	−0.014	−0.068	0.014
$\not\!\!E_T$ resolution	−0.0090	-	−0.024	−0.0060	0.017
$\not\!\!E_T$ scale down	−0.0040	-	−0.018	0.0070	0.014
$\not\!\!E_T$ scale up	0.041	-	0.0010	0.16	−0.037
Pileup up	0.017	-	0.054	−0.044	0.037
Pileup down	−0.0080	-	−0.022	0.035	−0.050
Top Generator	0.090	-	0.066	0.19	0.045
Top Generator Stat	0.18	-	-	0.53	-
W Generator	0.012	-	0.	0.031	0.040
W Generator Stat	0.25	-	0.58	-	-
Z Generator	0.065	-	0.21	0.023	1.0
Z Generator Stat	0.	-	-	-	0.
Dibosons Generator	0.0070	-	0.010	0.011	0.0030
Dibosons Generator Stat	0.	-	-	-	-
JVF up	0.0030	-	0.0050	0.0030	0.
JVF down	−0.0020	-	−0.0030	−0.0010	−0.0010
QCD Tails up	−0.016	−0.22	0.016	−0.0010	−0.0030
QCD Tails down	0.056	0.46	0.022	−0.0010	−0.0040
QCD gauss	−0.010	0.011	−0.023	−0.0040	0.0050
Total systematic uncertainty	0.36	0.34	0.64	0.60	1.1
Statistical uncertainty	0.18	0.48	0.32	0.31	0.38
Total uncertainty	0.40	0.59	0.71	0.68	1.2

Table F.5: Breakdown of all systematic and statistical uncertainties for the bRPV$m_{1/2}$ signal region. Acronyms are introduced in Section 7.2. Systematic uncertainties are evaluated as relative changes in the background prediction for the signal region including changes in the data-driven background prediction due to changes in the transfer factors.

Systematic	Total	Dibosons	Multijets	W	Top	Z
JER	0.023	0.042	-	0.028	0.033	-0.023
JES up	0.016	0.55	-	-0.14	0.044	0.15
JES down	-0.0040	-0.23	-	0.11	0.0060	-0.25
TES up	0.014	0.	-	-0.055	0.024	0.14
TES down	0.	0.	-	0.0050	0.017	-0.077
Tau ID up	0.0090	0.064	-	0.027	0.0040	-0.023
Tau ID down	-0.010	-0.062	-	-0.029	-0.0040	0.025
Tau EVETO up	-0.0040	0.	-	-0.0050	-0.0060	0.0010
Tau EVETO down	0.0040	0.	-	0.0050	0.0060	-0.0010
BTag down	0.045	0.	-	0.020	0.079	-0.013
BTag up	-0.040	0.	-	-0.016	-0.072	0.012
$\not{E}_T$ resolution	0.0040	0.	-	0.0010	0.0040	0.016
$\not{E}_T$ scale down	0.0080	0.	-	-0.050	0.032	0.051
$\not{E}_T$ scale up	0.011	0.	-	0.075	-0.012	-0.038
Pileup up	-0.019	-0.080	-	-0.023	-0.026	0.025
Pileup down	0.020	0.065	-	0.032	0.025	-0.035
Top Generator	0.17	-	-	0.057	0.27	0.039
Top Generator Stat	0.098	-	-	-	0.19	-
W Generator	0.039	-	-	0.20	0.033	0.043
W Generator Stat	0.073	-	-	0.29	-	-
Z Generator	0.0030	-	-	0.40	0.028	1.0
Z Generator Stat	0.	-	-	-	-	1.0
Dibosons Generator	0.030	0.39	-	0.021	0.023	0.0060
Dibosons Generator Stat	0.018	0.40	-	-	-	-
JVF up	0.0020	0.	-	-0.0040	0.0070	0.
JVF down	-0.0020	0.	-	-0.0050	-0.0010	0.
QCD Tails up	-0.0020	-	-0.072	-0.0030	0.	0.0010
QCD Tails down	0.0090	-	0.32	0.0080	0.	-0.0010
QCD gauss	0.028	-	1.4	0.010	-0.014	0.
Total systematic uncertainty	0.22	0.69	1.4	0.56	0.35	1.4
Statistical uncertainty	0.15	0.62	0.40	0.36	0.24	0.37
Total uncertainty	0.27	0.93	1.5	0.67	0.42	1.5

Table F.6: Breakdown of all systematic and statistical uncertainties for the bRPVm_0 signal region. Acronyms are introduced in Section 7.2. Systematic uncertainties are evaluated as relative changes in the background prediction for the signal region including changes in the data-driven background prediction due to changes in the transfer factors.

F.4 Detailed plots of signal uncertainties

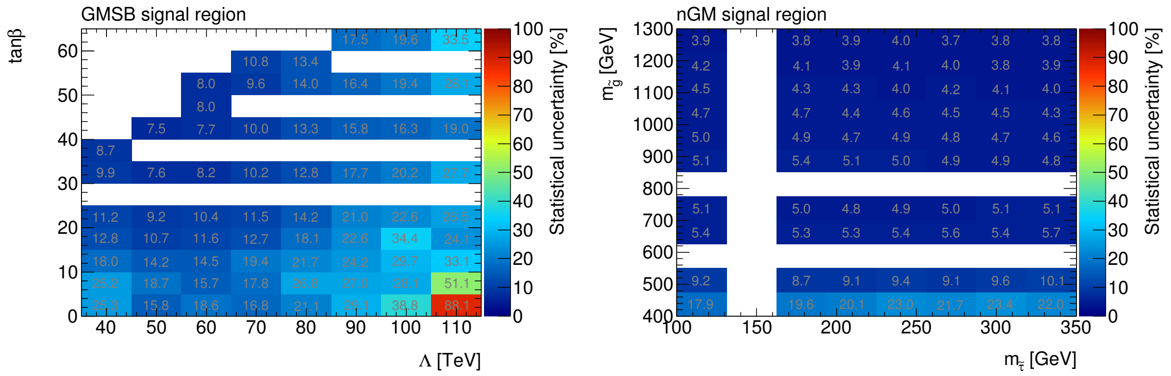

(a) GMSB statistical uncertainty
(b) nGM statistical uncertainty

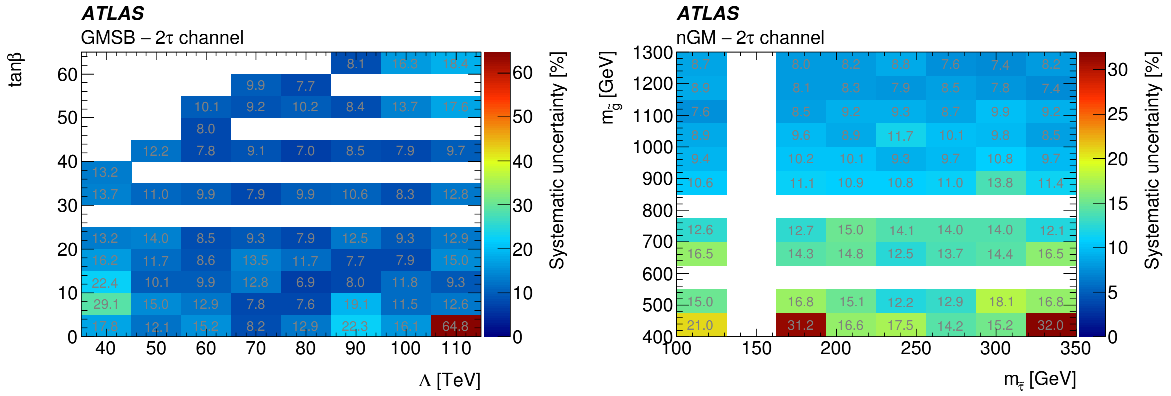

(c) GMSB systematic uncertainty
(d) nGM systematic uncertainty

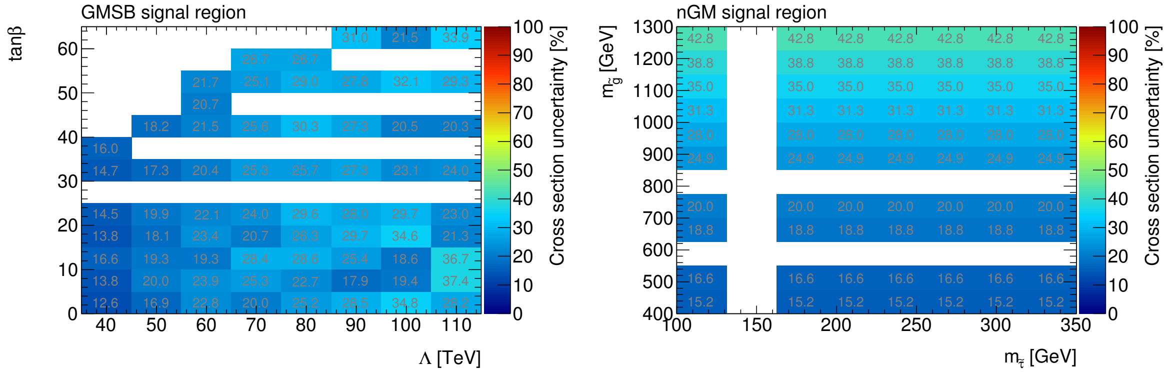

(e) GMSB cross section uncertainty
(f) nGM cross section uncertainty

Figure F.5: Details on the uncertainties of the GMSB (lef column) and nGM (right column) signal regions for the respective signal grids. Empty columns and rows are due to the non-regular spacing of the grid.

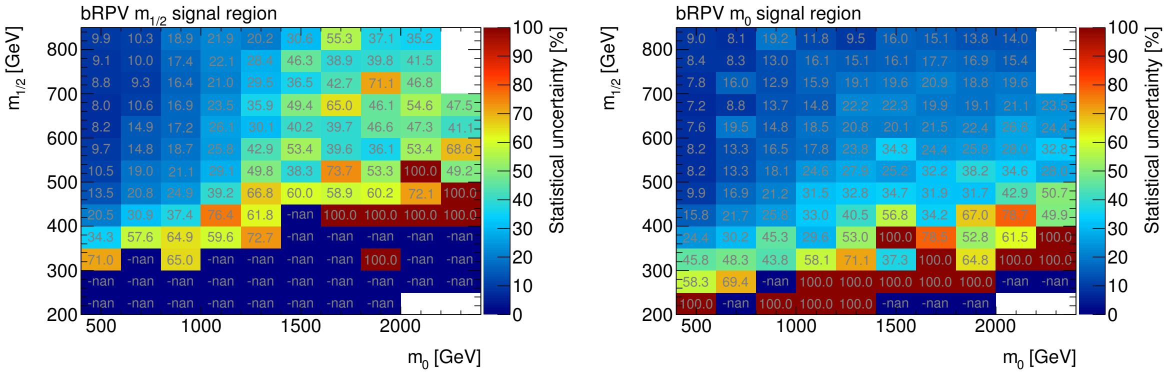

(a) bRPV $m_{1/2}$ statistical uncertainty (b) bRPV m_0 statistical uncertainty

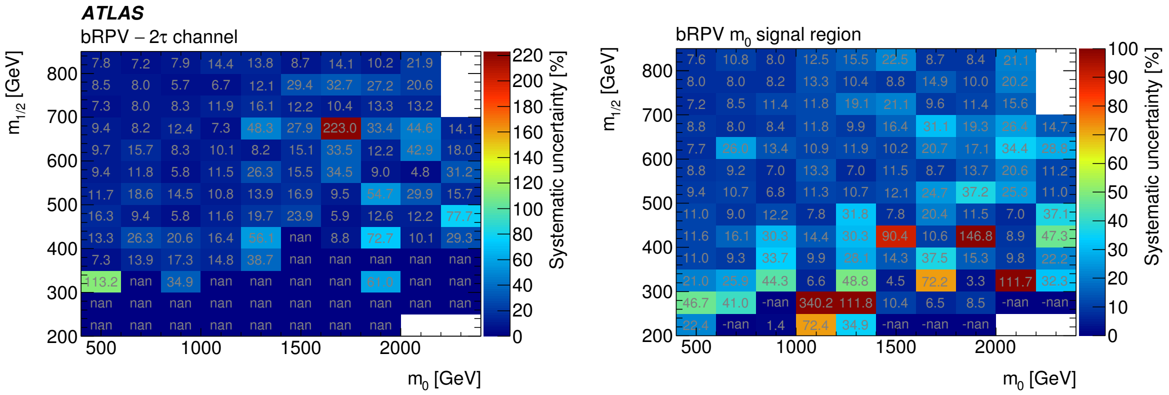

(c) bRPV $m_{1/2}$ systematic uncertainty (d) bRPV m_0 systematic uncertainty

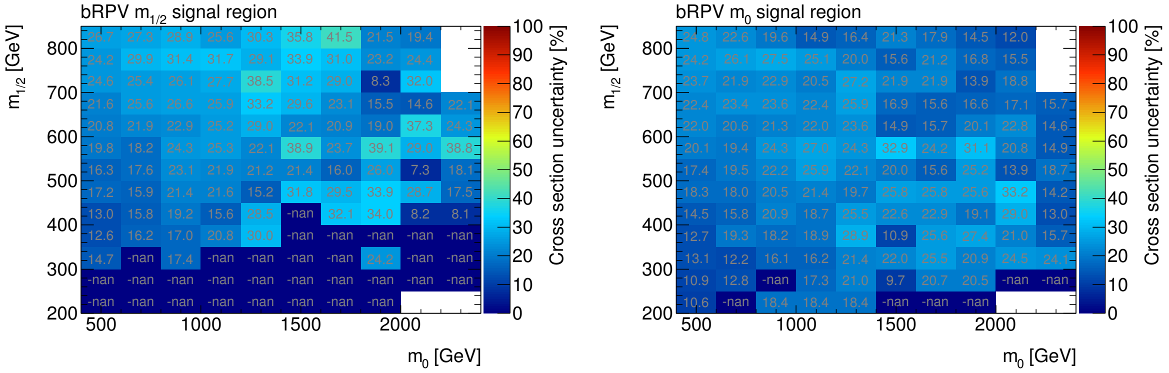

(e) bRPV $m_{1/2}$ cross section uncertainty (f) bRPV m_0 cross section uncertainty

Figure F.6: Details on the uncertainties of the bRPV signal regions for the bRPV signal grid. Empty columns and rows are due to the non-regular spacing of the grid.

G

Event Displays

In this appendix detector displays of the data events selected in the 2τ analysis are compiled. Details on kinematic properties of these events can be found in Table 8.4 in Section 8.

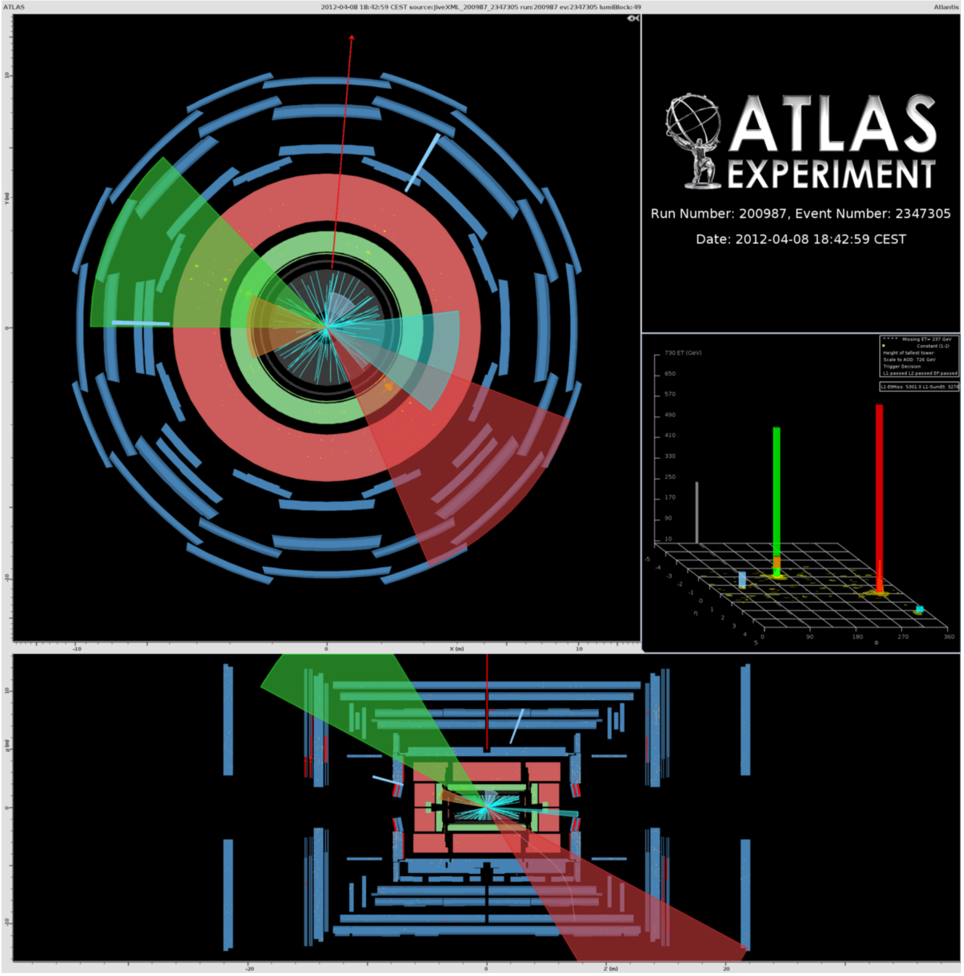

Figure G.1: Display of event 2347305 in run 200987. This event is part of the Inclusive signal region. $\not\!\!E_T$ is marked by the red arrow.

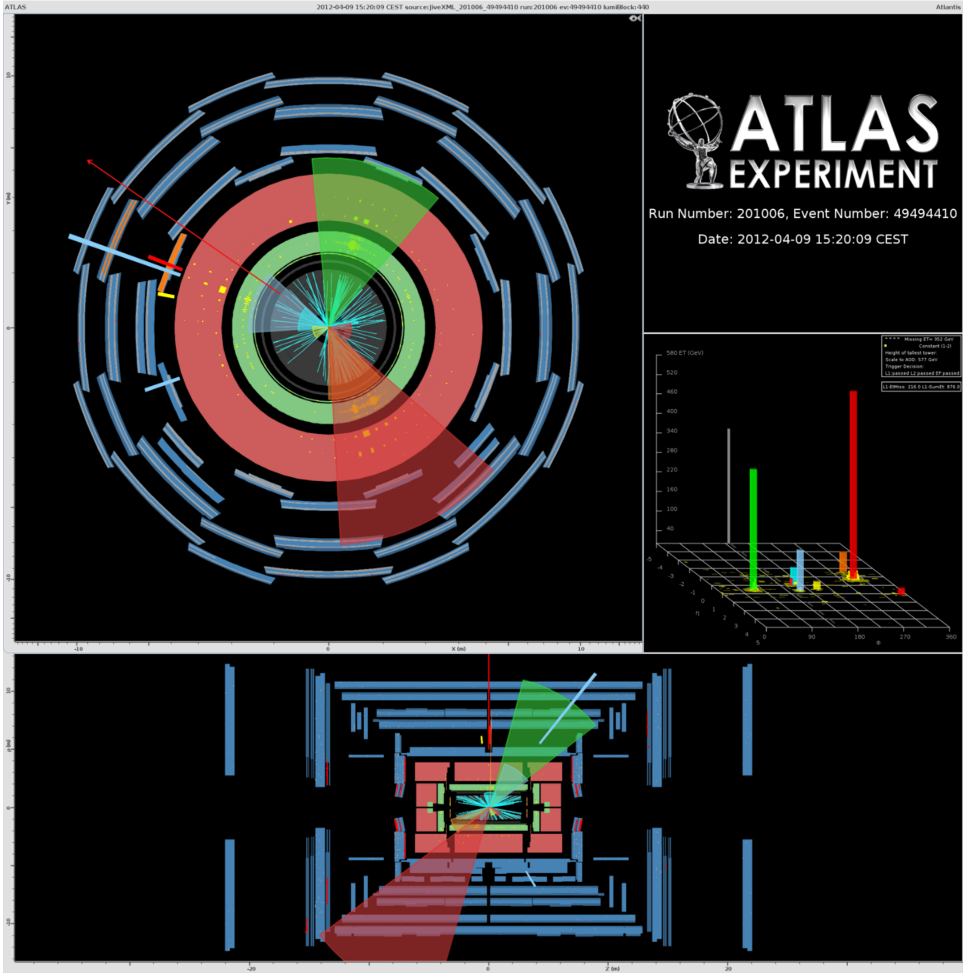

Figure G.2: Display of event 49494410 in run 201006. This event is part of the Inclusive and the bRPV $m_{1/2}$ signal region. $\not\!\!E_T$ is marked by the red arrow.

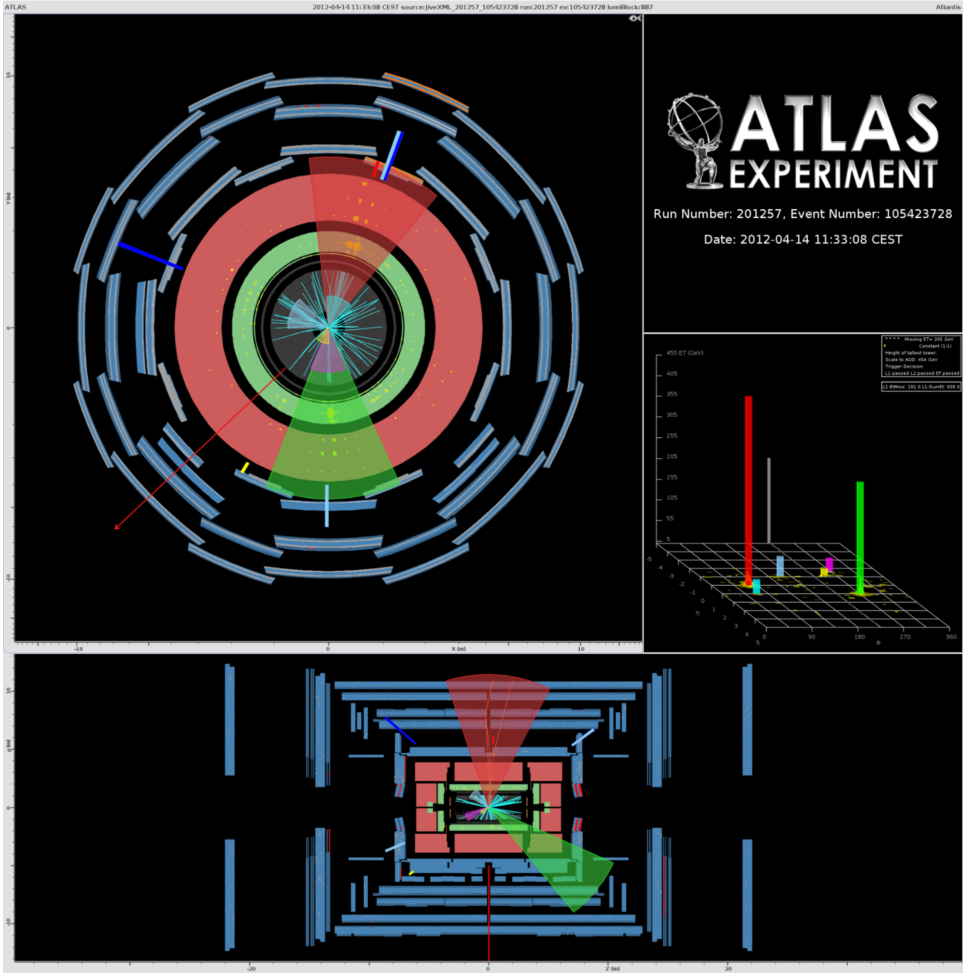

Figure G.3: Display of event 105423728 in run 201257. This event is part of the bRPV m_0 signal region. $\not{E}_T$ is marked by the red arrow.

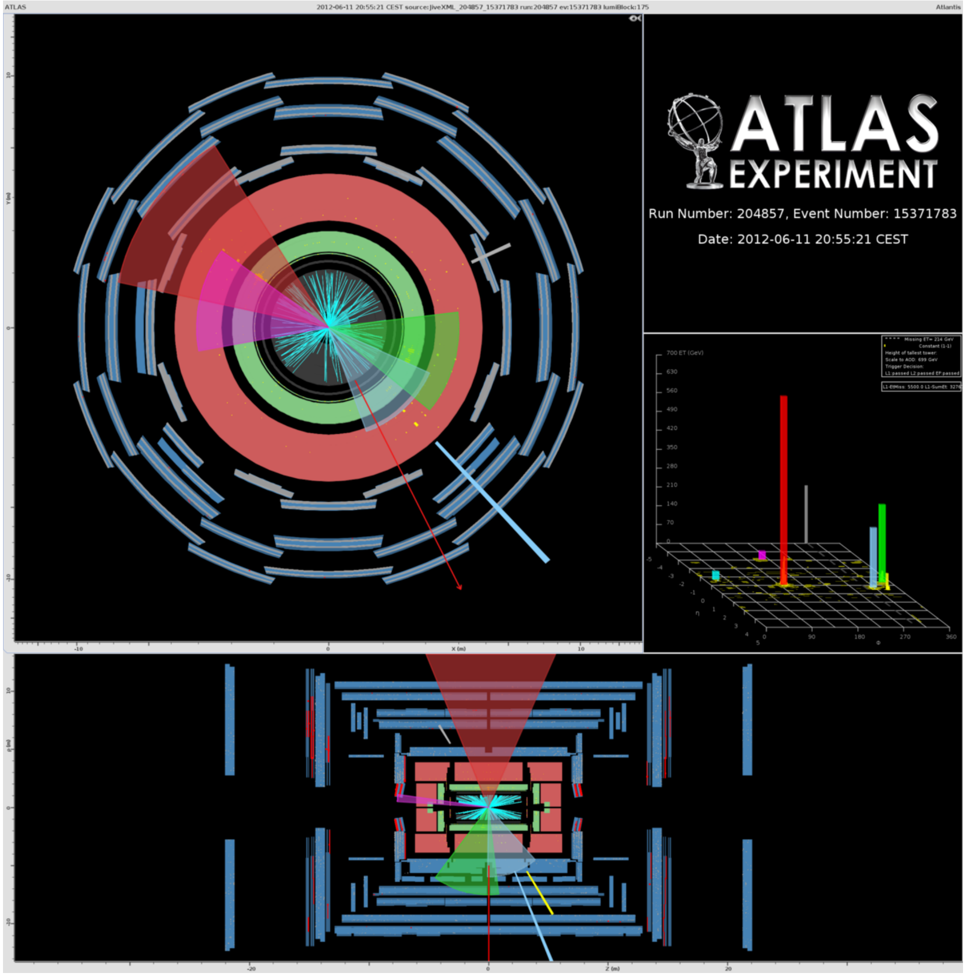

Figure G.4: Display of event 15371783 in run 204857. This event is part of the Inclusive signal region. $\not{E}_T$ is marked by the red arrow.

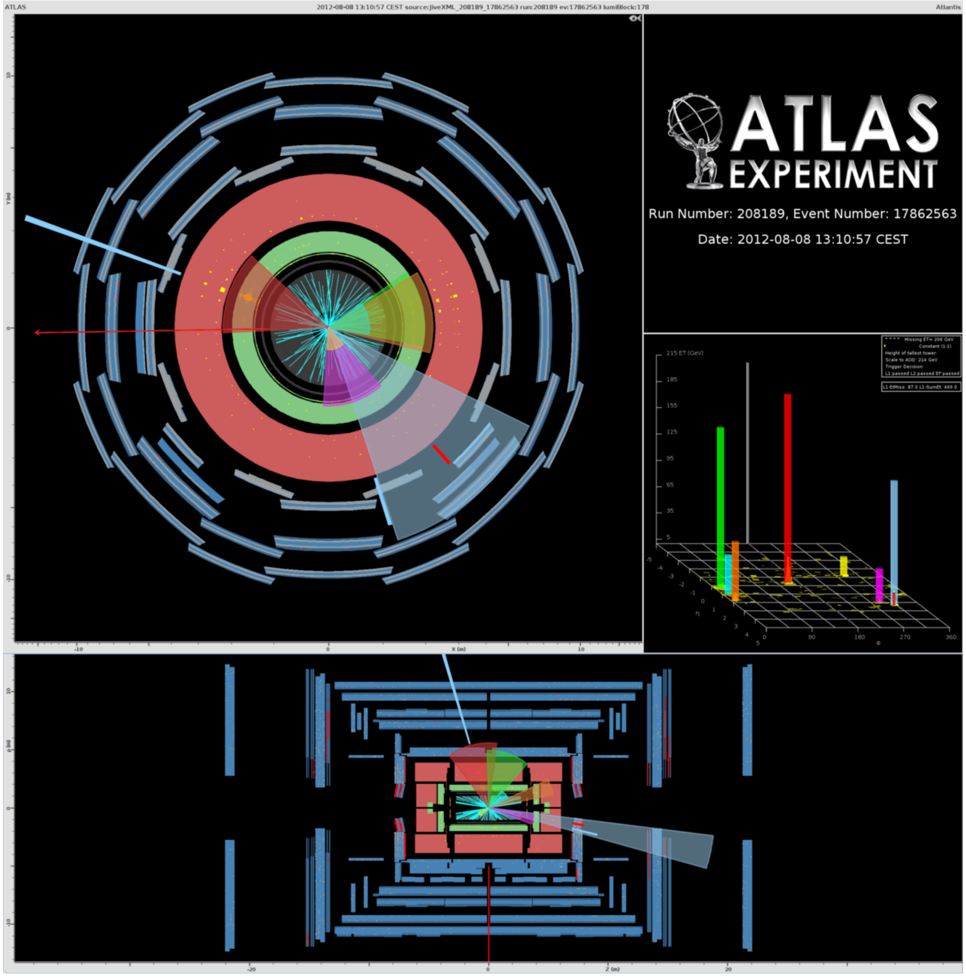

Figure G.5: Display of event 17862563 in run 208189. This event is part of the bRPV m_0 signal region. $\not\!\!E_T$ is marked by the red arrow.

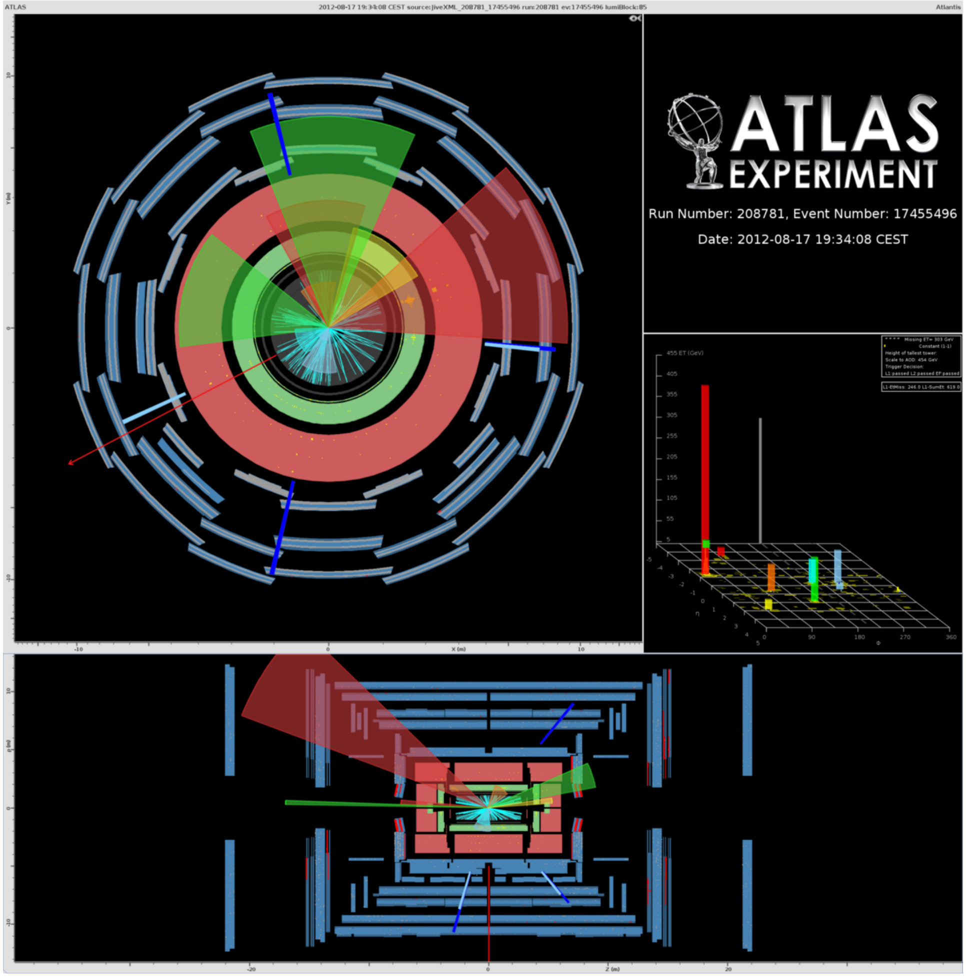

Figure G.6: Display of event 17455496 in run 208781. This event is part of the bRPV m_0 signal region. $\not{E}_T$ is marked by the red arrow.

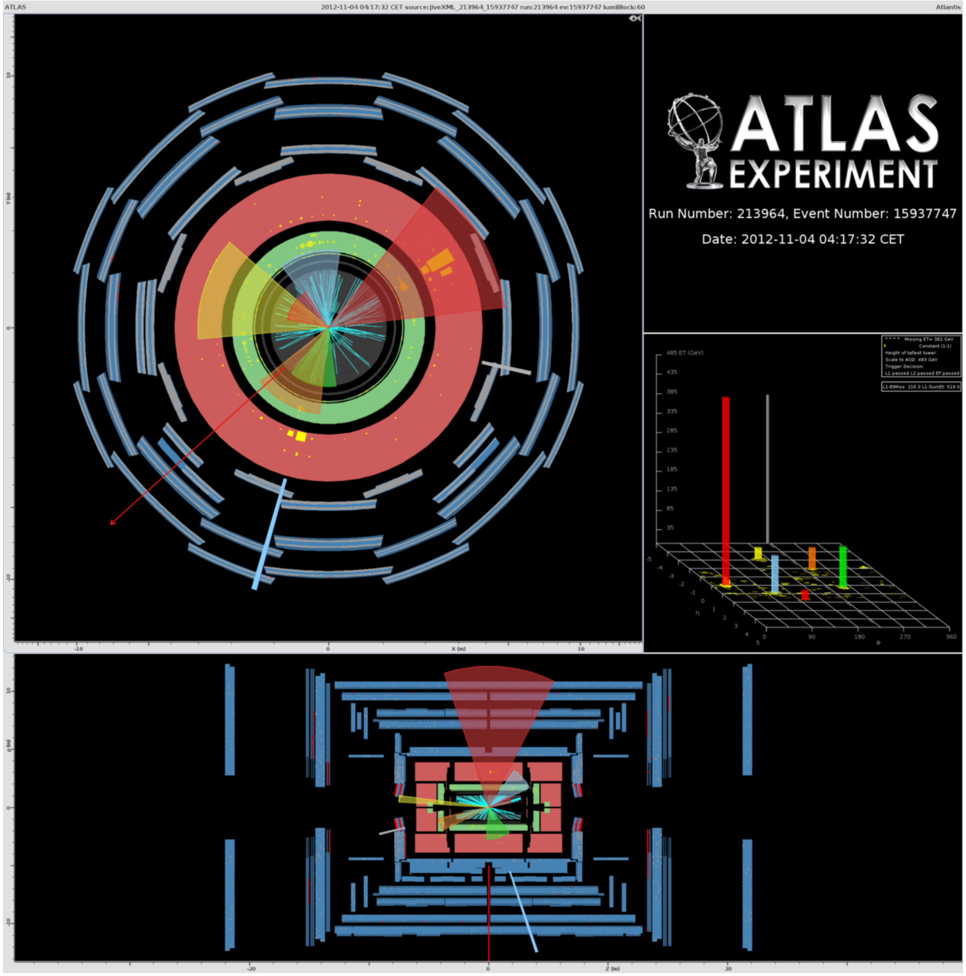

Figure G.7: Display of event 15937747 in run 213964. This event is part of the bRPV m_0 and the nGM signal region. $\not{E}_T$ is marked by the red arrow.

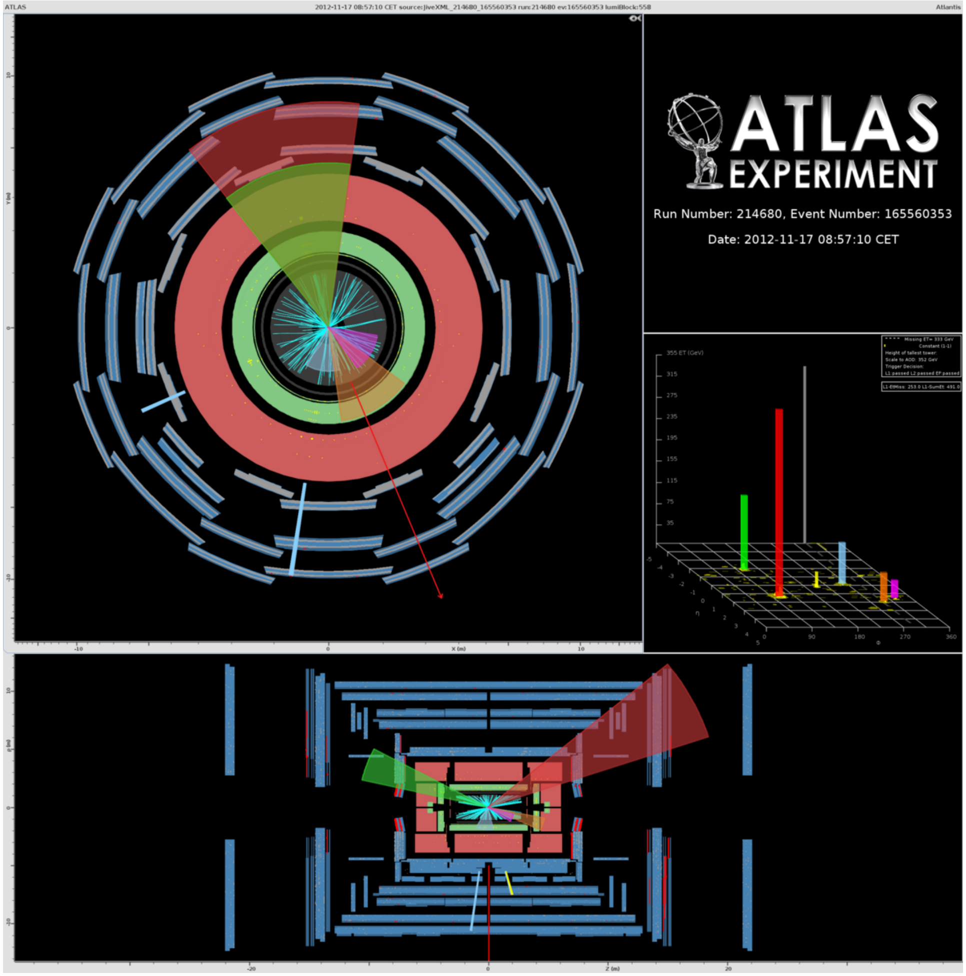

Figure G.8: Display of event 165560353 in run 214680. This event is part of the bRPV m_0 signal region. $\not{E}_T$ is marked by the red arrow.

Bibliography

[1] G. Aad et al., *Observation of a new particle in the search for the Standard Model Higgs boson with the ATLAS detector at the LHC*, Phys.Lett. **B716** (2012) 1–29, arXiv: `1207.7214 [hep-ex]`.

[2] *INSPIRE-HEP*, 2015, URL: `http://inspirehep.net/` (visited on 19/05/2015).

[3] K. Olive et al., *Review of Particle Physics*, Chin.Phys. **C38** (2014) 090001.

[4] G. Aad et al., *Search for events with large missing transverse momentum, jets, and at least two tau leptons in 7 TeV proton-proton collision data with the ATLAS detector*, Phys.Lett. **B714** (2012) 180–196, arXiv: `1203.6580 [hep-ex]`.

[5] G. Aad et al., *Search for Supersymmetry in Events with Large Missing Transverse Momentum, Jets, and at Least One Tau Lepton in 7 TeV Proton-Proton Collision Data with the ATLAS Detector*, Eur.Phys.J. **C72** (2012) 2215, arXiv: `1210.1314 [hep-ex]`.

[6] G. Aad et al., *Search for supersymmetry in events with large missing transverse momentum, jets, and at least one tau lepton in 20 fb*$^{-1}$ *of* $\sqrt{s} = 8$ *TeV proton-proton collision data with the ATLAS detector*, JHEP **1409** (2014) 103, arXiv: `1407.0603 [hep-ex]`.

[7] S. Schaepe et al., *Summary of the Searches for Inclusive Squarks and Gluinos with Run I LHC data at ATLAS*, To be published, 2015.

[8] S. Schaepe et al., *The impact of ATLAS supersymmetry searches on the phenomenological MSSM*, To be published, 2015.

[9] Dörthe Kennedy, *Search for Supersymmetry in Tau Final States at ATLAS and Constraints on New Physics Using Electroweak Precision Data*, PhD thesis: University of Hamburg and DESY, 2012.

[10] Anthony Rose, *Search for supersymmetry in events with leptons (e,* μ*,* τ*), jets and missing transverse energy with the ATLAS detector at the LHC*, PhD thesis: University of Sussex, 2013.

[11] Therese Sjursen, *Search for Supersymmetry with Tau Leptons in Data from the ATLAS Experiment at the LHC*, PhD thesis: University of Bergen, 2014.

[12] Till Nattermann, *Search for Supersymmetry with Tau Leptons, Muons, Missing Transverse Momentum and Jets with the ATLAS Experiment at the Large Hadron Collider*, PhD thesis: University of Bonn, 2013.

[13] N. MissMJ et al., *Standard Model of Elementary Particles, modified version*, 2014, URL: `http://commons.wikimedia.org/wiki/File:Standard_Model_of_Elementary_Particles_modified_version.svg` (visited on 26/11/2014).

[14] F. Halzen and A. Martin, *Quarks and leptons: an introductory course in modern particle physics*, Wiley, 1984.

[15] J. D. Jackson, C. Witte and K. Muller, *Klassische Elektrodynamik (Uberarbeitete Auflage) (German Edition)*, Walter de Gruyter, 2006, ISBN: 3110189704.

[16] W. E. Lamb and R. C. Retherford, *Fine Structure of the Hydrogen Atom by a Microwave Method*, Phys. Rev. **72** (3 Aug. 1947) 241–243, URL: `http://link.aps.org/doi/10.1103/PhysRev.72.241`.

[17] C. S. Wu et al., *Experimental Test of Parity Conservation in Beta Decay*, Phys. Rev. **105** (4 Feb. 1957) 1413–1415, URL: `http://link.aps.org/doi/10.1103/PhysRev.105.1413`.

[18] M. Goldhaber, L. Grodzins and A. W. Sunyar, *Helicity of Neutrinos*, Phys. Rev. **109** (3 Feb. 1958) 1015–1017, URL: `http://link.aps.org/doi/10.1103/PhysRev.109.1015`.

[19] S. L. Glashow, *Partial-symmetries of weak interactions*, Nuclear Physics **22**.4 (1961) 579–588, ISSN: 0029-5582, URL: `http://www.sciencedirect.com/science/article/pii/0029558261904692`.

[20] A. Salam and J. Ward, *Electromagnetic and weak interactions*, Physics Letters **13**.2 (1964) 168–171, ISSN: 0031-9163, URL: `http://www.sciencedirect.com/science/article/pii/0031916364907115`.

[21] S. Weinberg, *A Model of Leptons*, Phys. Rev. Lett. **19** (21 Nov. 1967) 1264–1266, URL: `http://link.aps.org/doi/10.1103/PhysRevLett.19.1264`.

[22] N. Cabibbo, *Unitary Symmetry and Leptonic Decays*, Phys.Rev.Lett. **10** (1963) 531–533.

[23] M. Kobayashi and T. Maskawa, *CP Violation in the Renormalizable Theory of Weak Interaction*, Prog.Theor.Phys. **49** (1973) 652–657.

[24] M. Gell-Mann, *A Schematic Model of Baryons and Mesons*, Phys.Lett. **8** (1964) 214–215.

[25] G. Zweig, *An SU_3 model for strong interaction symmetry and its breaking; Version 2*, CERN-TH-412 (Feb. 1964) 80 p, Version 1 is CERN preprint 8182/TH.401, Jan. 17, 1964.

[26] M. Gell-mann and Y. Ne'eman, *The Eightfold Way*, Westview Press, 2000, ISBN: 0738202991, URL: `http://www.amazon.com/The-Eightfold-Way-Murray-Gell-mann/dp/0738202991?SubscriptionId=0JYN1NVW651KCA56C102&tag=techkie-20&linkCode=xm2&camp=2025&creative=165953&creativeASIN=0738202991`.

[27] D. Mendelejew, *Über die Beziehungen der Eigenschaften zu den Atomgewichten der Elemente*, Zeitschrift für Chemie (1869) 405–406.

[28] V. E. Barnes et al., *Observation of a Hyperon with Strangeness Minus Three*, Phys. Rev. Lett. **12** (8 Feb. 1964) 204–206, URL: `http://link.aps.org/doi/10.1103/PhysRevLett.12.204`.

[29] M. Han and Y. Nambu, *Three Triplet Model with Double SU(3) Symmetry*, Phys.Rev. **139** (1965) B1006–B1010.

[30] H. Fritzsch, M. Gell-Mann and H. Leutwyler, *Advantages of the color octet gluon picture*, Physics Letters B **47**.4 (1973) 365–368, ISSN: 0370-2693, URL: `http://www.sciencedirect.com/science/article/pii/0370269373906254`.

[31] D. J. Gross and F. Wilczek, *Ultraviolet Behavior of Nonabelian Gauge Theories*, Phys.Rev.Lett. **30** (1973) 1343–1346.

[32] H. D. Politzer, *Reliable Perturbative Results for Strong Interactions?*, Phys.Rev.Lett. **30** (1973) 1346–1349.

[33] U. Loring et al., *Relativistic quark models of baryons with instantaneous forces: Theoretical background*, Eur.Phys.J. **A10** (2001) 309–346, arXiv: `hep-ph/0103287 [hep-ph]`.

[34] U. Loring, B. C. Metsch and H. R. Petry, *The Light baryon spectrum in a relativistic quark model with instanton induced quark forces: The Nonstrange baryon spectrum and ground states*, Eur.Phys.J. **A10** (2001) 395–446, arXiv: `hep-ph/0103289 [hep-ph]`.

[35] U. Loring, B. C. Metsch and H. R. Petry, *The Light baryon spectrum in a relativistic quark model with instanton induced quark forces: The Strange baryon spectrum*, Eur.Phys.J. **A10** (2001) 447–486, arXiv: `hep-ph/0103290 [hep-ph]`.

[36] R. D. Ball et al., *Parton distributions with {LHC} data*, Nuclear Physics B **867**.2 (2013) 244–289, ISSN: 0550-3213, URL: `http://www.sciencedirect.com/science/article/pii/S0550321312005500`.

[37] P. Higgs, *Broken symmetries, massless particles and gauge fields*, Physics Letters **12**.2 (1964) 132–133, ISSN: 0031-9163, URL: `http://www.sciencedirect.com/science/article/pii/0031916364911369`.

[38] P. Higgs, *Broken Symmetries and the Masses of Gauge Bosons*, Phys. Rev. Lett. **13** (16 Oct. 1964) 508–509, URL: `http://link.aps.org/doi/10.1103/PhysRevLett.13.508`.

[39] P. Higgs, *Spontaneous Symmetry Breakdown without Massless Bosons*, Phys. Rev. **145** (4 May 1966) 1156–1163, URL: `http://link.aps.org/doi/10.1103/PhysRev.145.1156`.

[40] F. Englert and R. Brout, *Broken Symmetry and the Mass of Gauge Vector Mesons*, Phys. Rev. Lett. **13** (9 Aug. 1964) 321–323, URL: `http://link.aps.org/doi/10.1103/PhysRevLett.13.321`.

[41] G. Aad et al.,
Evidence for the Higgs-boson Yukawa coupling to tau leptons with the ATLAS detector (2015),
arXiv: `1501.04943 [hep-ex]`.

[42] S. Banerjee et al., *Status Report from Tau subgroup of the HFAG*,
Nucl.Phys.Proc.Suppl. **218** (2011) 329–334, arXiv: `1101.5138 [hep-ex]`.

[43] B. Andersson et al., *Parton fragmentation and string dynamics*,
Physics Reports **97**.2–3 (1983) 31–145, ISSN: 0370-1573, URL: `http://www.sciencedirect.com/science/article/pii/0370157383900807`.

[44] S. Weinberg, *Implications of Dynamical Symmetry Breaking*, Phys. Rev. **D13** (1976) 974–996.

[45] E. Gildener, *Gauge Symmetry Hierarchies*, Phys. Rev. **D14** (1976) 1667.

[46] S. Weinberg, *Implications of Dynamical Symmetry Breaking: An Addendum*,
Phys. Rev. **D19** (1979) 1277–1280.

[47] L. Susskind, *Dynamics of Spontaneous Symmetry Breaking in the Weinberg- Salam Theory*,
Phys. Rev. **D20** (1979) 2619–2625.

[48] S. Dimopoulos and H. Georgi, *Softly Broken Supersymmetry and SU(5)*,
Nucl. Phys. **B193** (1981) 150.

[49] E. Witten, *Dynamical Breaking of Supersymmetry*, Nucl. Phys. **B188** (1981) 513.

[50] M. Dine, W. Fischler and M. Srednicki, *Supersymmetric Technicolor*,
Nucl. Phys. **B189** (1981) 575–593.

[51] S. Dimopoulos and S. Raby, *Supercolor*, Nucl. Phys. **B192** (1981) 353.

[52] N. Sakai, *Naturalness in Supersymmetric Guts*, Zeit. Phys. **C11** (1981) 153.

[53] R. Kaul and P. Majumdar, *Cancellation of Quadratically Divergent Mass Corrections in Globally Supersymmetric Spontaneously Broken Gauge Theories*, Nucl. Phys. **B199** (1982) 36.

[54] P. Ade et al., *Planck 2013 results. XVI. Cosmological parameters*,
Astron.Astrophys. **571** (2014) A16, arXiv: `1303.5076 [astro-ph.CO]`.

[55] H. Goldberg, *Constraint on the photino mass from cosmology*, Phys. Rev. Lett. **50** (1983) 1419.

[56] J. Ellis et al., *Supersymmetric relics from the big bang*, Nucl. Phys. **B238** (1984) 453–476.

[57] S. Dimopoulos, S. Raby and F. Wilczek, *Supersymmetry and the Scale of Unification*,
Phys. Rev. **D24** (1981) 1681–1683.

[58] L. E. Ibanez and G. G. Ross,
Low-Energy Predictions in Supersymmetric Grand Unified Theories,
Phys. Lett. **B105** (1981) 439.

[59] M. B. Einhorn and D. R. T. Jones,
The Weak Mixing Angle and Unification Mass in Supersymmetric SU(5),
Nucl. Phys. **B196** (1982) 475.

[60] W. J. Marciano and G. Senjanovic, *Predictions of Supersymmetric Grand Unified Theories*,
Phys. Rev. **D25** (1982) 3092.

[61] C. Giunti, C. W. Kim and U. Lee, *Running coupling constants and grand unification models*, Mod. Phys. Lett. **A6** (1991) 1745–1755.

[62] J. Ellis, S. Kelley and D. Nanopoulos, *Probing the desert using gauge coupling unification*, Phys. Lett. **B260** (1991) 131–137.

[63] U. Amaldi, W. de Boer and H. Furstenau, *Comparison of grand unified theories with electroweak and strong coupling constants measured at LEP*, Phys. Lett. **B260** (1991) 447–455.

[64] P. Langacker and M.-X. Luo, *Implications of precision electroweak experiments for M(t), rho(0), sin**2-Theta(W) and grand unification*, Phys. Rev. **D44** (1991) 817–822.

[65] I. J. Aitchison, *Supersymmetry and the MSSM: An Elementary introduction* (2005), arXiv: `hep-ph/0505105 [hep-ph]`.

[66] S. P. Martin, *A Supersymmetry primer*, Adv.Ser.Direct.High Energy Phys. **21** (2010) 1–153, arXiv: `hep-ph/9709356 [hep-ph]`.

[67] H. Miyazawa, *Baryon Number Changing Currents*, Prog. Theor. Phys. **36 (6)** (1966) 1266–1276.

[68] P. Ramond, *Dual Theory for Free Fermions*, Phys. Rev. **D3** (1971) 2415–2418.

[69] Y. A. Gol'fand and E. P. Likhtman, *Extension of the Algebra of Poincare Group Generators and Violation of p Invariance*, JETP Lett. **13** (1971) 323–326, [Pisma Zh.Eksp.Teor.Fiz.13:452-455,1971].

[70] A. Neveu and J. H. Schwarz, *Factorizable dual model of pions*, Nucl. Phys. **B31** (1971) 86–112.

[71] A. Neveu and J. H. Schwarz, *Quark Model of Dual Pions*, Phys. Rev. **D4** (1971) 1109–1111.

[72] J. Gervais and B. Sakita, *Field theory interpretation of supergauges in dual models*, Nucl. Phys. **B34** (1971) 632–639.

[73] D. V. Volkov and V. P. Akulov, *Is the Neutrino a Goldstone Particle?*, Phys. Lett. **B46** (1973) 109–110.

[74] J. Wess and B. Zumino, *A Lagrangian Model Invariant Under Supergauge Transformations*, Phys. Lett. **B49** (1974) 52.

[75] J. Wess and B. Zumino, *Supergauge Transformations in Four-Dimensions*, Nucl. Phys. **B70** (1974) 39–50.

[76] S. Coleman and J. Mandula, *All Possible Symmetries of the S Matrix*, Phys. Rev. **159** (5 July 1967) 1251–1256, URL: `http://link.aps.org/doi/10.1103/PhysRev.159.1251`.

[77] R. Haag, J. T. Łopuszański and M. Sohnius, *All possible generators of supersymmetries of the S-matrix*, Nuclear Physics B **88**.2 (1975) 257–274, ISSN: 0550-3213, URL: `http://www.sciencedirect.com/science/article/pii/0550321375902795`.

[78] P. Fayet, *Supersymmetry and Weak, Electromagnetic and Strong Interactions*, Phys. Lett. **B64** (1976) 159.

[79] P. Fayet, *Spontaneously Broken Supersymmetric Theories of Weak, Electromagnetic and Strong Interactions*, Phys. Lett. **B69** (1977) 489.

[80] G. R. Farrar and P. Fayet, *Phenomenology of the Production, Decay, and Detection of New Hadronic States Associated with Supersymmetry*, Phys. Lett. **B76** (1978) 575–579.

[81] P. Fayet, *Relations Between the Masses of the Superpartners of Leptons and Quarks, the Goldstino Couplings and the Neutral Currents*, Phys. Lett. **B84** (1979) 416.

[82] P. Nath and R. L. Arnowitt, *Generalized Supergauge Symmetry as a New Framework for Unified Gauge Theories*, Phys.Lett. **B56** (1975) 177.

[83] R. L. Arnowitt, P. Nath and B. Zumino, *Superfield Densities and Action Principle in Curved Superspace*, Phys.Lett. **B56** (1975) 81.

[84] D. Z. Freedman, P. van Nieuwenhuizen and S. Ferrara, *Progress Toward a Theory of Supergravity*, Phys.Rev. **D13** (1976) 3214–3218.

[85] S. Deser and B. Zumino, *Consistent Supergravity*, Phys.Lett. **B62** (1976) 335.

[86] D. Z. Freedman and P. van Nieuwenhuizen, *Properties of Supergravity Theory*, Phys.Rev. **D14** (1976) 912.

[87] E. Cremmer et al., *Spontaneous Symmetry Breaking and Higgs Effect in Supergravity Without Cosmological Constant*, Nucl.Phys. **B147** (1979) 105.

[88] J. A. Bagger, *Coupling the Gauge Invariant Supersymmetric Nonlinear Sigma Model to Supergravity*, Nucl.Phys. **B211** (1983) 302.

[89] E. Cremmer et al., *Yang-Mills Theories with Local Supersymmetry: Lagrangian, Transformation Laws and SuperHiggs Effect*, Nucl.Phys. **B212** (1983) 413.

[90] S. Dimopoulos and D. Sutter, *The supersymmetric flavor problem*, Nuclear Physics B **452**.3 (1995) 496–512, ISSN: 0550-3213, URL: `http://www.sciencedirect.com/science/article/pii/055032139500421N`.

[91] M. Dine and W. Fischler, *A Phenomenological Model of Particle Physics Based on Supersymmetry*, Phys. Lett. **B110** (1982) 227.

[92] L. Alvarez-Gaume, M. Claudson and M. B. Wise, *Low-Energy Supersymmetry*, Nucl. Phys. **B207** (1982) 96.

[93] C. R. Nappi and B. A. Ovrut, *Supersymmetric Extension of the SU(3) x SU(2) x U(1) Model*, Phys. Lett. **B113** (1982) 175.

[94] M. Dine and A. E. Nelson, *Dynamical supersymmetry breaking at low-energies*, Phys. Rev. **D48** (1993) 1277–1287, arXiv: `hep-ph/9303230`.

[95] M. Dine, A. E. Nelson and Y. Shirman, *Low-energy dynamical supersymmetry breaking simplified*, Phys. Rev. **D51** (1995) 1362–1370, arXiv: `hep-ph/9408384`.

[96] M. Dine et al., *New tools for low-energy dynamical supersymmetry breaking*, Phys. Rev. **D53** (1996) 2658–2669, arXiv: `hep-ph/9507378`.

[97] F. Salvatore et al., *Search for Events with Large Missing Transverse Momentum, Jets, and Leptons (e/mu/tau) in 7 TeV Proton-Proton Collision Data with the ATLAS Detector*, tech. rep. ATL-COM-PHYS-2012-567, CERN, May 2012.

[98] S. P. Martin and J. D. Wells, *Implications of gauge-mediated supersymmetry breaking with vector-like quarks and a 125 GeV Higgs boson*, Phys.Rev. **D86** (2012) 035017, arXiv: `1206.2956 [hep-ph]`.

[99] P. Meade, N. Seiberg and D. Shih, *General Gauge Mediation*, Progress of Theoretical Physics Supplement **177** (2009) 143–158, eprint: `http://ptps.oxfordjournals.org/content/177/143.full.pdf+html`, URL: `http://ptps.oxfordjournals.org/content/177/143.abstract`.

[100] P. Draper et al., *Implications of a 125 GeV Higgs for the MSSM and Low-Scale SUSY Breaking*, Phys.Rev. **D85** (2012) 095007, arXiv: `1112.3068 [hep-ph]`.

[101] R. Barbieri and G. Giudice, *Upper Bounds on Supersymmetric Particle Masses*, Nucl.Phys. **B306** (1988) 63.

[102] B. de Carlos and J. Casas, *One loop analysis of the electroweak breaking in supersymmetric models and the fine tuning problem*, Phys.Lett. **B309** (1993) 320–328, arXiv: `hep-ph/9303291 [hep-ph]`.

[103] J. Barnard et al., *Natural gauge mediation with a bino NLSP at the LHC*, Phys.Rev.Lett. **109** (2012) 241801, arXiv: `1208.6062 [hep-ph]`.

[104] A. H. Chamseddine, R. Arnowitt and P. Nath, *Locally Supersymmetric Grand Unification*, Phys. Rev. Lett. **49** (1982) 970.

[105] R. Barbieri, S. Ferrara and C. A. Savoy, *Gauge Models with Spontaneously Broken Local Supersymmetry*, Phys. Lett. **B119** (1982) 343.

[106] L. E. Ibanez, *Locally Supersymmetric SU(5) Grand Unification*, Phys. Lett. **B118** (1982) 73.

[107] L. J. Hall, J. D. Lykken and S. Weinberg, *Supergravity as the Messenger of Supersymmetry Breaking*, Phys. Rev. **D27** (1983) 2359–2378.

[108] N. Ohta, *Grand Unified Theories Based on Local Supersymmetry*, Prog. Theor. Phys. **70** (1983) 542.

[109] G. L. Kane et al., *Study of constrained minimal supersymmetry*, Phys. Rev. **D49** (1994) 6173–6210.

[110] W. Porod et al., *Testing neutrino mixing at future collider experiments*, Phys.Rev. **D63** (2001) 115004, arXiv: `hep-ph/0011248 [hep-ph]`.

[111] M. A. Diaz, J. C. Romao and J. Valle, *Minimal supergravity with R-parity breaking*, Nucl.Phys. **B524** (1998) 23–40, arXiv: `hep-ph/9706315 [hep-ph]`.

[112] B. Sarrazin, personal communication, 7th May 2015.

[113] P. Bechtle et al., *How alive is constrained SUSY really?* (2014), arXiv: `1410.6035 [hep-ph]`.

[114] C. F. Berger et al., *Supersymmetry Without Prejudice*, JHEP **0902** (2009) 023, arXiv: `0812.0980 [hep-ph]`.

[115] M. W. Cahill-Rowley et al., *The New Look pMSSM with Neutralino and Gravitino LSPs*, Eur.Phys.J. **C72** (2012) 2156, arXiv: `1206.4321 [hep-ph]`.

[116] K. de Vries et al., *The pMSSM10 after LHC Run 1* (2015), arXiv: `1504.03260 [hep-ph]`.

[117] ATLAS, *Summary of Standard Model total production cross section measurements*, 2014, URL: `https://atlas.web.cern.ch/Atlas/GROUPS/PHYSICS/CombinedSummaryPlots/SM/` (visited on 23/09/2014).

[118] O. S. Brüning et al., *LHC Design Report*, CERN-2004-003-V-1, CERN-2004-003-V-2, CERN-2004-003-V-3, Geneva: CERN, 2004.

[119] K. Schindl, *The PS Booster as Preinjector for LHC*, Part. Accel. **58**.CERN-PS-97-011. CERN-PS-97-11. CERN-PS-97-011 (1997) 63–78. 16 p.

[120] R. Cappi, *The PS in the LHC injector chain*, Part. Accel. **58**.CERN-PS-97-016-CA (Apr. 1997) 79–89. 13 p.

[121] P. Collier et al., *The SPS as Injector for LHC: Conceptual Design*, tech. rep. CERN-SL-97-007-DI, CERN, Mar. 1997.

[122] F. Marcastel, *CERN's Accelerator Complex. La chaîne des accélérateurs du CERN*, OPEN-PHO-CHART-2013-001 (Oct. 2013), General Photo.

[123] M. Aicheler et al., *A Multi-TeV Linear Collider Based on CLIC Technology* (2012), ed. by M. Aicheler.

[124] T. Behnke et al., *The International Linear Collider Technical Design Report - Volume 1: Executive Summary* (2013), ed. by T. Behnke, arXiv: `1306.6327 [physics.acc-ph]`.

[125] G. W. Records, *The Large Hadron Collider*, 2015, URL: `http://www.guinnessworldrecords.com/search?term=%22Large+Hadron+Collider%22&page=1&max=20` (visited on 27/05/2015).

[126] D. M. Bonn, *Wolfgang Paul - Der Teilchenfänger*, 2014, URL: `http://www.deutsches-museum.de/bonn/ausstellungen/ausstellungen-2013/wolfgang-paul/` (visited on 21/10/2014).

[127] *The ATLAS Experiment at the CERN Large Hadron Collider*, J. Instrum. **3** (2008) S08003. 437 p, Also published by CERN Geneva in 2010.

[128] S. Mehlhase, *The ATLAS LEGO model*, 2014, URL: `http://build-your-own-particle-detector.org/models/atlas-lego-model` (visited on 21/10/2014).

[129] J. Pequenao, "Computer generated image of the ATLAS inner detector", Mar. 2008.

[130] S. Schaepe, *Commissioning and performance of the ATLAS Transition Radiation Tracker with first high energy pp and Pb-Pb collisions at LHC*, 2nd International Conference on Advancements in Nuclear Instrumentation Measurement Methods and their Applications (ANIMMA) (2011).

[131] T. A. T. collaboration, *The ATLAS Transition Radiation Tracker (TRT) proportional drift tube: design and performance*, Journal of Instrumentation **3**.02 (2008) P02013, URL: `http://stacks.iop.org/1748-0221/3/i=02/a=P02013`.

[132] W. Leo, *Techniques for Nuclear and Particle Physics Experiments: A How-To Approach*, U.S. Government Printing Office, 1994, ISBN: 9783540572800, URL: `http://books.google.de/books?id=8VufE4SD-AkC`.

[133] T. A. T. collaboration, *The ATLAS TRT Barrel Detector*, Journal of Instrumentation **3**.02 (2008) P02014, URL: `http://stacks.iop.org/1748-0221/3/i=02/a=P02014`.

[134] T. A. T. collaboration, *The ATLAS TRT end-cap detectors*, Journal of Instrumentation **3**.10 (2008) P10003, URL: `http://stacks.iop.org/1748-0221/3/i=10/a=P10003`.

[135] T. A. T. collaboration, *The ATLAS TRT electronics*, Journal of Instrumentation **3**.06 (2008) P06007, URL: `http://stacks.iop.org/1748-0221/3/i=06/a=P06007`.

[136] *Calibration of the ATLAS Transition Radiation Tracker*, tech. rep. ATLAS-CONF-2011-006, CERN, Feb. 2011.

[137] J. Pequenao, “Computer Generated image of the ATLAS calorimeter”, Mar. 2008.

[138] J. Pequenao, “Computer generated image of the whole ATLAS detector”, Mar. 2008.

[139] V. Boisvert et al., *Final Report of the ATLAS Reconstruction Task Force*, tech. rep. ATL-SOFT-2003-010, See http://atlas-proj-rtf.web.cern.ch/ for more information.: CERN, Sept. 2003.

[140] R. Brun and F. Rademakers, *{ROOT} — An object oriented data analysis framework*, Nuclear Instruments and Methods in Physics Research Section A: Accelerators, Spectrometers, Detectors and Associated Equipment **389**.1–2 (1997) 81–86, New Computing Techniques in Physics Research V, ISSN: 0168-9002, URL: `http://www.sciencedirect.com/science/article/pii/S016890029700048X`.

[141] G. Aad et al., *Improved luminosity determination in pp collisions at $\sqrt{s}$ = 7 TeV using the ATLAS detector at the LHC*, Eur.Phys.J. **C73**.8 (2013) 2518, arXiv: `1302.4393 [hep-ex]`.

[142] D. Quality, *ATLAS Data Quality Operations in 2012*, tech. rep. ATL-DAPR-INT-2015-001, CERN, Jan. 2015, URL: `https://cds.cern.ch/record/1982821`.

[143] J. Pequenao and P. Schaffner, “An computer generated image representing how ATLAS detects particles”, Jan. 2013, URL: `https://cds.cern.ch/record/1505342`.

[144] S. D. Ellis and D. E. Soper, *Successive combination jet algorithm for hadron collisions*, Phys.Rev. **D48** (1993) 3160–3166, arXiv: `hep-ph/9305266 [hep-ph]`.

[145] Y. L. Dokshitzer et al., *Better jet clustering algorithms*, JHEP **9708** (1997) 001, arXiv: `hep-ph/9707323 [hep-ph]`.

[146] M. Wobisch and T. Wengler, *Hadronization corrections to jet cross-sections in deep inelastic scattering* (1998), arXiv: `hep-ph/9907280 [hep-ph]`.

[147] M. Cacciari, G. P. Salam and G. Soyez, *The Anti-k(t) jet clustering algorithm*, JHEP **0804** (2008) 063, arXiv: `0802.1189 [hep-ph]`.

[148] W. Lampl et al., *Calorimeter Clustering Algorithms: Description and Performance*, tech. rep. ATL-LARG-PUB-2008-002. ATL-COM-LARG-2008-003, CERN, Apr. 2008.

[149] G. Aad et al., *Jet energy measurement and its systematic uncertainty in proton-proton collisions at $\sqrt{s} = 7$ TeV with the ATLAS detector* (2014), arXiv: `1406.0076 [hep-ex]`.

[150] M. Cacciari and G. P. Salam, *Pileup subtraction using jet areas*, Phys.Lett. **B659** (2008) 119–126, arXiv: `0707.1378 [hep-ph]`.

[151] *Tagging and suppression of pileup jets with the ATLAS detector*, tech. rep. ATLAS-CONF-2014-018, CERN, May 2014.

[152] *Commissioning of the ATLAS high-performance b-tagging algorithms in the 7 TeV collision data*, tech. rep. ATLAS-CONF-2011-102, CERN, July 2011.

[153] *Calibration of the performance of b-tagging for c and light-flavour jets in the 2012 ATLAS data*, tech. rep. ATLAS-CONF-2014-046, CERN, July 2014.

[154] *Calibration of b-tagging using dileptonic top pair events in a combinatorial likelihood approach with the ATLAS experiment*, tech. rep. ATLAS-CONF-2014-004, CERN, Feb. 2014.

[155] G. Aad et al., *Electron and photon energy calibration with the ATLAS detector using LHC Run 1 data*, Eur.Phys.J. **C74**.10 (2014) 3071, arXiv: `1407.5063 [hep-ex]`.

[156] G. Aad et al., *Electron reconstruction and identification efficiency measurements with the ATLAS detector using the 2011 LHC proton-proton collision data*, Eur.Phys.J. **C74** (2014) 2941, arXiv: `1404.2240 [hep-ex]`.

[157] S. Hassani et al., *A muon identification and combined reconstruction procedure for the ATLAS detector at the LHC using the (MUONBOY, STACO, MuTag) reconstruction packages*, Nuclear Instruments and Methods in Physics Research Section A: Accelerators, Spectrometers, Detectors and Associated Equipment **572**.1 (2007) 77–79, Frontier Detectors for Frontier Physics Proceedings of the 10th Pisa Meeting on Advanced Detectors, ISSN: 0168-9002, URL: `http://www.sciencedirect.com/science/article/pii/S0168900206019863`.

[158] *Muon Momentum Resolution in First Pass Reconstruction of pp Collision Data Recorded by ATLAS in 2010*, tech. rep. ATLAS-CONF-2011-046, CERN, Mar. 2011.

[159] *A measurement of the ATLAS muon reconstruction and trigger efficiency using J/psi decays*, tech. rep. ATLAS-CONF-2011-021, CERN, Mar. 2011.

[160] G. Aad et al., *Identification and energy calibration of hadronically decaying tau leptons with the ATLAS experiment in pp collisions at $\sqrt{s}$=8 TeV*, tech. rep., 2014, arXiv: `1412.7086 [hep-ex]`.

[161] B. P. Roe et al., *Boosted decision trees as an alternative to artificial neural networks for particle identification*, Nuclear Instruments and Methods in Physics Research Section A: Accelerators, Spectrometers, Detectors and Associated Equipment **543**.2–3 (2005) 577–584, ISSN: 0168-9002.

[162] P. Speckmayer et al., *The toolkit for multivariate data analysis, TMVA 4*, J.Phys.Conf.Ser. **219** (2010) 032057.

[163] G. Aad et al., *Performance of missing transverse momentum reconstruction in proton-proton collisions at $\sqrt{s} = 7$ TeV with ATLAS*, The European Physical Journal C **72**.1, 1844 (2012), ISSN: 1434-6044.

[164] *Performance of Missing Transverse Momentum Reconstruction in ATLAS studied in Proton-Proton Collisions recorded in 2012 at 8 TeV*, tech. rep. ATLAS-CONF-2013-082, CERN, Aug. 2013.

[165] A. Harmon, *Sherpa and Open Science Grid: Predicting the emergence of jets*, 2014, URL: `http://www.isgtw.org/feature/sherpa-and-open-science-grid-predicting-emergence-jets` (visited on 30/09/2014).

[166] T. Sjöstrand, S. Mrenna and P. Skands, *PYTHIA 6.4 Physics and Manual*, JHEP **0605** (2006) 026, arXiv: `hep-ph/0603175 [hep-ph]`.

[167] T. Sjöstrand, S. Mrenna and P. Skands, *A Brief Introduction to PYTHIA 8.1*, Comp. Phys. Comm. **178** (2007) 852–867, arXiv: `0710.3820 [hep-ph]`.

[168] G. Corcella et al., *HERWIG 6: An Event generator for hadron emission reactions with interfering gluons (including supersymmetric processes)*, JHEP **0101** (2001) 010, arXiv: `hep-ph/0011363 [hep-ph]`.

[169] M. Bahr et al., *Herwig++ Physics and Manual*, Eur. Phys. J. **C58** (2008) 639–707, arXiv: `0803.0883v3 [hep-ph]`.

[170] Gleisberg, T. and others, *Event generation with SHERPA 1.1*, JHEP **0902** (2009) 007, arXiv: `0811.4622 [hep-ph]`.

[171] S. Höche et al., *QCD matrix elements and truncated showers*, JHEP **0905** (2009) 053, arXiv: `0903.1219 [hep-ph]`.

[172] T. Gleisberg and S. Höche, *Comix, a new matrix element generator*, JHEP **0812** (2008) 039, arXiv: `0808.3674 [hep-ph]`.

[173] S. Schumann and F. Krauss, *A Parton shower algorithm based on Catani-Seymour dipole factorisation*, JHEP **0803** (2008) 038, arXiv: `0709.1027 [hep-ph]`.

[174] M. L. Mangano et al., *ALPGEN, a generator for hard multiparton processes in hadronic collisions*, JHEP **0307** (2003) 001, arXiv: `hep-ph/0206293 [hep-ph]`.

[175] S. Frixione and B. R. Webber, *Matching NLO QCD computations and parton shower simulations*, JHEP **0206** (2002) 029, arXiv: `hep-ph/0204244 [hep-ph]`.

[176] S. Frixione, P. Nason and B. R. Webber, *Matching NLO QCD and parton showers in heavy flavor production*, JHEP **0308** (2003) 007, arXiv: `hep-ph/0305252 [hep-ph]`.

[177] S. Frixione et al., *Single-top production in MC@NLO*, JHEP **0603** (2006) 092, arXiv: `hep-ph/0512250 [hep-ph]`.

[178] P. Nason, *A new method for combining NLO QCD with shower Monte Carlo algorithms*, JHEP **0411** (2004) 040, arXiv: `hep-ph/0409146 [hep-ph]`.

[179] S. Frixione, P. Nason and C. Oleari, *Matching NLO QCD computations with Parton Shower simulations: the POWHEG method*, JHEP **0711** () 070, arXiv: `0709.2092 [hep-ph]`.

[180] S. Alioli et al., *A general framework for implementing NLO calculations in shower MC programs: the POWHEG BOX*, JHEP **1006** (2010) 043, arXiv: `1002.2581 [hep-ph]`.

[181] S. Jadach et al., *The Tau Decay Library TAUOLA, Version 2.4*, Comput. Phys. Commun. **76** (1993) 361.

[182] P. Golonka et al., *The Tauola-Photos-F Environment for the TAUOLA and PHOTOS Packages, Release II*, Comput. Phys. Commun. **174** (2006) 818.

[183] E. Barberio and Z. Was, *PHOTOS - a Universal Monte Carlo for QED Radiative Corrections: Version 2.0*, Comput. Phys. Commun. **79** (1994) 291.

[184] S. Agostinelli et al., GEANT4*: A simulation toolkit*, Nucl. Instrum. Meth. **A506** (2003) 250.

[185] *The ATLAS Simulation Infrastructure*, Eur. Phys. J. **C70** (2010) 823.

[186] *The simulation principle and performance of the ATLAS fast calorimeter simulation fastcalosim*, ATL-PHYS-PUB-2010-013, `https://cds.cern.ch/record/1300517`, 2010.

[187] S. Allwood-Spires et al., *Monte Carlo samples used for top physics*, tech. rep. ATL-PHYS-INT-2010-132, CERN, Dec. 2010.

[188] J. Butterworth, J. R. Forshaw and M. Seymour, *Multiparton interactions in photoproduction at HERA*, Z. Phys. **C72** (1996) 637, arXiv: `hep-ph/9601371 [hep-ph]`.

[189] S. Catani et al., *Vector boson production at hadron colliders: A Fully exclusive QCD calculation at NNLO*, Phys. Rev. Lett. **103** (2009) 082001, arXiv: `0903.2120 [hep-ph]`.

[190] A. Martin et al., *Parton distributions for the LHC*, Eur. Phys. J. **C63** (2009) 189–285, arXiv: `0901.0002 [hep-ph]`.

[191] M. Cacciari et al., *Top-pair production at hadron colliders with next-to-next-to-leading logarithmic soft-gluon resummation*, Phys. Lett. **B710** (2012) 612–622, arXiv: `1111.5869 [hep-ph]`.

[192] M. Czakon and A. Mitov, *Top++: A Program for the Calculation of the Top-Pair Cross-Section at Hadron Colliders* (2011), arXiv: `1112.5675 [hep-ph]`.

[193] B. P. Kersevan and E. Richter-Was, *The Monte Carlo event generator AcerMC version 2.0 with interfaces to PYTHIA 6.2 and HERWIG 6.5* (2004), arXiv: `hep-ph/0405247 [hep-ph]`.

[194] N. Kidonakis, *NNLL resummation for s-channel single top quark production*, Phys. Rev. **D81** (2010) 054028, arXiv: `1001.5034 [hep-ph]`.

[195] N. Kidonakis, *Two-loop soft anomalous dimensions for single top quark associated production with a W- or H-*, Phys. Rev. **D82** (2010) 054018, arXiv: `1005.4451 [hep-ph]`.

[196] N. Kidonakis, *Next-to-next-to-leading-order collinear and soft gluon corrections for t-channel single top quark production*, Phys. Rev. **D83** (2011) 091503, arXiv: `1103.2792 [hep-ph]`.

[197] J. M. Campbell, R. K. Ellis and C. Williams, *Vector boson pair production at the LHC*, JHEP **1107** (2011) 018, arXiv: `1105.0020 [hep-ph]`.

[198] H. L. Lai et al., *New parton distributions for collider physics*, Phys. Rev. **D82** (2010) 074024, arXiv: `1007.2241 [hep-ph]`.

[199] P. Z. Skands, *Tuning Monte Carlo Generators: The Perugia Tunes*, Phys. Rev. **D82** (2010) 074018, arXiv: `1005.3457 [hep-ph]`.

[200] *ATLAS tunes of* PYTHIA *6 and Pythia 8 for MC11*, ATL-PHYS-PUB-2011-009, `https://cdsweb.cern.ch/record/1363300`, 2011.

[201] J. Pumplin et al., *New generation of parton distributions with uncertainties from global QCD analysis*, JHEP. **0207** (2002) 012, arXiv: `hep-ph/0201195 [hep-ph]`.

[202] *Summary of ATLAS Pythia 8 tunes*, ATL-PHYS-PUB-2012-003, `https://cdsweb.cern.ch/record/1474107`, 2012.

[203] P. M. Nadolsky et al., *Implications of CTEQ global analysis for collider observables*, Phys. Rev. **D78** (2008) 013004, arXiv: `0802.0007 [hep-ph]`.

[204] W. Beenakker et al., *Squark and Gluino Production at Hadron Colliders*, Nucl. Phys. **B492** (1997) 51–103, arXiv: `hep-ph/9610490 [hep-ph]`.

[205] A. Kulesza and L. Motyka, *Threshold resummation for squark-antisquark and gluino-pair production at the LHC*, Phys. Rev. Lett. **102** (2009) 111802, arXiv: `0807.2405 [hep-ph]`.

[206] A. Kulesza and L. Motyka, *Soft gluon resummation for the production of gluino-gluino and squark-antisquark pairs at the LHC*, Phys. Rev. **D80** (2009) 095004, arXiv: `0905.4749 [hep-ph]`.

[207] W. Beenakker et al., *Soft-gluon resummation for squark and gluino hadroproduction*, JHEP **0912** (2009) 041, arXiv: `0909.4418 [hep-ph]`.

[208] W. Beenakker et al., *Squark and gluino hadroproduction*, Int. J. Mod. Phys. **A26** (2011) 2637–2664, arXiv: `1105.1110 [hep-ph]`.

[209] M. Kramer et al., *Supersymmetry production cross sections in pp collisions at* $\sqrt{s} = 7\,\mathrm{TeV}$ (2012), arXiv: `1206.2892 [hep-ph]`.

[210] ATLAS Inner Detector Group, *Inner Detector Tracking Performance Guidelines - Pile-up Rescaling*, tech. rep. Link: `https://twiki.cern.ch/twiki/bin/viewauth/AtlasProtected/InDetTrackingPerformanceGuidelines`, Revision 20, Sept. 2013.

[211] G. Aad et al., *Search for pair-produced third-generation squarks decaying via charm quarks or in compressed supersymmetric scenarios in pp collisions at* $\sqrt{s}$*=8 TeV with the ATLAS detector* (2014), arXiv: `1407.0608 [hep-ex]`.

[212] *Measurements of top quark pair relative differential cross-sections with ATLAS in pp collisions at* $\sqrt{s} = 7\,\mathrm{TeV}$, Eur. Phys. J **C73** (2013) 2261, arXiv: `1207.5644 [hep-ex]`.

[213] *Measurement of top-quark pair differential cross-sections in the l+jets channel in pp collisions at* $\sqrt{s} = 7\,\mathrm{TeV}$ *using the ATLAS detector* (), URL: `http://cdsweb.cern.ch/record/1600778`.

[214] G. Aad et al., *Search for the direct production of charginos, neutralinos and staus in final states with at least two hadronically decaying taus and missing transverse momentum in pp collisions at* $\sqrt{s} = 8$ *with the ATLAS detector*, English, Journal of High Energy Physics **2014**.10, 96 (2014), URL: `http://dx.doi.org/10.1007/JHEP10(2014)096`.

[215] G. Aad et al., *Search for squarks and gluinos with the ATLAS detector in final states with jets and missing transverse momentum using* $\sqrt{s} = 8$ *TeV proton-proton collision data*, Journal of High Energy Physics **2014**.9, 176 (2014), URL: `http://dx.doi.org/10.1007/JHEP09(2014)176`.

[216] S. Amoroso et al., *Search for squarks and gluinos with the ATLAS detector in final states with jets and missing transverse momentum and 20.3* fb^{-1} *of* $\sqrt{s} = 8$ *TeV proton–proton collision data: supporting documentation*, tech. rep. ATL-COM-PHYS-2013-1224, CERN, Aug. 2013.

[217] G. Cowan et al., *Asymptotic Formulae for Likelihood-Based Tests of new Physics*, Eur. Phys. J. **C71** (2011) 1554, eprint: `arXiv:1007.1727`.

[218] G. Cowan, *Expected discovery significance for counting experiment with background uncertainty*, `www.pp.rhul.ac.uk/~cowan/atlas/cowan_statforum_8may12.pdf`, 2012.

[219] *Search for Supersymmetry in Events with Large Missing Transverse Momentum, Jets, and at Least One Tau Lepton in 21* fb^{-1} *of* $\sqrt{s} = 8$ *TeV Proton–Proton Collision Data with the ATLAS Detector* (), URL: `http://cdsweb.cern.ch/record/1525882`.

[220] S. Owen, *Data-driven estimation of the QCD multijet background to SUSY searches with jets and missing transverse momentum at ATLAS using jet smearing* (), URL: `http://cdsweb.cern.ch/record/1423310`.

[221] *Jet energy measurement with the ATLAS detector in proton-proton collisions at sqrt(s) = 7 TeV* (2011), arXiv: `1112.6426 [hep-ex]`.

[222] *Procedure for the LHC Higgs boson search combination in Summer 2011*, tech. rep. CMS-NOTE-2011-005. ATL-PHYS-PUB-2011-11, CERN, Aug. 2011.

[223] J. Neyman and E. S. Pearson, *On the Problem of the Most Efficient Tests of Statistical Hypotheses*, Philosophical Transactions of the Royal Society of London A: Mathematical, Physical and Engineering Sciences **231**.694-706 (1933) 289–337, ISSN: 0264-3952.

[224] K. Cranmer, *Statistical challenges for searches for new physics at the LHC* (2005) 112–123, arXiv: `physics/0511028`.

[225] A. L. Read, *Presentation of search results: The CL_s technique*, J. Phys. **G 28** (2002) 2693.

[226] M. Baak et al., *HistFitter software framework for statistical data analysis* (2014), arXiv: `1410.1280 [hep-ex]`.

[227] L. Moneta et al., *The RooStats Project*, PoS **ACAT2010** (2010) 057, arXiv: `1009.1003 [physics.data-an]`.

[228] A. S. group, *SUSY summary plots*, 2014, URL: `https://atlas.web.cern.ch/Atlas/GROUPS/PHYSICS/CombinedSummaryPlots/SUSY/index.html` (visited on 14/01/2015).

[229] G. Aad et al., *Search for supersymmetry at $\sqrt{s} = 8$ TeV in final states with jets and two same-sign leptons or three leptons with the ATLAS detector*, Journal of High Energy Physics **2014**.6, 35 (2014), URL: `http://dx.doi.org/10.1007/JHEP06(2014)035`.

[230] Oliver Ricken, *Development and Analysis of Simplified Models in the Search for Supersymmetry with Tau Leptons in the Final State at the ATLAS Experiment*, MA thesis: University of Bonn, Nov. 2014.

[231] Philipp Thomas König, *Studie zur Suche nach SUSY am ATLAS-Experiment am LHC für Run II*, B Sc thesis: University of Bonn, July 2014.

[232] ATLAS Top Group, *2012 Top Cross Sections*, tech. rep. Link: `https://twiki.cern.ch/twiki/bin/viewauth/AtlasProtected/TopCommonParametersMC12`, Revision 12, Aug. 2013.

[233] J. Abdallah et al., *Search for Scalar Top Quarks in final states with two charm jets and missing transverse momentum at sqrt(s) = 8 TeV: INT supporting note*, tech. rep. ATL-COM-PHYS-2013-1642, Draft of the supporting note: CERN, Dec. 2013.

List of Figures

List of Tables

Acknowledgements

First and foremost I would like to thank my mum. From being a young child, she has opened my eyes for the marvels of nature, has always endured and answered my nosy questions about everything as good as she could and supported me in my plans and wishes, often to her own disadvantage. Thank you, mum, for everything.

Now to the scientific part.

I would like to thank Klaus Desch for providing me with the opportunity to do my PhD in his group. The great academic freedom he allowed and the insightful suggestions he gave – together with his powerful backup if needed – made it possible to acquire all the knowledge needed to finally compile this document. The same holds for Philip Bechtle, who has been a great motivator, idea creator and discussion partner, and for Adrian Vogel who helped me to get started with ATLAS at the first place.

The good interaction with the other SUSY PhD students, Martin Schultens, Till Nattermann, Robert Zimmermann and Carolin Zendler allowed for a lot of fast internal discussion and collaboration and facilitated my work a lot. The same holds for the students that contributed to this work with their Master or Bachelor theses, Oliver Ricken and Philip König.

In the years working on my PhD I met a lot of colleagues from Bonn outside my own analysis subject that quickly became close friends, more than I could list here. Among those I would like to mention especially Jan Stillings and Kristof Schmieden, whom I shared a fantastic year in Geneva with. A special honorable mention also goes to Christian Limbach and Mathias Uhlenbrock, the masters of Doktorwagen design. Without this lively and friendly atmosphere around me I would probably not have had the patience to overtake all the obstacles on the way.

Outside my group, I had the pleasure to work with a lot of talented and motivated people that contributed – directly and indirectly – to this thesis. At first I would like to mention Fabrizio Salvatore, who supported and guided me in many ways and whom I'm really thankful for the lot of opportunities he provided me with and the lot of fights he fought for our team. But also other people like Wolfgang Ehrenfeld and Wolfgang Liebig have supported me over a long time and I'm really thankful for that! I especially would like to thank Dörthe Kennedy and Anthony Rose who have been working with me on this analysis and had a large share in the results we could finally obtain. But also the many other students working on similar analyses where always a pleasure to work with.

Throughout my work I met a few people that supported me in a special way, that boosted my career and that I have a special connection to. Here I would especially like to mention Hartmuth Kalinowsky, who was the first to draw me into experimental particle physics at all, Ulrike Thoma, in whose group I had the pleasure to work as a student and to do my Diploma thesis, Norbert Wermes, who has been – and still is – supporting me in many ways and Christoph Rembser who was and still is my good spirit at CERN. Herbi Dreiner and the Physikshow he started have a good part in my career as well. There I learned about how to present things to "normal" people and how to spread my own fascination on science. I had a lot of fun and great times with many other students developing, rehearsing and presenting shows to many people in different countries and locations.

Although this thesis is meant to be the product of a single person, in reality there are a lot of people behind, without whom it would be impossible to create such a document. They are the people that keep the institute running, from providing computing resources and organizational assistance to the many small things needed so that we scientist are in the lucky position to focus on our science. I would like to thank all of them, they have their part in this thesis as much as any other colleague from physic has.

Then I also want to thank my proof-reading team (Jan, Robert, Philip, Olli, Martin, Christoph Krieger and Michael Lupberger) for desperately trying to iron out my English kinks and to make me sound a bit less like QVC.

Besides all the personal acknowledgements, I would also like to thank the Bonn-Cologne-Graduate-School for their scientific and financial support as well as all the other funding agencies, mainly the BMBF, that happened to pay for my position over the years.

I'm sure I forgot a lot of people that would highly deserve to be mentioned here. I apologize to all of them, you are for sure aware of my gratitude even without your name standing here.

Last but not least I would like to thank my whole family and in particular Christina Hansmeier for their patience, the interest they took in my work and their endurance when I started talking over my physics and couldn't find an end.

Guys, you all rock!